# Estimating pre-historic earthquake parameters in the Hamilton lowlands using laboratory geotechnical analyses of seismically liquefied volcanic-ash layers in lakes

*A thesis*

*submitted in fulfilment*

*of the requirements for the degree*

*of*

**Doctor of Philosophy in Earth Sciences**

*at*

**The University of Waikato**

*by*

**Jordanka Chaneva**


THE UNIVERSITY OF
WAIKATO
*Te Whare Wānanga o Waikato*

2024

# Abstract

Soft-sediment deformation structures caused by pre-historic earthquakes were discovered in volcanic-ash (tephra) units preserved as discrete layers within soft, organic lake sediments in the Hamilton lowlands, North Island, New Zealand. Complementing a broader paleoliquefaction project that involves geological and seismological perspectives as well, this PhD research was focused on a geotechnical approach in analysing the paleoliquefaction features in the tephra layers across multiple 20 cal-ka-aged lakes in the Hamilton lowlands. Aiming to back-analyse pre-historic earthquakes that might have caused the palaeoliquefaction features, this thesis also had to address literature and knowledge gaps related to cyclic undrained behaviour and liquefaction resistance of pumiceous silts and sand-silt mixtures. Thus, the scope of this research covered the following objectives: (1) analyses of the geotechnical properties of the tephras of interest in order to define their liquefaction susceptibility, (2) investigation of the undrained monotonic and cyclic behaviour of a pumiceous silt (Tuhua silt, from lacustrine Tuhua tephra aged 7.6 cal ka) in order to fill knowledge gaps related to potential particle crushing affecting undrained cyclic behaviour as well as liquefaction resistance in pumiceous silts, (3) identification of the potential threshold of pumice content and/or fines content, at which pumiceous sand-silt mixtures (internal beds from lacustrine Mamaku tephra aged 8.0 cal ka) become crushable, and finally (4) developing a framework, that extends laboratory obtained liquefaction resistance ratios of three different beds of one of the tephras of interest, that provided enough volume for cyclic undrained triaxial testing (Mamaku tephra), into the rest of the tephras across the studied lakes (that only provided small volumes for sampling). The last objective assisted in reaching the main aim of this thesis which was to obtain the equivalent triggering earthquake parameters, i.e., peak ground acceleration, $a_{max}$ and earthquake magnitude, $M$ for the tephras across the lakes, based on their estimated liquefaction resistances. It was found that the tephras in the lakes are pumiceous and liquefiable within the grain-size range: silts to sandy silts to silty sands. The results from undrained triaxial testing on the pumiceous silt showed that no particle crushing occurred and that the silty material behaved closer to the typical trends established for hard-grained soils than to those associated with pumiceous sands. Furthermore, the undrained cyclic triaxial testing program on three different beds, one silt and two silty sands, from one of the tephras of interest (Mamaku tephra), suggested a fines threshold below which begin to crush during cyclic triaxial testing to be somewhere between 31% and 20%. Empirical correlations used to estimate earthquake parameters from liquefaction resistance that are derived for hard-grained soils were, thus, considered reasonable for application to the pumiceous materials considered in the current study. The final results of this study showed that the tephra layers across the lakes were very sensitive and vulnerable to liquefaction at very low peak ground accelerations, i.e. $a_{max}$ ranging from 0.02 to 0.08 g within the range of magnitudes, $M$ = 5 to 8.5. The high vulnerability to liquefaction across all the Mamaku tephra layers in the Hamilton lowlands (~13 lakes) was considered to be the result of the very low in-situ overburden stresses, consequence of their shallow burial depths in the lake environment, as well as the relatively low liquefaction resistance in situ. The results presented in this dissertation, (1) supply valuable information about the liquefaction potential of pre-historically liquefied tephra layers, assisting local paleoliquefaction studies in the Hamilton lowlands area, (2) explore the possibility of applying laboratory-based liquefaction resistance analysis in paleoliquefaction studies, and (3) contribute to better understanding of the undrained behaviour and liquefaction resistance of pumiceous sand-silt mixtures.

# Acknowledgments

I am endlessly grateful to my chief supervisor, Dr Vicki Moon, as well as my co-supervisors, Prof David Lowe, Dr Max Kluger, and Prof Rolando Orense, for their superb guidance, support, and encouragement during my PhD study. Overcoming the challenges, especially in the experimental part of my research, as well as the essential field investigations, during a global pandemic, full of uncertainties, was barely an inconvenience having you as my team of supervisors. I have learned so much from you all, not only from a scientific and engineering point of view but also from perspectives of collegiality, patience, and openness to those from other research backgrounds and disciplines. I am lucky and feel privileged to have been given the chance to be a part of the "Tephra Seismites" project (see funding sources acknowledged below).

I also want to acknowledge and thank Richard Melchert, Dr Tehnuka Ilanko, Vittoria Gibbons, Josh Hughes, and Dr Marcus Vandergoes and Dr Susie Wood, co-leaders of the Lakes380 project, and their lake coring team including Henry Gard (GNS Science) and Dr Andrew Rees, VUW), along with boat masters Chris Morcom (University of Waikato) and Joe Butterworth (JFB Enviro). Prof Rich Johnston (Swansea University, UK) provided valuable help with an initial CT scan and subsequent interpretations, Nic Ross (Hamilton Radiology) undertook CT scanning of all lake sediment cores, and Dr Drew Lorrey and John-Mark Woolley (NIWA) led and helped evaluate ground-penetrating radar undertaken at Lake Rotoroa. Kirsty Vincent, Helen Turner, Dr Stella Reynova, Tom Robertson, Annette Rogers, and Ben Roche are additionally thanked for their assistance and help during the field or laboratory work, or both.

Sincere thanks go to Dr Sean Rees (University of Canterbury) for his unselfish, patient and invaluable technical help and support to overcome setbacks related to the experimental triaxial equipment, as well as necessary equipment accessories.

Dr Pillar Villamor and Jose Moratalla Campuzano are thanked for their contributions in the discussions in the broader scientific sense, yet related to my specific topic, that were more than helpful and useful.

Private landowners, staff from councils (Hamilton City, Waikato District, and Waipā District) and Department of Conservation, Mrs. Hekeiterangi Broadhurst and Wiremu Puke (Ngāti Wairere, Ngāti Porou), and Hazel Coromandel-Wander and Gaylene Roberts (representing Ngā Iwi Tōpū O Waipā), are thanked for providing access for lake coring and other information and support. Carol Robinson and Stephen Turner (School of Science Research Office) helped facilitate payments and other support during my PhD enrollment.

Finally, I want to thank and acknowledge my family and my close friends for their moral support and complete faith in me during my PhD research.

Funding acknowledgement

I gratefully acknowledge the New Zealand Government funding agencies, and the Royal Society of New Zealand, for funding support both for my research and for the wider "Tephra seismites" project as follows: the MBIE Endeavour Fund (Smart Ideas) (grant UOWX1903) and the Waikato Regional Council (Hamilton) (facilitated by Dr Rick Liefting) provided funding specifically for my PhD; the Marsden Fund (grant UOW1902); Earthquake Commission EQC (contracts 15/U713, BIG0122020); and a University of Waikato 2016-SIF grant. I thank the School of Science and the wider University of Waikato for providing the facilities and workspace during the duration of my PhD research.

## Table of Contents

# List of figures

# List of tables

# Nomenclature

## Roman symbols

| | |
|---|---|
| $a_{max}$ | maximum ground acceleration |
| $A_c$ | angular coefficient |
| $A_r$ | aspect ratio |
| $D_{50}$ | median grain size |
| $D_{10}$ | grain size at 10% passing |
| $D_{90}$ | grain size at 90% passing |
| $Dr$ | relative density |
| $Dr,_i$ | initial relative density |
| $Dr,_c$ | consolidated relative density |
| $e$ | void ratio |
| $e_c$ | consolidated void ratio |
| $e_i$ | initial void ratio |
| $e_{in\text{-}situ}$ | in-situ void ratio |
| $e_{max}$ | maximum void ratio |
| $e_{min}$ | minimum void ratio |
| $e_{ss}$ | void ratio at the steady state line |
| $f$ | loading frequency |
| $FC$ | fines content |
| $F_{SL}$ | factor of safety against liquefaction |
| $Gs$ | specific gravity |
| $Ko$ | lateral stress coefficient |
| $M$ | earthquake magnitude |
| $N_{A,pumice}$ | number of points over pumiceous particles in SEM images |

| | |
|---|---|
| $N_{A,total}$ | total number points over particles (pumice and non-pumice) in SEM images |
| $N_C$ | number of cycles |
| $N_{CL}$ | number of cycles to liquefaction |
| $p'$ | mean effective stress |
| $PC$ | pumice content |
| $q_{dev}$ | deviator stress |
| $R_c$ | roundness coefficient |
| $r_d$ | stress reduction coefficient |
| $r_u$ | pore pressure ratio |
| $u$ | pore pressure |
| $V_s$ | shear wave velocity |

## Greek symbols

| | |
|---|---|
| $\sigma_c'$ | effective consolidation pressure |
| $\sigma_v'$ | effective vertical stress |
| $\varepsilon_{da}$ | double amplitude axial strain |
| $\psi$ | state parameter |
| $\rho_{dry}$ | in-situ dry density |
| $\rho_{sat}$ | in-situ saturated density |
| $\rho_p$ | particle density |
| $\rho_{water}$ | density of water |

## Acronyms / Abbreviations

| | |
|---|---|
| CPT | cone penetration test |
| *CRR* | cyclic resistance ratio |
| CSL | critical state line |
| *CSR* | cyclic stress ratio |

| | |
|---|---|
| DEM | discrete element method |
| EPWP | excess pore water pressure |
| PI | plasticity index |
| SD | standard deviation |
| SEM | scanning electron microscope |
| SSDS | soft sediment deformation structures |
| SPT | standard penetration test |
| MSF | magnitude scaling factor |

# Chapter 1. Introduction

## 1.1. Previous research and motivation

Paleoliquefaction studies are a branch of paleoseismology that focuses on analysing soft-sediment deformation structures preserved in geological deposits caused by earthquake-induced liquefaction (Tuttle et al. 2019). For regions where the recorded seismic case studies are poor, as well as regions where active faults might be difficult to identify, paleoliquefaction studies provide insight into pre-historical earthquakes, and help scientists understand fault zones and seismic sources better as well as minimize uncertainties in seismic hazard assessments (Obermeier 1998; Saucier 1991; Tuttle et al. 2002). Lacustrine environments have been studied in the context of paleoliquefaction before, as the calm nature of the lakes provides good geological preservation of past sediment disturbances (Ghazoui et al. 2019; Gladkov et al. 2016; Monecke et al. 2007; Rodríguez-López et al. 2007; Rodríguez-Pascua et al. 2010; Shilts and Clague 1992; Üner 2014; Vardanyan et al. 2018).

Very recently, in southern New Zealand, the 2010-2011 Canterbury earthquake sequence created extensive scientific data in the paleoliquefaction area as it was found that a system of crustal faults, some of which did not rupture the surface, produced the earthquakes (Villamor et al. 2016). Considering the lessons learned from the Canterbury earthquakes, which redefined the seismic hazard of the Canterbury region (Van Dissen et al. 2021), as well as the relatively short seismic catalogue of New Zealand, other regions in the country, such as the Hamilton lowlands and the Waikato area became a subject of interest for seismic geologists. In fact, the primary recommendation of the Royal Commission (2012) into the Canterbury earthquakes was that research should be continued into the location of active faults in population centres in New Zealand (additional to Christchurch), and that areas of low to moderate seismicity be examined to discover if hidden active faults lie under or near major cities to provide realistic assessments of earthquake hazards and risks.

In 2015, newly discovered faults (Moon and Lange 2017) within the Hamilton lowlands (also known as the Hamilton Basin) and the subsequent identification of liquefaction features within the 20,000 calendar-year-old volcanogenic alluvial sediments infilling the lowlands in

part (Hinuera Formation), the latter indicating that at least one earthquake had probably taken place within the past 20,000 years to generate the liquefaction structures (Kleyburg et al. 2015), led to a re-evaluation of an earlier study of pumiceous volcanic-ash (tephra) layers preserved in lake sediments in the Hamilton lowlands (Lowe 1988). Tephra deposits are the explosively-erupted, unconsolidated, pyroclastic (fragmental) products of a volcanic eruption of any grain size or composition (Lowe 2011). They include volcanic ash, which is used both as a technical term for grain size (particles < 2 mm in diameter) in volcanological studies and also more broadly as a term encompassing fine grained pyroclastic material. In his previous tephrochronology studies, Lowe (1988) documented structural deformation features (voids, ash-filled 'cracks') in some tephra-fall layers (mainly comprising volcanic ash) preserved in lake sediments in the Hamilton lowlands cored in the late 1970s to mid-1980s. An earlier tentative hypothesis was that the deformation features may have been the result of bioturbation (Lowe 1988). A possible seismic origin, although considered, was disregarded because there were no known active faults in the Hamilton Basin at that time (David J. Lowe, person communication 2024). A similar reasoning (lack of known active faults) was applied to the interpretation of liquefaction structures observed within the fine alluvium of the Hinuera Formation (Hume et al. 1975), which were instead explained at that time by sedimentary mechanisms (Cam S. Nelson, personal communication 2023). However, the "bioturbation" hypothesis was subsequently discarded because the so-called 'burrows' did not have rounded ends. Another hypothesis, that the deformation features represented desiccation features, was also discounted because paleolimnological evidence shows that the lakes had never dried out (Green 1979; Green and Lowe 1985, 1994, 2024). Hence it was realized that the deformation features, for which the term 'tephra seismites' was created, must represent the effect of shaking because of seismic activity on one or more nearby faults, either within the Hamilton Basin or in the adjacent Hauraki Basin/lowlands (or elsewhere) (Persaud et al., 2016). Moreover, the deformation structures have been found in multiple locations (lakes) with similar geological and ground water settings, and so seismically induced liquefaction was considered the most probable cause to explain the deformations (Fig. 1.1).

A multidisciplinary project that analysed the paleoliquefaction features in the tephra layers across the lakes in the Hamilton lowlands was thus initiated and included (1) a spatial and temporal analysis of the deformation features as well as (2) a geotechnical approach to study the liquefaction potential of the tephra materials. The presented PhD thesis focuses on the latter aspect, and studies the tephras from a geotechnical point of view in order to estimate

the potential pre-historic earthquakes (i.e. $a_{max}$ and $M$) that might have caused the seismically-induced deformation structures. The deformation structures were described in meticulous detail by Kluger et al. (2023), where their seismic origin was confirmed as most likely, after considering all other possible causes. (Kluger et al. 2023, see Appendix D).

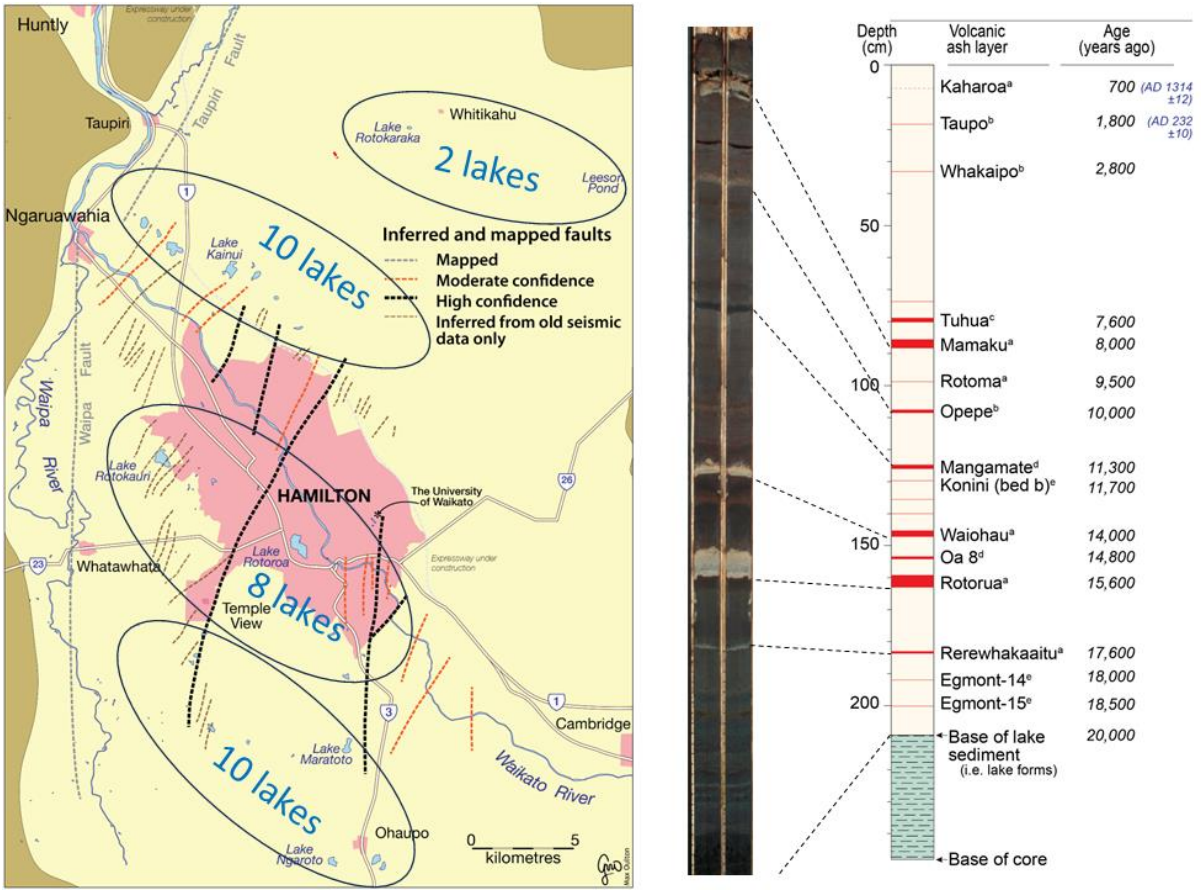


Fig. 1.1 (Left) Map showing how lakes are scattered amidst the newly-identified faults in the Hamilton lowlands (after Moon and de Lange, 2017; Kluger et al., 2023). (Right) Photograph of a lake sediment core and the stratigraphy and ages of the main tephra layers (mainly pale layers in the dark organic sediment) in Lake Rotoroa (Hamilton Lake). Photo of core by D.A. Speirs; stratigraphy/ages (in calendar [cal] years ago) after Lowe (2024)

Please note that where ages are reported in the thesis, they are usually reported in calendar or calibrated (cal) years before present (BP), 'present' in the radiocarbon ($^{14}C$) timescale being 1950 AD/CE. Sometimes the abbreviation, ka, is used – meaning x1000 years.

The next section of this chapter (1.2) presents a review of the key aspects from the literature that helped (1) identify the research gaps that need to be addressed and overcome, (2) establish the research objectives that will fill the research gaps, and (3) define the main aim of the thesis after identifying existing methodologies that would be most applicable and appropriate to use. The literature review starts by defining the liquefaction phenomenon, as

well as presenting the most common (laboratory and in situ) methods for liquefaction triggering assessment. It then continues into summarizing the methodologies and tools used in geotechnical paleoliquefaction studies, in order to back-estimate pre-historic earthquake parameters. Finally, the addition of an overview of published research and findings related to soil mixtures containing pumiceous particles, funnels this introductory chapter into the main research aim and research objective section - 1.3. Pumiceous particles are volcanically-derived, vesicular, lightweight glassy particles of grain-sizes varying between gravel (lapilli), sand (coarse to medium volcanic-ash), and fines (fine ash) (White, J.D.L. and Houghton, 2006). They are characterized by rough texture, high angularity, and in general higher potential to crushing than hard-grained (e.g. quartzitic) particles.

## 1.2. Liquefaction

### 1.2.1. Liquefaction definitions

The term liquefaction has been used in reference to a variety of failure mechanisms in soils. The first liquefaction phenomena definition was described in the early research and work of Casagrande and his student, Castro, about soils and their unique behaviour characteristic to change volume when sheared (Castro 1969, 1975). Note that throughout the thesis, the term 'soil' is used in the broad engineering sense (e.g., see Holtz 1969) rather than pedological sense (e.g., see (Hewitt et al. 2021). The research following the two devastating earthquakes of 1964 ($M$ = 9.2 in Alaska, USA and $M$ = 7.5 in Niigata, Japan) that caused earthquake-induced liquefaction failures (Ishihara and Koga 1981; Seed and Idriss 1971), however emphasized the need for a technical understanding between liquefaction definitions related to soil failure. Today, the scientific and engineering community recognizes two main definitions of liquefaction, i.e., flow liquefaction and cyclic liquefaction (Ishihara 1993; Kramer 1996; Robertson et al. 2000). Flow liquefaction can be triggered by both monotonic and cyclic loading and is characterized with strain-softening response in undrained loading when the in-situ shear stress is greater than the undrained shear strength. Cyclic liquefaction, also commonly referred to as seismic liquefaction, is exclusively triggered by cyclic loading and is characterized with pore water pressure build-up leading to effective stress reversal to zero.

### 1.2.2. Liquefaction susceptibility analysis

The liquefaction potential analysis starts with a liquefaction susceptibility analysis. It has long been recognized that relatively "clean" sandy soils, with few fines, are potentially vulnerable

to seismically-induced liquefaction (Seed et al. 2003). Today the susceptibility of a soil to liquefaction can be evaluated using a combination of different sets of criteria, such as historic, geologic, compositional and state criteria (Kramer 1996).

Historical criteria are a simple consideration of whether or not the type of soil in consideration has liquefied in the past (Youd 1984). One way that this can be evaluated is via documented case histories and physical evidence of previous liquefaction manifestations such as sand boils or mud spouts on ground.

The geological setting, i.e., depositional and hydrological environment, as well as the age of the deposit have all been found to contribute to the liquefaction susceptibility of a soil deposit and are typically considered in the geological liquefaction susceptibility criteria (Youd and Hoose 1977; Youd and Perkins 1978).

The state set of criteria refers to the initial state of the soil by means of its initial void ratio and effective consolidation stress in relation to the critical state line, CSL values (Been and Jefferies 1985). The state parameter, $\psi$, that describes the initial state of a soil sample is defined as the difference between a given void ratio, $e$, and the corresponding void ratio of the critical or steady state line, $e_{ss}$, for the effective consolidation stress of interest, and it incorporates the combined effect of both the void ratio and the effective consolidation stress. Positive values of the state parameter indicate a loose and contractive soil, susceptible to liquefaction, whereas negative values indicate a dense and dilative soil, susceptible to cyclic mobility - a failure mechanism where the applied shear stress is not greater than the shear strength of the material, meaning stress reversal and zero effective stress is not reached.

The compositional set of criteria, that consider physical soil properties, such as particle shape, fines content, gradation, and plasticity are the most thoroughly investigated and updated and thus most commonly used for evaluating liquefaction susceptibility today. For example, round particle soils are known to densify more easily than soils with angular grains, and so they are considered more susceptible to liquefaction (Kramer, 1996). Furthermore, poorly graded soils have been considered to be less compact than well-graded ones and thus considered of a more liquefying nature (Fig. 1.2) (Japanese Technical standards, 2020). The most conclusive method for analysing liquefaction susceptibility today, however, is the one based on the plasticity of the fines portion of the soil mixture. In this context several authors had proposed criteria that were mostly empirical (Andrews and Martin 2000; Bray et al. 2004), until Boulanger and Idriss suggested a different approach in 2006. Their view was proposing

an estimation of the potential strength loss and large strain development depending on the type of the fine-grained soils. In other words, it should be differentiated what type of fine-grained soils should be evaluated using procedures that are similar to those that are appropriate for sands, as opposed to ones that are similar to those appropriate for clays. Soils that exhibit clay-like behaviour are considered non-susceptible to liquefaction, conversely, soils that exhibit sand-like behaviour are considered liquefiable. Their results are expressed through the plasticity index, (PI). Fine-grained soils with a PI > 7, can confidently be considered to exhibit clay-like behaviour and are thus non-liquefiable. Note that the soil classification in this thesis was after the Unified Soil Classification System (ASTM-D-2487 2018).

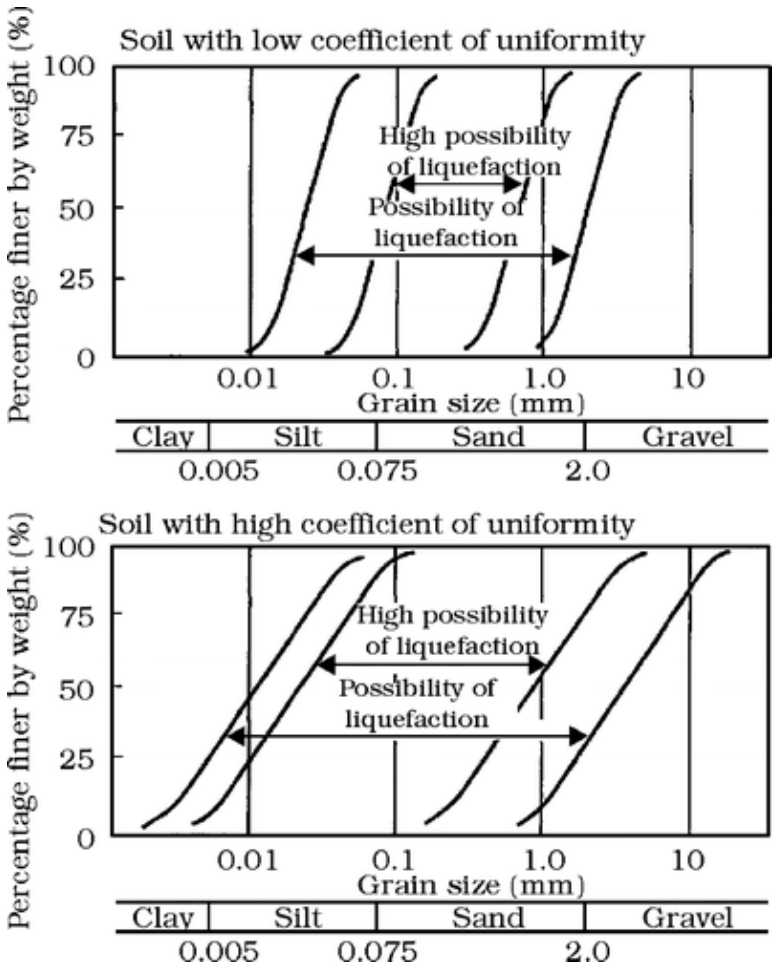


Fig. 1.2 Example of grain-size distribution of liquefaction prone sandy soils (Japanese Technical Standards, 2020)

### 1.2.3. Liquefaction triggering analysis

While liquefaction susceptibility is dependent on soil properties mainly, such as grain-size properties, plasticity, and initial state by means of the state parameter, the liquefaction potential

of soils takes into account the input load characteristics, such as earthquake magnitude and ground motion characteristics.

Generally, there are two approaches when assessing the liquefaction potential in soils, (1) cyclic strain-based methods, and (2) cyclic stress-based methods. Both methods have their advantages and disadvantages, but the fact that it is often difficult to measure the strain in a soil subjected to earthquake loading (Seed 1979a), has made the cyclic stress-based methods more commonly used in practice.

The liquefaction potential in the cyclic stress-based methods is commonly expressed through the Factor of Safety ($F_{SL}$) against liquefaction:

$$F_{SL} = \frac{CRR}{CSR} \tag{1.1}$$

where *CRR* is the cyclic resistance ratio, representing the soil resistance against liquefaction, and *CSR*, the cyclic stress ratio, is the stress component, representing the cyclic loading characteristics.

The liquefaction potential can be evaluated (1) experimentally, through laboratory tests, or (2) by in-situ based methods.

#### 1.2.3.1. Laboratory-based methods for liquefaction triggering analysis

In the group of laboratory-based methods, there are two different types of testing, depending on the scale and scope of the test: (1) element, and (2) model testing. Model testing, such as centrifuge tests and seismic shaking table tests, if done properly, can be more advantageous in seismic studies of soils than element testing, due to the fact that they can reproduce more realistic information about parameters such as ground acceleration, amplification or the seismic input, change in pore pressure, nonlinearities and the mechanism of failure (Aghaei Araei and Towhata 2014; Bojadjieva 2015; Cubrinovski, Kokusho, and Ishihara 2006). Element testing or sample testing, however, has been the favoured choice in examining the cyclic soil behaviour, due to its simpler nature. Element testing, in which small specimens are subjected to certain stress conditions, can be used to describe and investigate the variables that control liquefaction as opposed to model testing. In other words, it is less time consuming to investigate the stress conditions under different variables in element testing, such as fines content, consolidation, sample preparation methods, relative density, load amplitudes and effective stresses. The one serious disadvantage here is related to the difficulty in completely simulating the natural conditions as well as the representation of the measured quantities after the samples

liquefy. Different types of element laboratory testing procedures have been used to study soil behaviour, such as simple shear testing, direct shear testing (Cappellaro 2019; Ishihara and Yamazaki 1980; Talaganov 1996), torsional shear testing (Ishihara and Towhata 1983), resonant column testing (Ishihara 1997), and triaxial testing (Finn et al. 1971; Rees 2010; Seed and Peacock 1971; Wichtmann 2016). The triaxial apparatus, being the most common device available in most research facilities, has been the most referenced testing device related to liquefaction studies.

In the triaxial equipment, the samples are usually subjected to harmonic, sinusoidal loading until failure is observed (Ishihara and Yasuda 1972; Seed and Idriss 1971). The cyclic stress ratio, *CSR*, in a triaxial experimental setting is expressed as:

$$CSR = \frac{(1+2Ko)}{3} * \frac{|q_{dev}|}{2*\sigma'_c} \quad (1.2)$$

where,

$q_{dev}$ – input deviator stress

$\sigma_c$' – effective consolidation pressure

*K*o – lateral stress coefficient

For isotropic conditions (where *K*o = 1)

$$CSR = \frac{|q_{dev}|}{2*\sigma'_c} \quad (1.3)$$

The liquefaction potential is usually represented by plotting *CSR* versus $N_{CL}$ (number of cycles to liquefaction) curves. The failure is defined on the basis of the number of cycles required to reach one of the following: effective stress reversal to zero (or build-up of pore pressure), limiting double amplitude ($\varepsilon_{da}$) strain of 3%, 5% or 7.5%, or, where none of the previously mentioned can be reached, an $N_{CL}$ = 500 is appointed (ASTM D 5311 - 92 2004).

#### 1.2.3.2. In situ-based methods for liquefaction triggering analysis

Several authors have proposed empirical in-situ based liquefaction triggering procedures. The procedures are based on a significant number of data points marking locations/soil layers that have liquefied, have not liquefied or showed marginal signs of liquefaction (Andrus and Stokoe 2000; Boulanger and Idriss 2014; Cetin et al. 2004; Youd and Idriss 1997). In-situ soil characterization parameters based on procedures such as the standard penetration test (SPT), the cone penetration test (CPT) and geophysical (shear wave velocity, *V*s based) methods, were

used as a basis to develop deterministic as well as probabilistic corelations, i.e. curves that separate liquefied and non-liquefied cases. The *CRR* (cyclic resistance ratio) of the soil layer(s) of interest is calculated based on the in-situ soil characterization parameters (e.g. SPT number of blows, N) and then compared to the *CSR* in order to estimate the factor of safety against liquefaction (Eq. 1.1) and/or the probability of liquefaction. The simplified procedures have been widely adopted in the engineering practice in the past few decades.

## 1.3. Geotechnical approach in paleoliquefaction studies

The geotechnical approaches in paleoliquefaction studies analyse the liquefaction resistance of soil deposits that have been previously identified as historically liquefied through geological field observations (Monecke et al. 2007; Shilts and Clague 1992). The liquefaction resistance, commonly expressed through the cyclic resistance ratio, *CRR*, is estimated using empirical correlations based on field investigations, such as CPT and SPT (Rodríguez-López et al. 2007; Rodríguez-Pascua et al. 2010). Then, for an assumed factor of safety $F_{SL} = 1$ (i.e., the *CRR* is equal to the cyclic stress ratio, *CSR* (Eq. 1.1), the peak ground acceleration, $a_{max}$, and earthquake magnitudes, $M$, are evaluated (Shilts and Clague 1992). This analysis is sometimes complemented with regional attenuation evaluations of the credible $a_{max} - M$ combinations for the site or sites of interest, in order to evaluate the range of possible $a_{max} - M$ pairs that caused the liquefaction at the sites.

## 1.4. Liquefaction of pumiceous, volcanic-ash soils

Liquefaction failure of volcanic-ash soils has been registered in the recent past in Japan, South and North America as well as New Zealand (Ishihara 1996; Orense et al. 2002; Pender et al. 1987). However, experimental and empirical data on volcanic-ash pumiceous soils, are quite limited in the literature compared to hard-grained quartzitic soils and the cyclic behaviour and liquefaction of volcanic-ash soils have not been as extensively studied to date. The main distinction between pumiceous and hard-grained soils, is the lightweight and potentially crushable properties that pumiceous particles have due to their vesicular nature. The next sub chapter summarizes findings from studies about pumiceous, volcanic-ash soils.

### 1.4.1. Previous findings from liquefaction studies of pumiceous, volcanic-ash soils

One of the earliest studies on crushable soils was by Hyodo et al. (1998), and involved liquefaction investigation of a non-plastic, pumiceous, volcanic-ash sand, Shirasu sand (the local name for the unconsolidated, non-welded product of a voluminous pyroclastic flow in

Kyushu, southern Japan, namely the 30 cal-ka to ignimbrite: Kobayashi (2010)). It was found that, crushable soils, when sheared in a dense state, have similar stress paths to those of loose sands of a less crushable nature. More recently, in 2012, Orense et al. (2012), performed an extensive cyclic triaxial testing campaign of rhyolitic (silica-rich) pumiceous sands originating from eruptions in the central Taupo Volcanic Zone in the North Island of New Zealand. The pumiceous samples showed higher liquefaction resistance than non-pumiceous specimens reconstituted to the same relative density. Moreover, the difference in the liquefaction resistance between dense and loose pumiceous sands was not as remarkable as the one observed on hard-grained sand such as the Toyora sand. These findings were described to be a result of the crushability of pumice grains that enables the erasing of their natural particle structure when reconstructing and applying load on the soil samples. Orense et al. (2012) also concluded that even at large strain level, pumiceous sands did not reach the steady state of deformation and inferred that the critical soil mechanics may not be applicable to crushable soils. Asadi et al. (2018), first looked into the cyclic undrained behaviour of pumiceous sands in comparison to hard-grained sands and found that unlike hard-grained sands, where the excess pore water pressure (EPWP) as well as the axial strain increased in a sudden manner in the loading cycles before failure, pumiceous sands tend to show immediate increase of both the EPWP and the axial strain in the first loading cycles. Moreover, because of the dilative response of pumiceous sands in the succeeding loading cycles, after the initial cycles, the liquefaction resistance of the pumice sands may be significantly higher than that obtained for hard-grained soils.

In regard to pumiceous sand-silt mixtures, Licata et al. (2018), found that a pumiceous silty sand mixture with 30% non-plastic fines exhibited a higher liquefaction resistance compared with hard-grained silica sand having the same proportion of fines. They reported negligible particle crushing in their pumiceous material. In a more recent study, Hyodo et al. (2022) examined a pumiceous silty sand (Shirasu) with 28% fines and found the pumiceous silty sand to be less resistant to liquefaction than pure Shirasu sand (whose fines had been washed out). Hyodo et al. did not discuss the level of particle crushing that might have occurred in the Shirasu sand.

Liquefaction procedures using in-situ methods for large scale studies have also been used at locations where volcanic soils are prevalent (Evangelista and Santucci 2011; Gill and Orense 2019; Orense et al. 2020; Santucci de Magistris and Evangelista 2007). However, in a comparative study between in-situ based assessments of the liquefaction potential of the pumice sands in the North Island of New Zealand it has been found that the penetration methods

such as CPT and SPT as well as dilatometer tests can underestimate the liquefaction resistance of these soils (Wesley, 1999; Orense et al. 2012). This is because of their crushable nature, and it is why non-penetrating geophysical methods (*V*s based) were considered more appropriate. In contrast, in more recent studies, it is concluded that *V*s based methods can underestimate the liquefaction resistance of these soils as well (M. B. Asadi et al. 2018; Orense et al. 2020).

## 1.5. Research objectives

The main research aim of this thesis was to perform geotechnical analysis on the lacustrine tephra layers preserved in the Hamilton lowlands with identified SSDSs (Kluger et al. 2023), in order to estimate, or back-analyse pre-historic earthquakes that might have caused the deformation structures and thus to better understand the past seismic activity in the region.

Significant literature knowledge gaps, related to liquefaction potential research on pumiceous silts and sand-silt mixtures, were identified and needed to be filled, which mainly defined the research objectives in this PhD study.

In order to attain the main aim and fill the research gaps the following objectives were defined:

(1) Investigate the geotechnical properties of the tephras of interest in the studied lakes in order to define their liquefaction susceptibility.
(2) Investigate the undrained monotonic and cyclic behaviour of a pumiceous silt ('Tuhua silt', derived from 7.6 cal ka Tuhua tephra) in order to overcome knowledge gaps, rela ted to potential particle crushing affecting undrained cyclic behaviour as well as liquef action resistance.
(3) Identify the potential threshold of pumice content and/or fines content, at which sand-silt mixtures become crushable.
(4) Develop a framework, that extends the laboratory-obtained liquefaction resistance resu lts on tephras analysed in one lake (able to be sampled in enough volume for triaxial te sting), to multiple tephras preserved in many other lakes in the Hamilton lowlands (on ly able to be sampled for small volume testing, i.e., geotechnical properties). Achievin g this objective was crucial as the results provided the liquefaction resistance ratios for each Mamaku tephra within every studied lake in this Hamilton lowlands, that were us ed to achieve the main aim i.e., back-analysis of past earthquake parameters.

## 1.6. Organization of thesis and publication contributions

This section gives an outline of the presented thesis and briefly summarizes the scientific publications which were produced in the scope of the PhD project. The three publications are reprinted in full text as chapters 3 – 5. My contribution and the individual contributions of the co-authors, in the publications are described in detail after each chapter. A further manuscript ready for submission is included as Chapter 6.

*Chapter 1* provides an overview of the previous research that motivated this PhD study. It then summarizes the relevant literature about liquefaction as a phenomenon and the common method used in the evaluation of liquefaction potential of soils. It presents relevant literature about liquefaction of pumiceous, volcanic-ash soils, and it ends with stating the main research aim and research objectives of this PhD project.

*Chapter 2* provides a short overview of the methods that were used to collect data needed for the research objectives, and discussed the data collecting constraints that defined the methodologies in this research. A more detailed description of the methods is presented in the method sections of each of the publications, i.e. chapters 3 – 6.

*Chapter 3* presents the part of this study that addressed the first research objective where the geotechnical properties of the tephra layers across the lakes of interest were analysed, in order to investigate their liquefaction susceptibility. This research was published in the Proceedings of the 7$^{th}$ Young Geotechnical Engineering Conference, Sydney, 2022.

*Chapter 4* is about the investigations that addressed the second research objective about the undrained monotonic and cyclic behaviour of Tuhua silt in order to fill the knowledge gaps related to liquefaction resistance of pumiceous silts. This research was published in *Soil Dynamics and Earthquake Engineering*, March 2023.

*Chapter 5* covers the third research objective and involves the study about the level of particle crushing during cyclic triaxial testing and/or sample reconstitution of three different beds of the Mamaku tephra, with different pumice contents and fines contents. The full paper about the study has been accepted for the conference proceedings for the 8$^{th}$ International Conference of Earthquake Geotechnical Engineering, to be held in Osaka, in May, 2024. Extended version of the conference paper will be submitted to the official journal of the Japanese Geotechnical Society – Soils and Foundations, after the conference (as per recommendations of the ICEGE committee).

In *Chapter 6* the main aim of this thesis through objective four is addressed. The liquefaction resistance of three beds within the Mamaku tephra layer (each bed having a different grain-size distribution and pumice content) are presented and used to back-calculate the corresponding minimum peak ground acceleration and magnitude combinations required to generate liquefaction. A framework that extends the liquefaction resistances of the three beds of Mamaku tephra obtained in the triaxial testing campaign to the rest of the Mamaku tephra layers in other lakes (that didn't provide enough material for triaxial testing) in the Hamilton lowlands is then developed. Ultimately the derived liquefaction resistances of all the Mamaku tephras in each of the cored lake, are used for obtaining minimum peak ground acceleration and magnitude combinations at the locations of each lake, and thus addressing the main aim of this thesis. This study will be submitted to *Soil Dynamics and Earthquake Engineering* in February 2024 immediately after the submission of this thesis.

*Chapter 7* summarizes the conclusions of this doctoral thesis with respect to the aim and how it has been met through the research objectives and gives recommendations for future research and engineering practice.

*Appendix A* provides the supplementary figures, table and equation.

*Appendix B.1* and *B.2* provide all the results from the undrained cyclic triaxial testing campaign.

*Appendix C* presents the abstracts submitted to the annual meetings of QuakeCoRE, 2022 and 2023, as well as the abstract from the 2022 Disastrous Doctorates Symposium.

*Appendix D* presents a co-authored manuscript, published in Sedimentary Geology, 2023. The study presents the spatial and temporal distribution of the tephras, as well as detailed description of the discovered SSDSs, concluding their seismic origin.

# Chapter 2: Methods

This chapter presents broad discussion of the methods used to achieve the objectives defined in Chapter 1. More detailed descriptions of the specific methods used are given in chapters 3 – 6. Initially, a discussion of the constraints associated with the environment and materials in question that impacted the choices of data collection methods is presented, followed by a summary of the field and laboratory methods that were used to collect data for this PhD project.

## 2.1. Constraints on data collection methodology

Several data collecting constraints that needed to be overcome dictated the method choices in this thesis. The tephra layers of interest are deposited in around 35 lakes aged ~20,000 years in the Hamilton lowlands. Around 40 distal tephra deposits, as well as numerous cryptotephras (glass-shard concentrations insufficiently numerous to be visible as a layer to the naked eye: Lowe 2011) are preserved in ~3–6 m of organic lake sediment (Green and Lowe 2024; Kluger et al. 2023; Lowe 1988). The tephras range in thickness from sub-millimetre to ~8 cm, with many a few centimetres in thickness (e.g. see Figs. 1.1, 2.1, and 2.3).

The relatively small thicknesses of the main tephra layers imposed the following constraints:

(1) In-situ based liquefaction assessment methods, such as the CPT, that are commonly used in geotechnical paleoliquefaction studies, are not known to provide accurate results for soil layers with small thicknesses (Boulanger and Dejong 2018). Therefore, the choice of methods for obtaining the liquefaction resistance ratios for the tephras was narrowed down to laboratory-based methods, i.e., triaxial testing.

(2) The triaxial apparatus samples require a significant volume of soil (~0.0002 $m^3$), which would have required ~10 cores per lake, in order to sample enough tephra material from all the relevant layers for *one* triaxial test. This limitation resulted in the selection of the two topmost tephras, Tuhua and Mamaku, for the triaxial testing campaign. These two tephras were found on-shore at Lake Areare, shallow enough to provide large enough volumes, for an extensive triaxial testing program.

(3) Tephras were found to have internal bedding with variable grain-size distribution. Alongside the already thin tephras, this eliminated the possibility for undisturbed sample testing. Therefore, reconstituted samples were tested instead.

(4) Finally, some standardised geotechnical laboratory tests, that require significant volume for testing, e.g., Atterberg limits (ASTM-D4318-17e1 2017), were only able to be performed for the Tuhua and Mamaku tephras from lake Areare, so all of the geotechnical properties of the tephras from the other lakes had to be analysed using small volume test procedures. These procedures include:

- Gas pycnometer testing for particle density analysis
- Laser-sizer testing for grain-size distribution analysis
- SEM based methods for pumice content analysis
- Minimum and maximum density testing using a modified procedure (of the Japanese Geotechnical Society Standard 2009) for small volumes of soils proposed by Mijic et.al. 2021.

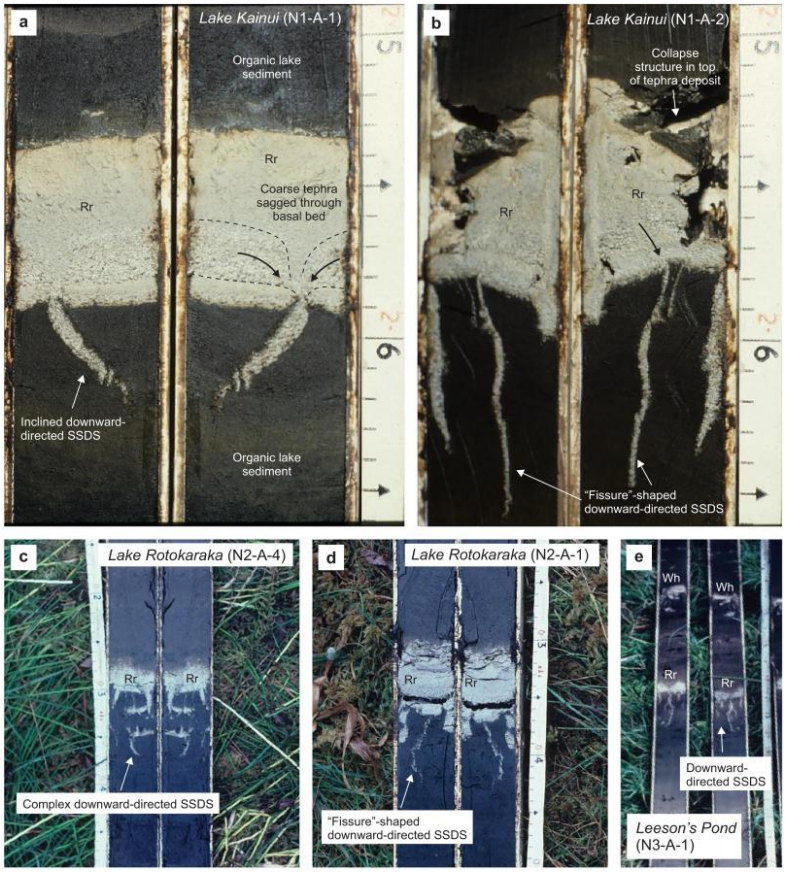


Fig. 2.1. SSDSs in Rorotua (Rr) tephra layers in historic cores from various lakes (i.e. Kainui, Rotokaraka, Leeson's Pond) (Kluger et al. 2023; Lowe 1988). The tephra ranges in thickness from a few centimetres to nearly 8cm (marks on tapes for scale are in centimetres). All photos by D.J. Lowe.

A flowchart summarizing the methods used as well as the chapters that they are presented in detail in is given in Fig. 2.2. The following sections describe the field and laboratory methods in more detail.

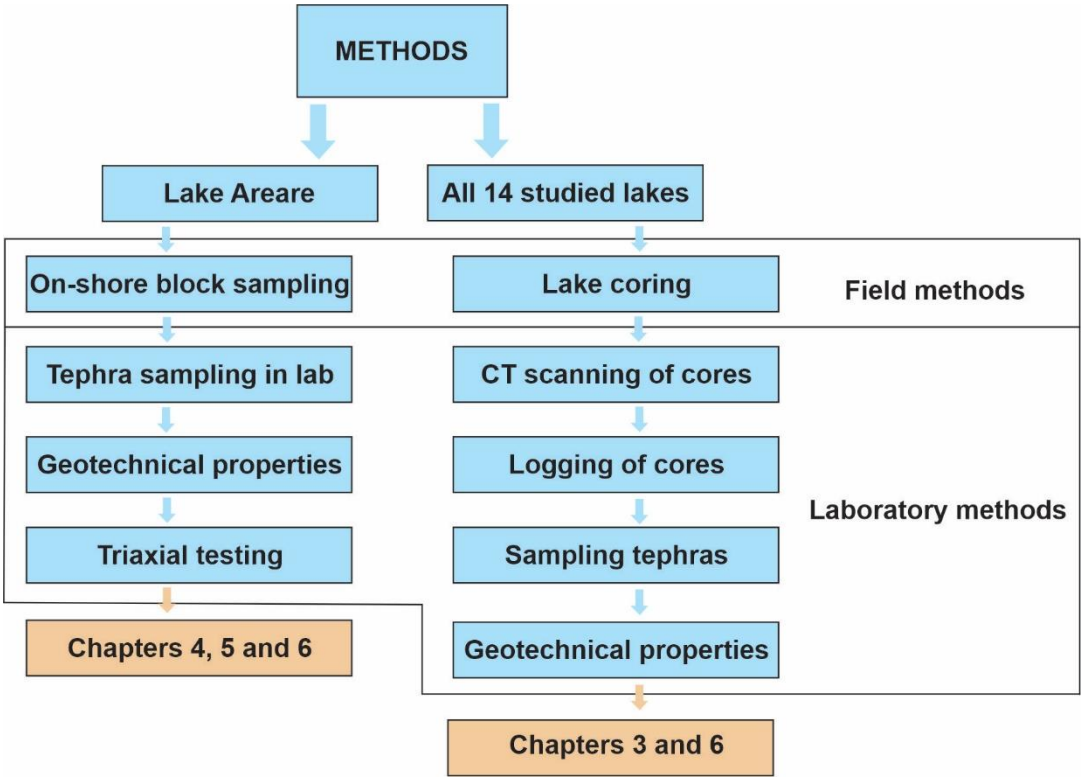


Fig. 2.2. Flowchart summarizing the used methods

## 2.2. Field methods

### 2.2.1. Coring and onshore block sampling

The principal sampling was through (1) coring for all the 14 studied lakes and (2) onshore block sampling at Lake Areare.

The coring was undertaken by using a modified Livingstone piston corer with a 50-mm internal diameter PVC coring tube (Rowley and Dahl 1956) for historical cores taken in the 1980s, and 65- or 80-mm internal diameter for cores taken more recently in 2016, 2020, and 2022 (Fig. 2.3). One or more cores typically ~1.5–2 m in length were collected from partly overlapping sediment depths. Once sampled the PVC tubes were closed at both ends and transported to an icebox, kept at a temperature of 4°C. The coring procedure is described in more detail in Kluger et al. 2023 (Appendix D). The locations of the samples from each lake used in this study are presented in table 2.1.

The onshore block sampling of the two topmost tephras, Tuhua and Mamaku, at Lake Areare was performed so that a large number of small block samples (each with volumes of ~0.0075 m3) comprising the tephra layers in between organic lake sediment layers were taken. In the lab, the tephra materials were carefully scooped out, cleaned from organics and oven-dried at 40°C. More details and figures of the procedure can be found in the corresponding methods sections of Chapters 4, 5 and 6.

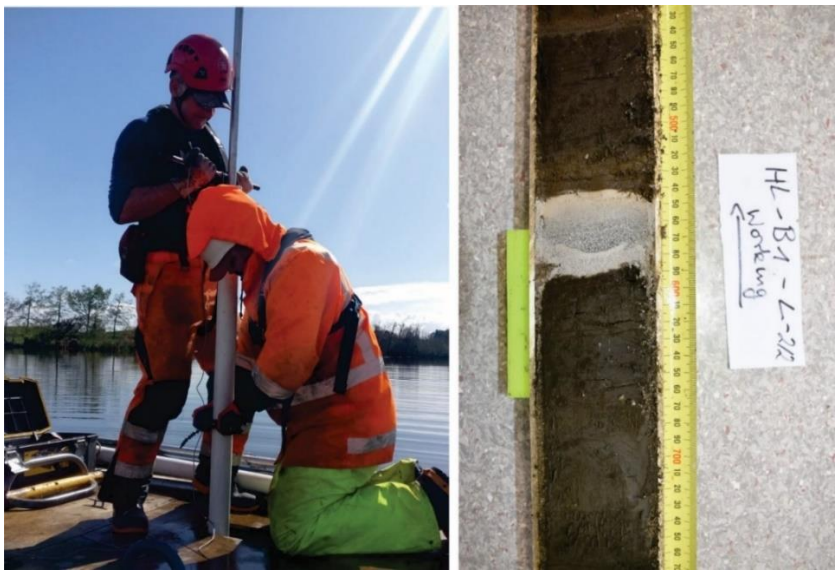


Fig. 2.3. Coring at lake Ngarotoiti, September 2022 (left). Split core from Lake Rotoroa/Hamilton Lake showing ~4cm thick Rotorua tephra encapsulated within the dark-coloured organic lake sediment (right). Numbered scale marks in centimetres.

Table 2.1. Sampled core locations for each lake and approximate Tuhua and Mamaku tephra depths in the lakebed at the sampled locations. Coordinate system: NZGD2000 NZ Transverse Mercator 2000

| Lake | Abbreviation | Latitude | Easting | Tuhua tephra depth in lakebed [m] | Mamaku tephra depth in lakebed [m] |
|---|---|---|---|---|---|
| Areare | AR | 5828797 | 1794027 | 1.30 | 1.35 |
| Rotokaeo/Forest Lake | FL | 5816942 | 1798262 | 1.98 | 2.01 |
| Rotoroa/Hamilton Lake | HL | 5814616 | 1799780 | 2.05 | 2.10 |
| Kaituna | KT | 5827418 | 1798204 | 2.05 | 2.10 |
| Whakatangi | WT | 5826262 | 1799125 | 1.75 | 1.80 |
| Koromatua | KM | 5809879 | 1795705 | 5.25 | 5.30 |
| Manghia | MH | 5805246 | 1795961 | 1.85 | 1.90 |
| Ngarottoiti | NI | 5797984 | 1801803 | 2.30 | 2.40 |
| Mangakaware | MK | 5799268 | 1795100 | 1.25 | 1.30 |
| Kainui | KN | 5827679 | 1796861 | 1.15 | 1.20 |
| Rotokauri | RI | 5818463 | 1793490 | 1.75 | 1.80 |
| Pikopiko | PP | 5829445 | 1793379 | 1.95 | 2.00 |
| Karaeotahi/Cameron Lake | CL | 5807704 | 1802607 | 1.35 | 1.40 |
| Ruatuna | RT | 5799799 | 1801370 | 0.75 | 0.80 |

## 2.3. Laboratory methods

### 2.3.1. CT scanning and logging

X-ray computed tomography (CT) imaging was performed using a medical CT scanner on all whole-round cores prior to opening (Fig. 2.4). The purpose of the CT scans was to provide 3D visual insight of the tephra layers in the cores, in order to assist the SSDS characterization, beyond what is visible in an opened core. Drishti and imageJ were used to create tiff slices from DICOM files. More details and processed high-resolution CT images of the cores can be found in Melchert et al. (2022).

After scanning, the cores were taken into the Geotechnical laboratory at University of Waikato, where the PVC tubes were carefully cut both transversely and longitudinally. One of the longitudinal pieces of each core was kept intact and labelled as the archive core, whereas the other was used for sampling (Fig. 2.5). Detailed sediment description was then done on the opened split cores, where the layers were matched and correlated using the distinctive physical properties of the tephra layers (colour, thickness, internal bedding, grain sizes, etc), and their stratigraphic superpositioning. The sediment description is covered in detail in Kluger et al. (2023).


Fig. 2.4. Left: Sediment cores e scanned using a new medical CT scanner at Hamilton Radiology. Right: X-ray image of a sediment core, live in Hamilton radiology, showing SSDSs in a tephra layer

### 2.3.2. Geotechnical properties

The analyses of the geotechnical properties of the Tuhua and Mamaku tephras from the cores (one for each of the 14 lakes) was done on small volume samples (~ 1 to 3g), that were scooped out from the cores (sample containers with samples shown in Fig. 2.5). The details of the methods used for the geotechnical characterization are listed in the following paragraphs. The limitations of the methods and thus potential implications to the results/conclusions is also discussed where relevant:

- The particle density was obtained following ASTM-D5550-14, (2014) using a Quantachrome Ultrapyc 1000 nitrogen-filled gas pycnometer. In terms of the particle density of pumiceous particles, previous studies have shown that the chosen method for particle density analysis can affect the results significantly (Bielders et al. 1990; Wesley 2001). Unlike hard-grained soils where particle density is a constant parameter independent of the used testing method, the vesicular nature of the pumiceous particles, i.e. presence of internal voids makes pumiceous soil mixtures sensitive to the type of procedure used to test for this parameter. In particular the use of vacuum to extract the air from the soil mixture before testing (in the case of pumice both from the intra and inter-particle voids) has been found to significantly influence the final results, especially for grain-sizes larger than 0.6mm (Wesley, 2001). In this context, two terms have been used to describe pumiceous particles: (1) solid particle density - referring to the density of the particle without the internal voids, and (2) apparent particle density referring to the density of the pumiceous particles that includes the internal voids in the volume (Orense and Pender, 2016). Orense and Pender, (2016) reported a solid density of a sandy pumice particle using CT scan images, of 2.2 g/cm$^3$. The gas pycnometer method used in this study, which used a light gas (Nitrogen), and vacuum air extraction prior testing accurately recorded the solid particle density of a pure pumiceous sand (2.2 g/cm$^3$), meaning that the gas is able successfully penetrate the internal voids of the particles. Therefore, the particle densities obtained in this study as the *solid* particle densities of the pumiceous soil mixtures, and not directly comparable to particle densities of pumiceous mixtures obtained otherwise.

- The grain-size distribution was determined by means of laser diffraction analysis (LDA) using a Malvern Mastersizer 3000. SOP material 'tephra' was used in the input settings. The maximum obscuration level allowed was 15%. In this procedure the volume of the soil particles (dispersed in water) is estimated through laser diffraction. Therefore, unlike the sieving/hydrometry method, which is the commonly used grain-size distribution procedure and is based on retained *weight* of soils for each grain-size fraction, the results from the laser

diffraction procedure are presented in terms of the *volume* distribution of the fractions. In general laser diffraction and sieving can provide similar results when characterizing spherical or semi-spherical particles. A study comparing the hydrometry and laser diffraction method, found the results for silt and sand-sized particles to be very similar (Eshel G. et al., 2004). The tephras presented in this thesis are within the fine sand and silt range, but with a high particle angularity (Chaneva et al., 2023). Thus, a conclusive statement whether the GSD curves are directly comparable to GSD curves of soils obtained with the classic sieving/hydrometry method, cannot be made without further studies.

- Scanning electron microscopy (SEM) was undertaken using a Hitachi S-4700 FE SEM. The images were used to estimate the pumice content (*PC* [%]) of the tephras. The pumice contents in this study are thus obtained using the visual approach for distinguishing pumiceous and non pumiceous particles:

$$PC = \frac{N_{Apumice}}{N_{Atotal}} \cdot 100\%$$

where $N_{A,pumice}$ is the number of crossing points that lay over a particle with pumiceous features (i.e., being vesicular) and $N_{A,total}$ is the total number of crossing points classified for a specific tephra sample. This method was used for estimating the *PC* of all the samples in this study. Additionally, for chapter 4, the pumice content of Tuhua silt was also calculated by introducing weighting factors for each grain-size fraction. The results, however, were almost identical to those calculated without grain-size fractions weightings - 48% vs 47% *PC*.

The X-ray diffraction (XRD) analysis was undertaken using a Panalytical Empyrean Series 2 XRD. Bulk samples were run from 5-80 °2θ, at 50 seconds per step, and a scan speed of 0.1347 degrees per second.

Additionally, for the Tuhua and Mamaku tephras sampled from the Lake Areare block samples, the minimum and maximum dry densities (thus, maximum and minimum void ratios, respectively) as well as Atterberg limits were determined. The minimum and maximum dry densities for the Areare tepthras were determined following the Japanese standard method, (Japanese Geotechnical Society Standard 2009) modified by Mijic et al., (2021). The Atterberg limits were determined following ASTM-D4318-17e1, (2017).

Bulk density was determined by cutting tephra layers and organic lake sediments into rectangular prisms of varying dimensions depending on the available volume. A cutter knife was used in order to cut prisms without causing too much disturbance to the soil structures of

the samples. Volumes of bulk density samples varied from 1 to 40 $cm^3$. Dry bulk densities were determined on eight samples to aid the reliable (reproducible) calculation of mean values with sufficient confidence.

For more detailed descriptions of the used methods refer to chapters 3 to 6, in the corresponding method sections.

Fig. 2.5. Left: 19 sediment cores cut and logged. Right: Samples taken from the cores, awaiting physical and geotechnical properties analyses

### 2.3.3. Undrained triaxial testing

The material used for the undrained triaxial testing of both Tuhua and Mamaku tephras was manually sampled from the block samples, taken onshore at Lake Areare, as described in chapter 2.3.2. A GDS Advanced Dynamic Triaxial Testing System was used for the triaxial testing of the samples (Figure 2.5).

The samples were reconstituted using the under-compaction method following the procedure of Ladd (1978). The design of the tamping guidance collar and tamper, proposed by Ladd (1978) was 3D printed and is shown in Figure 2.6. The samples were reconstituted with a moisture content of 15%. Moisture contents in the range of 10 to 18% are considered the optimum moisture contents for sand silt mixtures (i.e. enable maximum compaction) (Rollins, K. M. et al. 1998). Note that the optimum moisture content ranges found in published literature are based and obtained on hard-grained soils. The maximum compaction method (Proctor testing) is not applicable for pumiceous soil mixtures as would most probably crush the pumiceous particles (Asadi et al., 2019). Therefore, the adopted value of 15% moisture content in this study is indicative and did guarantee achieving maximum density of pumiceous samples.

Instead, it was found that, for some of the sandy (Mamaku) tephras, relative densities higher than 60% could not be achieved during the moist tamping procedure.

Monotonic and cyclic triaxial tests were performed following ASTM D-5311 (2004) and DIN EN ISO 17892-9 (2018). Membrane penetration effects are not prescribed in the standard, therefore were not considered. Moreover, all the tephra materials studied in this thesis were fine sand-silt mixtures or silts, so the membrane penetration effects were considered to be insignificant (Sladen and Handford, 1987).

The details about the triaxial testing conditions can be found in method sections of Chapters 4 to 6.


Fig. 2.5. GDS Advanced Dynamic Triaxial Equipment at the University of Waikato

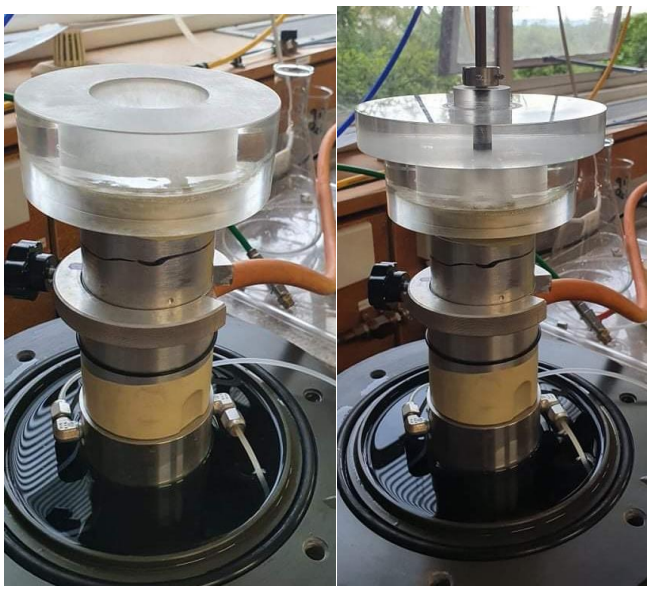

Fig. 2.6. Membrane protection collar (left) and full moist tamping guidance (membrane protection collar, guidance collar and tamper) assembled (right) as per Ladd (1978)

# Chapter 3: Geotechnical properties of liquefied pumiceous layers in lakes

**Jordanka Chaneva**[1], Max O. Kluger[1], Vicki G. Moon[1], David J. Lowe[1] & Rolando P. Orense[2]

[1]*School of Science/Te Aka Mātuatua, University of Waikato, New Zealand, jc409@students.waikato.ac.nz*
[2]*Department of Civil and Environmental Engineering, University of Auckland, New Zealand*

Published in the Proceedings of the 7th International Young Geotechnical Engineers Conference – Scott (Ed.)  ISBN 978-0-9946261-5-8

## 3.1. Abstract

Earthquake failures in volcanic-ash soils are relatively common, considering their physical nature and the fact that such deposits tend to occur in areas with high seismicity in which the volcanism, responsible for their emplacement, shares some tectonic-related origin. However, experimental and empirical data related to geotechnical properties and mechanical behaviour of volcanic-ash soils are still quite limited compared to those for hard-grained soils. Moreover, the limited data largely focus on pumiceous sands, whereas pumiceous silts have not been significantly investigated to date. This study summarizes relevant geotechnical properties of volcanic-ash layers preserved in lake sediments in the Hamilton lowlands in North Island, New Zealand. These highly pumiceous layers are hypothesized to have liquefied within the past 20,000 years, based on paleo-liquefaction features observed in some of the lakes. The layers that are liquefaction susceptible were identified. Additionally, the pumiceous layers were characterized by means of specific gravity, fines content, and pumice content. Finally, the characteristic void ratios (i.e., $e_{min}$, $e_{max}$) of five samples were analyzed. Pumiceous silts exhibit higher characteristic void ratios than those for hard-grained soils.

KEYWORDS: geotechnical properties, pumice, liquefaction, lacustrine volcanic-ash deposits

## 3.2. Introduction

Earthquake failure (e.g., liquefaction, landslides) of volcanic-ash soils has been observed in the recent past, including in Japan, South and North America, and New Zealand (Bommer and Rodríguez 2002; Ishihara et al. 1986; Orense et al. 2002; Pender et al. 1987; Uzuoka et al. 2005). Yet, experimental and empirical data related to relevant geotechnical properties and their mechanical behaviour are still quite limited compared to those obtained on hard-grained quartzitic soils. Moreover, the limited data are largely focused on pumiceous sands (Hyodo et al. 1998; Orense et al. 2012; Pender et al. 2006; Wesley et al. 1999), whereas pumiceous silts have not been sufficiently investigated to date (Rolo et al. 2004). Existing studies often label these vesicular sands as 'problematic' because of their crushability, compression characteristics, liquefaction resistance, etc. These soil properties are highly dependent on the grain size and pumice content (Hyodo et al. 1998; Miura et al. 2003; Orense et al. 2012). Related research also shows that geotechnical properties (e.g., particle density) of these soils strongly depend on the laboratory method adopted, mainly because of their vesicularity (Pender et al. 2006; Wesley 2001). This means that, unlike quartzitic soils, where, e.g., the specific gravity is considered constant ($G$s = 2.65–2.67) and independent of the method used, the determination of geotechnical properties of pumiceous soil mixtures is challenging. Their problematic nature makes these soils challenging in conventional engineering liquefaction studies. This is because both the laboratory and in-situ methods that are commonly used for liquefaction potential estimation can induce particle crushing thus, affecting the assessment (M. S. Asadi et al. 2018; Orense et al. 2020, 2012). It has been hypothesized that pumice content is the key property that needs to be evaluated prior to a relevant geotechnical study in areas with volcanic-ash soils (Orense et al. 2020; Stringer 2019).

This study summarizes relevant geotechnical properties of numerous volcanic-ash samples. Volcanic ash is also referred to hereafter as tephra. The tephra samples were taken from layers of known age preserved in lake sediments in the Hamilton lowlands in North Island, New Zealand. Many of the layers are highly pumiceous and show paleo-liquefaction features in some lakes (Kluger et al. 2023). Their characterization and liquefaction susceptibility assessment are crucial first steps in assessing their liquefaction potential from which the timing and occurrence of past earthquakes in the lowlands could be estimated. The geotechnical properties of the mainly pumiceous silts reported in this study will be a valuable

addition to the existing pumice sand database. Specifically, it was aimed at answering the question of how geotechnical properties of silty pumiceous soil mixtures change with pumice content. In this direction, the dependence of specific gravity on the pumice content was explored. Additionally, the potential trend between the pumice content and the characteristic void ratios ($e_{min}$, $e_{max}$), was also discussed. These dependences contribute into guiding researchers and engineers to the most optimal solution for determining the pumice content in a soil mixture.

## 3.3. Study area

The Hamilton lowlands lie within the pre-Quaternary tectonically-formed Hamilton Basin. Volcanic-ash layers deposited from numerous eruptions from active rhyolitic (silica-rich) volcanic centres and andesitic volcanoes in central and western North Island are found in lakes in the lowlands (Fig. 3.1) (Lowe 1988). Around 30 lakes in total, each ~20,000 years old and underlain and empounded by volcanogenic alluvium (Green and Lowe 1985), lie scattered amidst the faults in the lowlands. Designated as having a low to moderate seismic risk (Stirling et al. 2012), the Hamilton lowlands, until recently, also lacked any known active faults (Edbrooke 2005; Langridge et al. 2016). The recently identified faults, as well as the evidence of past seismic activity from paleo-liquefaction studies, supported the hypothesis of potential liquefaction features found in the lacustrine volcanic-ash layers in the area (Van Dissen et al. 2021; Kleyburg et al. 2015; Moon and Lange 2017).

This study focuses on volcanic-ash samples retrieved from seven lakes: Areare, Kainui, Rotokauri, Waiwhakareke, Rotokaeo, Rotoroa, and Ngaroto (Fig. 3.1).

## 3.4. Materials and methods

The focus of this paper is four rhyolitic pumiceous tephra layers: Tuhua (Tu), Mamaku (Ma), Waiohau (Wh), and Rotorua (Rr). The tephra layers, each between ~2 and ~8 cm thick (Kluger et al. 2023), were sampled from a number of ~1.5 m-long piston cores collected at six lakes (Fig 3.1). The layers occurred at different depths in the lake sediments ranging from 0.5 m to 2.0 m (Kluger et al. 2023; Lowe 1988) and mainly comprised volcanic glass (in the form of glass shards and glassy pumice fragments) and minor crystals (Fig. 3.2) (Lowe 1988). They showed differences in composition in terms of grain size and pumice content in the different lakes (Lowe 1988).

Because the layers were relatively thin (2–8 cm), it was not possible to analyze all the relevant physical and geotechnical properties from the small volumes provided by the cored samples. Therefore, additional onshore in situ block sampling was undertaken at Lake Areare (Fig 3.1), where lowered lake levels facilitated easy access to near-surface deposits of Tu and Ma tephra layers. This sampling provided sufficient material to characterize the pumiceous tephra layers more comprehensively by Atterberg limits and characteristic void ratios.

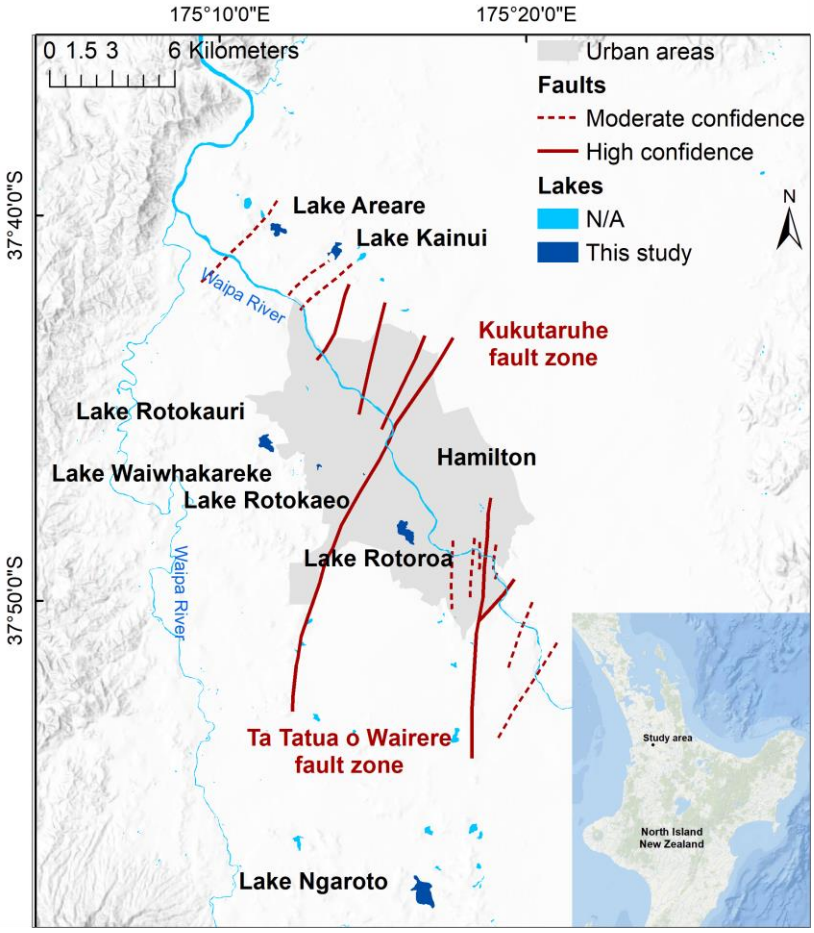


Fig. 3.1. Study area: Hamilton Basin with locations of lakes considered in this study (dark blue) and faults (red lines)

In total, 45 individual samples were taken from cores and block samples, comprising 17 samples of Tu, 11 samples of Ma, 17 samples of Rr, and four samples of Wh. For each of the 45 samples, particle density (thus, specific gravity, *Gs*) and grain-size distribution analyses were performed. The particle density of the samples was obtained following ASTM-D5550-14, (2014) using a Quantachrome Ultrapyc 1000 nitrogen-filled gas pycnometer. Potential influences of the method used to determine particle density (Bielders et al. 1990; Wesley 2001) is not further discussed in this study.

The particle-size distribution was determined on small-volume samples by means of laser diffraction analysis (LDA) using a Malvern Mastersizer 3000.

Scanning electron microscopy (SEM) and X-ray diffraction (XRD) analysis were undertaken using a Hitachi S-4700 FE SEM and a Panalytical Empyrean Series 2 XRD, respectively. Both measurements were performed on a number of representative samples from each tephra in order to examine their pumice content and clay mineralogy.

Quantification of pumice content based on counting individual particles under the SEM has been used before (Asadi et al. 2019). This approach has been referred to as time consuming and not fully representative of large soil volumes as a relatively small number of particles are commonly examined (Stringer 2019). The present study, however, dealt with thin layers on which most of the laboratory tests (i.e., particle density, grain-size distribution) were already made using small quantities. Therefore, it was considered that estimating pumice content from the number of pumiceous particles in SEM images is the most effective approach. The pumice content was estimated using a point-counting method (Frolov and Maling 1969). In this method, five SEM images of representative pumice clusters were chosen for each sample and were counted systematically on crossing points (> 200 points per sample) of rectangular grids. The pumice content (*PC*) was calculated from Eq. 3.1.

$$PC = \frac{N_{Apumice}}{N_{Atotal}} \cdot 100\% \quad (3.1)$$

where $N_{A,pumice}$ is the number of crossing points that lay over a particle with pumiceous features (i.e., being vesicular) and $N_{A,total}$ is the total number of crossing points classified for a specific tephra sample.

Dominant clay minerals in selected silty samples were determined qualitatively by XRD. Samples were prepared following standard methods based on Lowe and Nelson, (1983 and Whitton and Churchman, (1987). Mineral identifications were based mainly on clay mineral identification diagrams formulated by USGS (USGS - Open file report 01-041 2001).

The minimum and maximum dry densities (thus, maximum and minimum void ratios, respectively) as well as Atterberg limits were determined on samples retrieved from the onshore location at Lake Areare. The minimum and maximum densities of five samples (three Ma and two Tu) were determined following the Japanese standard method, (Japanese Geotechnical Society Standard 2009) modified by Mijic *et al.*, 2021. The JGS procedure has been proven to cause negligible particle crushing in natural pumiceous soils found in the North

Island of New Zealand (Asadi et al. 2019). The silty samples from the onshore blocks from lake Areare (Table 3.1.) were tested for their liquid and plastic limits following ASTM-D4318-17e1, (2017).

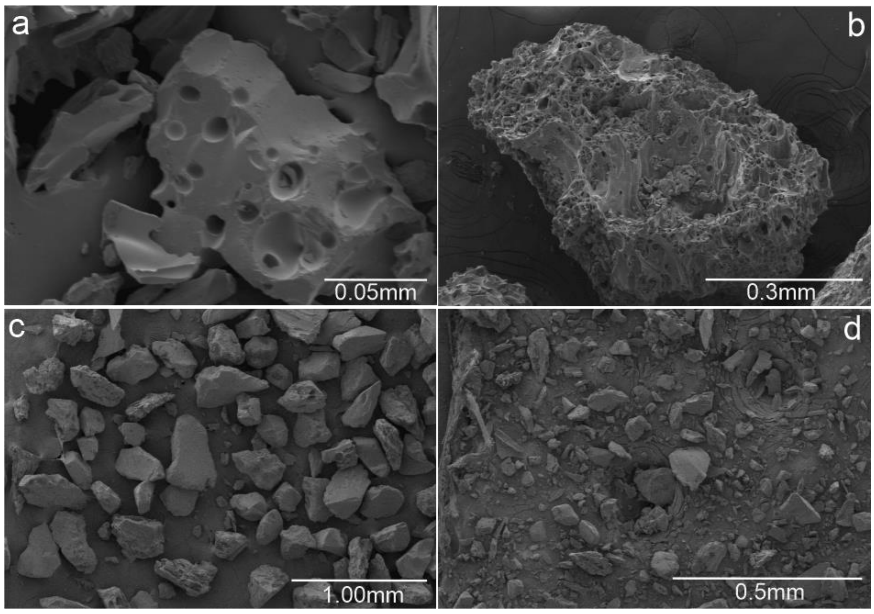


Fig. 3.2. (a) and (b): SEM images of particles in Rr tephra, Lake Kainui; (c) and (d) SEM images of mainly glass shards and pumice particles in Ma tephra, Lake Areare

## 3.5. Liquefaction susceptibility

The grain-size distribution curves of all samples retrieved from the seven lakes are presented in Fig. 3.3. Blue solid curves denote Rr tephra samples taken from different lakes, whereas orange dashed curves denote Ma tephra from onshore Lake Areare that comprised three thin layers of different grain-size distributions. The *FC* (fines content, particles %<0.075 mm) for all these samples ranged from ~10% to 99%. The silty samples from the lakes contained up to ~10% clay-sized particles (<0.002 mm). According to the Unified Soil Classification System-USCS, (ASTM-D-2487 2018), the samples were classified as silts, sandy silts (37 samples) or silty sands (eight samples).

Each tephra (Tu, Ma, Wh, Rr) exhibited different grain-size compositions when comparing different lakes. For example, Rr tephra was found to be silty in lakes Waiwhakareke and Ngaroto, yet it was found to be sandy in lakes Kainui and Rotoroa (Fig. 3.3). The thickness and interlayering within each tephra layer also varied between lakes. Some tephra layers comprised a homogeneous silt unit, whereas others comprised a number of thin, well distinguishable internal layers of different grain size (e.g., Ma tephra from Lake Areare: Fig.

3.3). Additional information about thicknesses of the different tephras in the lakes are reported in Kluger *et al.*, (2023).

The geological conditions (such as age and origin) and the grain-size composition are an important preliminary check for the liquefaction susceptibility of soils. In this regard, there is a general agreement that young Holocene sands, non-plastic silts and gravels, and their mixtures, are susceptible to liquefaction.

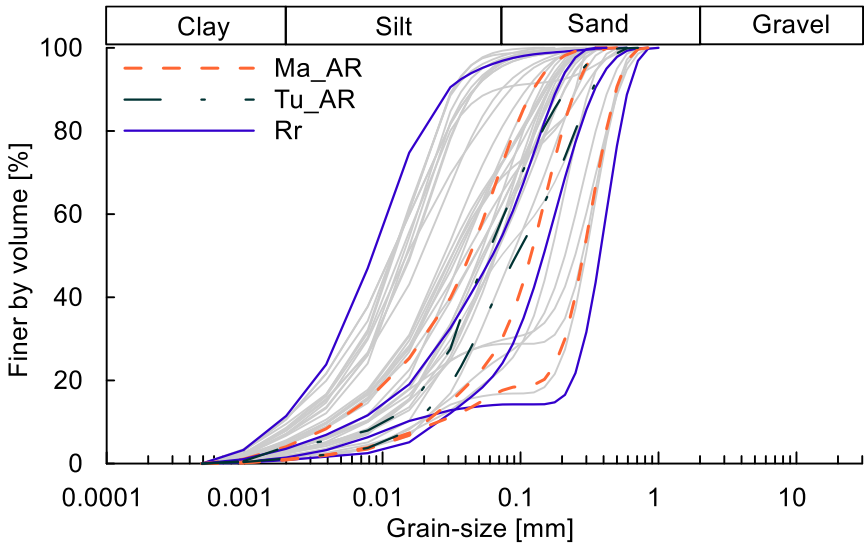


Fig. 3.3. Grain-size distribution curves of all samples (grey curves). The highlighted curves are referred to in the text

The geological and compositional characteristics are not enough when it comes to characterizing fine soils that contain clay-sized particles because of the many significant differences in undrained behaviour of sands versus clays. Plasticity characterization is considered the conclusive method when it comes to liquefaction susceptibility of fine-grained soils (Boulanger and Idriss 2006; Bray and Sancio 2006).

The silty samples from the onshore blocks from Lake Areare (Table 3.1.) were tested as non-plastic (ASTM-D4318-17e1 2017), which confirms their liquefaction susceptibility.

Table 3.1. Grain-size characteristics for silty onshore samples from Lake Areare

| Sample | Lake | $D_{50}$ [mm] | *FC* [%] | *CC* [%] |
|---|---|---|---|---|
| Tu | Areare | 0.06 | 59 | 4 |
| Ma | Areare | 0.04 | 72 | 6 |

For the purpose of extending the non-plastic classification to the layers in the lakes, XRD analysis on the clay-sized portion of some selected samples (containing 8–10% clay-sized particles, referred to as *CC*) was performed.

Three of six samples tested by XRD did not comprise any clay minerals (Table 3.2). These samples were therefore considered to be non-plastic and, thus, liquefaction susceptible. The remaining three samples showed evidence of low-activity clay minerals (e.g., halloysite). Therefore, no final conclusion could be drawn whether or not these three samples are susceptible to liquefaction.

Table 3.2. Minerals in clay-sized fraction of selected samples

| Sample | Lake | *FC* [%] | *CC* [%] | Minerals |
|---|---|---|---|---|
| Tu | Rotokaeo | 97 | 8 | Glass >> mica |
| Tu | Rotokauri | 99 | 9 | Glass |
| Ma | Kainui | 87 | 7 | Glass >> 1.0 nm halloysite |
| Rr | Kainui | 87 | 10 | Glass >> 1.0 nm halloysite |
| Rr | Rotokauri | 98 | 10 | Glass |
| Rr | Ngaroto | 95 | 10 | Glass >> 0.7 nm halloysite |

## 3.6. Specific Gravity

The relationship between specific gravity and fines content is presented in Fig. 3.4. The specific gravity values range from 2.10 to 2.68, for tephras with fines content from ~14 to 99%. For comparison purposes, data for Toyoura sand (quarzitic, hard-grained sand), Shirasu sand (pumiceous sand), pure pumice sand (commercially available), and the Tierra Bianca silt (volcanic-ash silt) were plotted as well. Specific representative samples were selected in order to investigate the relationship between the pumice content and the specific gravity. Fig. 3.5 plots the specific gravity vs. pumice content of ten samples, including four of the onshore block samples from Lake Areare.

In general, the first observation from the results (Fig. 3.4) is that the specific gravity of pumiceous soils depends on fines content. As the content of fine particles increases, the specific gravity values increase as well. All data points lie in the range between the value for pure pumice sand (Asadi et al. 2019) and that for the representative hard-grained Toyoura sand.

The increase of specific gravity with increasing fines content is especially evident in the Tu and Rr trendlines (blue dash-dotted and dark green solid line, respectively). Additionally, it could be observed that the trendline of Tu tephra was systematically higher than those derived for the other tephras tested in this study. This is most probably a result of small differences in glass shard major elemental compositions, with Tu notably enriched in Fe (FeOt ~6 wt%) compared to Rr (~1 wt%) (Lowe 1988; Lowe et al. 2008). Subscript t denotes total Fe expressed as FeO.

An interesting exception in the relationship between specific gravity and fines content is the trendline of Ma tephra, where specific gravity is seemingly independent of the fines content. All specific gravity values are close to 2.4 (ranging from 2.30 to 2.43), resulting in an almost flat trendline. It is inferred that this could be a result of a potential lesser (if not completely lacking) content of internal voids within the pumiceous particles, as the values tend towards a specific gravity of 2.4, which is the specific gravity typical of volcanic glass shards. Moreover, in the case of Ma tephra, the specific gravity also seems to be less sensitive to the pumice content in comparison with that of the other two tephras (Tu and Rr) (Fig. 3.5).

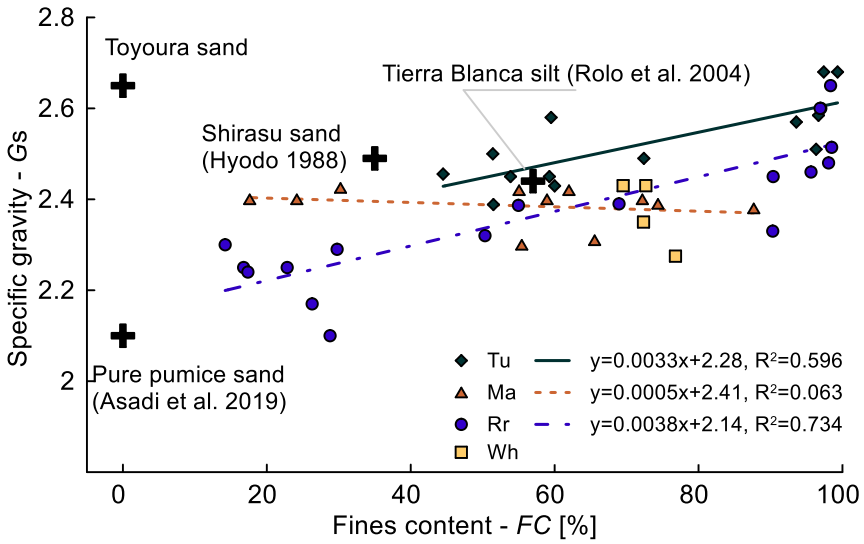


Fig. 3.4. Specific gravity (*Gs*) vs. fines content (*FC*) graph for the four tephra samples (Tu, Ma, Rr, Wh) from different lakes compared with values of relevant sands/silt in published literature.

This indicates that an isolated tephra with these characteristics will still probably be crushable (having pumiceous particles varying from 30 to 50%), yet it would not contribute to a trendline that would assist in deriving pumice content from *Gs* values. This observation may support pumice content estimation methods that are based on the crushability characteristics of pumiceous soil mixtures rather than of those based on weight properties. Nevertheless, the fitted line in Fig. 3.5 (which corresponds to a value of 2.64 for 0% pumice content) supports possible *Gs*-*PC* correlations which, could be used as an indicator for the pumice content of a soil mixture based on the specific gravity value (determined in an identical way – i.e., via gas pycnometer).

## 3.7. Characteristic void ratios

Characteristic void ratios of Tu and Ma tephra samples collected from the block samples at Lake Areare, as well as the trendlines and data point zone from Cubrinovski and Ishihara, (2002), are presented in Fig. 3.6 and 3.7.

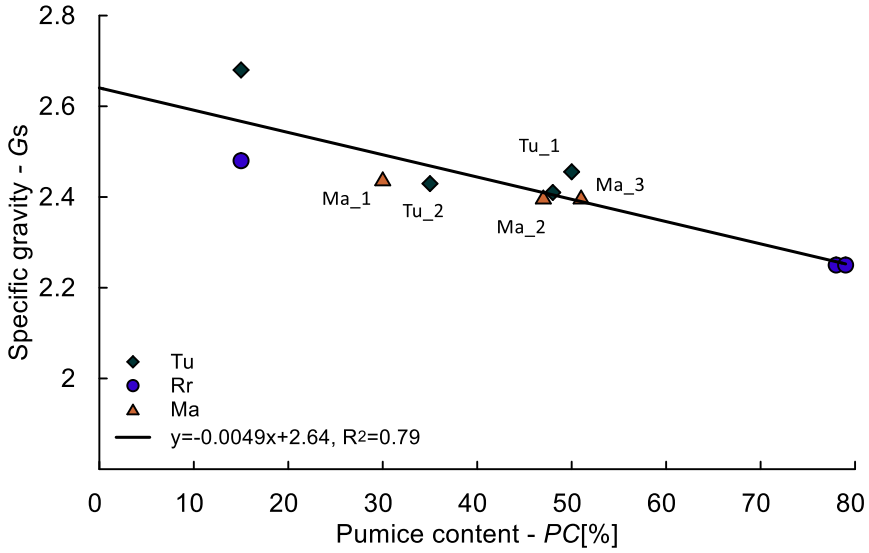


Fig. 3.5. Specific gravity (*Gs*) vs. pumice content (*PC*) for ten selected samples of tephras (Tu, Rr, Ma) from the lakes

Cubrinovski and Ishihara (2002) found that the void ratio range ($e_{max}$-$e_{min}$) embodies the combined effects of mean grain size, grain-size distribution, fines content and grain shape. Note that the characteristic void ratios in this study were determined using the same procedure as the one used by Cubrinovski and Ishihara (2002), modified for small quantities of soil.

By using a large database of more than 300 soil samples, Cubrinovski and Ishihara (2002) established correlations between the characteristic void ratios and the material properties mentioned above (Fig. 3.6 and 3.7).

These correlations are widely recognized when it comes to hard-grained soils, yet as their database did not include pumiceous soils, it is of particular interest to examine whether this trend extends to volcanic-ash materials as well.

In their study, Cubrinovski and Ishihara (2002) found that, there was less scatter and better correlation between the void ratio range and the fines content of sandy soil samples with less than 30% fines, but that in general, the void ratio range increases with the increase in fines content (Fig. 3.6). The five pumiceous samples from the present study show the same trend when observing the fines content. Moreover, the silty samples also show higher offsets from

the trendline when compared to the sandy ones, which also indicates that they are in accordance with the results of Cubrinovski and Ishihara's study mentioned above.

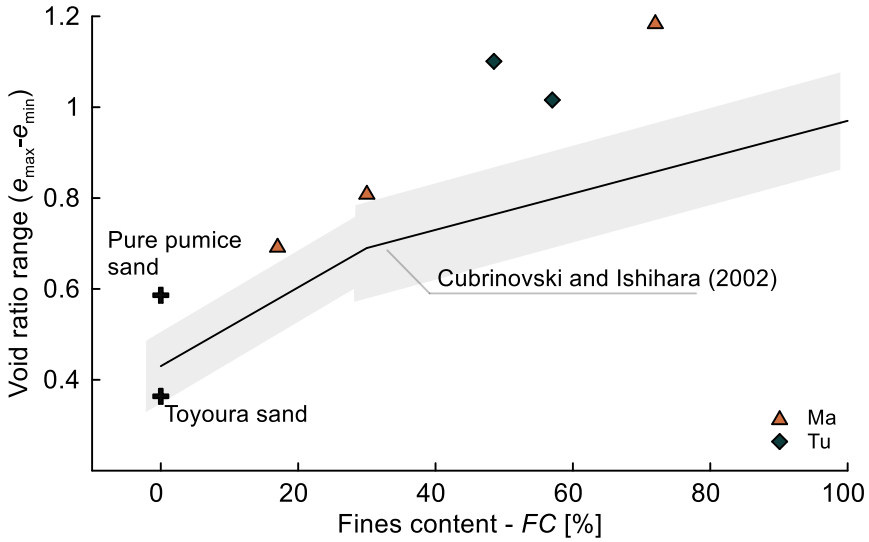


Fig. 3.6. Void ratio range ($e_{max}$-$e_{min}$) vs. fines content (*FC*) graph for the two tephras (Ma, Tu) sampled onshore at Lake Areare compared to trendlines and values found in published literature

The five volcanic-ash samples, as well as the pure pumice sand (Asadi et al. 2019), have higher maximum void ratios compared to those of the hard-grained Toyoura sand (Table 3.3.), meaning in the loosest state (minimum density), the voids-to-solid volume ratio is much higher for the same fines content, which is expected as the pumice particles contain voids. The minimum void ratios also follow this trend but not to the same extent in general. This results with the data points plotting above the void ratio range vs. fines content trendline (Fig. 3.6). This indicates that the difference between the characteristic void ratio values is generally high for pumiceous soils, which may result in higher compressibility because of the bigger range of potential void ratio values (between $e_{max}$ and $e_{min}$). More research needs to be conducted in order to further analyze and interpret if that is indeed the case.

The mutual effects of fines content, mean grain size, and particle shape on the void ratio range are presented in Fig. 3.7 (Cubrinovski and Ishihara 2002). The five tephra samples from our study generally seem to fit in the trends of the grain size and the fines content, with the exception of the Ma_2 and Ma_3.

Ma_2 has lower fines content and higher $D_{50}$ than Ma_3 (Table 3.3), despite plotting above Ma_3. In other words, Ma_2 should have lower characteristic void ratios, or more voids in these two states (minimum and maximum densities achieved in laboratory conditions), so

that it would be in accordance with the trendline. A possible reason for this might be the fact that Ma_3 has higher pumice content than Ma_2, thus resulting in a higher minimum void ratio on account of the voids in the pumice (Table 3.3.).

Table 3.3. Characteristic void ratios and pumice content for Tu and Ma samples, Lake Areare (onshore samples), and relevant void ratios from literature

| Sample | Lake/Ref | $D_{50}$ [mm] | $FC$ [%] | $PC$ [%] | $e_{min}$ | $e_{max}$ |
|---|---|---|---|---|---|---|
| Tu_1 | Areare | 0.09 | 44 | 48±14 | 1.047 | 2.148 |
| Tu_2 | Areare | 0.06 | 59 | 35±11 | 1.152 | 2.168 |
| Ma_1 | Areare | 0.04 | 72 | 30±10 | 0.881 | 2.069 |
| Ma_2 | Areare | 0.3 | 18 | 47±10 | 0.817 | 1.513 |
| Ma_3 | Areare | 0.13 | 30 | 51±11 | 0.705 | 1.518 |
| Toyoura sand | (Zlatovic 1994) | 0.17 | 0 | 0 | 0.616 | 0.988 |
| Pumice sand | (Asadi et al. 2019) | 1.3 | 0 | 100 | 1.679 | 2.266 |

Moreover, if we observe how the five tephra data points plot in the graph, a trend by means of the effect of pumice content can be observed. This would indicate the pumice content may have an effect on the void ratio range values. The observation is not based on enough data to be conclusive but it does inspire the idea for further research in defining to what extent is the pumice content relevant in the characteristic void ratio trendlines for pumiceous soil mixtures.

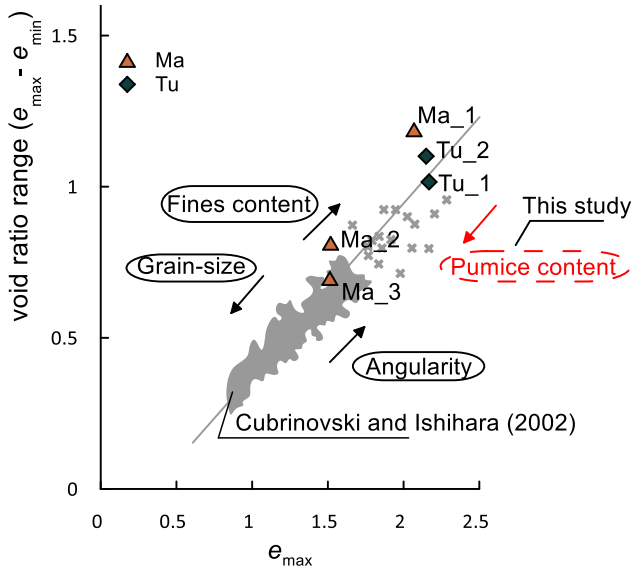


Fig. 3.7. Void ratio range ($e_{max}$-$e_{min}$) vs. maximum void ratio ($e_{max}$) for the two volcanic-ash samples, Lake Areare compared with the values from Cubrinovski and Ishihara, (2002) (Cubrinovski and Ishihara 2002)

## 3.8. Conclusions

Geotechnical properties of up to 45 pumiceous volcanic-ash samples were presented in this paper, with the purpose of characterizing their liquefaction susceptibility as well as assessing the dependence of the void ratios and specific gravity on the pumice content. The main findings can be summarized as follows:

(1) The tephra layers found in lakes in the Hamilton lowlands can be categorized into two groups: (i) liquefaction susceptible sands, silty sands, and silts with no clay minerals; and (ii) samples with a potential but unconfirmed liquefaction susceptibility: silts that contain more than 5% clay-sized particles (in the form of clay minerals).

(2) In general, the specific gravity increased as the fines content increased. An exception to this trend was noted for one of the tephras (Ma). It was hypothesized that this exception could be due to a significantly lower (if not completely lacking) presence of internal voids in the pumiceous particles of this tephra that are non-penetrable by the gas in the gas pycnometer.

(3) Soils with higher pumice content (*PC*) showed lower values of specific gravity (*G*s), indicating that the effect of pumice content could be exploited to derive *G*s–*PC* correlations, which could potentially be used in practice to determine the pumice content from a known value of specific gravity.

(4) The five pumiceous samples from Lake Areare were found to have relatively higher characteristic void ratios compared with values for hard-grained soils. It was found that they fit reasonably well into relevant void ratio range trends derived for hard-grained soils. Further research with a larger database is needed for a more conclusive result.

## Authorship contribution statement

**Jordanka Chaneva:** Investigation, Conceptualization, Methodology, Data curation, Writing – original draft. **Max O. Kluger:** Conceptualization, Methodology, Supervision, Writing - review and editing, Funding acquisition. **Vicki G. Moon:** Methodology, Supervision, Writing - review and editing, Funding acquisition. **David J. Lowe:** Supervision, Funding acquisition, Writing - review and editing. **Rolando P. Orense:** Supervision, Writing - review and editing, Funding acquisition.

## Acknowledgments

This research was funded mainly by MBIE Endeavour Fund (Smart Ideas) project (UOWX1903), and Marsden Fund project (UOW1902). Support was also received from the Earthquake Commission (EQC) project (15/U713), University of Waikato SIF Research Grant (to Lowe 2016), Waikato Regional Council, and QuakeCoRE. The authors thank the iwi of Ngāti Wairere and Ngā Iwi Tōpū O Waipā and the Hamilton City Council, for their support in allowing access to lakes for coring. Marcus Vandergoes, Susie Wood and Andrew Rees, representing the Lakes380 project, are thanked for sediment coring in 2019 and Nic Ross from Hamilton Radiology for CT scanning on sediment cores. T. Ilanko, V. Gibbons, R. Melchert, T. Robertson, K. Vincent, and H. Turner from the University of Waikato are acknowledged for their technical support both in the laboratory and in the field. Finally, three anonymous reviewers are thanked for their comments, which enabled us to improve the paper.

## Addendum

The *PC* values of Toyoura Sand (Zlatovic, 1994) and Pumice Sand (Asadi et al., 2019) were published with a typing error which has been corrected in Table 3.3. of this thesis.

# Chapter 4: Monotonic and cyclic undrained behaviour and liquefaction resistance of pumiceous, non-plastic sandy silt

**Jordanka Chaneva**[1], Max O. Kluger[1], Vicki G. Moon[1], David J. Lowe[1] & Rolando P. Orense[2]

[1]*School of Science/Te Aka Mātuatua, University of Waikato, New Zealand, jc409@students.waikato.ac.nz*
[2]*Department of Civil and Environmental Engineering, University of Auckland, New Zealand*

Published in Soil Dynamics and Earthquake Engineering 168, 2023; 107825
Doi: 10.1016/j.soildyn.2023.107825; © 2023 Elsevier Ltd.

## 4.1. Abstract

Experimental data related to the mechanical behaviour of crushable pumiceous soils are limited compared with those for hard-grained soils. The main focus of previous studies has been on pumiceous sands, whereas pumiceous silts have not been investigated to date. In this paper, several series of monotonic and cyclic triaxial tests were performed to investigate the undrained behaviour and liquefaction resistance of a natural volcanic-ash derived non-plastic pumiceous silt from northern New Zealand. Particle crushing due to sample reconstitution and triaxial testing was analysed by quantifying the changes in grain-size parameters and pumice contents. The main results can be summarized as follows. (1) The pumiceous silt showed a contractive response, even at medium to high relative densities, leading to high flow liquefaction susceptibility. (2) When subjected to cyclic undrained loading, the silt exhibited similar trends in terms of excess pore water pressure and axial strain accumulation to those established for hard-grained soils as opposed to those for pumiceous sands. (3) The liquefaction resistance of both medium-dense and dense samples was within the lower range compared to published cyclic resistance curves of both hard-grained soils and pumiceous sands. (4) The material did not undergo significant particle crushing after testing. Result (4) was considered to be the main factor that contributed to the fact that, in general, the cyclic undrained behaviour of the pumiceous silt was close to the trends established for those of hard-grained soils.

KEYWORDS: pumice; volcanic soil; silt; liquefaction; undrained triaxial tests; state parameter; lake sediment; tephra

## 4.2. Introduction

Earthquake-induced liquefaction can be a major natural hazard in tectonically active regions (Cubrinovski et al. 2011; Ishikawa et al. 2021), hence undrained soil response and liquefaction initiation analyses have been of particular interest in the past six decades. The scientific and engineering community recognizes two main definitions of liquefaction, (1) flow liquefaction, characterized with strain-softening response in undrained loading and it requires in-situ shear stress greater than the undrained shear strength, and (2) cyclic liquefaction, characterized with pore water pressure build up on account of the effective stress reversal to zero. Flow liquefaction can be triggered by both monotonic and cyclic loading. It is also commonly used when defining cyclic liquefaction susceptibility based on the state criteria: in critical soil mechanics, soils susceptible to flow liquefaction are also defined as contractive, thus loose materials that are highly susceptible to cyclic liquefaction as well (Ishihara 1993; Kramer 1996; Robertson et al. 2000).

Since the early works from the 1970s (Castro 1975; Ishihara, Tatsuoka, and Yasuda 1975; Seed and Lee 1966), most of the research related to soil liquefaction has been focused on hard-grained sands and silts, because the common liquefaction susceptible soils were originally considered to be young (i.e., of Holocene age), non- or low-plastic, normally consolidated, hard-grained sandy soils (Boulanger and Idriss 2006; Youd and Perkins 1978). More recent case studies, however, have confirmed the vulnerability of crushable materials, such as pumiceous volcanic soils, to liquefaction as well (M. S. Asadi et al. 2018; de Cristofaro et al. 2022; Hyodo et al. 1998; Licata et al. 2018; Orense et al. 2012). Therefore, in the last few decades, pumiceous sands have become a topic of interest for researchers and geotechnical engineers working in tectonically active areas, such as Italy, South America, Japan, and the North Island of New Zealand (Bommer and Rodríguez 2002; Kokusho 2020; Orense et al. 2002; Pender et al. 1987). Pure pumiceous soils consist of volcanically-derived vesicular, lightweight glass-shard particles of grain sizes varying between gravel (lapilli), sand (coarse to medium ash), and fines (fine ash) (White and Houghton 2006).

For coarse-grained pumiceous soils mainly comprising sand-sized particles, it has been demonstrated that under monotonic undrained loading, the relative density did not have significant effect on the behaviour, as samples in both loose and dense states practically showed similar response (Orense et al. 2012). Orense et al., (2012) found that even at large strain level, pumice sands did not reach steady state of deformation, and inferred that the critical soil

mechanics may not be applicable to crushable soils. During cyclic undrained tests, pumiceous sands show different trends in terms of axial strain and excess pore water pressure (EPWP) development (M. S. Asadi et al. 2018), when compared with those for hard-grained sands. For example, Asadi et al. (2018) found that unlike hard-grained sands, where the development of the EPWP as well as the axial strain increased in a sudden manner in the last loading cycles, pumiceous sands tend to show immediate increase of both the EPWP and the axial strain in the first loading cycles. Moreover, because of the dilative response of pumiceous sands in the succeeding loading cycles, after the initial cycles, the liquefaction resistance of the pumice sands may be significantly higher than that obtained for hard-grained soils (M. S. Asadi et al. 2018; Hyodo et al. 1998). The findings related to the monotonic undrained behaviour of pumice sands (Orense et al. 2012), as well as the different EPWP development and the higher liquefaction resistance of pumiceous sands compared with that of hard-grained sands (M. S. Asadi et al. 2018; Hyodo et al. 1998), have all been attributed to the vesicular nature as well as the complex surface texture of the pumiceous particles, which which leads to significant particle crushing during cyclic loading, especially in samples with high relative densities.

Studies on undrained behaviour and liquefaction resistance of pumiceous sands containing non-plastic fines are even more scarce than studies on pure pumiceous sands (Hyodo et al. 2022; Licata et al. 2018). In the study by Licata et al. (2018), it was found that a pumiceous silty sand mixture with 30% non-plastic fines exhibited a higher liquefaction resistance compared with hard-grained silica sand having the same proportion of fines. They reported negligible particle crushing in their pumiceous material. In contrast, in a more recent study, Hyodo et al. (2022) examined a pumiceous silty sand (Shirasu) comprising pumiceous sand with 28% fines and found the pumiceous silty sand to be less resistant to liquefaction than pure Shirasu sand. However, Hyodo et al. did not discuss the level of particle crushing that might have occurred in the Shirasu sand.

Studies focusing on cyclic undrained behaviour and liquefaction resistance of pumiceous silts (mixtures containing >50% fines) have not been reported to date. Therefore, filling the knowledge gaps for this type of soil materials will assist scientists as well as geotechnical practitioners who are unsure whether they should treat silt-size pumice materials the same as sand-size ones.

This paper is based on a wider testing campaign studying the undrained behaviour and liquefaction resistance of non-plastic pumiceous sandy silt sampled from a silica-rich tephra layer of mid-Holocene age. Tephra deposits are volcanic-eruption-derived, pyroclastic

products of a volcanic eruption of any grain size or composition (Lowe 2011). The tephra layer, preserved within sediments of riverine-peat lakes in the Hamilton lowlands, North Island, New Zealand, has been found to show proof of paleoliquefaction (Kluger et al. 2023). Knowledge about the undrained response of the tephra is crucial in evaluating the loading conditions that caused the tephra to liquefy in the past and will enable assessment of potential future hazards in this region.

For those purposes a series of undrained monotonic and cyclic triaxial tests were performed on reconstituted pumiceous samples, comprising ~52% non-plastic, pumiceous fines. The main aims of this study were to determine: (1) the monotonic behaviour; (2) the undrained cyclic behaviour; (3) the liquefaction resistance; and (4) the extent of particle crushing after testing, of the pumiceous sandy silt. The monotonic tests were also used to develop the critical state line (CSL) of the material in order to analyse the cyclic testing results within the critical state framework. Comments on the meaning of the results from the three main objectives with regards to the paleoliquefaction features found in this tephra are given as well.

## 4.3. Study area

The North Island lies on the Australian Plate and is dominated by tectonic activity and active volcanism as the Pacific Plate is subducted beneath it (Nicol et al. 2017; Shane 2017). Although identified as having low to medium seismic hazard, a short historical record means that an understanding of the magnitude of past earthquakes in the Hamilton lowlands area is poor (Van Dissen et al. 2021; Downs 2005). The lowlands are within the depocentre of numerous tephra-fall deposits derived from eruptions of volcanic centres in the Taupō Volcanic Zone, Egmont/Taranaki volcano, and Tuhua Volcanic Centre (Mayor Island) during the late Quaternary, and contain a number of ~20,000-year-old riverine-peat lakes in which many tephra layers have been well-preserved with minimal post-depositional alteration (Lowe 1986, 1988) (Fig. 4.1a). Several of these tephra layers preserved within the sediments of the lakes have liquefied due to past earthquakes (Kluger et al. 2023). The tephra layers are pumiceous silts, sandy silts, silty sands and sands (Chaneva et al. 2022). This study analysed the cyclic undrained behaviour and liquefaction resistance of the Tuhua tephra, a peralkaline rhyolitic fall-bed derived from an eruption of Mayor Island 7,600 (calendar) years ago (Lowe 1986, 1988).

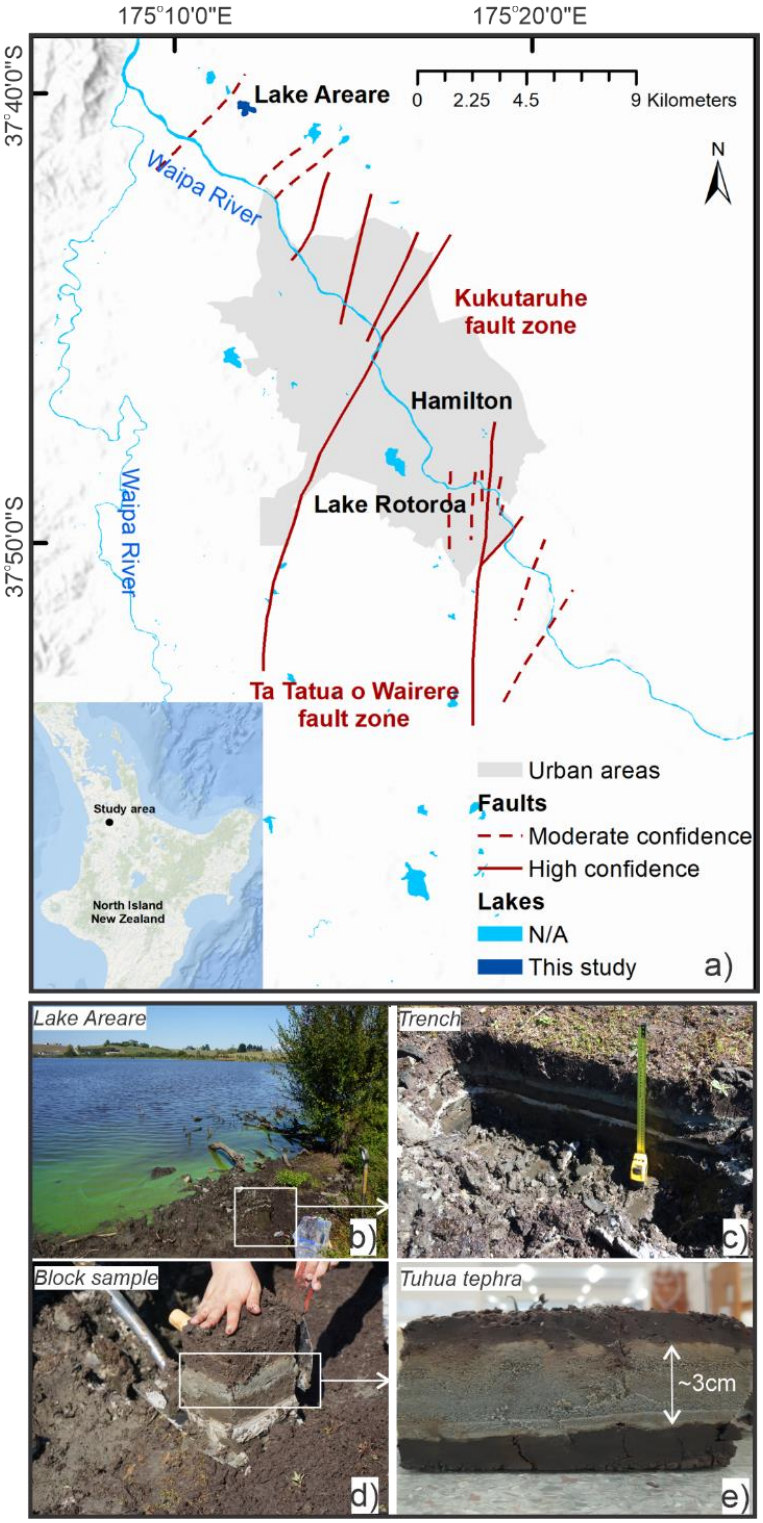


Fig. 4.1. Location of the sampling area for Tuhua silt (i.e., Tuhua tephra) at Lake Areare in the Hamilton lowlands and faults in the area, North Island, New Zealand. Recently identified faults are from (Van Dissen et al. 2021; Moon and Lange 2017) (a). Figure also shows (b) Lake Areare, (c) trench where the blocks were sampled, (d) block samples containing Tuhua tephra in between organic lake sediment layers, and (e) Tuhua tephra isolated from the block sample ready for contamination (organic leftovers) clean up.

## 4.4. Methods and material

### 4.4.1. Sampling procedure

Sampling of Tuhua tephra was undertaken at the shore of Lake Areare (Fig. 4.1a and b), where the material was located at a relatively shallow sediment depth of <0.5 m in the exposed lake bed (Fig. 4.1c). A large number of small block samples (each with volumes of ~0.0075 m3) were taken (Fig. 4.1d), which comprised the ~3 cm-thick Tuhua tephra layer and organic lake sediment above and below the tephra layer. The Tuhua tephra layer (Fig. 4.1e) was then carefully sampled using a spoon, cleaned from organic contamination, and oven-dried at 40°C.

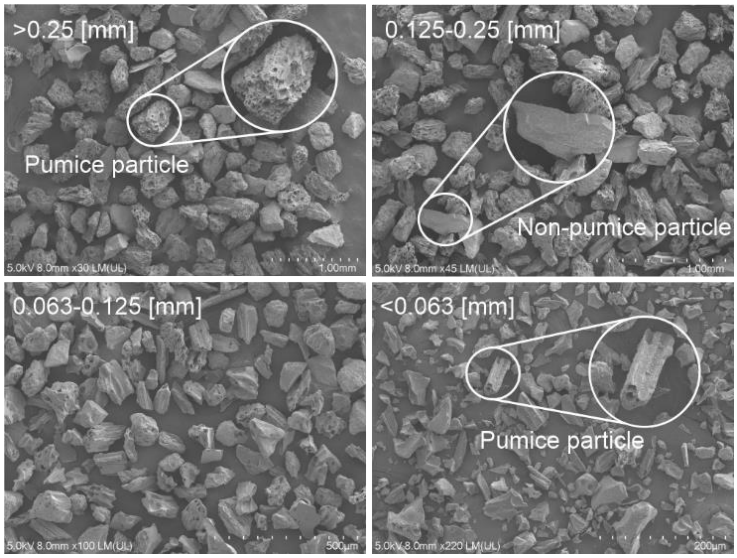


Fig. 4.2. SEM images of Tuhua silt separated in four grain-size fractions (< 0.063 mm, 0.063-0.125 mm, 0.125-0.25 mm and > 0.25 mm)

### 4.4.2. Sample properties

A number of physical and geotechnical properties for the Tuhua tephra were obtained to accompany the triaxial testing campaign, including grain-size distribution, particle density, minimum and maximum dry densities, Atterberg limits, pumice content, and particle shape indices. The grain-size distribution of Tuhua tephra was obtained before (virgin soil) and after triaxial testing (i.e. after reconstitution, consolidation and shearing) through laser diffraction analysis using a Malvern Mastersizer 3000. The tephra soil classification and fines content threshold (%<0.075 mm) were defined following the ASTM D2487-11 (2011). The particle density was determined using a Quantachrome Ultrapyc 1000 nitrogen-filled gas pycnometer following ASTM-D5550-14, (2014). The minimum and maximum dry densities of the samples were obtained following the Japanese standard method (Japanese Geotechnical Society

Standard 2009) as modified by Mijic et al. (2021). Atterberg limits were obtained following ASTM-D4318-17e1, (2017).

The pumice content was quantified in a similar manner to that of Asadi *et al.*, (2019): a sample was separated into different grain-size fractions (i.e., <0.063 mm, 0.063-0.125 mm, 0.125-0.25 mm and >0.25 mm) by dry sieving. The mass of each fraction was determined. Then, images of clusters representing the different grain-size fractions were obtained using scanning electron microscopy (SEM) (Fig. 4.2). The pumice content for each fraction was then defined by means of visual inspection of the pumiceous vs non-pumiceous particles based on three SEM images per fraction, which corresponded to a total count of about 100-140 particles per fraction. The highly vesicular rough-textured particles were defined as pumiceous particles, whereas the fragments of the pumice particles that were found to lack internal voids, namely glass shards, were considered as non-pumiceous particles (Fig. 4.2). In the final step, the total pumice content of the sample was calculated by averaging the pumice contents of fractions defined based on the number of pumiceous particles against the total number of particles with respect to a correction factor based on their relative mass to the total mass of the sample (Asadi et al. 2019).

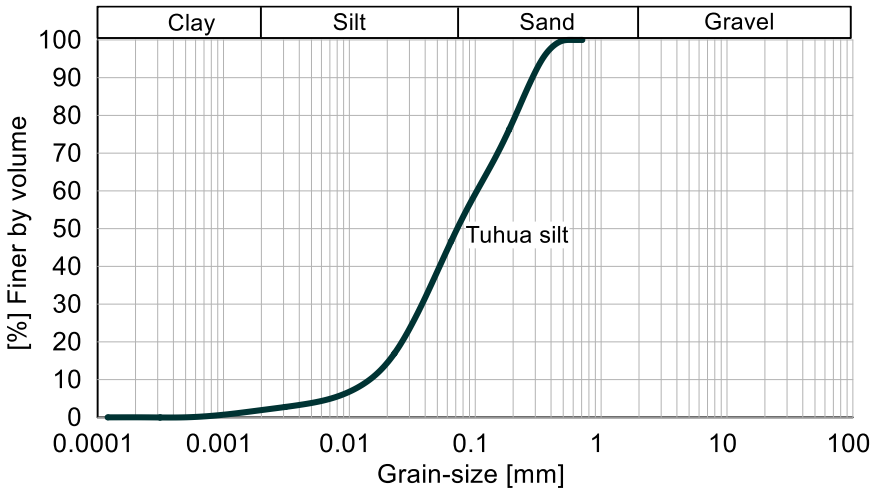


Fig. 4.3. Grain-size distribution of Tuhua silt prior to triaxial testing

The particle shape analysis was performed following the methodology of Kikkawa et al. (2013). The method is based on SEM images of the different fractions (i.e., <0.063 mm, 0.063–0.125 mm, 0.125–0.25 mm and >0.25 mm) of the original Tuhua tephra using 20 particles per fraction, thus 80 particles in total. The quantification of the particle shape characteristics through the roundness coefficient (*R*c), aspect ratio (*A*r), and angular coefficient (*Ac*), are defined as follows:

$$R_c = \frac{L^2}{4\pi A} \tag{4.1}$$

$$A_r = \frac{b}{a} \tag{4.2}$$

$$A_r = \left| R_c - 1 + \frac{A_r^2}{2A_r} \right| \tag{4.3}$$

In the above equations, $L$ is the perimeter of the particle, $A$ is the surface area of the particle, and $a$ and $b$ are the dimensions of the particles along the minor and major axes respectively. The particle shape indices were calculated for all 80 particles, averaged by fraction and the final values were calculated with respect to the correction factor of each fraction based on the relative mass to the total mass of sample. A supplementary table S2, showing the results for all 80 particles can be found in Appendix A.

The grain-size distribution curve of the Tuhua tephra (i.e. virgin soil) prior to triaxial testing is shown in Fig. 4.3. With fines content of 51% (of which only 4% were clay sized particles) and having tested as a non-plastic sandy silt following ASTM D-2487 (2018), the tested material will be referred to as Tuhua silt (ML) hereafter. The minimum and maximum void ratios are 1.06 and 2.18, respectively. The pumice content of the silt is 48%. The roundness coefficient ($R$c), aspect ratio ($A$r), and angular coefficient ($A$c), are 1.829, 1.466 and 1.38 respectively, classifying the particles of the Tuhua silt material as ellipsoidal, elongated and highly angular (Asadi et al. 2017; Kikkawa et al. 2013). All the material properties of the Tuhua silt are summarized in Table 4.1.

Table 4.1. Index properties of Tuhua silt

| Material | $G_S$ | $D_{50}$ [mm] | $FC$ [%] | $PC$ [%] | $e_{min}$ | $e_{max}$ | $R_c$ | $A_r$ | $A_c$ |
|---|---|---|---|---|---|---|---|---|---|
| Tuhua silt | 2.41 | 0.073 | 51.2 | 48 | 1.06 | 2.18 | 1.83 | 1.47 | 1.38 |

### 4.4.3. Triaxial testing

A GDS Advanced Dynamic Triaxial Testing System was used for the triaxial testing of the samples. The samples were reconstituted using the under-compaction method following the procedure of Ladd, (1978). The compressive response of the tested material in the medium-high density range (i.e. $0.35 \leq D\text{r} \leq 0.65$) in the initial tests, was indicative of the redundancy in testing looser samples, as medium-high to high dense samples already captured the transition from contractive to dilative behaviour. Moreover, loose samples are known to exhibit higher

degree of soil heterogeneities affecting the undrained soil response (Hariprasad et al. 2016; Kluger et al. 2021). Therefore, the target densities in the testing campaign were above the medium-dense range according to the relative density designations as per Terzaghi and Peck, (1967).

The target size of the triaxial samples was 50 mm in diameter and 100 mm in height. Deaired and demineralised water was added to the samples until a water content of 15% was obtained. Then, samples were reconstituted in eight layers into a split mould mounted on top of the triaxial base plate. For the first layers a percent undercompaction ratio of 0% was selected for reconstituting samples at high relative densities, whereas an undercompaction ratio of 15% was chosen for reconstituting samples at medium to medium-high relative densities. The definition of the undercompaction ratio is defined in the original publication of Ladd (1978). The density distribution throughout the sample was checked by observing the shape of the sample once reconstituted and its failure pattern, following the recommendations of Ladd (1978).

After reconstituting the sample, the top cap was placed on the sample and the cell was assembled and filled with water. Before the saturation phase, the sample was flushed with deaired and demineralized water through the back-pressure pump. A B-value of more than 0.95 was reached once the sample was subjected to back pressures of at least 800 kPa over 15 h in the saturation stage. During the B-value check, the cell pressure was increased by 70 kPa and 20 kPa for effective consolidation pressures $\sigma_c$' corresponding to 100 kPa and 20 kPa, respectively (DIN EN ISO 17892-9, 2018). More details about the tests and their specific conditions are summarized in Table 4.2. Two levels of consolidation pressure were used in this study. The effective consolidation pressure $\sigma_c$' = 20 kPa was considered to most accurately represent the stress conditions in the in-situ Tuhua silt and $\sigma_c$' = 100 kPa effective consolidation stress was used in order to compare the undrained behaviour and liquefaction resistance of the studied material with other soil types from the literature. Many other researchers have performed triaxial tests on soil materials under low confining stresses before (Fannin, Eliadorani, and Wilkinson 2005; Y. Huang et al. 2015; Lancelot et al. 2006). However, because the consolidation pressure of 20 kPa is considered to be at the lower end of what the sensors of the triaxial apparatus are able to measure, a supplementary Fig. S1. is provided to show that the data quality of the 20 kPa consolidation pressure tests in this study. The results or a representative test (Tu-CY-21, Table 4.2.) by means of pore water pressure, deviator stress and axial strain development for a single cycle are presented. The oscillation variations of the

sensors vary between 0%, for the last cycle in the axial strain vs. time plot (Fig. S1, (d)) to 12.5% in the pore water pressure vs. time plot (Fig. S1, (a)) of the corresponding amplitude. The oscillation variations are calculated by dividing the amplitude of the oscillation (e.g. 0.5/2 = 2.5 kPa, Fig.S1 (a)) with the amplitude in the corresponding peak of the cycle (e.g. 2 kPa, Fig.S1 (a)) and converting into percentage (2.5/2 x 100 = 12.5%). The sensors provided sufficiently high signal-noise ratios that do not affect the soil response analysis, thus generated meaningful results.

The post-consolidation void ratios of the samples were obtained following two different approaches. In the first approach, the volume change of the sample due to consolidation was measured by the back-pressure pump. In the second approach, the volume change due to consolidation was derived after completing the test following the procedure proposed by Verdugo and Ishihara (1996). The post-consolidation void ratios considered in this study were calculated by either (1) averaging the values from both approaches or (2) using the one value for the tests where results from both methods were not available (Table S1).

Seven monotonic undrained triaxial tests were performed on the reconstituted samples. Five tests were performed in compression and two tests in extension. The details about the testing conditions are presented in Table 4.2. A constant displacement rate of $\dot{s}$ = 0.1 mm/min was chosen following DIN EN ISO 17892-9 (2018). Shearing was performed until the axial strain reached ±10 to 15%.

A total of 18 cyclic undrained, stress-controlled triaxial tests were performed (Test series 2 to 6, Table 4.2). The cyclic stress amplitudes in these tests were applied with a frequency of $f$ = 0.02 Hz. Additional two tests were performed to explore the frequency influence on the cyclic undrained response of the tested material (Test series 7, Table 4.2). Both tests were a replicate of Tu-CY-10 (Table 4.2) by means of effective consolidation stress, relative density, and cyclic stress ratio ($CSR = q_{dev}/(2\sigma_c')$, where q is deviator stress), with the only difference being the frequency ($f$ = 0.1 Hz and f = 1 Hz). The results confirm that the response of the non-plastic silt is frequency independent (supplementary Fig. S2). The calculation of the cyclic stress ratio, double axial strain amplitude ($\varepsilon_{da}$), pore water pressure ratio ($r_u=u/\sigma_c'$, where u is the excess pore water pressure (EPWP) in kPa), and number of loading cycles to liquefaction ($N_{CL}$) followed ASTM D 5311 - 92 (2004). The initiation of cyclic liquefaction according to the ASTM D 5311 - 92 (2004) is considered when either the double axial strain amplitude ($\varepsilon_{da}$) reached 5 % or when the pore water pressure ratio ($r_u$) reached 0.9.

## 4.5. Results

### 4.5.1. Monotonic triaxial tests results

The effect of relative density, *D*r, on the monotonic undrained response of Tuhua silt was analysed for the tests performed at the low effective consolidation pressure of 20 kPa (Fig. 4.4). The test with *D*r = 0.51 (Tu-CU-2) exhibited a low peak strength with fully contractive behaviour. The response of the *D*r = 0.65 (Tu-CU-4), started with a similar stiffness as the *D*r = 0.51 test (Tu-CU-2,) at small strains, peaked soon after at the phase transformation point (Ishihara et al. 1975) and then strain-softened as the stress path approached the critical state line in a contractive manner. The dense sample (Tu-CU-5, *D*r = 0.77) exhibited a higher initial stiffness when compared to the other two (medium-dense) tests and was found to be purely dilative. The peak strength was found to increase with the increase in relative density.

The effect of effective consolidation pressure on the monotonic undrained response of Tuhua silt was analysed by plotting together all the tests performed (Fig. 4.5). As expected, the initial stiffness and peak strength increased with effective consolidation pressure (when comparing tests performed at similar relative densities). Furthermore, it was observed from Fig. 4.5 that Tuhua silt exhibited contractive behaviour within the range of relative densities $0.51 \leq D\text{r} \leq 0.69$ which are considered to be within the medium-high to high density range.

The results from the monotonic tests were used to obtain the critical state line for the material (Fig. 4.6a). The start point, phase transformation point, and critical state point of individual tests as well as the critical state line are presented in Fig. 4.6a in the e-*p*' plane. The minimum and maximum void ratios obtained for Tuhua silt (i.e., at zero mean effective stress) are also plotted in the figure. It can be observed that the critical state line of Tuhua silt is located approximately in the middle between its minimum and maximum void ratios within the mean effective stress range 1 to 1000 kPa.

### 4.5.2. Cyclic triaxial tests results

The Tuhua silt samples were found to commonly exhibit one of two types of cyclic undrained behaviour: behaviour type 1, which was characterized by a gradual increase in axial strain and EPWP in the last cycles before failure, and behaviour type 2, where a sudden response was observed with axial strain development being restricted to the last cycle prior failure. In Fig. 4.7, typical experimental results representing these two types of cyclic undrained behaviour are presented.

Table 4.2. Experimental programme

| Test series | Type of test | Label | $\sigma_c$' [kPa] | $e_i$ | $Dr_{,i}$ | $e_c$ | $Dr_{,c}$ | $f$ [Hz] | $CSR$ | $N_{CL}$ | $\psi$ |
|---|---|---|---|---|---|---|---|---|---|---|---|
| 1 | M | Tu-CU-1 | 100 | 1.80 | 0.34 | 1.61 | 0.51 | n/a | n/a | n/a | 0.316 |
| | M | Tu-CU-3 | 100 | 1.51 | 0.60 | 1.42 | 0.69 | n/a | n/a | n/a | 0.124 |
| | M | Tu-CU-2 | 20 | 1.80 | 0.34 | 1.61 | 0.51 | n/a | n/a | n/a | 0.171 |
| | M | Tu-CU-4 | 20 | 1.53 | 0.58 | 1.46 | 0.65 | n/a | n/a | n/a | 0.021 |
| | M | Tu-CU-5 | 20 | 1.39 | 0.71 | 1.33 | 0.77 | n/a | n/a | n/a | -0.114 |
| | M | Tu-CUE-1 | 100 | 1.77 | 0.37 | 1.62 | 0.51 | n/a | n/a | n/a | 0.324 |
| | M | Tu-CUE-2 | 20 | 1.76 | 0.38 | 1.62 | 0.50 | n/a | n/a | n/a | 0.181 |
| 2 | Cy | Tu-CY-12 | 100 | 1.85 | 0.29 | 1.69 | 0.44 | 0.02 | 0.07 | 57 | 0.392 |
| | Cy | Tu-CY-11 | 100 | 1.79 | 0.35 | 1.62 | 0.50 | 0.02 | 0.09 | 17 | 0.328 |
| | Cy | Tu-CY-10 | 100 | 1.76 | 0.38 | 1.59 | 0.53 | 0.02 | 0.11 | 10 | 0.291 |
| | Cy | Tu-CY-7 | 100 | 1.82 | 0.33 | 1.65 | 0.47 | 0.02 | 0.13 | 4 | 0.356 |
| 3 | Cy | Tu-CY-4 | 100 | n/a | n/a | 1.45 | 0.65 | 0.02 | 0.11 | 45 | 0.154 |
| | Cy | Tu-CY-5 | 100 | 1.48 | 0.63 | 1.43 | 0.67 | 0.02 | 0.13 | 35 | 0.134 |
| | Cy | Tu-CY-2 | 100 | 1.45 | 0.65 | 1.38 | 0.72 | 0.02 | 0.15 | 31 | 0.083 |
| | Cy | Tu-CY-6 | 100 | 1.49 | 0.62 | 1.40 | 0.70 | 0.02 | 0.17 | 12 | 0.104 |
| 4 | Cy | Tu-CY-18 | 20 | 1.85 | 0.29 | 1.65 | 0.48 | 0.02 | 0.05 | 39 | 0.211 |
| | Cy | Tu-CY-16 | 20 | 1.83 | 0.32 | 1.74 | 0.40 | 0.02 | 0.07 | 9 | 0.299 |
| | Cy | Tu-CY-15 | 20 | 1.81 | 0.33 | 1.61 | 0.51 | 0.02 | 0.09 | 5 | 0.168 |
| | Cy | Tu-CY-14 | 20 | 1.81 | 0.34 | 1.69 | 0.43 | 0.02 | 0.11 | 3 | 0.256 |
| 5 | Cy | Tu-CY-19 | 20 | 1.49 | 0.61 | 1.42 | 0.68 | 0.02 | 0.1 | 50 | -0.016 |
| | Cy | Tu-CY-13 | 20 | 1.52 | 0.59 | 1.44 | 0.66 | 0.02 | 0.11 | 21 | 0.001 |
| | Cy | Tu-CY-8 | 20 | 1.34 | 0.76 | 1.43 | 0.67 | 0.02 | 0.15 | 11 | -0.009 |
| 6 | Cy | Tu-CY-21 | 20 | 1.33 | 0.76 | 1.29 | 0.80 | 0.02 | 0.15 | 23 | -0.149 |
| | Cy | Tu-CY-22 | 20 | 1.35 | 0.75 | 1.28 | 0.81 | 0.02 | 0.13 | 88 | -0.164 |
| | Cy | Tu-CY-23 | 20 | 1.34 | 0.75 | 1.30 | 0.79 | 0.02 | 0.17 | 29 | -0.139 |
| 7 | Cy | Tu-CY-17 | 100 | 1.83 | 0.31 | 1.67 | 0.45 | 0.1 | 0.11 | 10 | 0.378 |
| | Cy | Tu-CY-20 | 100 | 1.77 | 0.37 | 1.61 | 0.51 | 1 | 0.11 | 12 | 0.314 |

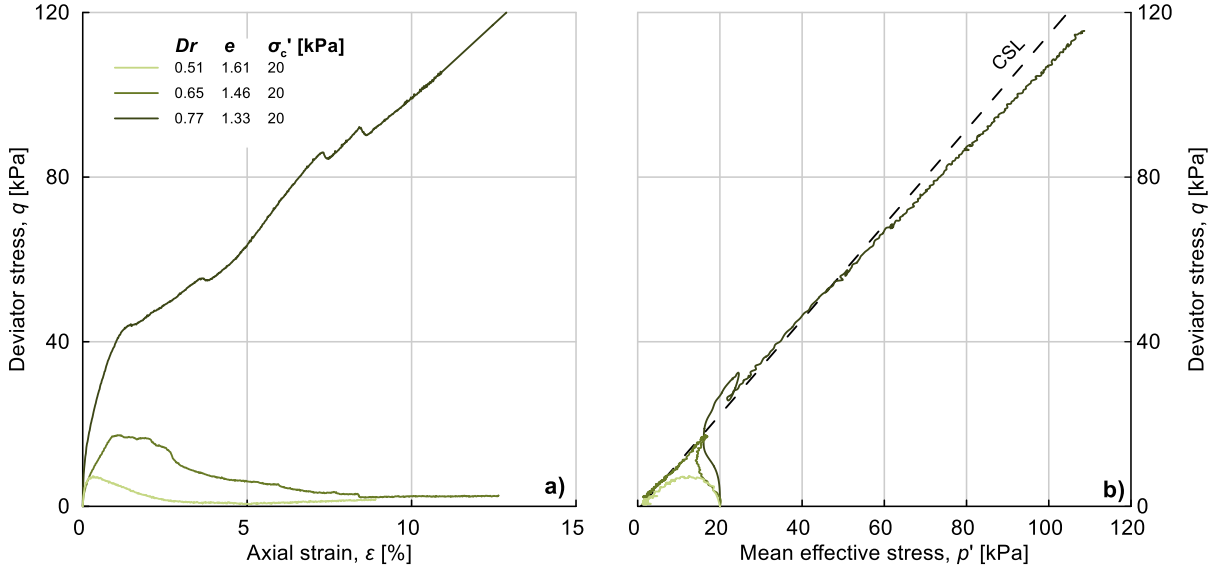


Fig. 4.4. Monotonic undrained compression behaviour of Tuhua silt tested at 20 kPa effective consolidation pressure. Results are presented by means of (a) stress-strain and (b) stress paths relationships

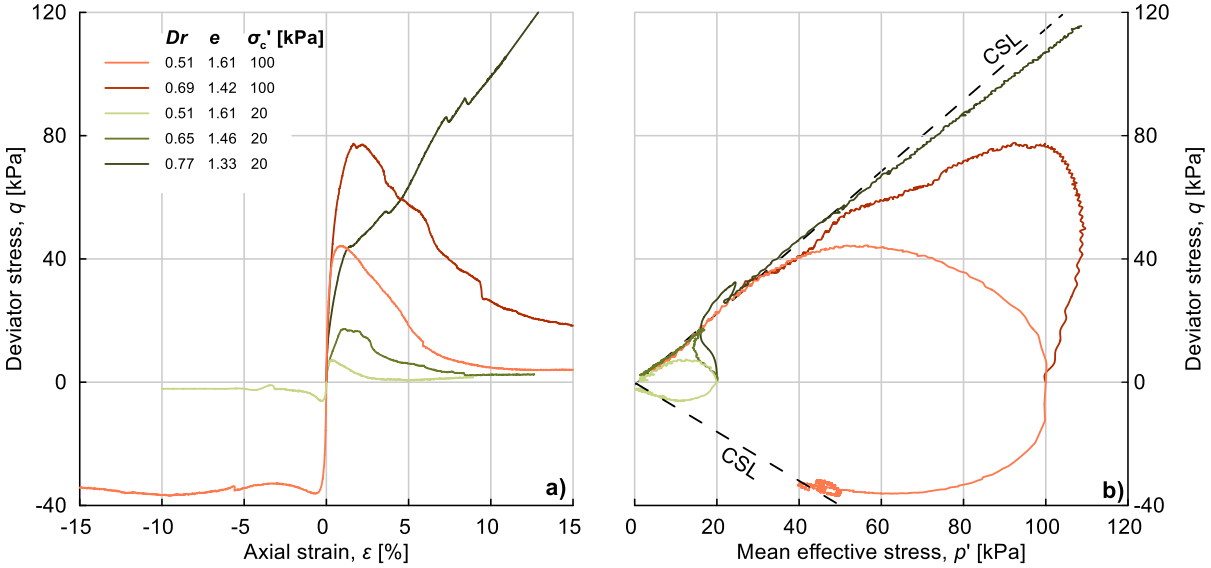


Fig. 4.5. Monotonic undrained behaviour of Tuhua silt tested at 20 kPa and 100 kPa effective consolidation pressure. Results are presented by means of (a) stress-strain and (b) stress paths

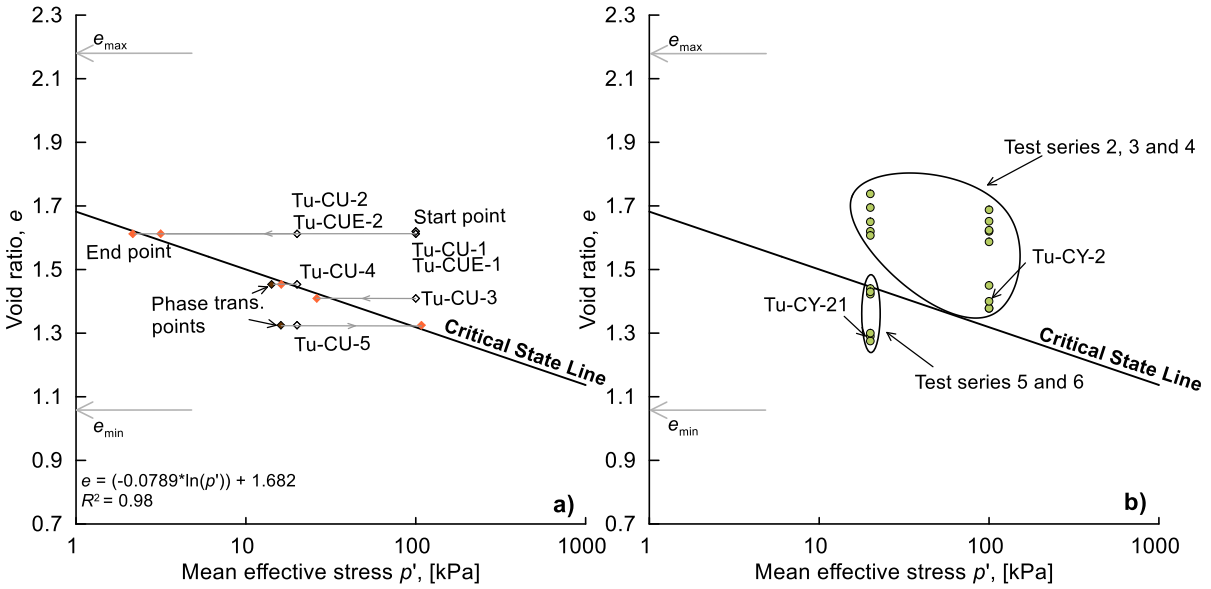


Fig. 4.6. (a) Critical state line (CSL) of Tuhua silt obtained from monotonic undrained triaxial tests presented together with the stress paths from monotonic compression and extension tests. White, black, and orange diamonds represent the start, phase transformation point, and critical state point, respectively. (b) Initial states (green) circles of the cyclic undrained triaxial tests presented together with the CSL of Tuhua silt

The first test (Tu-CY-21), representing cyclic undrained behaviour type 1, exhibited small axial strain for the first ~15 loading cycles, and then started to develop a gradual and steady increase in axial strain amplitude as it approached failure at 23 cycles (considering both axial strain and EPWP thresholds) (Fig. 4.7a). The EPWP increased in a linear manner with the loading cycles, reaching a value of around 0.95 of the initial effective consolidation pressure at failure (liquefaction). The gradual development of the liquefaction of this test under

cyclic undrained testing can also be observed by considering its deviator stress-axial strain hysteresis response (Fig. 4.7b), where the slopes of the hysteresis loops started to gradually decrease in the last cycles.

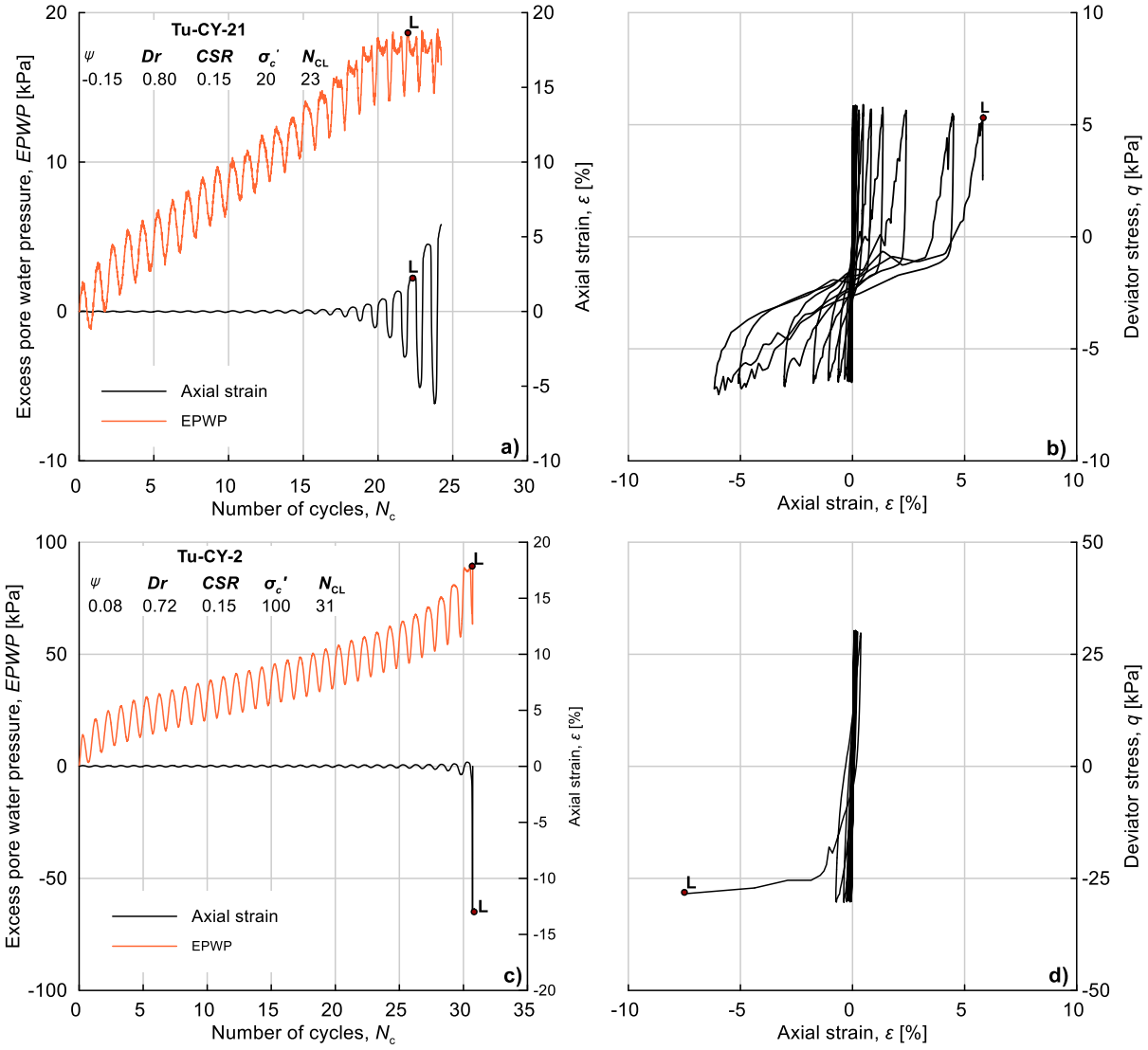


Fig. 4.7. Two typical examples of developments of axial strain and excess pore water pressure (left panels) and stress-strain curves (right panels). Tuhua silt samples tested in this study could be classified as exhibiting either (1) a gradual increase in axial strain and excess pore water pressure until failure – behaviour type 1 (a and b); or (2) a sudden axial strain development in the last cycle – behaviour type 2 (c and d). Note the letter "L" in the figure stands for liquefaction (initiation)

In the second example (Tu-CY-2), representing cyclic undrained behaviour type 2, the axial strain remained small for the most part of the cyclic loading, with significant axial strain developing only within the last loading cycles prior to liquefaction (Fig. 4.7c). Moreover, unlike the case with the behaviour type 1 tests where the accumulation of the EPWP was at a steady rate throughout the test, the EPWP in this case started off with a smaller increase in rate

and then increased more rapidly during the last half of the cyclic loading until liquefaction occurred after 31 loading cycles. This test exhibited a very narrow range of deviator stress-axial strain hysteresis loops slopes (indicating a constantly high stiffness), with the vast majority of axial strain occurring within the last loading cycle (Fig. 4.7d).

Both tests were performed on samples with relatively similar relative densities (i.e., *D*r of 0.72 and 0.80). Furthermore, both samples were tested at the same cyclic stress ratio (0.15), achieved failure after a similar number of loading cycles, but were consolidated under different effective consolidation pressures. Because of the effective consolidation pressures used in the present study (i.e., 20 and 100 kPa), it is more appropriate to present the cyclic undrained results using their state parameters (Been and Jefferies 1985) rather than using void ratios or relative densities.

The state parameter, $\psi$, is the difference between a given void ratio, $e$, and the corresponding void ratio of the steady state line, ess, for the effective consolidation stress of interest, and it incorporates the combined effect of both the void ratio and the effective consolidation stress (Been and Jefferies 1985). The state parameters of all of the cyclic tests are given in Table 4.2. The initial states in the cyclic tests are plotted against the critical state line in the e-$p$' plane in Fig. 4.6b.

The results by means of the development of the double amplitude axial strain, the excess pore water pressure, and the normalized number of loading cycles ($N_C/N_{CL}$) for all the cyclic tests performed in this study are presented in Fig. 4.8.

The samples tested in series 5 and 6 (i.e. with effective consolidation pressures of 20kPa and medium-dense to dense relative densities) showed negative state parameters of $-0.16 \leq \psi \leq 0.001$ (Table 4.2, Fig. 4.6b), and exhibited stable cyclic undrained responses that were characterized by a gradual increase in EPWP and as well as axial strain increase (i.e., cyclic undrained behaviour type 1). The remaining cyclic tests (series 2, 3, and 4), having positive state parameters of $0.08 \leq \psi \leq 0.39$, showed a sudden axial strain increase at the moment of failure (i.e., cyclic undrained behaviour type 2).

Finally, the cyclic resistance ratio (*CRR*) data points (i.e., liquefaction resistance) for all the cyclic tests as well as their corresponding liquefaction resistance curves were obtained. In all the tests, failure occurred in a simultaneous manner, with both the double axial strain amplitude, $\varepsilon_{da}$, exceeding 5 % and the pore water pressure ratio, $r_u$, reaching 0.9 in the same loading cycle. The liquefaction resistance curves were obtained using power functions in the

shape of $CRR = aN_{CL}$-b, and reflect the variations in relative density, effective consolidation pressure, and state parameter (Table 4.2, Fig. 4.9). Figure 4.9 illustrates that the liquefaction resistance of Tuhua silt generally increased with relative density and consolidation pressure. In relation to the state parameter, higher values of the state parameter indicate lower resistance of liquefaction.

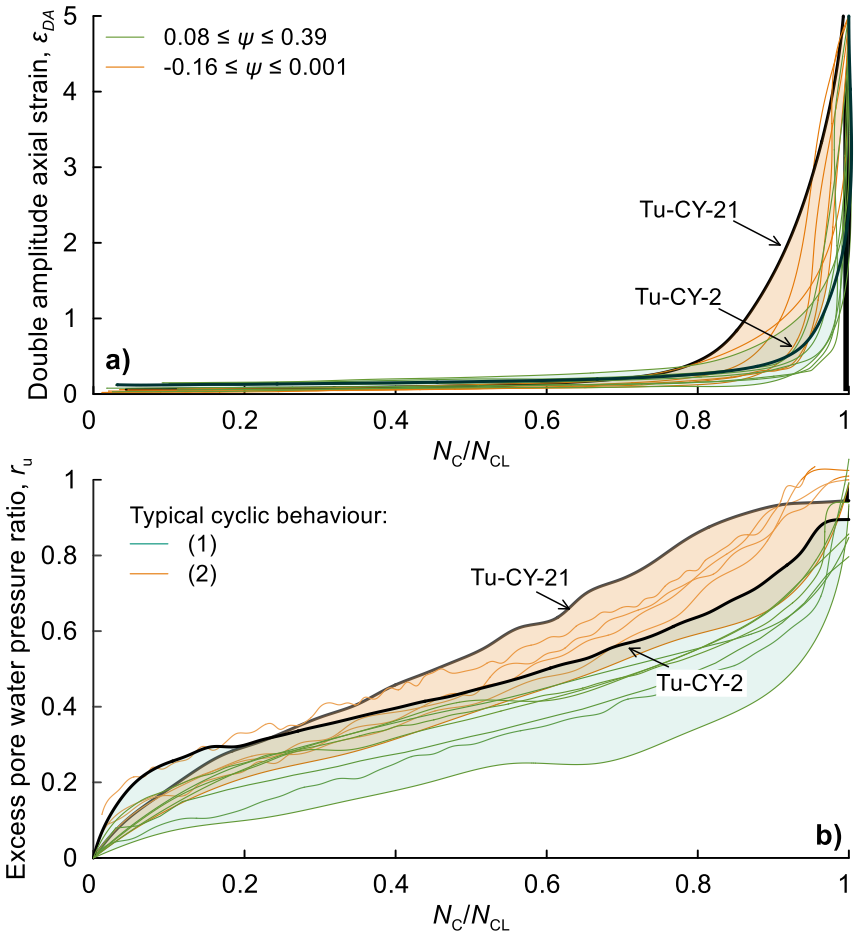


Fig. 4.8. Cyclic undrained behaviour of Tuhua silt presented by means of (a) double amplitude axial strain and (b) excess pore water pressure both being plotted vs. the normalized number of cycles. Green and orange shadings represent the range observed for baheviour types 1 and 2 respectively. Bold lines represent the two typical examples presented in Fig 4.7.

### 4.5.3. Particle crushing

Considering the fact that the non-pumiceous particles in the Tuhua silt are defined to be the pumice fragments that no longer contain internal voids, thus are considered to be less crushable (although not exactly hard-grained), the potential particle crushing due to sample reconstitution, consolidation, and shearing during triaxial testing was analysed by quantifying

the changes in grain-size parameters and pumice contents in the samples after testing. The assumption here is that if particle crushing occurred, the number of pumiceous particles would have decreased and the number of non-pumiceous particles (glass shards) would have increased.

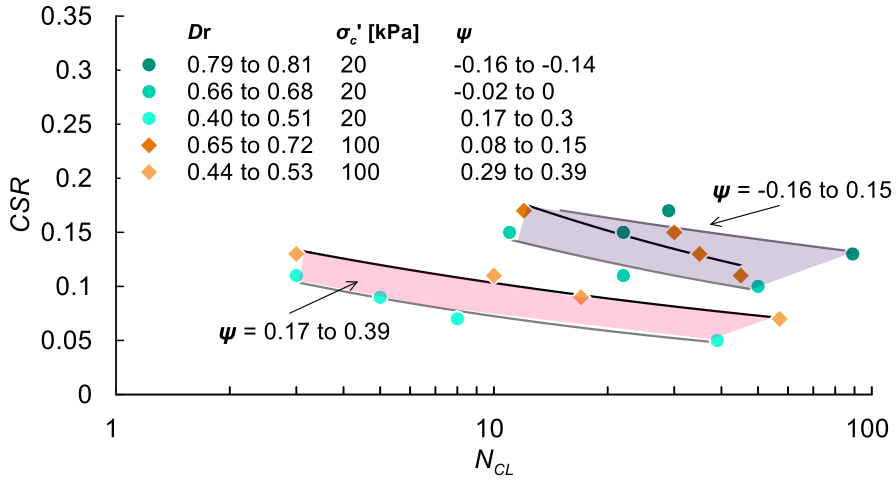


Fig. 4.9. Liquefaction resistance curves of Tuhua silt tested at three different relative densities and two effective consolidation pressures, with their associated values of the state parameter. Shaded areas indicate two clusters around curves which are associated with $\psi$ = -0.16 to 0.15 and $\psi$ = 0.17 to 0.39, respectively

The $D_{10}$, $D_{50}$, and $D_{90}$ grain-size parameters measured after sample reconstitution and triaxial testing were plotted for all samples with respect to their built-in consolidated void ratios and effective consolidation stresses (Fig. 4.10). By observing the mean values and their standard deviations presented in Fig. 4.10, it is evident that (1) the effective consolidation pressure used in this study did not significantly affect the amount of particle crushing, and (2) the pre-testing median grain size generally lies within $\pm$ 1standard deviation (SD) derived from the post-testing samples for most of the test conditions. Based on this, it can be inferred that there is no meaningful change in the grain-size distribution after testing, thus, no particle crushing occurred.

The second approach used SEM images of the soil particles from selected tests within a range of relative densities (1.28–1.69) for both effective consolidation pressures (20 and 100 kPa), from which the pumice contents were defined before and after testing. The hypothesis with this approach is that if the pumice content did not change, no particle crushing occurred. The five tests that were selected over a range of void ratios (relative densities) for both effective consolidation pressures are Tu-CU-5, Tu-CY-10, Tu-CY-6, Tu-CY-14 and Tu-CY-22 (Table 4.2).

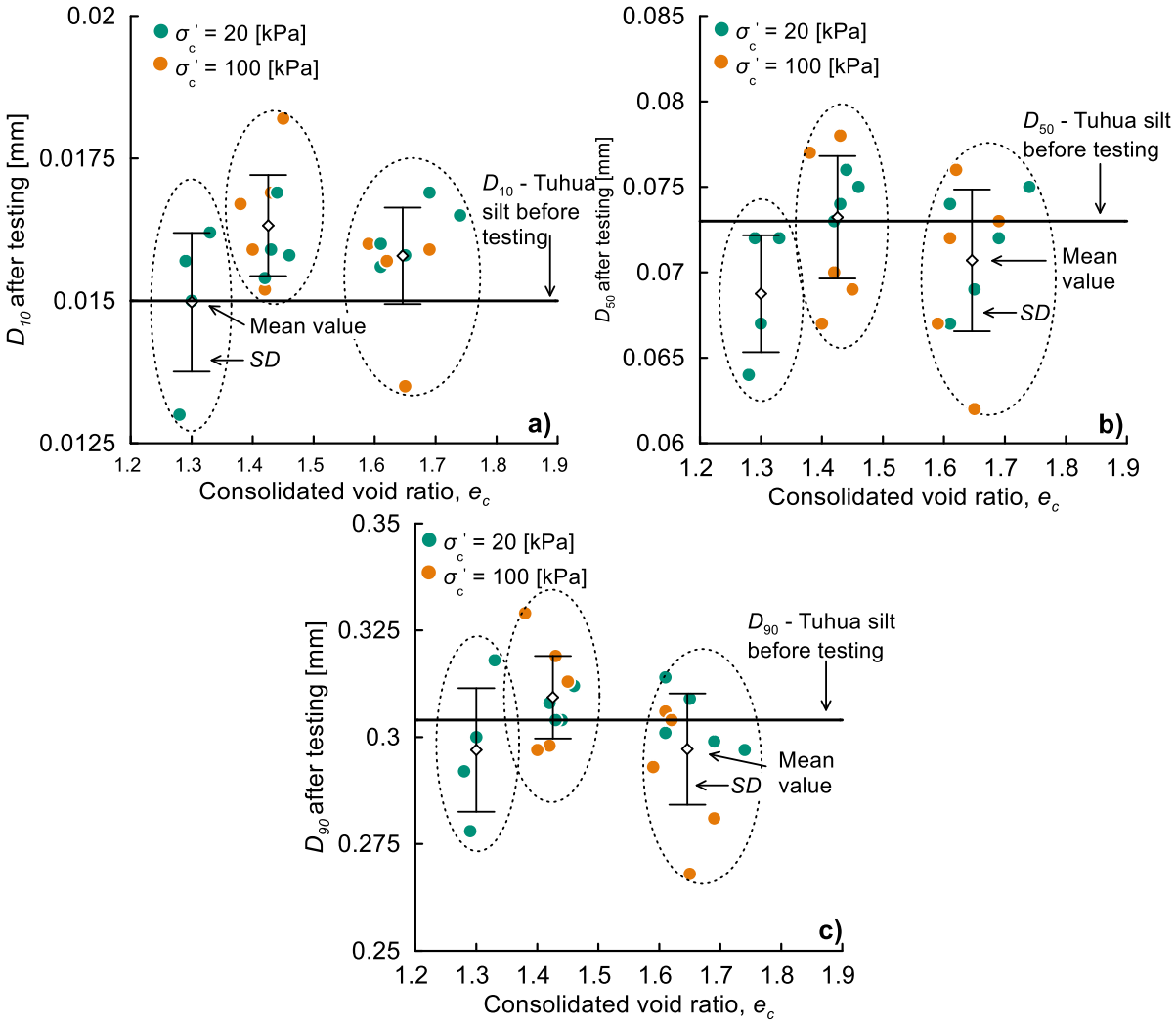


Fig. 4.10. Change in grain-size parameters (a) $D_{10}$, (b) $D_{50}$, and (c) $D_{90}$ due to cyclic and monotonic triaxial tests of Tuhua silt

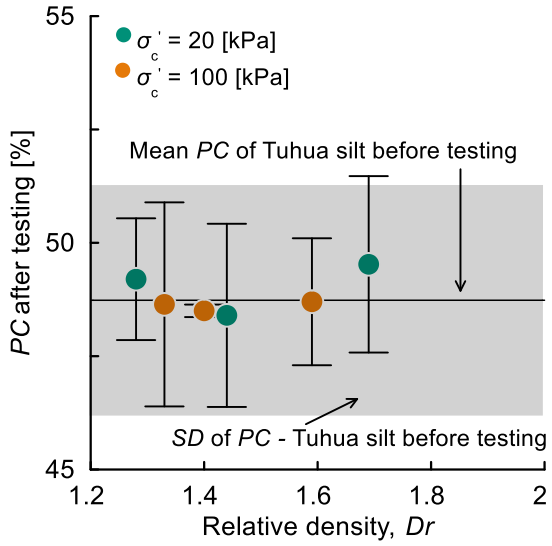


Fig. 4.11. Pumice contents after monotonic and cyclic triaxial testing for different relative densities

The mean pumice content per fraction for all of the selected samples is presented in Fig. 4.11. The mean pumice content determined before testing (grey area in Fig. 4.11 denotes one SD) falls within one SD derived from the post-testing samples, suggesting no meaningful change in the pumice content, hence no particle crushing. The mean pumice contents per fraction, for the selected samples are presented in Fig. 4.12. These results show that the majority of the pumiceous particles are in the coarse particle range, above the fines content threshold (0.075 mm). Within the smallest fraction, the fines particles are mostly glass shards that are not particularly hard-grained but do lack the vesicularity that makes up for the lightweight and crushable characteristics of pumiceous particles.

The results from both approaches that studied the potential particle crushing of the Tuhua silt indicate that no particle crushing occurred as a result of the testing and/or sample preparation method.

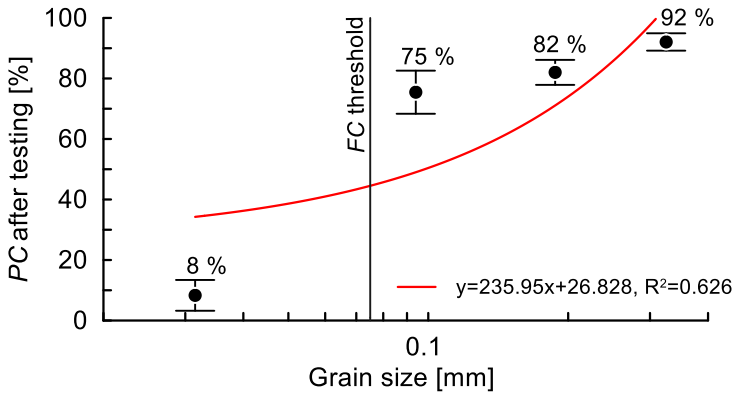


Fig. 4.12. Pumice contents of the four grain size fractions (< 0.063 mm, 0.063-0.125 mm, 0.125-0.25 mm and > 0.25 mm) after monotonic and cyclic triaxial testing

## 4.6. Interpretation of results and discussion

This section discusses the previously presented results by comparing the critical state line, the cyclic response, and the liquefaction resistance of Tuhua silt to these properties for other sandy and silty materials from literature, both pumiceous and hard-grained. For the interpretation, the results from the particle crushing analysis were considered as well.

### 4.6.1. Critical state line

The critical state line (or steady state line) is defined as the locus of points that describe the relationship between the void ratio and the effective confining stress in the steady state of deformation (Castro 1969; Kramer 1996). As a unique line that describes a particular soil, it has been used as a tool to define single physical parameters that describe sand behaviour, such

as the state parameter (Been and Jefferies 1985) or the modified state parameter (Bobei et al. 2009). The critical state framework is well established and confirmed for hard-grained soils, yet its applicability to crushable pumiceous sands is still subject to investigation. In their study, Orense et al. (2012), performed monotonic undrained tests on pure pumiceous sand samples, and found that they could not reach the steady state of deformation. They hypothesised that the breakage of particles resulted in a resistant soil structure that did not exhibit deformations at constant shear stress. De Cristofaro *et al.* (2022), on the other hand, undertook tests on two pumiceous sands (Rangiriri and Cervinara sand). They observed contractive behaviour under a range of void ratios where they were able to obtain the corresponding critical state lines (CSL). De Cristofaro et al. compared their results with those obtained on Toyoura sand and noted differences in the positioning as well as the slopes of their critical state lines. They inferred that, as the steady-state condition represents the final state of the triaxial tests, corresponding to relatively high axial strains of ~15% where particle breakage would occur if the material were crushable, the CSL is a good indicator of the nature of the particles (pumiceous or not) and possible particle crushing. The hypothesised effect of the crushability of the soil material on the slope and relative positioning of the CSL was not clearly discussed by De Cristofaro et al. (2022). Kramer stated that the vertical location of the CSL is influenced by gradation, whereas the slope is sensitive to the particle shape, where soils with rounded particles usually have flat CSLs (Kramer 1996).

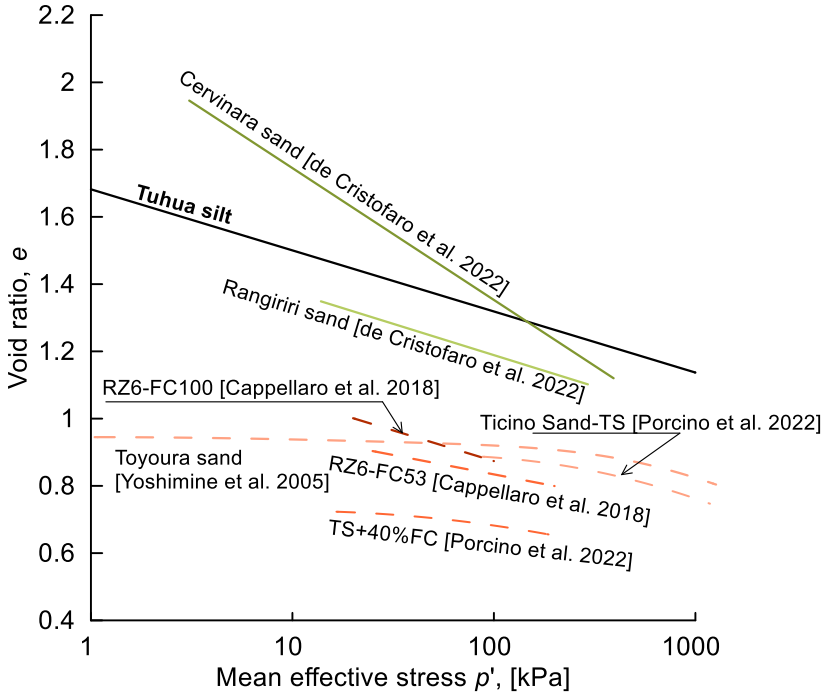


Fig. 4.13. Critical state lines of Tuhua silt and of representative hard-grained soils and pumiceous sands from literature

As pumiceous sandy silts have not been studied in the context of the critical state framework before, and considering the findings of De Cristofaro et al. (2022), and Kramer (1996), an attempt to discuss the positioning and slope of the CSL of Tuhua silt against other relevant CSLs from the literature was made. The selected materials from published literature are presented in Table 4.3 (Materials 1 to 7).

Fig. 4.13 shows the CSL of Tuhua silt as well as the for two natural pumiceous sands, one from New Zealand (Rangiriri sand) and the second from Italy (Cervinara sand) (de Cristofaro et al. 2022), the hard-grained representatives for sand (Toyoura and Ticino clean sands and Ticino sand with 40% fines content (*FC*)) (Porcino et al. 2022; Yoshimine et al. 2006) and non-plastic silts from Christchurch, New Zealand (with *FC* of 53% (RZ6-FC53) and 100% (RZ6-FC100)) (Cappellaro et al. 2021). The silt material tested in our study plots in between the CSLs of the two pumiceous sands (Rangiriri sand and Cervinara sand), and well above those of the hard-grained Toyoura and Ticino sand as well as the hard-grained silts. The gradation of soils (Kramer 1996) would be a relevant parameter when comparing the vertical position of the CSLs of different hard-grained soils. A more relevant parameter that would partially explain the positioning of the CSL of the pumiceous Tuhua silt in relation to the other CSLs (those of hard-grained soils included) with confidence, is the light weight of the silt, a result of its vesicular properties. If we consider that Tuhua silt is a material that contains ~48% pumice particles, its CSL, being closely positioned to that of the pumice sands is reasonable and expected, because the void ratio range (Cubrinovski and Ishihara 2002) of Tuhua silt is closer to the void ratio ranges of other pumiceous materials. When analysing the different slopes of the CSLs in Fig. 4.13, one would have to study the combined effect of particle shape and crushability (de Cristofaro et al. 2022; Kramer 1996). Considering comments from both Cristofaro et al. and Kramer' (de Cristofaro et al. 2022; Kramer 1996), the authors hypothesised the following: particle breakage in soil particles (pumiceous or not) leads to less spherical, more angular soil particles. That would result in the original soil (with more rounded particles) having a flatter CSL than the final soil mixture (after the particle breakage). In case of a pumiceous soil, the loss of internal voids, thus lightweight properties of the vesicular particles, because of particle breakage, would also lead to a vertical offset of the CSL of the final soil mixture.

The pumiceous silt in this study was proven not crushable (Section 4.5.3) and therefore the slope can be discussed based on the particle shape alone. Asadi et al. (2017) compared the particle shapes of Toyoura sand and a natural pumice sand from the central North Island of

New Zealand and found the pumiceous particles to be ~five times more angular than the particles of Toyoura sand particles. Considering the particle shape indices of Toyoura sand according to the Asadi et al. (2017), which are Rc = 1.258, Ar = 1.483 and, Ac = 0.179 and the particle shape indices for Tuhua silt (Table 4.1), we conclude that the particles of Tuhua silt are ~45% more ellipsoidal, and close to eight times more angular than Toyoura sand particles. Thus, the different slopes of the CSLs of Toyoura sand and Tuhua silt, are in accordance with the findings in Kramer (1996), in other words, the more angular nature of the particles of Tuhua silt compared to the particles of Toyoura sand, has resulted in a higher slope of the CSL.

Table 4.3. Geotechnical properties of selected materials from literature

| | Material | Reference | Soil Classification[1] | ***Gs*** | ***$D_{50}$*** | ***FC*** | ***PC*** | *Testing apparatus* |
|---|---|---|---|---|---|---|---|---|
| | | | | | [mm] | [%] | [%] | |
| 1 | Rangiriri sand | de Cristofaro *et al.*, (2022) | SP | 2.54 | 0.20 | 13 | 39 | Triaxial |
| 2 | Cervinara sand | de Cristofaro *et al.*, (2022) | SP | 2.58 | 0.40-0.60 | 10-20 | n/a | Triaxial |
| 3 | Toyoura sand | Yoshimine *et al.*, (2006) | SP | 2.65 | 0.18 | 0 | 0 | Triaxial |
| 4 | TS – Ticino sand | Porcino *et al.*, (2022) | SP | 2.68 | 0.56 | 0 | 0 | Triaxial |
| 5 | TS 40% FC | Porcino *et al.*, (2022) | SM | 2.68 | 0.4 | 40 | 0 | Triaxial |
| 6 | RZ6-FC53 | Cappellaro *et al.*, (2021) | ML | 2.69 | 0.071 | 53 | 0 | Direct simple shear |
| 7 | RZ6-FC100 | Cappellaro *et al.*, (2021) | ML | 2.63 | 0.026 | 100 | 0 | Direct simple shear |
| 8 | Pumice sand A | Orense *et. al.*, (2012) | SP | 1.95 | 1.15 | 2 | ~100 | Triaxial |
| 9 | Pumice sand C | Orense *et. al.*, (2012) | SM | 2.38 | 0.07 | 52 | ~100 | Triaxial |
| 10 | Shirasu Sand | Hyodo *et. al.*, (1998) | SM | 2.49 | 0.15 | 30 | n/a | Triaxial |
| 11 | PAR | Licata, D'Onofrio and Silvestri, (2018) | SM | 2.51 | 0.15 | 30 | n/a | Triaxial |
| 12 | FBM-30 | Rees, (2010) | SM | n/a | 0.11 | 30 | 0 | Triaxial |

[1]Following the Unified Soil Classification System (USCS); n/a = not available

### 4.6.2. Cyclic undrained response and liquefaction resistance

Whether or not cyclic liquefaction is initiated in the conventional sense ($r_u$=u/$\sigma_c$' reached 0.9), an analysis of the excess pore pressure as well as the axial strain development in soil during

cyclic loading is of a particular interest to researchers as it provides additional insights about the loss of stiffness and strength during the loading. Clean hard-grained sands and sand-silt mixtures have received solid attention by such means in the past 50 years (Dobry et al. 1982; Hazirbaba and Rathje 2009; Wang and Kavazanjian 1989). Dash and Sitharam (2009) analysed the undrained excess pore pressure development of a large number of hard-grained sand-silt mixtures (Fig. 4.14). They tested, under a vast range of relative densities ($0.14 \leq Dr \leq 0.91$), loading frequencies ($0.1 \leq f \leq 0.5$ Hz), consolidation pressures ($50 \leq \sigma_c' \leq 200$ kPa) and critical stress ratio ($0.0922 \leq CSR \leq 0.205$). Even though they discussed trends by means of looking at a single parameter, for example, the effect of fines or relative density, they reported that all the curves generated by plotting the excess pore water pressure response against the corresponding cycle ratio fell within a relatively narrow band.

For pumiceous sands, the cyclic undrained response by means of excess pore water pressure and axial strain development until failure has provided insight for interpreting the liquefaction resistance of crushable sands compared with that of hard-grained sands (M. S. Asadi et al. 2018; de Cristofaro et al. 2022). For example, Asadi et al. (2018) found that for the same relative density and effective consolidation pressure, the response of the pumiceous sand was much more stable and had a gradual failure mechanism compared with that of the hard-grained Toyoura sand, for which the onset of failure was sudden (Fig. 4.15). The main reason for this difference was considered to be the subsequent particle crushing in the pumiceous sand that led to a linear increase in the double amplitude strain and a significant increase in EPWP during the first cycles. This increase was more pronounced for dense samples, whereby the samples underwent higher initial deformations and higher EPWP, indicating that the relative density played a bigger role in the undrained cyclic behaviour for pumice sands than for hard-grained sands.

The cyclic undrained response of the Tuhua silt samples consolidated under 100 kPa for two relative densities (0.44-0.53 and 0.65-0.72) was plotted and compared with the response from the hard-grained sand-silt mixtures from Dash and Sitharam (2009) study and that of the pumiceous sand and Toyoura sand used in the study by Asadi et al. (2018) (Figs. 4.14 and 4.15). Note that the studies of both Dash and Sitharam and Asadi et al. were based on tests performed in a triaxial apparatus.

By observing Fig. 4.14, we noticed that the results for the EPWP development during cyclic testing of Tuhua silt fall perfectly into the range established by Dash and Sitharam (2009).

Fig. 4.15 (a) shows that for the dense pumice sand ($Dr \approx 0.8$), the pore water pressure reached high values very quickly after loading and at small strains, and the double amplitude axial strain (Fig. 4.15 (b)) has a generally linear increase throughout the testing until failure. For the looser samples ($Dr \approx 0.3$), EPWP accumulated in a steadier manner, whereas the double amplitude axial strain started increasing in the later stage of the test when the corresponding EPWP ratio $r_u$ was around 0.5. Fig. 4.15 (c) and (d) show the results for Toyoura sand for two densities, where it is evident that the dense samples ($Dr \approx 0.8$) exhibited a more gradual increase in both the pore water pressure and the axial strain, whereas the looser ones (medium-density $Dr \approx 0.5$) tend to have their axial strains and EPWP develop in the last cycles of failure.

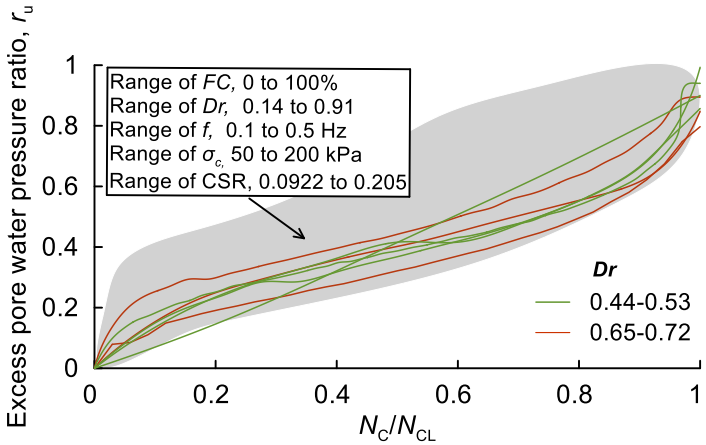


Fig. 4.14. Excess pore water pressure accumulation against normalized number of cycles for Tuhua silt ($\sigma_c$' = 100 kPa), plotted together with a database for the same parameters for hard-grained soil mixtures published by Dash and Sitharam (2009)

By analysing Fig. 4.15, we observed that the effect of relative density is evident in both the pumiceous sand and the Toyoura sand, with the effect being more pronounced for the pumice sand where the differences in the undrained response are more significant. In contrast, the relative density did not seem to have a clear effect on the EPWP or axial strain development under cyclic loading of the Tuhua silt samples. However, if we consider the results for Tuhua silt presented in Fig. 4.8 and in Section 4.5.2., we observed the discussed trend based on the state parameter. In other words, samples with a negative state parameter showed a more gradual development of axial strain and EPWP compared to that of the samples with a positive state parameter.

The liquefaction resistance is known to be dependent on relative density, effective consolidation pressure, fines content, particle shape, grain size and grain-size distribution of the material, sample reconstitution method, etc (Ishihara 1997). Given that the type of material tested in this study has not been tested before, we plotted its resistance against a few materials

chosen from published literature. The materials used for comparison and their geotechnical properties are given in Table 4.3 (Materials 8 to 12).

The liquefaction resistance of the Tuhua silt for the 100 kPa consolidation stress is plotted against selected representative pumiceous and hard-grained soils from literature in Figs. 4.16 and 4.17, respectively. By analysing the curves in Fig. 4.16 first, we saw that the dense samples of Tuhua silt ($0.65 \leq Dr \leq 0.77$) show lower resistance to liquefaction than the pure pumice sand (Pumice sand A (Orense *et. al*., 2012) $Dr \approx 0.7$), tested at a similar relative density.

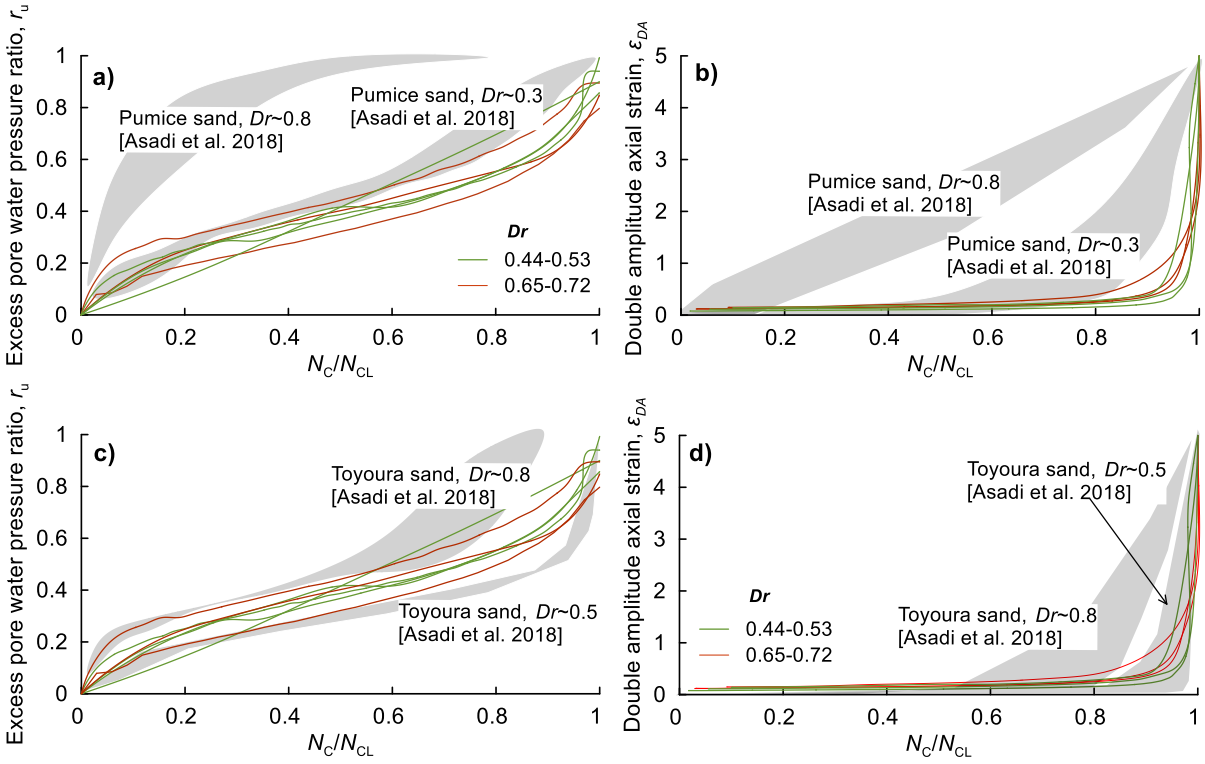


Fig. 4.15. (a) and (c). Excess pore water pressure ratio against normalized number of cycles for Tuhua silt against pumiceous sand and hard-grained Toyoura sand, respectively ($\sigma_c$' = 100 kPa), (b) and (d) double axial strain accumulation against normalized numberof cycles for Tuhua silt against pumiceous sand and Toyoura sand, respectively ($\sigma_c$' = 100 kPa)

The medium-dense Tuhua silt samples $0.44 \leq Dr \leq 0.53$), when compared to the Shirasu sand (pumiceous sand with 30% *FC*, (Hyodo *et. al.,* 1998) $Dr \approx 0.5$) and the PAR sand (pumiceous sand with 30% *FC*, (Licata et. al., 2018) $Dr \approx 0.4$), show lower resistance as well. The pumice sand with 50% *FC* from Orense *et. al.,* (2012) also shows higher liquefaction resistance in general.

The Tuhua silt in this study generally shows a lower resistance when compared with hard-grained sands as well (Fig. 4.17). For the lower density ($Dr$ = 0.44–0.53), Tuhua silt has lower resistance than Toyoura sand ($Dr \approx 0.5$) (Yamamoto et al. 2009), and the FBM-30

(30%*FC* sand, (Rees 2010) *D*r ≈ 0.5). The same is noted for the higher density (0.65 ≤ *D*r ≤ 0.72), where Tuhua silt has lower resistance than FBM-30 (30%FC sand, (Rees 2010) *D*r ≈ 0.7). An interesting observation is made when the liquefaction resistance curves from the higher density Tuhua silt samples are compared with those for the hard-grained silt RZ6-FC53 (53%*FC*, (Cappellaro et al. 2021), *D*r ≈ 0.74): the resistance of the Tuhua silt essentially matches that of the hard-grained sandy silt from Cappellaro's study.

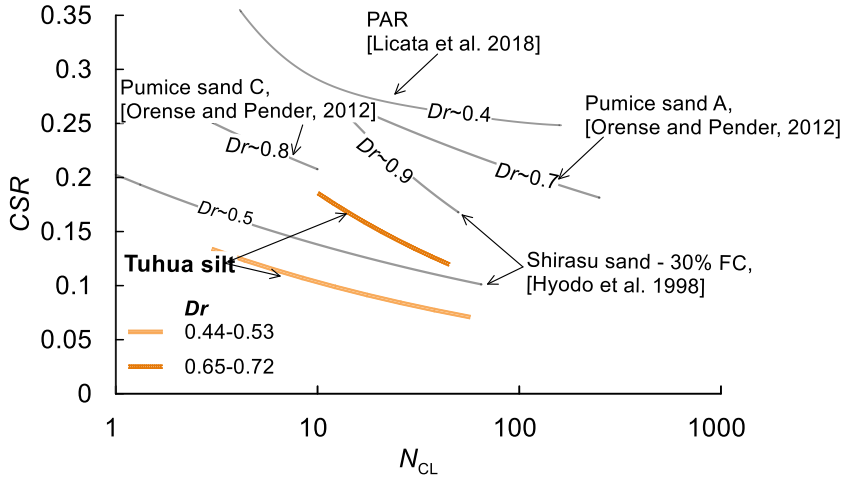


Fig. 4.16. Liquefaction resistance curves of Tuhua silt and relevant pumiceous soil sands ($\sigma_c$' = 100 kPa)

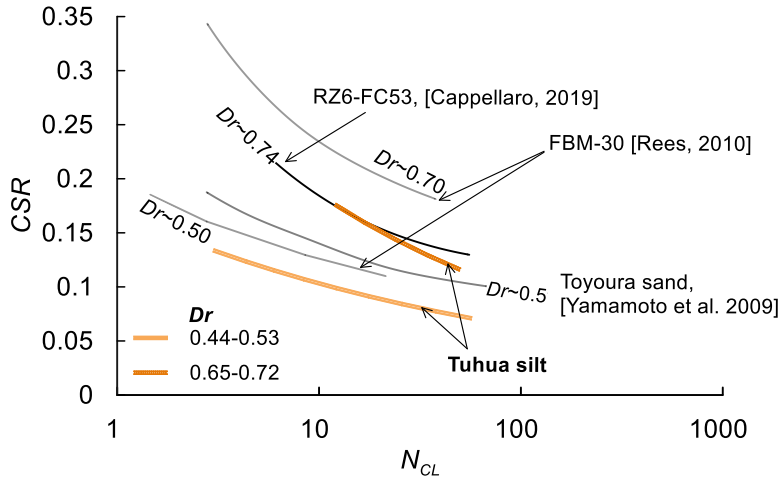


Fig. 4.17. Liquefaction resistance curves of Tuhua silt and relevant hard-grained sands ($\sigma_c$' = 100 kPa)

In summary the pumiceous Tuhua silt: (1) does not seem to fit into the observed trends for EPWP and axial strain development reported for pumiceous sand; (2) lies within the narrow band of a large database of hard-grained soils for the EPWP development during cyclic undrained testing; and (3) has a relatively lower liquefaction resistance than pumice and hard-grained sands, but comes remarkably close to the resistance of the hard-grained silt with the same amount of fines.

Concise and conclusive reasoning behind the mentioned findings requires a unified testing campaign where testing uncertainties would be eliminated so that one parameter at a time could be evaluated. Acknowledging all the parameters that influence the liquefaction resistance and cyclic undrained behaviour of soils, this next section will focus on commenting on the possible influence of the pumiceous properties (i.e. pumice content and potential particle crushing) of the materials and the fines content.

Firstly, we examined the possible influence of the pumice content of the soils. Considering the fact that the pumiceous particles are prone to particle crushing and have therefore been suggested to be the main contributor to the higher liquefaction resistance of pumiceous sands (M. S. Asadi et al. 2018), it is questionable why Tuhua silt (comprising a considerable amount of pumiceous particles in all grain size fractions) shows lower resistance. One explanation is that it has a moderate pumice content of 48% (compared with the ~100% pumice content in the pure pumiceous sands). In this regard, previous research on the influence of the pumice content in the liquefaction resistance of undisturbed samples found that major changes in the cyclic resistance of pumice-bearing sands were evident at relatively low proportions of pumice (i.e., 0% to 30%) in the soil mixture (Stringer 2022). This finding indicates that pumice content alone might not be enough to describe the behaviour and resistance of pumiceous soil mixtures. Hence, when it comes to pumiceous properties, the next parameter to analyse was the level of particle crushing. As presented in the results section, the Tuhua silt material did not show any signs of particle crushing consequent upon sample reconstitution and triaxial testing. The fact that no particle crushing occurred in the material (within the frame of testing conditions used in the study), even with the pumice content of nearly 50%, might be the reason why Tuhua silt, in general, compares more closely with hard-grained soils than with pumiceous sands. In the context of the fines content, Hardin (1985) introduced a potential for particle breakage that integrates individual fractions or grain sizes larger than 0.074 mm. He hypothesised that, the fines fraction particles are less susceptible to breakage under the same level of stresses that would cause particle crushing in coarse particles (sands and gravels), and therefore considered the potential of breakage of fines, zero. If we consider that the fines portion of Tuhua silt (particles < 0.075 mm) comprises less than 8% pumice content (Fig. 4.12), whereas the pumice content of the coarse particles is ~80%, we can hypothesise that the coarse particles are more susceptible to crushing than the fines. Considering the ratio of fines vs. coarse particles is almost 1:1, we assume that the fines are dominant in the soil matrix and are acting as a cushion that prevents the coarse particles from

breaking during the tamping method as well as during the undrained loading from the testing equipment (Fig. 4.18). In order to evaluate the threshold of fines content of the soil skeleton of the Tuhua tephra, where the role of the coarse grains becomes secondary and the fine grains govern the behaviour (Thevanayagam et al. 2002), a testing campaign that focuses on different fines contents in the Tuhua tephra is needed.

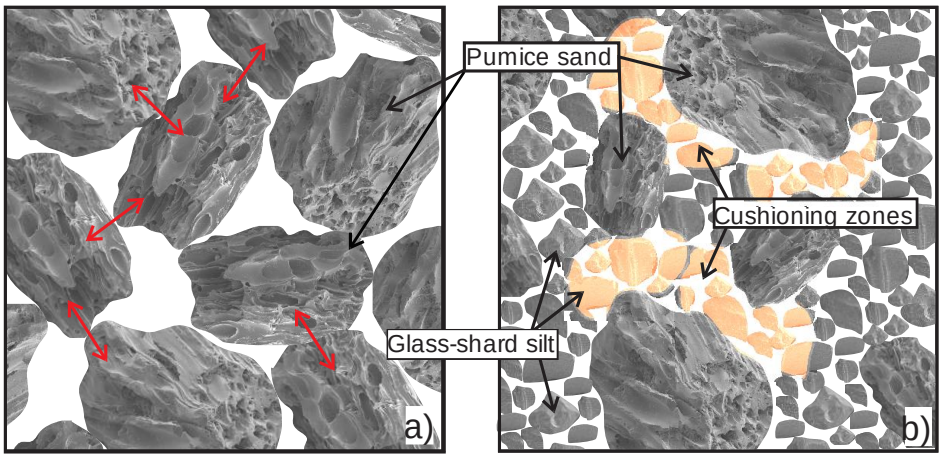


Fig. 4.18. Sketch of (a) pure poorly graded pumice sand and (b) sandy silt containing both pumiceous sand particles and silty glass-shard particles

Overall, the results from our study suggest that the absence of particle crushing in the Tuhua silt material during testing contributes to this material having an undrained response closer to that of hard-grained soils than to the response of pumiceous sands. These findings emphasize the possible influence of fines on the response of pumiceous soil mixtures and raise the question of whether the engineering empirical correlations (such as those based on SPT, CPT, etc.) that are considered unsuitable for pumice sands are applicable to pumice sand-silt mixtures and to what extent this applicability complicates the engineering practice when it comes to assessing the liquefaction potential of pumice soils. Furthermore, the results imply that not all pumiceous soil materials would be outside the established literature related to the development of paleoliquefaction features as well as methods for back-calculating past earthquakes based on paleoliquefaction evidence.

## 4.7. Conclusions

In this study, a natural tephra (volcanic ash) material, Tuhua silt (a distal mid-Holocene tephra layer preserved in lake sediments) with 51% fines content and 48% pumice content, sampled from the northern North Island of New Zealand, was subjected to a number of undrained triaxial tests performed at three different relative densities (medium to dense) and two different

effective consolidation pressures (20 and 100 kPa). The findings from this study are summarized as follows:

- The pumiceous Tuhua silt exhibited a strain-softening response during monotonic testi ng even for medium-dense samples ($D$r ≈ 0.65). A strain-hardening response was obse rved for a relative density of $D$r ≈ 0.77. The effect of the relative density, was in accor dance with the established trends for hard-grained soils but not for those for pumiceou s sands. The effect of the effective consolidation pressure is in accordance with the est ablished trends for both hard-grained soils and pumiceous sands.
- The vertical position of the critical state line of Tuhua silt against other critical state li nes from the literature was reasonable and expected when we consider the lightweight properties of the material (the void ratio range of Tuhua silt is closer to the void ratio r anges of other pumiceous materials). The high slope of the critical state line of Tuhua s ilt is a result of the high angularity of its particles.
- The cyclic undrained behaviour of Tuhua silt was dependent on the state parameter. Fo r samples with a negative state parameter ($-0.16 \leq \psi \leq 0.001$), a more gradual develop ment of failure was observed compared to that for samples with a positive state param eter ($0.08 \leq \psi \leq 0.39$). By means of the cyclic response, based on the observed excess pore water pressure and axial strain development, the tested material came closer to es tablished trends more typical for those of hard-grained soils than for those of pumice s ands.
- The liquefaction resistance curves of the tested material in our study were in accordan ce with the established trends by means of relative density i.e., higher density, resulted in higher resistance. Compared to that of both hard-grained soils and pumice sands, th e liquefaction resistance of Tuhua silt is relatively low.
- Particle crushing was analysed by two methods, one that examined the change in the p umice content and the other investigated the change in the grain-size distribution of th e sample before and after testing. The results from both methods indicated that no part icle crushing occurred in the samples during testing.
- In general, the Tuhua silt material behaves closer to the established trends typical for h ard-grained soils than to those for pumiceous sands. We infer that this conclusion is be cause the material did not undergo any significant particle crushing during sample rec onstitution and/or testing, most probably because of a cushioning effect from the fines that prevented the coarse pumiceous particles from breaking.

## Authorship contribution statement

**Jordanka Chaneva:** Investigation, Conceptualization, Methodology, Data curation, Writing – original draft. **Max O. Kluger:** Conceptualization, Methodology, Supervision, Writing - review and editing, Funding acquisition. **Vicki G. Moon:** Methodology, Supervision, Writing - review and editing, Funding acquisition. **David J. Lowe:** Supervision, Funding acquisition, Writing - review and editing. **Rolando P. Orense:** Supervision, Writing - review and editing, Funding acquisition.

## Acknowledgements

We acknowledge funding support from agencies of the New Zealand Government as follows: the MBIE Endeavour Fund (Smart Ideas) contract UOWX1903; the Marsden Fund contract UOW1902; the New Zealand Centre for Earthquake Resilience (QuakeCoRE); the Earthquake Commission Toka Tū Ake EQC (contract BIG 012 2020); and Waikato Regional Council (support for project on paleoseismicity and liquefaction). We thank Richard Melchert, Tehnuka Ilanko, Tom Robertson, Ben Roche, Helen Turner and Vittoria Gibbons for help in the field and/or lab, and Mrs Hekeiterangi Broadhurst (Kuia Kaumatua) and Wiremu Puke of Ngāti Wairere (Hukanui Marae), and the Department of Conservation, for supporting access to Lake Areare. Finally, we thank the anonymous referee for their constructive comments on our paper.

# Addendum

**A1:** The following paragraphs discuss the potential impact of the shift of the deviator stress to the negative during some of the undrained cyclic tests, in order to address the examiners, comment during the revision and defence of this thesis. In this context, the examiner pointed out that because of this phenomenon, the extension strain does not develop which could ultimately affect the number of cycles to liquefaction and suggested to check the accuracy of all experimental results. The shift of the deviator stress is noticeable in Fig. 4.7b, and as presented in Appendix B.1. it is present in all the tests from Test Series (TS) 5 and 6 as well as the two tests from TS3 (Tu-CY-2 and Tu-CY-4). It is also noticeable in TS 5, 6, 8, 9, 11 and 12 shown in Appendix B.2. which presents the results from the triaxial testing campaign of a tephra material studied in Chapters 5 and 6 of this thesis. It is worth mentioning that it is a phenomenon that is not uncommon and has been present in other published literature (Asadi et al., 2018; Gardiner et al., 2024), suggesting that is not unique to the materials or stresses being considered in this study. The reason behind this shift has not been identified/addressed in previous published literature to my knowledge. It could potentially be a mechanical or electronic triaxial machine issue as it seems that the load cell is not able to control a symmetrical compression/extension load in the cycles close to failure. Regardless, discussing the significance of this effect given the testing conditions considered in this study and the potential effect on the results is discussed in the following paragraphs.

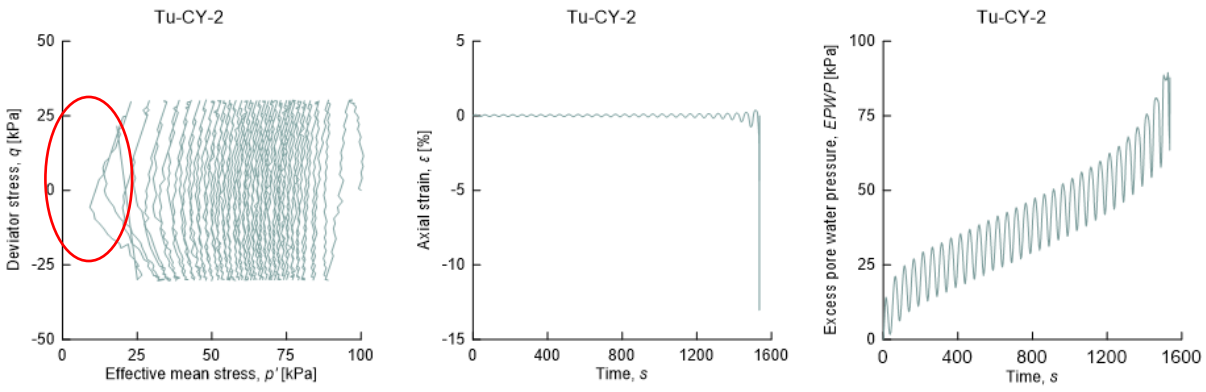


Figure A1. showing a test with the deviator stress shift – concentrated in the last cycle

For the tests in TS3 (and 6, 10 and 11 from Appendix B.2), that were consolidated under 100kPa consolidation stress, I consider this to have an insignificant impact to the number of cycles to liquefaction as it seems to be concentrated in the last few cycles and the shift is only small portion of the deviator stress, (less than 5%).

For the tests in TS5 and TS6 (as well as 5, 8, 9 and 12 from Appendix B.2), that were consolidated under 20kPa consolidation stress, the deviator stresses are quite small i.e. in the order of 5kPa, and the shift becomes more significant as in the last cycles the extension amplitude becomes 1.5 times larger than the compression amplitude. Here too, the shift is still only present and noticeable in the last few cycles. While it is arguable that the non-symmetric cyclic load in the last few cycles of the test might have affected the failure itself, the number of cycles to liquefaction for the samples tested and presented in this thesis is not affected. This is because in all of the tests the double strain amplitude of 5% and excess pore pressure development occur at the same cycle (or one cycle apart). This is especially true for the tests that develop a typical flow failure which was very typical for most samples (e.g. TS5). Furthermore, the type of failures in all of these tests are in accordance with the expected trends in regard to the initial states of the samples (i.e. their state parameters), which increases the confidence in all the undrained cyclic test results. The samples with positive state parameters (all except TS6 tests) failed in a typical flow liquefaction manner, whereas the three samples with negative state parameters (TS6) showed a dilative response. Samples consolidated under 20 kPa consolidation pressure had not been tested prior this study, to my knowledge. Thus, further research (on samples consolidated under 20 kPa), ideally on a commercialized and extensively tested soil under different testing conditions in published literature such as e.g. Toyoura sand, would potentially answer questions in this as well as other topics discussed in this thesis.

**A2**: The following paragraph is an extension (marked in bold letters) to the first paragraph on page 62:

*An interesting observation is made when the liquefaction resistance curves from the higher density Tuhua silt samples are compared with those for the hard-grained silt RZ6-FC53 (53%FC, (Cappellaro et al. 2021), Dr ≈ 0.74): the resistance of the Tuhua silt essentially matches that of the hard-grained sandy silt from Cappellaro's study.* ***Note that no correction factors were applied to the CSR results (curves) from Cappellaro et al. 2021. Even though there are studies that show that cyclic shear and triaxial test results can be comparable (e.g. Bojadjieva, 2019), the authors acknowledge that the results are not directly comparable by default. Regardless, the Tuhua silt CSRs will still be plotting in the lower range of CSR – typical for hard-grained soils and below the high ranges typical for pumiceous sands.***

**A3:** The following figures are a corrected versions of Figures 4.4 and 4.5 and address the noticed inconsistency in the curves for the Tu-CU-5 test (dark green) from one of the examiners of this thesis. A separate graph of this test is also presented below.

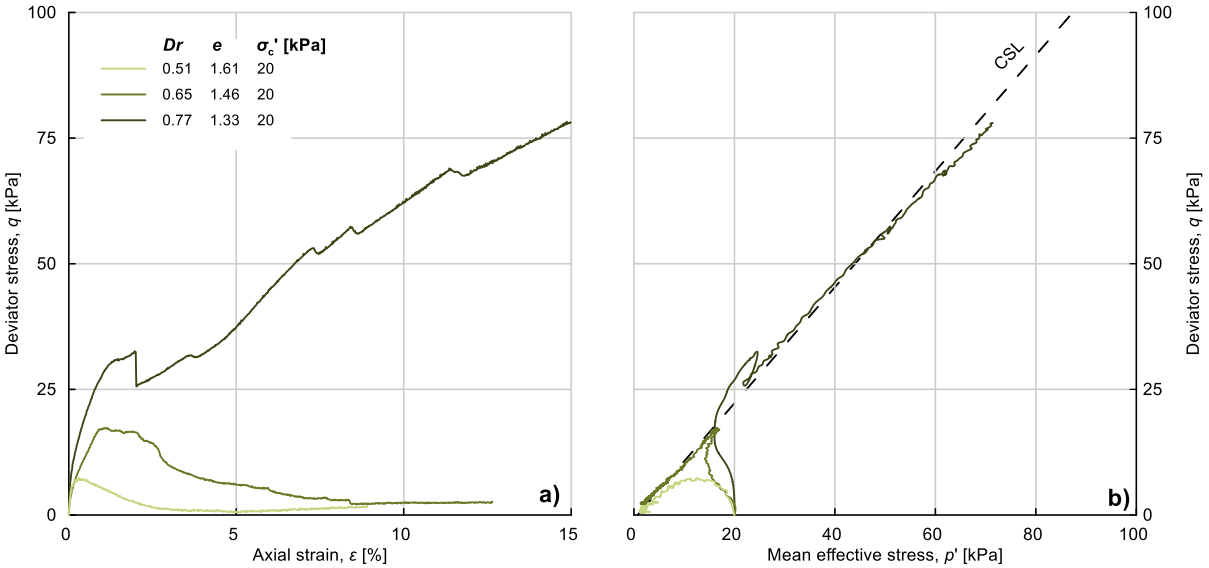


Fig. 4.4 – Corrections made in the graphs for Tu-CU-5, dark green curves

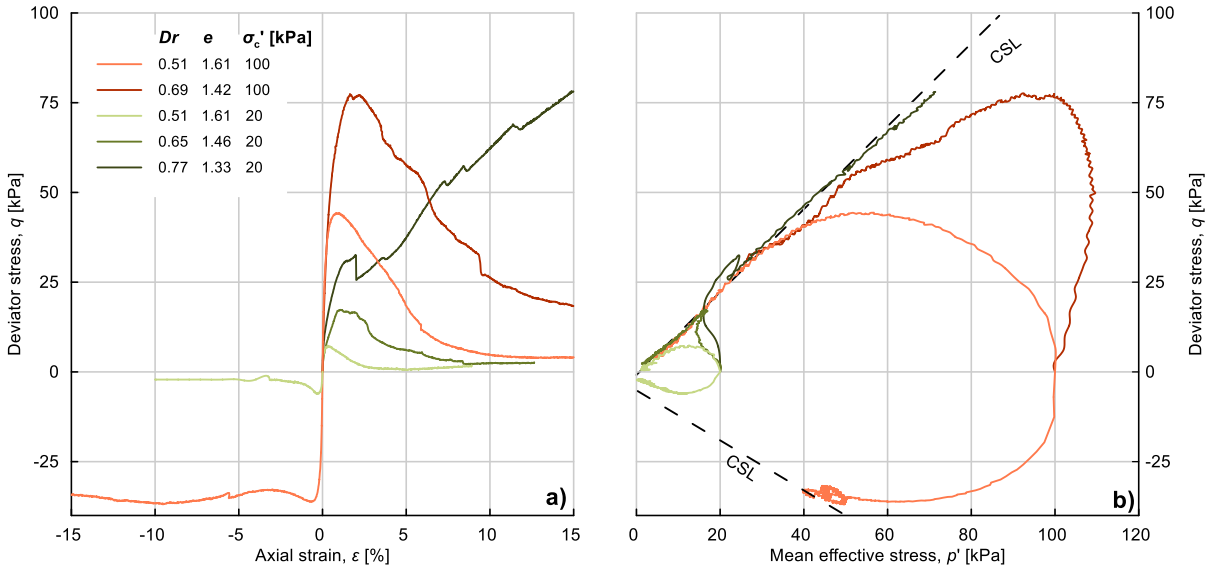


Fig. 4.5 – Corrections made in the graphs for Tu-CU-5, dark green curves

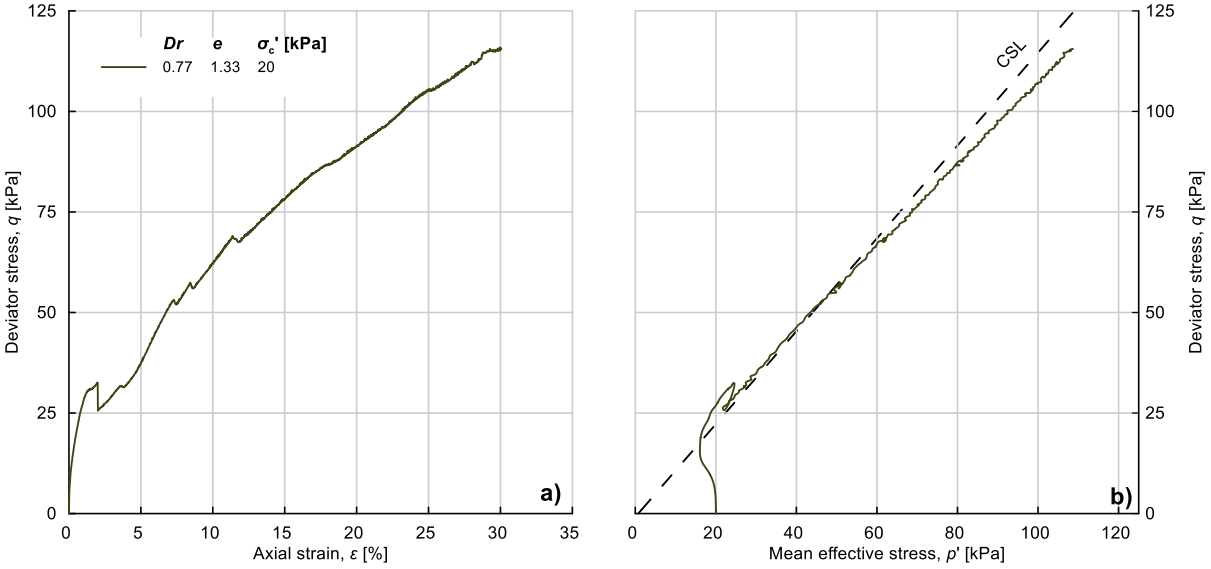


Figure A.2. Monotonic undrained compression test Tu-CU-5 (full version)

# Chapter 5: Influence of pumice and fines contents on the extent of particle crushing in pumiceous sand-silt mixtures during undrained cyclic triaxial loading

**Jordanka Chaneva[1],** Max O. Kluger[1], Vicki G. Moon[1], David J. Lowe[1] & Rolando P. Orense[2]

[1]*School of Science/Te Aka Mātuatua, University of Waikato, New Zealand, jc409@students.waikato.ac.nz*
[2]*Department of Civil and Environmental Engineering, University of Auckland, New Zealand*

Accepted for the Proceedings of the 8th International Conference on Earthquake Geotechnical Engineering, May 2024, Osaka Japan. Extended version will be submitted to the official journal of the Japanese Geotechnical Society – Soils and Foundations, after the conference (as per recommendations of the ICEGE committee).

## 5.1 Abstract

Pumiceous particles have a distinct vesicular nature as well as a complex surface texture that makes them potentially vulnerable to crushing under cyclic loading. Pumiceous sand mixtures have received more scientific attention than pumiceous silts in this regard. Researchers have found the undrained cyclic behaviour of pumiceous sands to be significantly different from that of hard-grained sands because of the particle crushing that occurs during cyclic testing and/or sample reconstitution. The liquefaction resistance of pumiceous sands is also considered to be higher because of the pore-water pressure distribution in the sample that occurs during particle crushing. The undrained behaviour of pumiceous silt has only been studied once previously: such material did not crush during sample reconstitution and undrained cyclic testing, which was attributed to a cushioning effect taking place between silty, non-crushable particles and coarse sandy pumice particles. Whether there are thresholds of fines content and/or pumice content at which pumiceous soil mixtures start to behave more similarly to hard-grained soils are yet to be unravelled and remain relevant for engineers and scientists. This paper analyses particle crushing after sample reconstitution and undrained cyclic triaxial testing of three pumiceous natural soil mixtures (lacustrine tephra deposits) from northern New Zealand having fines (< 0.075mm) and pumice contents ranging between 20% and 70% and 30% and 51%, respectively. The results examine potential changes in (1) fines content, (2) pumice content, and (3) undrained cyclic behaviour by comparing both pore-water pressure and axial strain development of the pumiceous soils with other crushable and non-crushable soils.

KEYWORDS: pumiceous sand-silt mixtures, particle crushing, pumice content, fines content, cyclic triaxial testing

## 5.2 Introduction

Pumiceous particles are vesicular, volcanic-ash soils that are characterised by a “foam-like”, lightweight structure with high angularity, making them particularly vulnerable to crushing compared to hard-grained, quartzitic soils. The occurrence of particle crushing in pumiceous sands under undrained cyclic loading has been considered the main reason for the differences in (1) undrained cyclic behaviour and (2) liquefaction resistance of pumiceous sands compared with hard-grained sands (M. S. Asadi et al. 2018; Hyodo et al. 1998; Orense et al. 2012). The above-mentioned studies discussed results for natural pumiceous sands containing both pumiceous and hard-grained (mostly quartzitic) particles. Whether the amount of pumice particles (i.e., pumice content) could be a relevant parameter influencing the extent of particle crushing, and thus the undrained cyclic behaviour and liquefaction resistance, is still an open question. Asadi et al. (2018) analysed the different levels of particle crushing of three different natural pumiceous mixtures with fines content (percentage of particles finer than 0.075mm) varying between 0 and 13%. They inferred that the different levels of particle crushing of the sands could have been caused by the different pumice contents. Stringer (2022) tested undisturbed pumiceous sand samples and found that major changes in liquefaction resistance occurred at relatively low pumice contents, suggesting that the effect of particle crushing can be present even in sands with low pumice content. To what extent the findings for pumiceous sands extend to pumiceous silts remains unknown. Until the present time, the research focus related to particle crushing during undrained cyclic testing has been almost exclusively on pumiceous sands and information about pumiceous materials dominated by silt and silty sand is scarce. A study about the undrained behaviour and liquefaction resistance of pumiceous sandy silt (51.2% fines) found the undrained cyclic behaviour of the silty material to be more similar to that of hard-grained soils than to that of pumiceous sands (Chaneva et al. 2023). The reason considered was that the high amount of fines acted as cushions between the sandy particles, thereby preventing significant particle crushing. Identifying the thresholds of both pumice and fines contents at which particle crushing becomes relevant is important to both geotechnical practitioners and researchers.

This paper investigates the particle crushing under undrained cyclic triaxial testing of three pumiceous soil materials with different pumice contents, ranging from 30 to 51%, and different fines content, ranging from 20 to 70%. All three materials are natural rhyolitic volcanic-ash (tephra fall) materials deposited in lakes. The extent of particle crushing is quantified and presented from three perspectives: (1) change in grain size distribution after

testing; (2) change in pumice content after testing; and (3) change in undrained cyclic behaviour after testing (through the pore water pressure and double axial strain development). The results from (1) and (2) are compared with the pumice content and fines content of the virgin (original) materials.

## 5.3 Methods and materials

### 5.3.1. Sampling location and procedure

The soil materials examined are derived from one rhyolitic pumiceous layer, Mamaku tephra, sampled at the shore of Lake Areare (Fig. 5.1a.), which is located in the Hamilton lowlands in the North Island of New Zealand. The Mamaku tephra layer (deposited ~8.0 cal ka) is one of many lacustrine pumiceous layers deposited in the area, which have liquefied due to earthquakes in the past ~17.5 cal ka (Kluger et al. 2023). At Lake Areare, the Mamaku tephra layer occurs in the exposed lake bed at a relatively shallow sediment depth of <0.5 m. In order to obtain the material, a large number of small block samples (each with a volume of ~0.0075 m3) containing the ~2 cm-thick Mamaku tephra layer were sampled. The Mamaku tephra lies a few centimetres below the ~7.6 cal ka-aged Tuhua tephra layer (Kluger et al., 2023) and both tephras are encapsulated by organic lake sediments. The Mamaku tephra layer contains three different sublayers, or beds, of different grain size distributions. The three beds have thicknesses (from the top) of ~1 cm, ~0.3 cm, and ~0.7 cm. Once in the lab, the beds were carefully sampled using a spoon after being cleaned from organic contamination and oven dried at 40°C.

### 5.3.2. Sample properties

Relevant physical and geotechnical properties for the three beds in the Mamaku tephra layer were obtained to accompany the triaxial testing, including grain size distribution, particle density, minimum and maximum dry density, Atterberg limits, and pumice content.

The grain size distributions were obtained before (i.e., virgin soils) and after testing (i.e., after reconstitution, consolidation, and shearing) on small-volume samples using laser diffraction analysis with a Malvern Mastersizer 3000 apparatus.

The particle density was determined using a Quantachrome Ultrapyc 1000 nitrogen-filled gas pycnometer following ASTM-D5550-14 (2014). Minimum and maximum dry densities of the samples were obtained following the Japanese standard method (Japanese Geotechnical Society Standard 2009) as modified by Mijic et al. (2021). Atterberg limits were

obtained following ASTM-D4318-17e1 (2017). Scanning electron microscopy (SEM) was undertaken using a Hitachi S-4700 FE SEM. SEM images of components of the three beds of Mamaku tephra are presented in Fig. 5.2.

The pumice content was estimated using a point-counting method (Frolov and Maling 1969). Four SEM images of representative grain clusters were chosen for each sample and were counted systematically on crossing points (150 points per image) of rectangular grids.

The top bed of Mamaku tephra, with 70% fines content, tested as non-plastic and will be referred to as Ma-ML70 hereafter (low plasticity silt, with 70% fines).

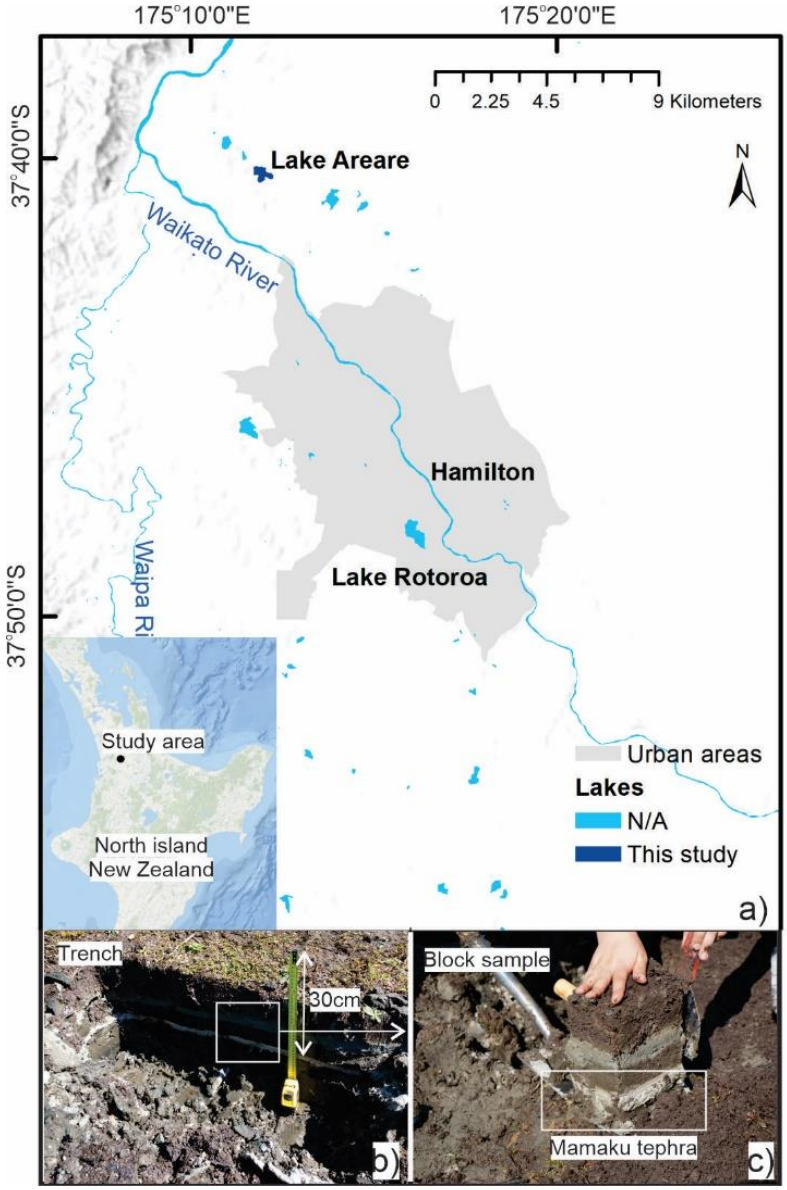


Fig. 5.1. (a) Location of the sampling area for Mamaku tephra at Lake Areare in the Hamilton lowlands and faults in the area, North Island, New Zealand; (b) shallow trench where the blocks were sampled; and (c) block samples containing Mamaku tephra (cream - coloured lower layer).

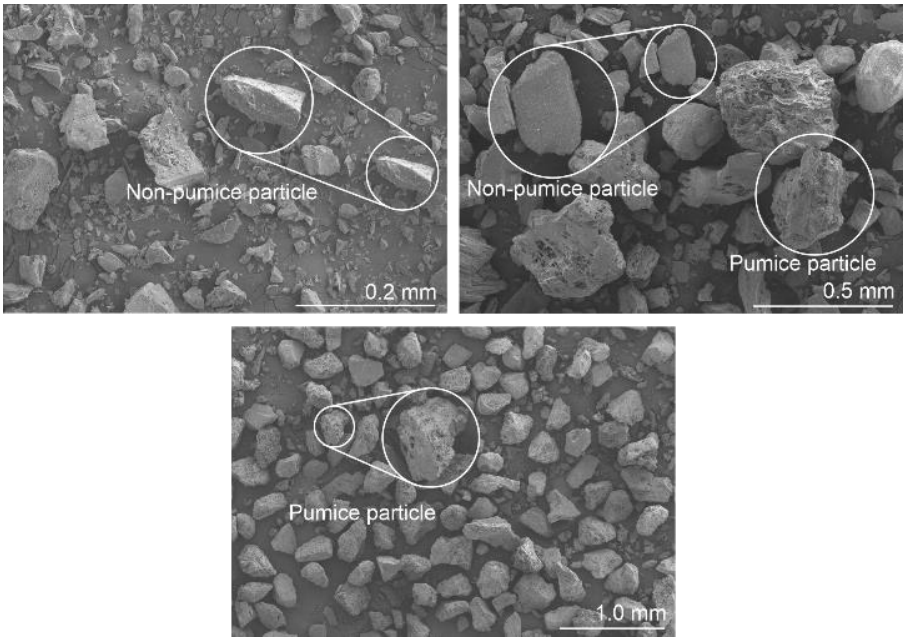


Fig. 5.2. SEM images of Ma-ML70 (top left), Ma-SM31(top right), and Ma-SM20 (bottom middle).

The middle and bottom beds of the Mamaku tephra layer were classified as sandy silts with 20% and 31% fines contents, respectively, and will be referred to as Ma-SM20 and Ma-SM31, respectively. The specific gravity $G_s$, mean diameter $D_{50}$, pumice content $PC$, and minimum and maximum void ratios $e_{min}$ and $e_{max}$, are summarized in Table 5.1. The grain size distribution curves of the virgin materials are presented in Fig. 5.3.

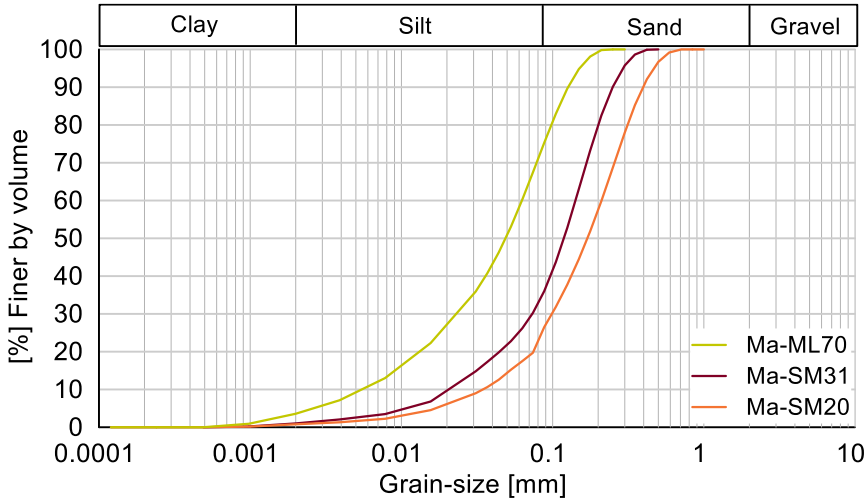


Fig. 5.3. Grain size distribution of virgin (before testing) pumiceous soil materials (beds of Mamaku tephra).

### 5.3.3. Triaxial testing

A GDS advanced dynamic triaxial testing system was used for the triaxial testing of the samples. The samples, with a target size of 50 mm in diameter and 100 mm in height, were

reconstituted using the under-compaction method following the procedure of Ladd (1978). Samples with 15% water content were reconstituted in eight layers into a split mould mounted on top of the triaxial base plate. Saturation pressures of at least 800 kPa were applied over 15 h to the samples. When the B-value of more than 0.95 was reached, the samples were considered to be saturated. Samples were tested at effective consolidation stresses of 20 and 100 kPa. The low consolidation stress was chosen because it best corresponded to the in-situ vertical stress of the Mamaku tephra, and the higher consolidation stress was used to enable direct comparison of the test results with those for other materials found in the literature.

The target relative densities were chosen so that a wide range of densities was covered. The sands were reconstituted within the lower range of medium-high density (as per Terzaghi and Peck, 1967), and the silt was reconstituted in the higher range of medium to high densities.

A total of 21 cyclic tests were performed. The cyclic stress amplitudes were applied with a frequency of $f$ = 0.02 Hz. The initiation of cyclic liquefaction, according to ASTM D 5311 - 92, was considered. The *CSR* (Cyclic Stress Ratio) range for all the presented tests was 0.06–0.18.

Table 5.1. Index properties of materials

| Material | $G_s$ | $D_{50}$ (mm) | *FC* (%) | *PC* (%) | $e_{min}$ | $e_{max}$ |
|---|---|---|---|---|---|---|
| Ma-ML70 | 2.41 | 0.049 | 70 | 30±11 | 0.88 | 2.07 |
| Ma-SM31 | 2.40 | 0.118 | 31 | 50±10 | 0.69 | 1.5 |
| Ma-SM20 | 2.40 | 0.169 | 20 | 51±8 | 0.7 | 1.28 |

## 5.4 Results

### 5.4.1. Grain size distribution

The change in grain size distributions after cyclic triaxial testing is presented by observing the changes in the $D_{10}$, $D_{50}$, and $D_{90}$ grain-size parameters (Fig. 5.4). Firstly, by analysing all the data points for the three Mamaku materials, it can be observed that there are no noticeable trends when considering the different consolidation stresses. The scatter in the data points implies that the consolidation stress did not affect any potential particle crushing of the samples.

Ma-ML70 samples (yellow-coloured data points), with fines content and pumice content of 70% and 30%, respectively, were only tested at a relative density ($D_{rc}$) of ~0.8, and the grain size parameters after testing are similar to those of the virgin material (indicated by dashed lines). Therefore, we infer that no crushing has occurred within the full range of testing

conditions (different consolidation stresses and cyclic stress amplitudes) for this pumiceous silt. Considering that Ma-ML70 did not show signs of crushing at a high relative density, it is expected that it would not crush at lower densities either.

The Ma-SM31 samples (red data points), with fines content and pumice content of 31% and 50%, respectively, were reconstituted under a relative density of ~0.6. The grain size parameters $D_{10}$ and $D_{50}$, after testing, exhibit a slight positive offset from those values obtained from the virgin material, whereas no significant difference was observed in $D_{90}$. Thus, the results imply a slight decrease in the silt to very fine sand grain size fractions. Note that the relative density of ~0.6 was the highest density that the samples could have been reconstituted using gentle moist tamping.

The Ma-SM20 samples (orange data points), with fines content and pumice content of 20% and 51%, respectively, were tested under two relative densities (~0.4 and ~0.6) and two consolidation stresses.

The grain-size parameters of samples with lower relative density (~0.4) all systematically plot beneath those of the virgin material, being especially evident for $D_{50}$ and $D_{90}$ values. The negative offset in grain size parameters is even more noticeable for the samples reconstituted at the higher density (~0.6), indicating that particles have crushed significantly and hence highlighting the effect of the relative density in the extent of particle crushing.

The grain-size distribution results for Ma-SM20 suggest that particle crushing occurred after testing the sand under the range of applied testing conditions.

### 5.4.2. Pumice content

The change in pumice content before and after testing was considered under the hypothesis that fewer pumiceous particles after testing would indicate particle crushing because the pumiceous particles, especially in the fine and medium sand size range, would break down down into glass shards – which are considered non-pumice. Note that the definition of non-pumice particles can be different for different pumiceous soil mixtures and, in this study, non-pumiceous particles are glass shard particles. The pumice content of the samples after testing, as well as the original pumice content of the Mamaku tephra materials, are plotted in Fig. 5.4d.

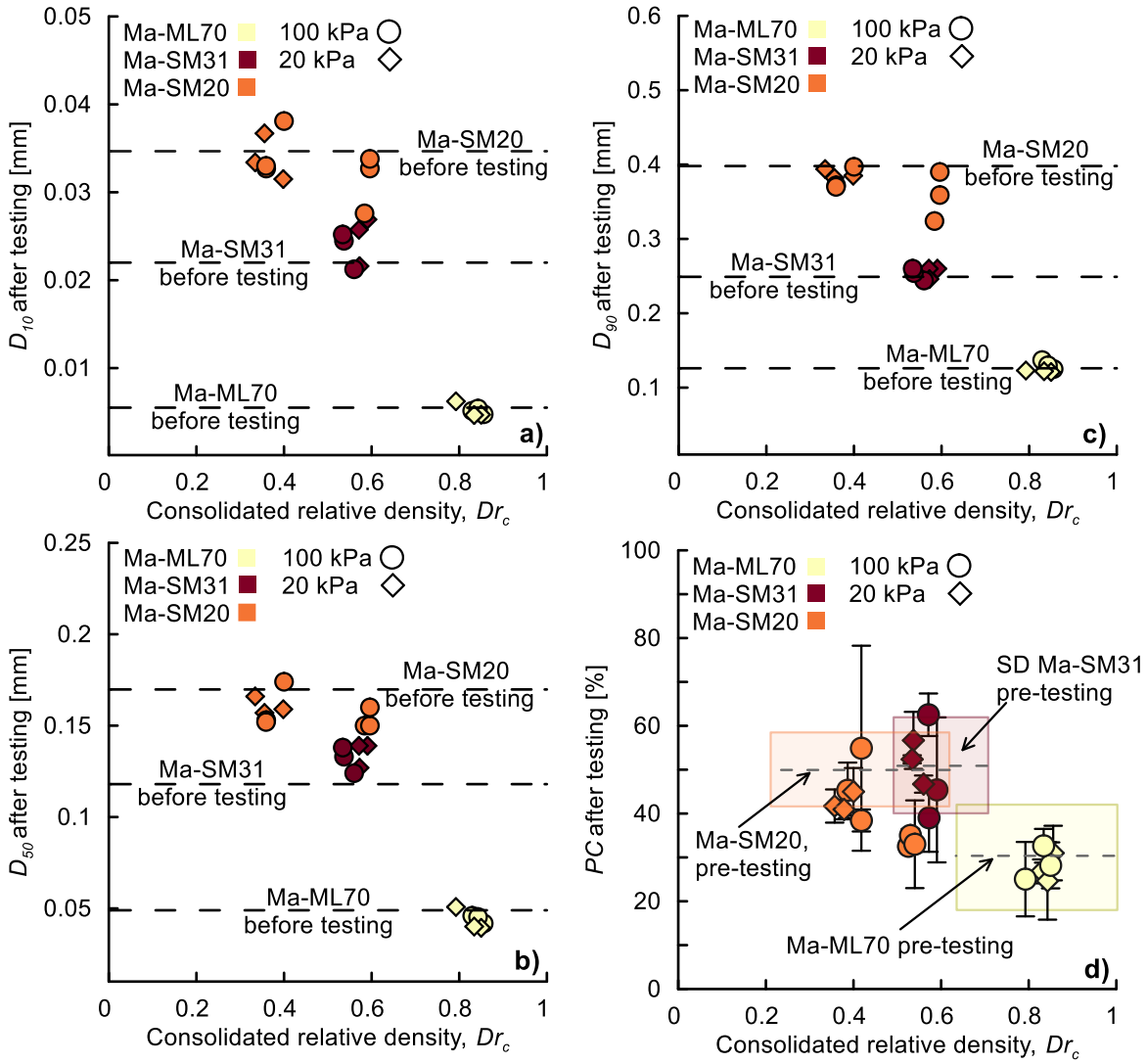


Fig. 5.4. Grain size parameters (a) $D_{10}$, (b) $D_{50}$ and (c) $D_{90}$ for virgin Mamaku tephra samples (of the three beds) before and after testing, and (d) pumice content for virgin Mamaku tephra sample materials (the three beds) before and after testing.

The coloured data points represent the pumice contents of the Mamaku materials after triaxial testing, together with their corresponding standard deviations, SD (vertical error bars). The dashed horizontal lines represent the virgin materials' pumice contents, and the coloured squares represent the standard deviations of the virgin materials' pumice content values. The pumice contents of Ma-ML70 and Ma-SM31 materials obtained after testing mostly lay within the standard deviations of the equivalent virgin materials, indicating that the pumice contents of those materials did not significantly change, and, therefore, no crushing occurred due to triaxial testing at the consolidation stresses and relative densities considered. The pumice contents of Ma-SM20 (orange data points) obtained after triaxial testing lie below the standard deviation of the equivalent virgin material, suggesting that particle crushing took place for this particular pumiceous sand, with it being most evident for the denser samples ($Dr_c \sim 0.55$).

### 5.4.3. Cyclic undrained behaviour

The normalised axial strain development and pore-water pressure development plots are presented in Fig. 5.6. The full line curves (yellow, red and orange) are median curves of the results from the three different Mamaku beds.

For discussion purposes, results from the studies of Asadi et al. (2018) and Chaneva et al. (2023) are plotted as well (Fig. 5.6). The dark green and grey zones (zones A and B) correspond to ranges typical for pumice sand (with a relative density of ~0.8) and hard-grained Toyoura sand (with a relative density of ~0.5), respectively, as per Asadi et al. (2018). The dashed black curve is a median curve taken from the results for the pumiceous silt (51% fines and 48% pumice content) from Chaneva et al. (2023).

In their study, Asadi et al. (2018) found that the cyclic behaviour of pumiceous sands is characterised by a gradual increase in axial strain until liquefaction occurs. Pumice sand exhibits a pronounced pore-water pressure accumulation at the beginning of undrained cyclic loading, reaching high values of $r_u > 0.8$, well before liquefaction is initiated. In contrast, hard-grained Toyoura sand typically exhibits a more stable undrained cyclic behaviour with pronounced axial strain and pore-water pressure increases limited to the final phase of the undrained cyclic loading. The differences in undrained cyclic behaviour were attributed to the crushing of the pumice particles that we argued to be largely dependent on the relative density and was most evident for samples with a high relative density, e.g., ~0.8. In the study by Chaneva et al. (2023), it was found that pumiceous silt with 51% fines and 48% pumice content was not crushable, and the undrained cyclic behaviour was similar to that of hard-grained sands.

If we consider the zones of the results for the pumice sand and the hard-grained sand from Asadi et al.'s study to be the boundaries between crushable and non-crushable undrained soil behaviour trends, we can discuss the results for the Mamaku tephra materials in a particle crushing manner. Note that other soil or particle properties that affect the undrained soil behaviour, such as particle shape and angularity, are not considered in the discussion. The different testing conditions, such as consolidation stress, density and cyclic stress ratios, are not discussed separately. Instead, a trend that considers the different soils by means of grain size and pumice content alone is observed. The Mamaku results, shown by analyses of samples Ma-ML70, Ma-SM31, and Ma-SM20, are presented with a single median curve per material.

The yellow line presents the median curve for all the Ma-ML70 tests and clearly plots closest to the hard-grained (i.e., non-crushable) Toyoura sand. Ma-SM20 is presented with the orange line, and it plots the closest to the natural crushable pumice zone published by Asadi et al. (2018). The results from the undrained cyclic behaviour tests for Ma-SM31 (red line) plot in the middle, between those for Ma-SM20 and Ma-ML70.

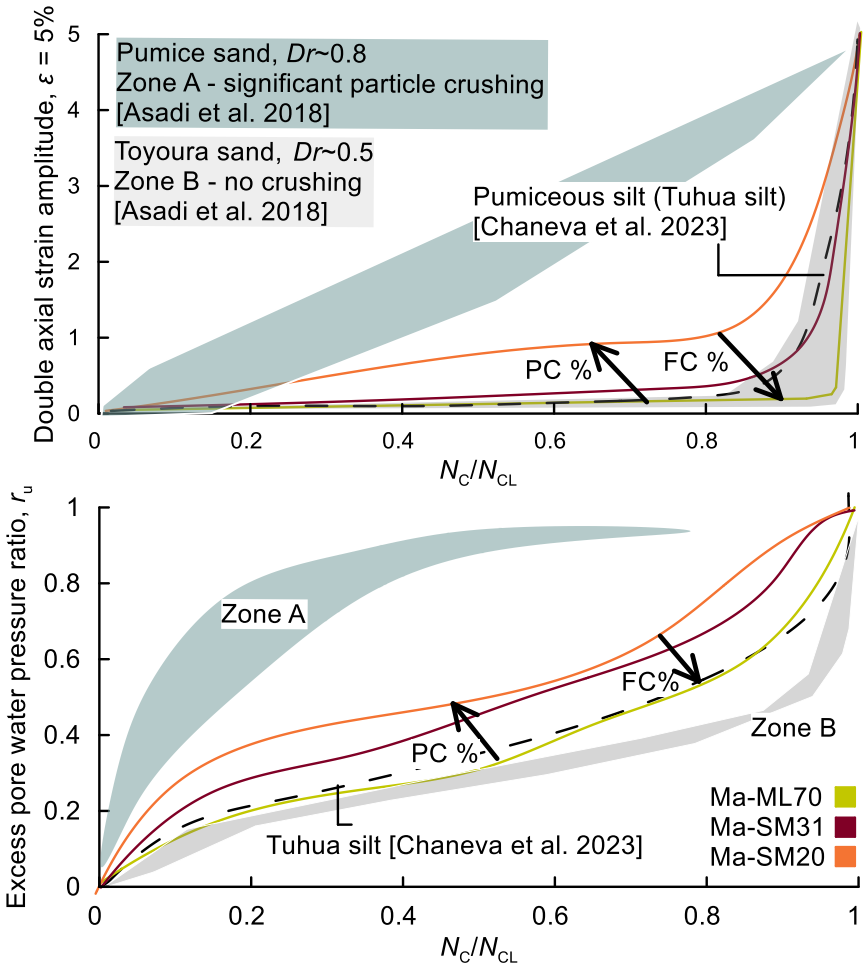


Fig. 5.5. Normalised axial strain and pore pressure development median curves for Ma-ML70, Ma-SM31, and Ma-SM20 (yellow, red and orange lines, respectively) plotted against relevant results (zones and median curves) from published literature.

The results for the three Mamaku materials show a clear trend based on the fines contents of the virgin soils. Namely, the coarser the soil particles are, the closer the results plot to the pumice crushable sand zone, indicating higher crushability. Moreover, the results for the pumiceous silt from Chaneva et al. (2023) (with fines content of 51%) also fall into the trend with the median curve of the silt (51% fines), plotting in between the Ma-ML70 and Ma-SM31.

Considering the fact that the pumice contents of Ma-SM31 and Ma-SM20 are relatively similar (50% and 51%, respectively) to the pumiceous silt (48%) from Chaneva et al. (2023), a pumice content-based trend is less conclusive. Yet, sample Ma-ML70 (the Mamaku tephra

bed with the lowest pumice content) plots closest to the hard-grained Toyoura sand zone (zone B), and sample SM20, with the highest pumice content (51%), plots closest to the Pumice sand zone (A), and so a subtle trend can be observed. Soil materials that cover a wider range of pumice content values should be tested in order to further investigate whether there is a threshold of pumice content upon which particle crushing starts.

## 5.5. Conclusions

Particle crushing of three tephra-derived pumiceous silt materials, Ma-ML70, Ma-SM31, and Ma-SM20, with different pumice and fines contents, based on 21 undrained triaxial cyclic tests, was analysed and evaluated. Observations based on grain size distribution, pumice content changes, and cyclic undrained behaviour allowed us to make the following conclusions:

- No change in grain size nor pumice content was observed for the silty Mamaku Ma-ML70. Moreover, the cyclic behaviour, by means of pore pressure distribution as well as double axial strain accumulation of Ma-ML70, is similar to that of hard-grained sands and non-crushable silts from the literature, indicating no particle crushing occurred.
- The silty Mamaku sand sample with 31% fines, Ma-SM31, showed no changes in grain size as well as pumice content after testing. The results from the undrained cyclic testing do not resemble the typical crushable trends. The results for this pumiceous material also indicate that no particle crushing occurred during the cyclic testing.
- For the coarsest Mamaku sand, with 20% fines, Ma-SM20, both for the grain size and the pumice content, changes indicating particle crushing were evident. The undrained cyclic behaviour results plot the closest to the crushable zone based on published data, compared to the other two Mamaku materials. Thus, it can be inferred that Ma-SM21 underwent particle crushing for the used testing condition.
- Considering the crushing results and the fines contents of the three materials as well as the available published data on pure pumiceous sand and a pumiceous (51% fines content) silt, if a fines threshold where particles begin to crush under cyclic triaxial testing is to be speculated, it would be in between 31% and 20%.
- Considering the fact that Ma-SM20 sand with a 50% pumice content is crushable, and that there are published data for pumiceous silt with 48% pumice content proven not to be crushable, a definitive conclusion based on the effect of pumice content alone cannot yet be made.

## Authorship contribution statement

**Jordanka Chaneva:** Investigation, Conceptualization, Methodology, Data curation, Writing – original draft. **Max O. Kluger:** Conceptualization, Methodology, Supervision, Writing - review and editing, Funding acquisition. **Vicki G. Moon:** Methodology, Supervision, Writing - review and editing, Funding acquisition. **David J. Lowe:** Supervision, Funding acquisition, Writing - review and editing. **Rolando P. Orense:** Supervision, Writing - review and editing, Funding acquisition.

## Acknowledgments

We acknowledge funding support as follows: the MBIE Endeavour Fund (Smart Ideas) contract UOWX1903; the Marsden Fund contract UOW1902; the New Zealand Centre for Earthquake Resilience (QuakeCoRE); the Earthquake Commission Toka Tū Ake EQC (Contract BIG 012 2020); and Waikato Regional Council (support for project on paleoseismicity and liquefaction). We thank Richard Melchert, Tehnuka Ilanko, Tom Robertson, Ben Roche, Helen Turner, and Vittoria Gibbons for help in the field and/or lab, and Mrs Hekeiterangi Broadhurst (Kuia Kaumatua) and Wiremu Puke of Ngāti Wairere (Hukanui Marae), Waikato District Council, and the Department of Conservation, for supporting access to Lake Areare.

# Chapter 6: Using undrained cyclic triaxial tests to examine liquefaction resistance of historically liquefied pumiceous volcanic-ash soil materials and back-estimate past earthquakes

**Jordanka Chaneva**[1], Max O. Kluger[1], Tehnuka Ilanko[1], Vicki G. Moon[1], David J. Lowe[1] & Rolando P. Orense[3]

[1]*School of Science/Te Aka Mātuatua, University of Waikato, New Zealand, jc409@students.waikato.ac.nz*
[3]*Department of Civil and Environmental Engineering, University of Auckland, New Zealand*
Manuscript will be submitted in Engineering Geology in August, 2024

## 6.1. Abstract

Back-analysis of ground motion characteristics, such as earthquake magnitude and peak ground accelerations, in paleoliquefaction studies are most commonly based on empirical CPT- and/or SPT-based correlations that estimate the liquefaction resistance of soil materials of relevance. Laboratory triaxial cyclic tests have not been explored for this purpose to date. Our study investigates the liquefaction resistance of three different beds (with differing grain-size distributions and pumice content) of a single rhyolitic (high-silica) volcanic-ash layer, referred to as Mamaku tephra, that was deposited ~8000 calendar years ago and preserved in lake sediments in multiple extant lakes in the Hamilton lowlands, North Island, New Zealand. Paleoliquefaction features observed in the silty and sandy beds of the Mamaku tephra indicate seismic activity in the past. With our main aim being to back-analyse potential past earthquakes that might have caused the paleoliquefaction features in Mamaku tephra (and other lacustrine tephras), the following steps were taken: (1) the liquefaction resistance of the three Mamaku tephra beds with different grain sizes and pumice contents from one site (Lake Areare, northern Hamilton lowlands) was investigated using undrained cyclic triaxial testing; (2) a framework extending the laboratory liquefaction resistance results of the tested Mamaku beds at Lake Areare to Mamaku tephra layers in the lake sediments across the lowlands was proposed; and (3) the equivalent peak ground acceleration and earthquake magnitude that would have caused liquefaction of all the lacustrine Mamaku tephra layers across the lowlands (in 13 lakes) were estimated using available empirical correlation methods. The limitations of the proposed framework are also discussed, alongside the qualitative implications on the results is also provided. It was found that the Mamaku tephra layers are very vulnerable to liquefaction and require very low triggering peak ground acceleration to liquefy, i.e. $a_{max}$ in the range between 0.02–0.08 g through the range of magnitudes, $M$ = 5 – 8.5.

KEYWORDS**:** liquefaction; tephra; lake sediments; pumiceous silts and sands; undrained cyclic triaxial tests; prehistoric earthquakes; earthquake magnitude; peak ground acceleration

## 6.2. Introduction

Paleoliquefaction studies are interdisciplinary and incorporate methods used in paleoseismology, geology, geochronology, geomorphology, geophysics, and geotechnical engineering (Tuttle et al. 2019). The aims of paleoliquefaction studies are to estimate prehistoric earthquakes, improve understanding and knowledge of the seismic sources, and ultimately help authorities re-evaluate seismic hazard and risk, especially in areas where the seismic historical record is shorter than the recurrence time of large earthquakes, such as in central and eastern North America and New Zealand (Talwani and Schaeffer 2001; Tuttle 2001; Villamor et al. 2016).

The geotechnical approaches in paleoliquefaction studies analyse the liquefaction resistance of soil deposits that have been previously identified as historically liquefied through geological field observations (Green, Obermeier, and Olson 2005; Olson, Obermeier, and Stark 2001). The liquefaction resistance, commonly expressed through the cyclic resistance ratio, *CRR*, is estimated using empirical correlations based on field investigations, such as CPT and SPT (Boulanger and Idriss 2014; Seed and Idriss 1971). Then, for an assumed factor of safety $F_{SL} = 1$ (i.e., the *CRR* is equal to the cyclic stress ratio, *CSR* (Seed and Idriss 1971)), the peak ground acceleration, $a_{max}$, and earthquake magnitude, *M*, are evaluated (Green et al. 2005). This analysis is sometimes complemented with regional attenuation evaluations of the credible $a_{max} - M$ combinations for the site or sites of interest, in order to evaluate the range of possible $a_{max} - M$ pairs that caused the liquefaction at the sites.

To date, laboratory triaxial cyclic tests have not been explored for the purpose of back-analysing past earthquakes from paleo-liquefaction features.

The 2010-11 Canterbury earthquake sequence in the South Island of New Zealand provided enough scientific data for paleoseismologists to find that the events were caused by ruptures in previously unmapped, hidden faults (Tuttle et al. 2017). Those findings, combined with the relatively young recorded seismic history of New Zealand, highlighted the significance of paleoliquefaction studies in the country. Recent studies in the Hamilton lowlands of northern North Island, New Zealand, posited that soft-sediment deformation structures (SSDSs) within pumiceous volcanic-ash (tephra) layers deposited in the lake sediments of ~35 lakes in the Hamilton Basin were the result of paleoliquefaction (Kluger et

al. 2023; Melchert 2023; Melchert et al. 2023). Tephras are defined as the explosively erupted pyroclastic (fragmental) products of volcanic eruptions that encompass all grain sizes and compositions irrespective of emplacement mechanism (Lowe 2011; Lowe et al. 2022), although the tephra layers in our study all represent fall deposits. Kluger *et al.*, (2023) described SSDSs in seven post-17,500 calendar (cal)-year-old lacustrine tephra layers by analysing them in multiple cores taken from ten lakes using sediment/tephra descriptions and X-ray computed tomography (CT) scanning. Melchert (2023) and Melchert *et al.*, (2023) focused on describing the SSDSs spatially and temporally in Lake Rotoroa (Hamilton Lake) using a combined approach of sediment/tephra description and CT scanning of cores taken from the lake as well as ground-penetrating radar (GPR). The findings from these studies (by Kluger et al. 2023 and Melchert et al., 2023) provided insight into the paleoseismic activity of the Hamilton lowlands and wider region and are further analysed spatially and temporally by Kluger et al., (unpublished data). In addition to the field- and GPR-based SSDSs identification studies, geotechnical studies that focussed on the liquefaction susceptibility and liquefaction resistance of the tephras of interest have also been performed (Chaneva et al. 2022, 2023, 2024). Chaneva *et al.*, (2022) analysed the geotechnical properties of four of the seven tephra layers of interest, Tuhua, Mamaku, Waiohau, and Rotorua, and found that they were non-plastic, pumiceous, and susceptible to liquefaction. Chaneva et al. (2023), presented a detailed triaxial testing study of the topmost (youngest) silt-rich tephra, the 7600 cal-year-old Tuhua tephra, taken from sediments in Lake Areare. The study investigated the liquefaction resistance of Tuhua tephra in relation to its fines and pumice content and, thus, filled in part the research gap about the effect of potential crushability of pumice particles in pumiceous silts on their undrained cyclic behaviour and liquefaction resistance. Chaneva et al. (2023) found lack of particle crushing in the pumiceous Tuhua silt, which was attributed to a likely cushioning effect of the silty particles, thus preventing the crushing of sandy particles. Lastly, Chaneva et al., (2024) discussed the effects of fines content and pumice content on the extent of the crushability of three different beds (two sands and one silt) of the single Mamaku tephra layer from Lake Areare. Mamaku tephra (deposited ~8000 cal years ago) is rhyolitic and typically ~2–3 cm thick, with each of the three constituent tephra beds being around ~0.5–1 cm thick. Chaneva et al. (2024) speculated that the threshold at which particles begin to crush in pumiceous sand-silt mixtures could be at a fines content between 20% and 31%.

The present study aims to continue and extend the previous geotechnical studies (Chaneva et al. 2022, 2023, 2024), as well as complement paleoseismology studies of the Hamilton lowlands and adjacent Hauraki Plain (Kluger et al. 2023; Melchert 2023; Villamor et al. 2024, Kluger et al. unpublished data; Ilanko et al. unpublished data), by investigating the liquefaction resistance of the three beds of Mamaku tephra from Lake Areare and extending those results into earthquake parameter evaluations, i.e. $a_{max} - M$ combinations. Because all tephra layers found in the lakes have varying thicknesses, with the maximum thickness being ~3 cm, it was not possible to perform field investigations such as CPT and SPT. Instead, a series of undrained cyclic triaxial tests were used to obtain the liquefaction resistance of Mamaku tephra from Lake Areare, which was then used as a basis to obtain $a_{max} - M$ combinations for Mamaku tephra across 13 lakes examined in the region.

The main objectives of the present study are as follows: (1) obtain the liquefaction resistance of three different (by grain size and pumice content properties) beds, of the Mamaku tephra from Lake Areare tested under two consolidation stresses, 20 kPa and 100 kPa, and two relative densities for each consolidation stress testing series; (2) derive a framework that extends the laboratory liquefaction resistance results performed for the three beds of Mamaku tephra at 20 kPa consolidation stress to all Mamaku tephra layers in the lake sediments across the 13 lakes we have cored in the Hamilton lowlands; and (3) obtain $a_{max} - M$ combinations for the three beds of Mamaku tephra, as well as the Mamaku tephra materials across the other 13 lakes. The challenges and limitations of the framework, as well as the qualitative implications on the results, are also discussed.

## 6.3. Study area

The Hamilton lowlands in northern North Island (Fig. 6.1a) lie on the Australian Plate with the Pacific Plate subducting beneath it, and are subjected to tectonic activity and the impacts of distant active volcanism (Nicol et al. 2017; Shane 2017). The Hamilton lowlands are currently classified as having low to medium seismic hazard on the basis of a short (<~150 years) historical record (Van Dissen et al. 2021; Downs 2005). Numerous tephra fall layers derived from eruptions of rhyolitic and andesitic volcanic centres in the Taupō Volcanic Zone, Taranaki (Egmont) Volcano, and Tuhua Volcanic Centre (Mayor Island) during the late Quaternary, are found in sediments in multiple blocked-valley riverine and riverine-phytogenic lakes formed ~20,000 cal years ago in the Hamilton lowlands (Lowe and Green 2024). The thickest tephra layers, mainly rhyolitic (silica-rich) in composition, have been preserved in organic lake

sediment continuously formed in the lakes since ~20,000 cal years ago. Hence, post-deposition alteration is negligible (Lowe 1986, 1988). Seven of these tephra layers preserved within the organic lake sediments have been liquefied because of past earthquakes (Kluger et al. 2023). All lakes are sufficiently distal from the source volcanoes and no measurable variation in terms of their grain-size and/or the liquefaction deformations was found. The tephra layers are pumiceous silts, sandy silts, silty sands, and sands (Chaneva et al. 2022). The study reported here is based on the analysis of liquefaction resistance of Mamaku tephra sampled from near-surface lake sediments exposed at the shore of Lake Areare (Fig. 6.1a). Previous studies based on sediment cores taken from 13 lakes have shown this tephra to be liquefied in eight lakes (Lake Rotokaeo/Forest Lake (FL), Lake Rotoroa/Hamilton Lake (HL), Lake Kaituna (KT), Lake Whakatangi (WT), Lake Koromatua (KM), Lake Mangahia (MH), Lake Ngarottoiti (NI), and Lake Mangakaware Lake (MK)), whereas no liquefaction of this tephra layer was found in the sediments in five other lakes (Lake Kainui (KN), Lake Rotokauri (RI) Lake Pikopiko (PP), Lake Karaeotahi/Cameron Lake (CA), and Lake Ruatuna (RT) (Kluger et al., unpublished data). Hence, these 13 lakes were considered in the present study (Fig. 6.1a).

## 6.4. Methods and materials

### 6.4.1. Sampling procedure

The three individual beds of the Mamaku tephra layer studied in the triaxial testing programme were sampled at the shore of Lake Areare, where the material was located at a relatively shallow sediment depth of <0.5 m in the exposed lakebed (Fig. 1b). Soil block samples (each with volume of ~0.0075 $m^3$) containing the Mamaku tephra layer were excavated (Fig. 1c) and transported to the laboratory. The block samples comprised the ~2 cm-thick Mamaku tephra layer, with its three internal beds, encapsulated within the organic lake sediments. The three Mamaku tephra beds were distinguishable by their grain-size distribution and pumice contents. The beds were carefully sampled in the laboratory using a spoon, manually cleaned from contamination of organic materials, and oven-dried at 40° C. The Mamaku tephra layers from the other 13 lakes could only be sampled for small-volume testing (i.e., grain-size analysis, particle density, pumice content) because of the limited tephra layer thickness and the limited number of ~2 m-long piston cores used to collect lake sediment and tephras in the lakes (Figs. 1d and e).

### 6.4.2. Sample properties

Some relevant physical and geotechnical properties, including grain-size distribution, particle density, in-situ density, and pumice content, were obtained for the Mamaku tephra layers from the 13 lakes. Additionally, the minimum and maximum dry densities and Atterberg limits were determined for the three individual beds of the Mamaku tephra that were used in the triaxial testing programme. Considering the thinness of the tephra layers, minimum and maximum dry densities and Atterberg limits could not be obtained for the Mamaku tephra samples (in sediment cores) from the other 13 lakes.

The grain-size distribution of the Mamaku soil materials was determined through laser diffraction analysis using a Malvern Mastersizer 3000. Atterberg limits were obtained following ASTM-D4318-17e1 (2017). The soil classification and fines content threshold (%<0.075 mm) were defined following ASTM D2487-11 (2011). The particle density, $\rho_p$ [kg/m$^3$], was determined using a Quantachrome Ultrapyc 1000 nitrogen-filled gas pycnometer following ASTM-D5550-14 (2014). The minimum and maximum dry densities were obtained following the Japanese standard method (Japanese Geotechnical Society Standard 2009) as modified by Mijic et al. (2021). The Japanese standard methods for minimum and maximum density has been proven to cause negligible crushing in natural pumiceous soils found in the North Island of New Zealand (Asadi et al. 2019), and their modification by Mijic et al. was suitable for the presented study as it provides a scaled procedure appropriate for small volumes of soils.

The saturated in-situ densities, $\gamma_{sat}$, were estimated using X-ray computed tomography (CT) images of the cores. CT scans have been successfully used to derive sediment densities from lake cores before (Flisch and Becker 2003; Fortin et al. 2013). A CT number (Hounsfield unit, *HU*) to density conversion was developed using a set of calibration materials whose volumes and masses were measured independently in the lab. The Hounsfield unit is a relative quantitative measurement of radio density used by radiologists in the interpretation of CT images (Hounsfield 1973). The calibration data encompass the range of densities expected within a lake core.

Using the MATLAB Volume Segmenter, each calibration material was segmented from the scan so that its mean CT number could be calculated. Our calibration is based on a provisional linear regression using this full set of calibration data.

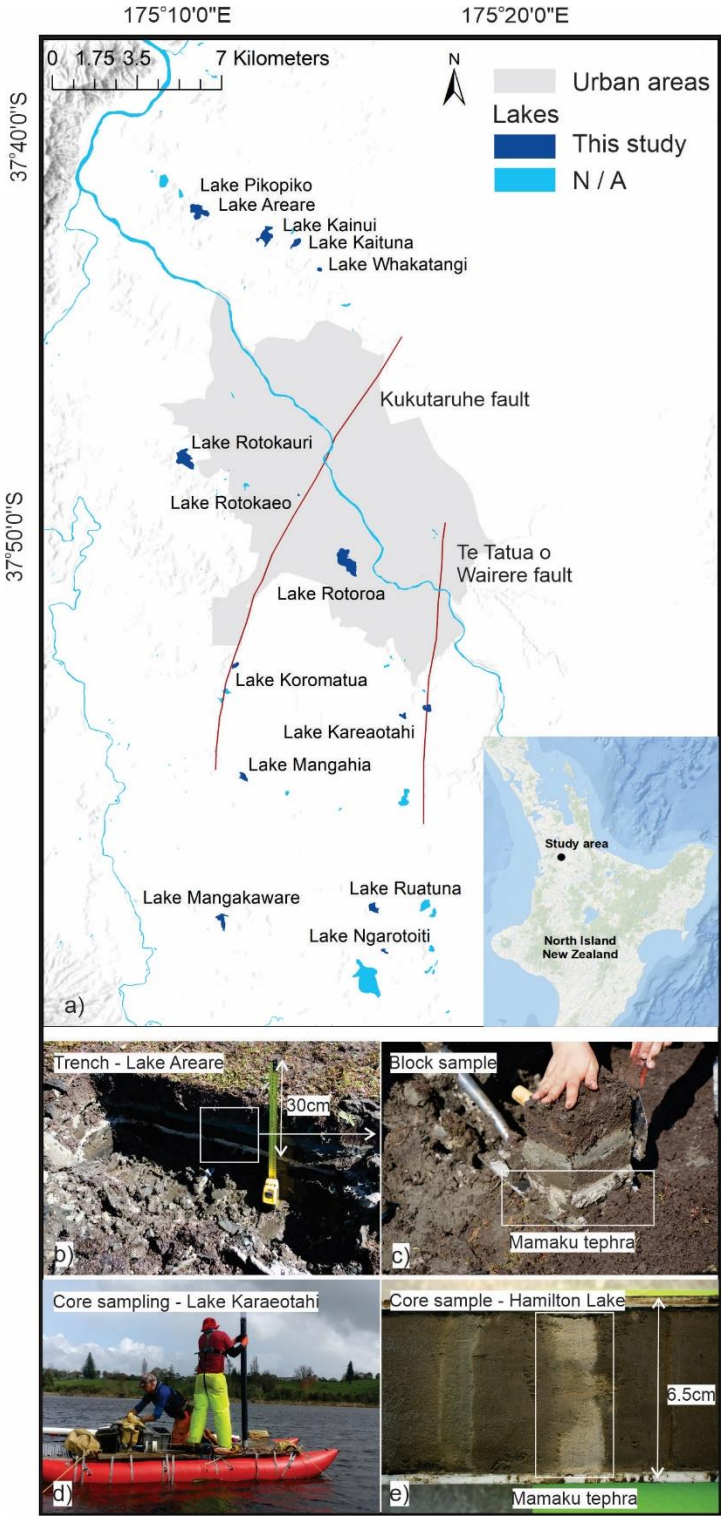


Fig. 6.1. Study area presenting the locations of 14 lakes in the Hamilton lowlands featured in this study, and faults in the area, North Island, New Zealand. Recently identified faults are from (Van Dissen et al. 2021; Shane 2017) (a). Figure also shows (b) trench where the Mamaku tephra layer at Lake Areare was sampled, (c) block samples containing Mamaku tephra in between organic lake sediments, (d) example of taking a sediment core from a lake, and (e) a representative core segment, placed horizontally, from a sediment core from Lake Rotoroa/Hamilton Lake, containing Mamaku tephra with a SSDS.

A supplementary Fig. S3 shows the materials used to estimate the regression equation for the purpose of this study, (Ilanko et al. unpublished data). This regression equation between the CT number and the density was used to calculate the mean in-situ saturated densities for each tephra segmented from the cores.

The in-situ void ratios, $e_{\text{in-situ}}$, were then obtained using the following equation:

$$\boldsymbol{e_{in-situ}} = \frac{\boldsymbol{\rho_{p,average}} - \rho_{sat}}{\rho_{sat} - \boldsymbol{\rho_{water}}} \tag{6.1}$$

where $\rho_{\text{water}}$ is the density of water, taken as 1000 kg/m$^3$, and $\rho_{\text{p,average}}$ is the average particle density for the Mamaku tephras (Table 6.1.). The average particle density was calculated from the Mamaku tephras from Lake Areare, Lake Kainui, Lake Rotokauri and Hamilton Lake (Table 6.1.). Please refer to Appendix A for the full derivation of Eq. 6.1. The dry in-situ densities, $\rho_{\text{dry}}$, were calculated through the in-situ void ratio using the following equation:

$$\rho_{\boldsymbol{dry}} = \frac{\boldsymbol{\rho_{p,average}}}{\boldsymbol{e_{in-situ}+1}} \tag{6.2}$$

The minimum and maximum dry densities could not be obtained for the Mamaku tephra layers of the 13 lakes due to inadequate sample volumes and, therefore, their relative density had to be estimated from the average minimum and maximum dry densities obtained from the three beds of the Mamaku tephra sampled from Lake Areare (Table 6.1).

The pumice content was quantified using the point counting approach (Frolov and Maling 1969; Kluger et al. 2017), based on scanning electron microscopy (SEM) images (Fig. 6.2). The SEM images were taken using a Hitachi S-4700 FE SEM system. In the point counting approach, a high-resolution SEM image with a magnification of x35 of representative grain clusters was chosen for each sample and counted systematically on crossing points of rectangular grids (285 points per image). The pumice content, *PC*, was calculated from Eq. 6.3.

$$PC = \frac{N_{A,pumice}}{N_{A,total}} \cdot 100\% \tag{6.3}$$

where $N_{\text{A,pumice}}$ is the number of points that crossed a particle with pumiceous features (i.e., being vesicular) and $N_{\text{A,total}}$ is the total number of crossing points classified (as either pumice or non-pumice) for a specific sample. Note that the particles classified as non-pumiceous in this study are primarily glass shards – broken-down pumiceous particles that no longer have vesicles.

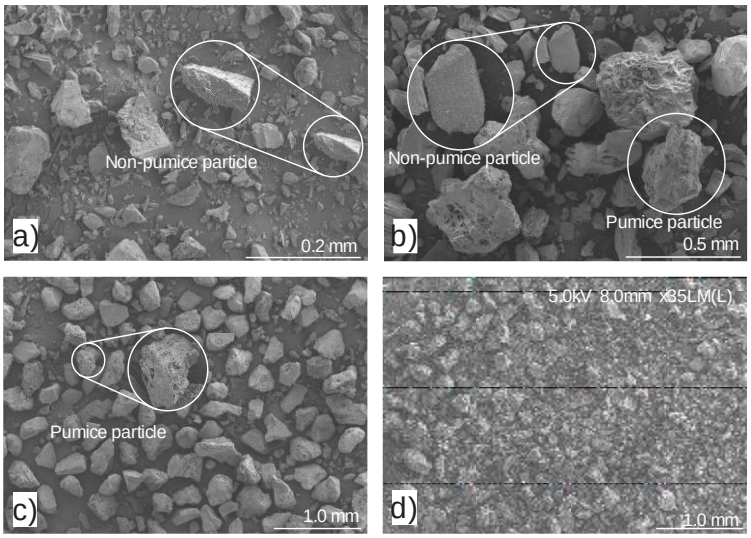


Fig. 6.2. High magnification SEM images of (a) Ma-ML70, (b) Ma-SM31 and (c) Ma-SM20, showing the constituent particles closely, and a representative low magnification (x35) SEM of grains from Mamaku tephra used in the SEM-based pumice content evaluation point-counting approach.

The grain-size distribution curves of all Mamaku tephra samples (including the three triaxial testing samples, i.e., the individual beds from Mamaku tephra from Lake Areare, and samples from the other 13 lakes) are shown in Fig. 6.3. The topmost bed of Mamaku tephra from Lake Areare exhibits 70% fines and is non-plastic and thus was classified as low plasticity silt: ML (ASTM D2487-11, 2011). The middle and lowermost beds of Mamaku tephra exhibit 31% and 20% fines, respectively, and were, thus, classified as silty sands: SM. The three beds of Mamaku tephra from Lake Areare, uppermost, middle, and lowermost, will be referred to hereafter as Ma-ML70, Ma-SM31, and Ma-SM20, respectively. The abbreviations denote the soil classification (i.e., ML or SM) followed by the corresponding value of the fines content (e.g., 70 for $FC$ = 70%). The Mamaku tephra layers from other lakes were labelled using the abbreviation of the lake from which the sample was taken (e.g., Ma-FL denotes Mamaku tephra from Forest Lake). Note that the Mamaku layers across the lakes have varying thicknesses and can have more than one bed. The presented Mamaku samples from the rest of the lakes, correspond to the beds that showed paleoliquefaction features in the lakes with SSDS, and the coarsest Mamaku beds for the lakes with no SSDS. The specific gravity, grain-size parameters, pumice content, minimum and maximum void ratios, in-situ void ratios, and in-situ relative densities of all Mamaku tephra samples are summarised in Table 6.1. The corresponding depths below the lakebed of the Mamaku tephra layers are also given in Table 6.1.

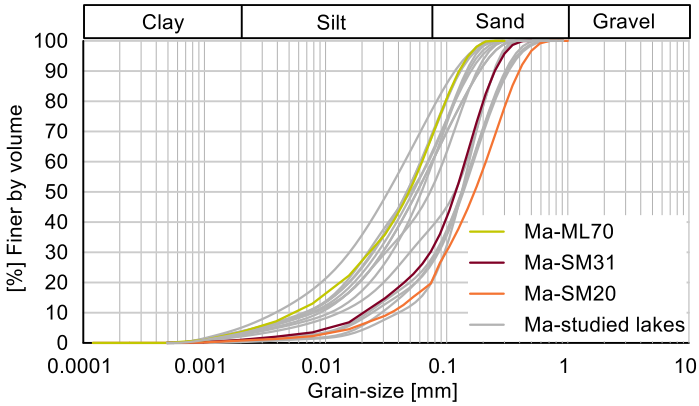


Fig. 6.3. Grain size distributions of Ma-ML70 (yellow), Ma-SM31 (red), and Ma-SM20 (orange), as well as for samples of Mamaku tephra in toto from cores taken from 13 lakes additional to Lake Areare (grey).

The mineralogical properties of Mamaku tephra have been studied before (Lowe 1988), and were found to be similar in all the lakes, being predominantly vitric with both platy and pumiceous glass shards, rhyolitic in composition, together with subordinate feldspar and mafic crystals or crystal fragments.

Table 6.1. Index properties of used Mamaku tephra (in toto) materials

| Material | *Gs* | $D_{50}$ [mm] | *FC* [%] | *PC* [%] | $\rho_{dry}$ [kg/m$^3$] | $e_{in\ situ}$ | $e_{min}$ | $e_{max}$ | Depth in lakebed [m] | $Dr_{in\text{-}situ}$ |
|---|---|---|---|---|---|---|---|---|---|---|
| Ma-ML70 | 2.41 | 0.049 | 70 | 23.4 | / | / | 0.88 | 2.07 | 2.3 | 1.11 |
| Ma-SM31 | 2.40 | 0.118 | 31 | 40 | / | / | 0.69 | 1.50 | 2.3 | 0.93 |
| Ma-SM20 | 2.40 | 0.169 | 20 | 53 | / | / | 0.70 | 1.28 | 2.3 | 0.92 |
| Ma-FL | 2.39 | 0.037 | 66.6 | 29.1 | 1354.3 | 0.77 | / | / | 2 | 1.12 |
| Ma-HL | 2.42 | 0.074 | 45 | 42.9 | 1320 | 0.82 | / | / | 2.1 | 1.00 |
| Ma-KT | / | 0.207 | 28.1 | 52.4 | 1405.7 | 0.79 | / | / | 2.1 | 0.89 |
| Ma-WT | / | 0.151 | 21.5 | 51.4 | 1337.1 | 0.77 | / | / | 1.8 | 1.04 |
| Ma-KM | / | 0.057 | 52.3 | 37.7 | 1422.9 | 0.75 | / | / | 5.3 | 0.90 |
| Ma-MH | / | 0.133 | 32.1 | 37.4 | 1474.3 | 0.71 | / | / | 1.9 | 0.93 |
| Ma-NI | / | 0.053 | 55.8 | 40.8 | 1405.7 | 0.79 | / | / | 2.4 | 0.91 |
| Ma-MK | / | 0.065 | 48.8 | 43 | 1405.7 | 0.69 | / | / | 1.3 | 1.03 |
| Ma-KN | 2.40 | 0.143 | 18.4 | 56.4 | 1337.1 | 0.82 | / | / | 1.2 | 0.99 |
| Ma-RI | 2.38 | 0.047 | 55.9 | 35.2 | 1354.3 | 0.63 | / | / | 1.8 | 0.95 |
| Ma-PP | / | 0.151 | 19.7 | 54.1 | 1371.4 | 0.77 | / | / | 2 | 1.03 |
| Ma-CA | / | 0.083 | 41.5 | 44 | 1320 | 0.71 | / | / | 1.4 | 1.04 |
| Ma-RT | / | 0.059 | 51.5 | 40.1 | 1354.3 | 0.71 | / | / | 0.8 | 1.02 |
| Average | 2.4 | | | | | | 0.757 | 1.617 | | 1.01 |
| SD | 0.012 | | | | | | 0.087 | 0.333 | | 0.06 |

### 6.4.3. Triaxial testing

Triaxial testing was undertaken using a GDS Advanced Dynamic Triaxial Testing apparatus. During the specimen preparation the samples were moist-tamped following the under-compaction procedure of Ladd (1978). Undisturbed sample testing in the triaxial setting was

not possible because of the small thickness of the tephras (~2 to 3cm). Sample reconstitution by water pluviation would have more realistically resembled the naturally occurring sedimentation process in the lake environment for tephra fall deposits. However, the water pluviation method is considered to cause segregation in sand-silt mixtures, and it is found that high densities are hard to achieve without an additional densifying technique, such as vibrations and compactions (A. Bin Huang et al. 2015; Ishihara 1997; Kuerbis and Vaid 1988). Hence, the moist-tamping method was considered to be more appropriate in order to achieve more homogeneous samples by means of density distribution. The reconstituted relative densities in the testing programme were above the medium-dense range ($Dr$ > 35%) according to the relative density designations, as per Terzaghi and Peck (1967). The relative density at which all three Mamaku tephras could be moist-tamped into the mould, without crushing the particles during the reconstitution of the samples, was chosen as the maximum relative density at which the Mamaku materials were tested (i.e., $0.5 \leq Dr \leq 0.6$ for Ma-SM20 and Ma-SM31, and $0.7 \leq Dr \leq 0.85$ for Ma-ML70).

The target size of the triaxial specimens was 50 mm in diameter and 100 mm in height. Deaired and demineralised water was added to the dry sample material. The sample material was soaked in water for 24 hours in order to achieve a homogeneous water content distribution. All samples were prepared at a water content of 15%. Then, samples were reconstituted in eight layers of equal weight into a split mould mounted on top of the triaxial base plate comprising the basal filter stone. For reconstituting samples at high relative densities, a 0% under-compaction ratio was selected for the first layers. For all other samples, an under-compaction ratio of 15% was chosen. The under-compaction ratio is defined in the original publication of Ladd (1978). The density distribution throughout the sample was checked by observing the shape of the sample once reconstituted and its failure pattern, following the recommendations of Ladd (1978).

After reconstituting the sample, a filter stone was added to the top of the sample and the initial height was measured at different positions of the filter stone using a calliper. Then, the top cap was placed on the sample and the cell was assembled and filled with water. The initial height was used to calculate the initial relative density of the sample. Before the saturation phase, the sample was slowly flushed with deaired and demineralised water through the back-pressure pump by applying a constant low pore water pressure of 1 kPa. A B-value of more than 0.95 was reached once the sample was subjected to a back-pressure of at least 800 kPa over 15 h. During the B-value check, the cell pressure was increased by 70 kPa and 20 kPa

for effective consolidation stresses, $\sigma_c$', corresponding to 100 kPa and 20 kPa, respectively (DIN EN ISO 17892-9, 2018). More details about the tests and their specific conditions are summarised in Table 6.2. The effective consolidation stress of $\sigma_c$' = 20 kPa was considered to most reasonably represent the in-situ stress conditions of the Mamaku tephra layer in its natural lake environment, considering the limitations in it being the lowest effective confining pressure that can be reproduced in the triaxial equipment, and the $\sigma_c$' = 100 kPa effective consolidation stress condition was used in order to compare the liquefaction resistance of the materials in the present study with those of the other soil types reported in the literature. Not many researchers have performed triaxial tests on soil materials at low confining stresses (Chaneva et al. 2023; Fannin et al. 2005; Y. Huang et al. 2015; Lancelot et al. 2006). Most recently, Chaneva et al. (2023) performed undrained triaxial tests on Tuhua silt under 20 kPa consolidation stress using the same triaxial apparatus and provided proof that the sensors can register sufficiently high signal-to-noise ratios to not affect the analysis of triaxial data. Hence, meaningful results can be generated at 20 kPa consolidation stress.

The post-consolidation void ratios of the samples were obtained following two different approaches. In the first approach, the volume change, in relation to the initial volume of the sample, due to consolidation was measured by the back-pressure pump. In the second approach, the volume change due to consolidation was derived after completing the test following the procedure proposed by Verdugo and Ishihara (1996). The post-consolidation void ratios considered in this study were calculated by either (1) averaging the values from both approaches, or (2) using one value for the tests where results only from one method was available.

A total of 37 undrained, stress-controlled, cyclic triaxial tests were performed (Test series 1 to 12, Table 6.2). A sinusoidal cyclic stress amplitude was applied with a frequency of $f$ = 0.02 Hz. The calculation of the *CSR*, double axial strain amplitude, $\varepsilon_{da}$, pore water pressure ratio, $r_u$=$u$/$\sigma_c$', where $u$ is the excess pore water pressure in kPa, and number of loading cycles to liquefaction, $N_{CL}$, followed ASTM D 5311 - 92 (2004). According to ASTM D-5311, the triggering of cyclic liquefaction is considered when either the double axial strain amplitude, $\varepsilon_{da}$, reaches 5% or when the pore water pressure ratio, $r_u$, reaches 0.9.

### 6.4.4. Calculation of earthquake magnitude and peak ground acceleration

The characterisation of seismic loading parameters, including earthquake magnitude, *M*, and peak ground acceleration, $a_{max}$, was performed using the simplified empirical liquefaction triggering models (Boulanger and Idriss 2014; Seed and Idriss 1971).

The irregular cyclic loading history that happens during an earthquake can be converted into an equivalent number of cycles from a constant-amplitude uniform cyclic loading, i.e., from undrained cyclic triaxial tests. Researchers have found that the equivalent number of cycles to liquefaction, $N_{CL}$, can be correlated to an earthquake magnitude, *M*. The corresponding CRR for the selected magnitude, usually 7.5, can then be corrected with a corresponding magnitude scaling factor, *MSF*, taking into account the duration effect of different magnitude earthquakes (Boulanger and Idriss 2015; Seed and Idriss 1971). This study, for an earthquake magnitude $M = 7.5$, considered equivalent number of cycles $N_{CL} = 18$ for sands (Boulanger and Idriss, 2004) and $N_{CL} = 26$ for silts (Verma et al. (2019)).

*CRR* values corresponding to an equivalent number of cycles to liquefaction $N_{CL} = 18$ were taken from the triaxial liquefaction curves at 20 kPa (Fig. 6.5a), for Ma-SM20 and Ma-SM31, whereas *CRR* values corresponding to an equivalent number of cycles to liquefaction $N_{CL} = 26$ from the triaxial liquefaction curves at 20 kPa (Fig. 6.5a), were taken for the silt Ma-ML70.

The liquefaction triggering potential is commonly expressed as a factor of safety against liquefaction $FS_L = 1$ and, thus, the following calculations were performed:

$$FS_L = \frac{resistance}{loading} = \frac{CRR}{CSR_{M,\sigma'_c}} \tag{6.4}$$

where $CSR_{M,\sigma'_c}$ is expressed as follows:

$$CSR_{M,\sigma'_c} = 0.65 \times \left(\frac{a_{max}}{g}\right) \times \left(\frac{\sigma_c}{\sigma'_c}\right) \times r_d \times \frac{1}{MSF} \tag{6.5}$$

$a_{max}$ (measured in m/s$^2$) is the peak ground acceleration; $g$ is the gravitational acceleration constant (9.81 m/s$^2$); $\sigma_c$ and $\sigma'_c$ are the in-situ total and effective consolidation stresses (measured in kPa), respectively; $r_d$ is a stress reduction coefficient, which accounts for local site amplifications depending on the model soil column's flexibility, and *MSF* is a magnitude scaling factor that is a function of *M*, and represents a proxy for the duration of the loading.

Assuming a $FS_L$ = 1 (i.e., $CRR = CSR_{M,\sigma'_c}$), the $a_{max}$ values for corresponding $M$ were calculated as follows:

$$a_{max} = \frac{CRR \times g \times \sigma'_c \times MSF}{0.65 \times \sigma_c \times r_d} \quad (6.6)$$

Table 6.2. Experimental programme – undrained cyclic triaxial tests

| Test series | Label | $\sigma_c$' [kPa] | $e_c$ | $Dr_{,c}$ | *CSR* | $N_{CL}$ |
|---|---|---|---|---|---|---|
| 1 | Ma-ML70-CY-2 | 100 | 1.08 | 0.83 | 0.12 | 4 |
| | Ma-ML70-CY-3 | 100 | 1.05 | 0.86 | 0.09 | 18 |
| | Ma-ML70-CY-4 | 100 | 1.07 | 0.84 | 0.07 | 47 |
| 2 | Ma-ML70-CY-5 | 20 | 1.13 | 0.79 | 0.1 | 9 |
| | Ma-ML70-CY-6 | 20 | 1.04 | 0.85 | 0.08 | 10 |
| | Ma-ML70-CY-7 | 20 | 1.08 | 0.83 | 0.06 | 27 |
| 3 | Ma-ML70-CY-8 | 100 | 1.39 | 0.57 | 0.07 | 35 |
| | Ma-ML70-CY-9 | 100 | 1.35 | 0.61 | 0.055 | 194 |
| | Ma-ML70-CY-10 | 100 | 1.38 | 0.58 | 0.075 | 29 |
| 4 | Ma-ML70-CY-12 | 20 | 1.36 | 0.60 | 0.07 | 4 |
| | Ma-ML70-CY-13 | 20 | 1.34 | 0.61 | 0.05 | 5 |
| | Ma-ML70-CY-14 | 20 | 1.29 | 0.65 | 0.03 | 6 |
| 5 | Ma-SM31-CY-2 | 20 | 1.04 | 0.57 | 0.15 | 9 |
| | Ma-SM31-CY-3 | 20 | 1.03 | 0.59 | 0.16 | 326 |
| 6 | Ma-SM31-CY-4 | 100 | 1.05 | 0.56 | 0.16 | 30 |
| | Ma-SM31-CY-5 | 100 | 1.06 | 0.54 | 0.18 | 12 |
| | Ma-SM31-CY-6 | 100 | 1.06 | 0.54 | 0.15 | 39 |
| 7 | Ma-SM31-CY-7 | 100 | 1.17 | 0.41 | 0.15 | 3 |
| | Ma-SM31-CY-8 | 100 | 1.18 | 0.39 | 0.14 | 5 |
| | Ma-SM31-CY-9 | 100 | 1.14 | 0.44 | 0.125 | 10 |
| 8 | Ma-SM31-CY-10 | 20 | 1.19 | 0.38 | 0.115 | 12 |
| | Ma-SM31-CY-11 | 20 | 1.18 | 0.39 | 0.1 | 175 |
| | Ma-SM31-CY-12 | 20 | 1.17 | 0.40 | 0.11 | 73 |
| 9 | Ma-SM20-CY-1 | 20 | 1.07 | 0.36 | 0.12 | 67 |
| | Ma-SM20-CY-2 | 20 | 1.05 | 0.40 | 0.15 | 6 |
| | Ma-SM20-CY-3 | 20 | 1.09 | 0.33 | 0.14 | 28 |
| 10 | Ma-SM20-CY-4 | 100 | 1.04 | 0.40 | 0.14 | 19 |
| | Ma-SM20-CY-5 | 100 | 1.07 | 0.36 | 0.15 | 24 |
| | Ma-SM20-CY-6 | 100 | 1.07 | 0.36 | 0.155 | 21 |
| | Ma-SM20-CY-13 | 100 | 1.05 | 0.40 | 0.13 | 66 |
| 11 | Ma-SM20-CY-7 | 100 | 0.99 | 0.51 | 0.17 | 11 |
| | Ma-SM20-CY-8 | 100 | 0.99 | 0.50 | 0.16 | 15 |
| | Ma-SM20-CY-9 | 100 | 1.00 | 0.49 | 0.125 | 206 |
| 12 | Ma-SM20-CY-10 | 20 | 0.94 | 0.58 | 0.15 | 45 |
| | Ma-SM20-CY-12 | 20 | 0.93 | 0.60 | 0.165 | 21 |

## 6.5. Results and discussion

### 6.5.1. Cyclic triaxial test results

Fig. 6.4 presents three examples of cyclic undrained behaviour for the denser samples, one for each of the three Mamaku tephra beds. Graphs show developments of axial strain, $\varepsilon$, and excess pore water pressure, $u$, with the number of loading cycles, $N_C$ (Figs. 6.4a, c, e), and deviator stress vs. axial strain hysteresis loops (Figs. 6.4b, d, f). In general, for Ma-ML70, regardless of the density, all samples exhibited flow liquefaction failure when the double axial strain amplitude, $\varepsilon_{da}$, exceeded 5% and the pore water pressure ratio, $r_u$, reached 0.9. For the other two Mamaku tephras, Ma-SM31 and Ma-SM20, the denser samples failed more gradually, whereas looser samples exhibited a typical flow liquefaction failure. Refer to Appendix B2 for the complete set of undrained cyclic triaxial testing results.

The cyclic resistance ratio, *CRR*, and the data points (i.e., liquefaction resistance) for all cyclic tests, together with their corresponding liquefaction resistance curves, are shown in Fig. 6.5 (Table 6.2). The liquefaction resistance curves were obtained using power functions in the form of $CSR = a \cdot N_{CL}{}^{b}$ and depend on relative density and effective consolidation stress (Table 6.2, Fig. 6.5). The results for the 20 kPa and 100 kPa consolidation stresses are shown in Fig. 6.5a and Fig. 6.5b, respectively. The Ma-ML70 material (yellow diamond data points and line) showed extremely low liquefaction resistance at 20 kPa consolidation stress for the lower density ($0.60 \leq Dr \leq 0.65$), Fig. 6.5a. The samples of this silty Mamaku material were problematic during the docking process of the loading ram due to their very low stiffness. The confining pressure, i.e., the consolidation stress of 100 kPa, seemed to contribute to the sample's stiffness sufficiently for the docking process to pass. Yet with the samples under a confining stress of 20 kPa, we experienced difficulties in getting a satisfactory number of successful tests. Note that the presented tests results in this thesis (as shown in Appendix B) are all successfully sheared tests. The mentioned issues with the docking, applies to a large number of terminated tests before the shearing stage as the samples were essentially destroyed i.e. overly compressed from the loading ram. As the $N_{CL}$ results obtained were far from the range of the number of (equivalent) cycles that correspond to a magnitude of 7.5 for silts ($N_{CL}$ = 18), manual extrapolation was necessary for the next steps of the study (dashed yellow line). The results show that an increase in both the consolidation stress and relative density meant an increase in the liquefaction resistance of all three beds of the Mamaku tephra (Fig. 6.5 and Fig. S5).

If we consider the singular origin (same volcanic eruption) and similarity in mineralogical properties of all the Mamaku tephras (Lowe 1988), we can analyse the dependence of the cyclic resistance of the tested Mamaku tephras on their fines content or pumice content alone. In general, an increase in the fines content, *FC* meant lower liquefaction resistance, and an increase in pumice content, *PC* meant higher liquefaction resistance. The effect of the pumice content can, however, be correlated with the fines content. Namely, the fine particles in the Mamaku tephras are mainly glass shards, or broken-down pumice particles, so a higher fines content generally means lower pumice content. A correlation between the *FC* and *PC* of the three beds of Mamaku tephra at Lake Areare as well as the rest of the Mamaku tephras are presented in Fig. S4. The correlation proves that for the soil materials used in this study discussing a separate effect of the fines content and pumice content on the liquefaction resistance results would be redundant. In Fig. 6.6 the liquefaction resistance of the beds for the Mamaku tephra at Lake Areare, Ma-SM20, Ma-SM31, and Ma-ML70, at 100 kPa effective consolidation stress, is compared with that for some representative pumiceous and non-pumiceous sand-silt mixtures in published literature. The materials used for comparison and their geotechnical properties, as well as relative densities, *D*r, that they were tested under (all in the range of 0.4–0.7, mostly around 0.55), are given in Table 6.3.

By analysing the curves in Fig. 6.6, we observed that all three beds of the Mamaku tephra generally plot lower than the two pumiceous sands PAR (Licata et al. 2018) and Pumice sand A (Orense et al. 2012) and within the same range of liquefaction resistance as the 30% fines pumiceous Shirasu sand (Hyodo et al. 1998), hard-grained Toyoura sand (Yamamoto et al. 2009) and the pumiceous Tuhua silt (Chaneva et al. 2023). The higher liquefaction resistance of pumiceous sands (e.g. Pumice sand A) has been attributed to the vesicular nature as well as the complex surface texture of the pumiceous particles, which leads to significant particle crushing during cyclic loading, especially in samples with high relative densities (M. S. Asadi et al. 2018; Orense et al. 2012).

In contrast, for pumiceous silts, i.e., Tuhua silt, it was found that particle crushing does not occur, which is most probably the result of the cushioning effect: fines particles prevent the crushing of sandy pumiceous particles (Chaneva et al. 2023). Consequently, Tuhua silt was found to have liquefaction resistance plotting closer to the range of hard-grained soils rather than pumiceous sands.

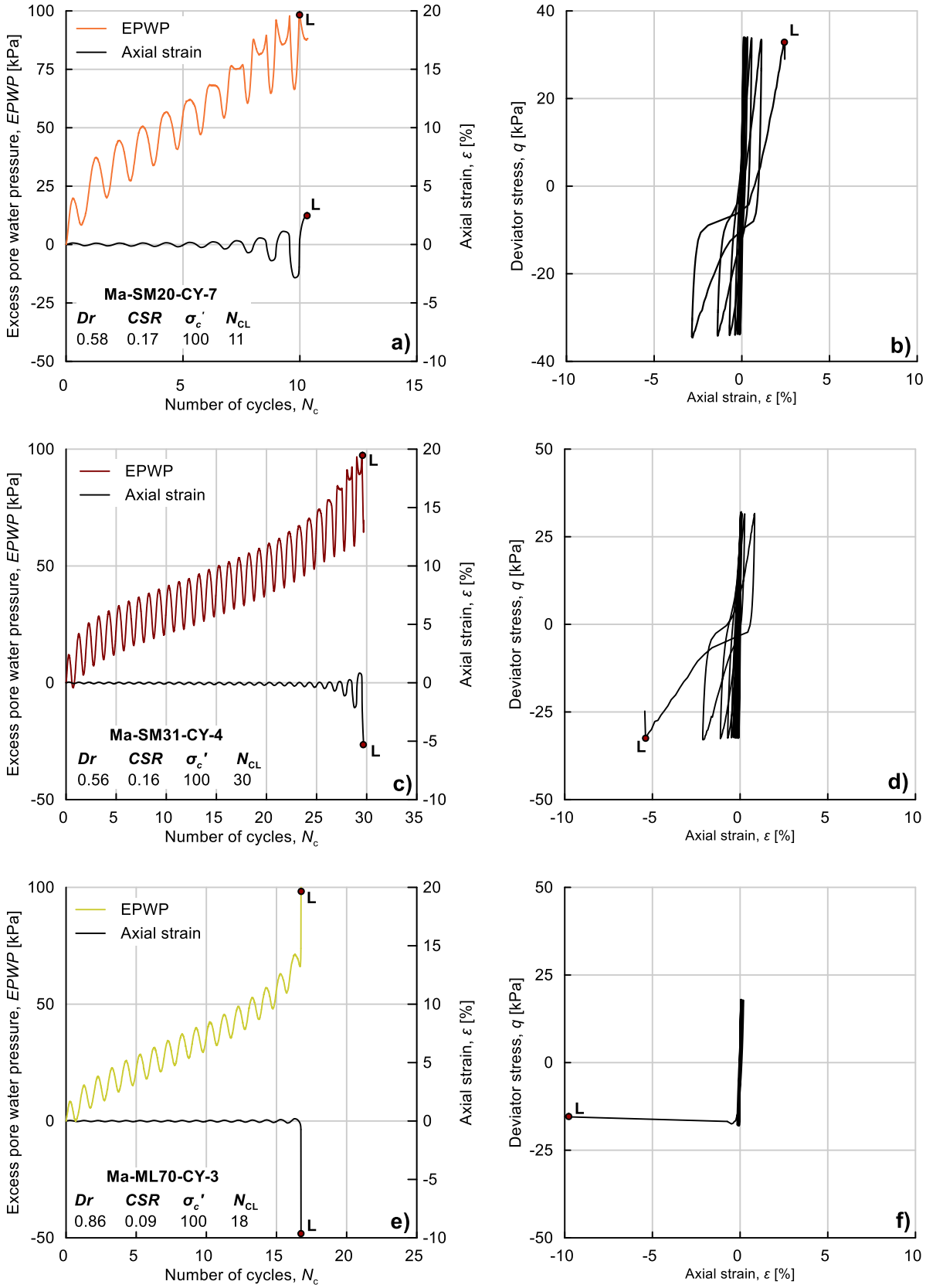


Fig. 6.4. Representative undrained cyclic responses by means of axial strain and excess pore water pressure development (a), (c), and (e), and deviator stress vs axial strain hysteresis (b), (d) and (f) graphs, for Ma-SM20 (a & b), Ma-SM31 (c & d) and Ma-ML70 (e & f)

In a previous study, we analysed the level of particle crushing of Ma-SM20, Ma-SM31, and Ma-ML70 (Chaneva et al. 2024) under undrained cyclic loading for medium-high and high relative densities. It was found that the silty Ma-ML70 showed no signs of particle crushing, whereas the sandy Ma-SM31 and, in particular, Ma-SM20, showed some changes in the grain size distribution and pumice content after testing. Yet, the extent of crushing did not dramatically affect the undrained cyclic behaviour, as, for example, found in the case of pumiceous sands (M. S. Asadi et al. 2018).

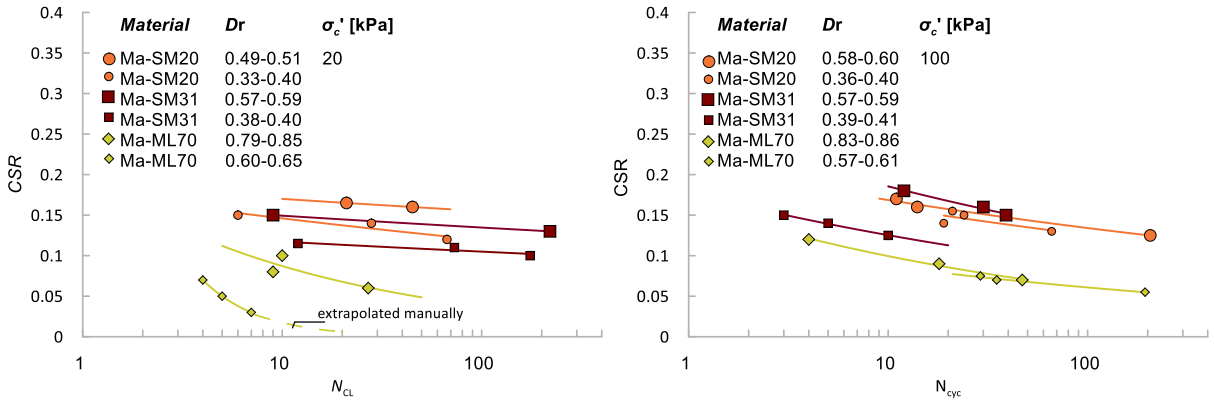


Fig. 6.5. Liquefaction resistance curves of Ma-SM20 (orange), Ma-SM31 (red), and Ma-ML70 (yellow), tested at two different relative densities and two effective consolidation pressures, 20 and 100 kPa.

Based on the liquefaction resistance curves presented in this study and the previously published data on the Mamaku materials from Lake Areare (Chaneva et al. 2024), it can be inferred that for the range of fines content between 20 and 70%, within the ranges of coarse silt to fine sand, this tephra material has liquefaction resistance values that reasonably fall into the range more typical for hard-grained soils as opposed to pumiceous soils. Therefore, typical empirical correlations based on hard-grained soils should be transferable to the Mamaku materials.

### 6.5.2. Proposed framework to extend the liquefaction resistance results to the Mamaku tephra materials across 13 lakes in the Hamilton lowlands

In order to extend the liquefaction resistance results from the tested beds of the Mamaku tephra into the in-situ lacustrine Mamaku tephras, several influencing factors were quantitatively addressed.

The influencing factors that were taken into consideration when extending the laboratory obtained liquefaction results onto the rest of the Mamaku tephras across the 13 lakes

are the: (1) in-situ density, (2) grain-size properties and (3) pumice content. Note that the effect of the grain-size properties was considered through a single grain-size parameter, i.e., the fines content (*FC*). Supplementary Fig. S5 shows a linear correlation exists between the *FC* and $D_{50}$, which suggests that a single grain-size parameter is sufficient to use in the analysis. Moreover, the mineralogical properties of Mamaku tephra are similar in all the lakes, (Lowe 1988) and the layers are all liquefiable, as they do not contain more than 5% clay sized particles (Chaneva et al. 2022), which furthermore supports the choice of a single geotechnical grain-size parameter to be used for the characterisation.

Table 6.3. Geotechnical properties of selected materials from literature

| Material | Soil Classification[1] | Specific gravity, *Gs* | Median grain size, $D_{50}$ [mm] | Fines content, *FC* [%] | Pumice content, *PC* [%] | Tested *Dr* | Testing apparatus | Reference |
|---|---|---|---|---|---|---|---|---|
| Toyoura sand | SP | 2.65 | 0.18 | 0 | 0 | ~0.5 | Triaxial | Yoshimine *et al.*, (2006) |
| Pumice sand A | SP | 1.95 | 1.15 | 2 | ~100 | ~0.7 | Triaxial | Orense, et al., (2012) |
| Shirasu Sand | SM | 2.49 | 0.15 | 30 | n/a | ~0.5 | Triaxial | Hyodo et al., (1998) |
| PAR | SM | 2.51 | 0.15 | 30 | n/a | ~0.4 | Triaxial | Licata et al., (2018) |
| Tuhua silt | ML w/S | 2.41 | 0.073 | 51.2 | 48 | ~0.5/0.7 | Triaxial | Chaneva *et al.*, (2023) |

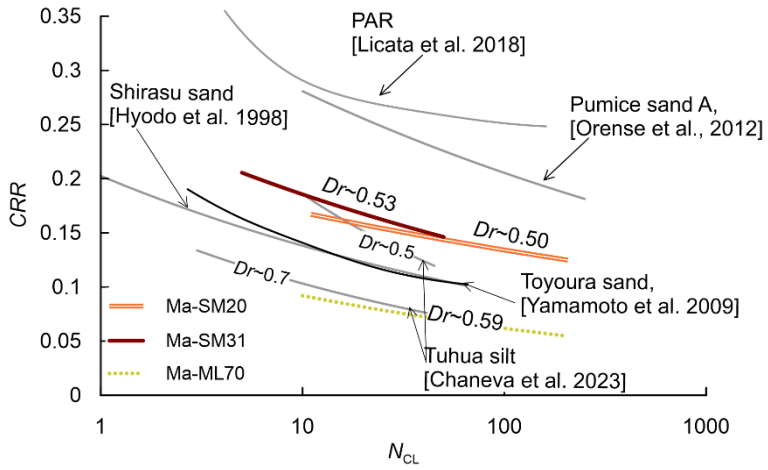


Fig. 6.6. Liquefaction resistance curves of Ma-SM20, Ma-SM31, and Ma-ML70 and relevant pumiceous and non-pumiceous sands ($\sigma'_c$ = 100 kPa). Note that the relative densities for the Mamaku are shown as the average values from the samples of the corresponding test series.

A flowchart showing the steps of the proposed framework is presented in Fig. 6.7.

The **first step** in this framework was to select the obtained $CRR_{7.5}$ values from the liquefaction curves for the samples tested at 20 kPa (Fig. 6.5a). Fig. 6.8a plots the $CRR_{7.5}$ values for each of the two tested densities for each of the three tested Mamaku beds. Namely, the orange circle data points correspond to the liquefaction resistance results and reconstituted densities of Ma-SM20 (e.g., the *CRR* that corresponds to 26 cycles to liquefaction, $N_{CL}$, from the Ma-SM20 liquefaction curves) for both densities, *D*r = 0.33–0.4 (~0.37) and *D*r = 0.58–0.6 (~0.59)). The red diamond data points and yellow triangle data points correspond to the $CRR_{7.5}$ values taken at 26 (for sands) and 18 cycles to liquefaction (for silts) (Verma et al. 2019) for Ma-SM31 and Ma-ML70, respectively.

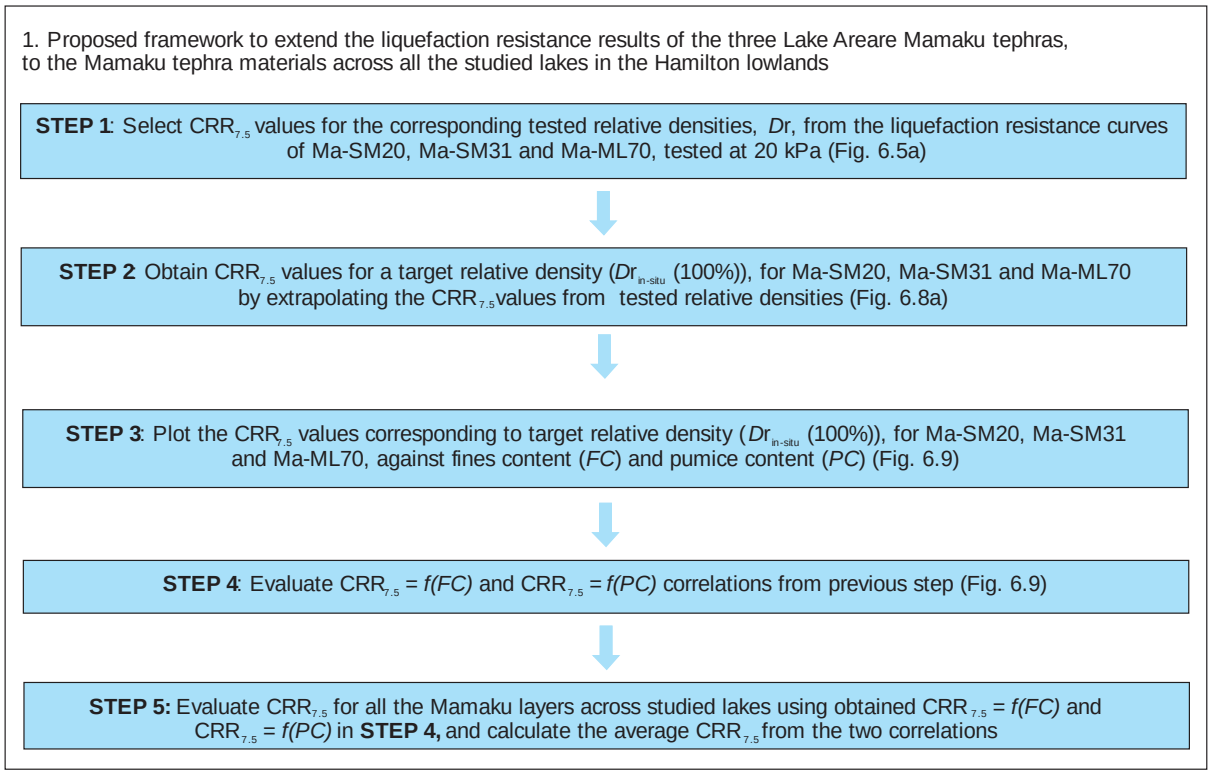


Fig. 6.7. Flowchart for the proposed framework to extend the liquefaction resistance results of the three beds of Mamaku tephra at Lake Areare to the resistance of the Mamaku tephra layer (in its entirety) in lake sediment cores across all 13 lakes in the Hamilton lowlands.

Considering the in-situ relative densities were all found to be around a value of 1, with the average in-situ density being *Dr* = 1.01 ± 0.06 (Table 6.1), the tested relative densities were considerably lower than the in-situ densities (Table 6.2). Relative densities of around 1 could not be achieved with light tamping in the sample reconstitution procedure. So, the range of the tested densities was used to extrapolate the values to the corresponding in-situ relative density, *Dr* = 1.01. Therefore, **step two**, was to obtain linear extrapolation equations, that correspond to the $CRR_{7.5}$ – Dr data points for Ma-SM20, Ma-SM31 and Ma-ML70, Fig. 6.8a. The linear

correlations (presented in the upper left corner in Fig. 6.8a) were then used to calculate the $CRR_{7.5}$ for a Dr = 1.01 for each of the three Lake Areare Mamaku tephras (cross symbol-data points).

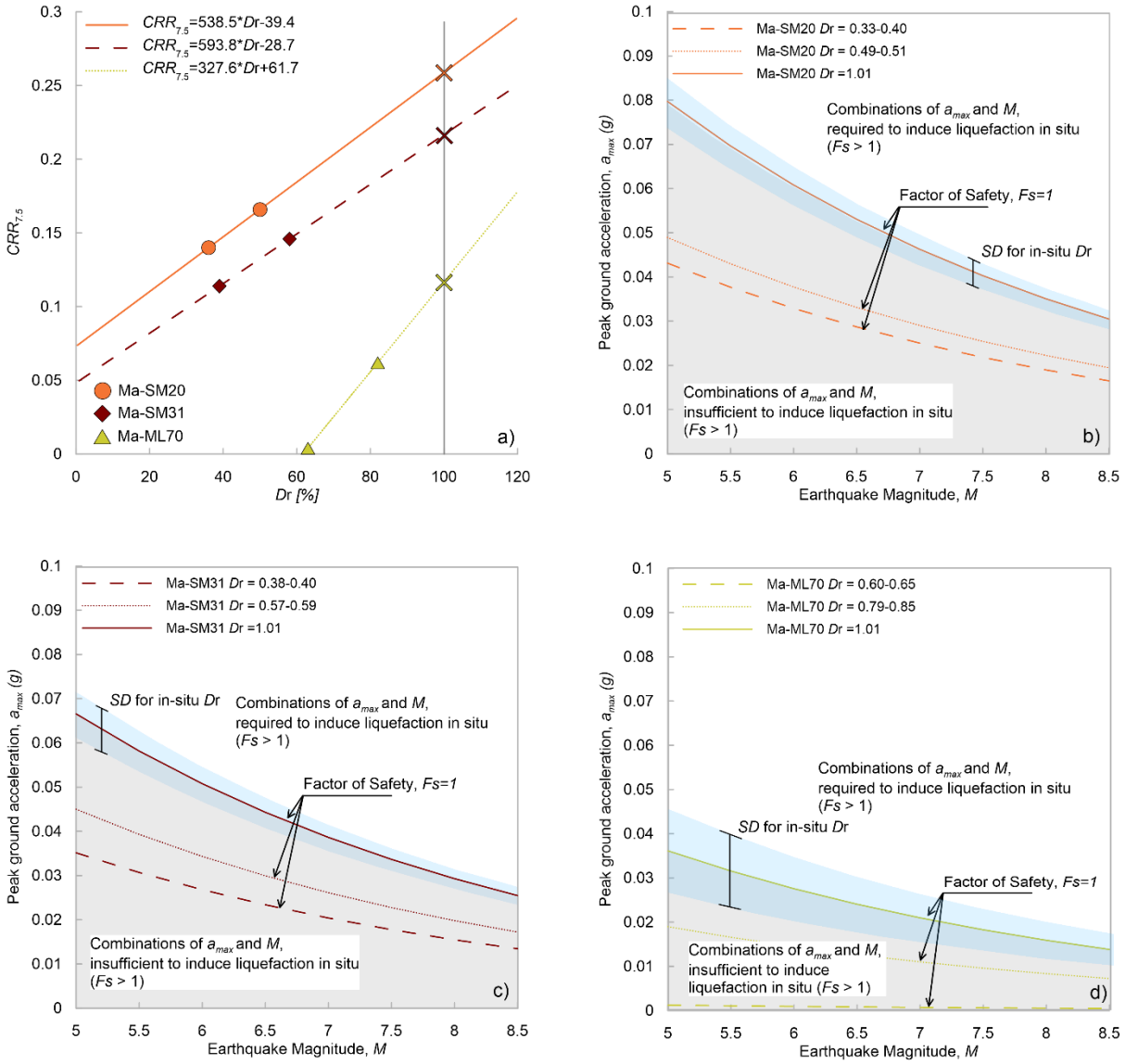


Fig. 6.8. (a) Extrapolated $CRR_{7.5}$ values from liquefaction curves (tested relative densities in the undrained cyclic triaxial campaign) to obtain the $CRR_{7.5}$ value for the tested relative density (in situ average relative density, $Dr_{in\text{-}situ}$ = 100%); $a_{max}$–$M$ combination curves for (b) Ma-SM20, (c) Ma-SM31 and (d) Ma-ML70, for three relative densities, dashed lines correspond to tested relative densities, and full lines correspond to the average in-situ relative densities for Mamaku tephra across the 13 lakes.

In the **third step**, the effect of the fines content, *FC*, and pumice content, *PC*, were taken into consideration, by plotting the $CRR_{7.5}$ vs *FC* and $CRR_{7.5}$ vs *PC* data points for the three beds of Mamaku tephra materials from Lake Areare. The plots were then used, in **step**

**four**, to obtain linear correlations where the cyclic resistance ratio can be described as a function of the fines content and pumice content, respectively (Figs. 6.9a and b).

Finally, **step five** consisted of calculating the $CRR_{7.5}$ for every Mamaku layer in the studied lakes. The average $CRR_{7.5,AV}$ from both $CRR_{7.5,FC}$ and $CRR_{7.5,PC}$ was then calculated for every Mamaku layer across the lakes. The $CRR_{7.5,FC}$, $CRR_{7.5,PC}$ and $CRR_{7.5,AV}$ values for all the Mamaku tephras across the lakes are presented in Table 6.5.

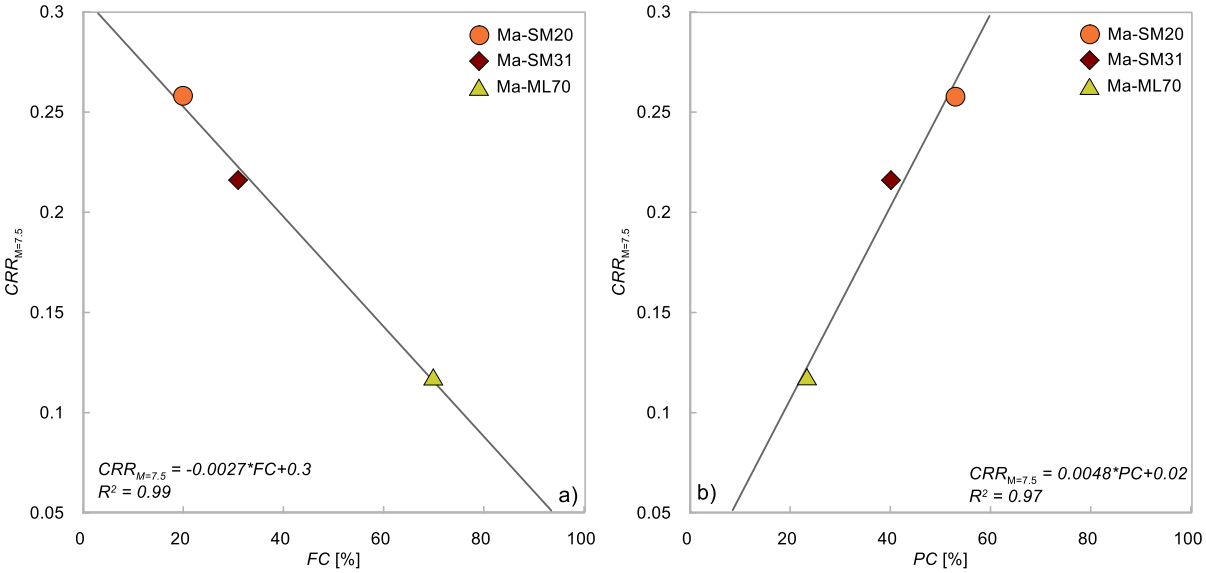


Fig. 6.9. $CRR_{7.5}$ vs FC and $CRR_{7.5}$ vs PC plots for the three beds of Mamaku tephra at Lake Areare showing fitted linear correlations (Table 6.4)

Table 6.4. $CRR_{7.5}$ values for the three beds of Mamaku tephra at Lake Areare

| Material | $Dr_{av,\ triaxial}$ [%] | $CRR_{7.5,triax}$ | $Dr_{av,\ in\text{-}situ}$ [%] | $CRR_{7.5,extrapolated}$ | $\sigma_v$ [kPa] | $\sigma'_v$ [kPa] | $r_d$ |
|---|---|---|---|---|---|---|---|
| Ma-SM20 (uppermost bed) | 36<br>50 | 0.140<br>0.166 | 100 | 0.259 | | | |
| Ma-SM31 (middle bed) | 39<br>58 | 0.114<br>0.146 | 100 | 0.216 | 24.81 | 2.45 | 0.99 |
| Ma-ML70 (lowermost bed) | 63<br>85 | 0.004<br>0.062 | 100 | 0.117 | | | |

### 6.5.3. Challenges and limitations of the proposed framework and implications on the results

This section discusses the challenges and limitations of the presented study in regard to the simplifications made in the calculations of the relative densities of the Mamaku tephras as well as the transferring of laboratory liquefaction resistance into field liquefaction resistance that was not able to be quantified.

Because of the limitations with not having enough volume of soil for all the Mamaku tephras in the studied lakes, in the relative density calculations of the in-situ Mamaku tephras, two simplifications were made: (1) The particle density of the tephras was taken to be the average particle density from Mamaku tephras from the lakes Areare, Hamilton lake, Rotokauri, Forest lake and Kainui lake, and (2) the average minimum and maximum void ratios for the Mamaku tephras sampled on-shore of Lake Areare, were taken for all the other Mamaku tephras across all the lakes. In this context, considering the conclusions in regard to the particle density of the Mamaku tephras from Chaneva et al. 2022 (i.e. all being close to 2.4 g/cm$^3$), we have a certain confidence in using the average particle density for all the Mamaku tephras. The use of average minimum and maximum dry density calculated from three Mamaku tephras across all 13 lakes, is a simplification that needs to be listed as a possible limitation that could impact the final results.

The use of liquefaction resistance obtained through undrained cyclic triaxial testing to study thin in-situ soil layers is not straightforward, and it demands a qualitative discussion of the influencing factors that were not able to be quantified in the framework.

The first important factor that was not quantified in the calculations was the ratio between the in-situ liquefaction resistance, $CRR_{\text{field}}$ and the laboratory liquefaction resistance, $CRR_{\text{TX.}}$ (Seed 1979b):

$$CRR_{field} = 0.9 * \left(\frac{1+2Ko_{field}}{3}\right) * CRR_{TX} \quad (6.7)$$

where *K*o is the coefficient of earth pressure at rest. Eq. 6.7 takes into account the type of soil material, through the Ko parameter, and the direction of cyclic loading, which is different in-situ compared with the loading in a triaxial test setting, i.e. uni-directional. Obtaining the *K*o coefficient is not trivial, and it depends on the materials, in particular, the peak friction angle of the Mamaku tephra layer. Monotonic undrained tests for the Mamaku tephra layers were not considered in this study, and so *K*o could not be evaluated. However, if we consider that *K*o normally varies between 0.31–0.67 for normally consolidated sand-silt mixtures (Mesri and Hayat 1993), then Eq. 6.7 would translate into:

$$CRR_{field} = (0.48 - 0.72) \times CRR_{TX} \quad (6.8)$$

The above ratio indicates that the *CRR* values in situ are expected to be considerably lower, i.e., by 28–52%, than the triaxial *CRR* values obtained in this study. The decrease in the

*CRR* values would translate into the trigger $a_{max}$, resulting in lower trigger peak ground accelerations to induce liquefaction.

A second influencing factor that was not quantified was the choice of sample preparation method. The reasoning behind the chosen moist tamping method for the triaxial campaign is given in Section 3.3. For hard-grained soils, it is commonly known that high-quality undisturbed testing most closely represents the liquefaction resistance of the soil in-situ (Ishihara 1997). Recent studies on sandy silts from Christchurch noticed that moist-tamped reconstituted samples exhibit similar overall liquefaction strength as high-quality undisturbed gel-pushed samples (Taylor et al. 2013). Published research about high-quality undisturbed pumiceous samples is relatively scarce (Asadi et al. 2015; de Cristofaro et al. 2022; Orense et al. 2020; Stringer 2022; Suzuki and Yamamoto 2004). Moreover, studies that compare undrained cyclic behaviour and liquefaction resistance between undisturbed and reconstituted pumiceous samples is even more limited. Suzuki and Yamamoto (2004) found that the liquefaction resistance of undisturbed pumiceous samples of Shirasu sand is higher than of that of equivalent air-pluviated ones, independently of the initial effective confining stress. Considering the gaps in literature, and the grain-size and pumice content variability of the Mamaku tephras (Table 6.1), the potential over- or underestimation of the liquefaction resistance in the presented study is hard to be speculated without further research.

Table 6.5. CRR7.5 values for Mamaku tephra (in toto) across the lakes

| Material | Depth in lakebed [m] | $\sigma_v$ [kPa] | $\sigma'_v$ [kPa] | $r_d$ | *FC* [%] | *PC* [%] | $CRR_{7.5,FC}$ | $CRR_{7.5,PC}$ | $CRR_{7.5,AV}$ | $a_{max}$, $M$ = 5 (g) | $a_{max}$, $M$ = 7.5 (g) |
|---|---|---|---|---|---|---|---|---|---|---|---|
| Ma-FL | 2 | 21.58 | 1.96 | 0.99 | 66.6 | 29.1 | 0.098 | 0.160 | 0.129 | 0.039 | 0.020 |
| Ma-HL | 2.1 | 22.66 | 2.06 | 0.99 | 45 | 42.9 | 0.179 | 0.226 | 0.202 | 0.062 | 0.031 |
| Ma-KT | 2.1 | 22.66 | 2.06 | 0.99 | 28.1 | 52.4 | 0.224 | 0.272 | 0.248 | 0.076 | 0.038 |
| Ma-WT | 1.8 | 19.42 | 1.76 | 0.99 | 21.5 | 51.4 | 0.242 | 0.267 | 0.254 | 0.077 | 0.039 |
| Ma-KM | 5.3 | 57.19 | 5.19 | 0.96 | 52.3 | 37.7 | 0.159 | 0.201 | 0.180 | 0.060 | 0.029 |
| Ma-MH | 1.9 | 20.50 | 1.86 | 0.99 | 32.1 | 37.4 | 0.213 | 0.200 | 0.207 | 0.063 | 0.032 |
| Ma-NI | 2.4 | 25.89 | 2.35 | 0.99 | 55.8 | 40.8 | 0.149 | 0.216 | 0.183 | 0.056 | 0.028 |
| Ma-MK | 1.3 | 14.03 | 1.27 | 1.00 | 48.8 | 43 | 0.168 | 0.226 | 0.197 | 0.059 | 0.030 |
| Ma-KN | 1.2 | 12.95 | 1.18 | 1.00 | 18.4 | 56.4 | 0.250 | 0.291 | 0.270 | 0.081 | 0.042 |
| Ma-RI | 1.8 | 19.42 | 1.76 | 0.99 | 55.9 | 35.2 | 0.149 | 0.189 | 0.169 | 0.051 | 0.026 |
| Ma-PP | 2 | 21.58 | 1.96 | 0.99 | 19.7 | 54.1 | 0.247 | 0.280 | 0.263 | 0.080 | 0.041 |
| Ma-CA | 1.4 | 15.11 | 1.37 | 1.00 | 41.5 | 44 | 0.188 | 0.231 | 0.210 | 0.063 | 0.032 |
| Ma-RT | 0.8 | 19.42 | 1.76 | 0.99 | 51.5 | 40.1 | 0.161 | 0.212 | 0.186 | 0.056 | 0.029 |

The third influencing factor was the effective consolidation stress. Namely, in the triaxial setting, the samples were tested at a 20 kPa effective consolidation stress (isotropic conditions). In-situ, the stress conditions were somewhat different, with the in-situ vertical

effective consolidation (overburden) stresses being even lower at 1.2–5.2 kPa (Table 6.5), because of the low depths in the lakebed as well as the low density of the organic lake sediments. Cyclic undrained triaxial tests at 1–5 kPa could not be performed, so the test results from the 20 kPa consolidation stress were used without correcting the effect of the consolidation stress. Furthermore, the overburden correction factor $K_\sigma$ (Boulanger and Idriss 2014), was omitted in the calculations of $a_{max}$ in the present study. The reason for not taking $K_\sigma$ into consideration is the fact that this study used consolidation stresses of 20 kPa and 100 kPa and noticed that the *CRR* increased with consolidation stress, which contradicts the commonly accepted behaviour of soil to decrease in *CRR* with consolidation stress (e.g., Vaid & Sivathayalan's study (1996) (see supplementary Figure S6). Qualitatively, not considering the $K_\sigma$ factor overestimates the liquefaction resistance of the tephras.

Finally, the effect of ageing of soils in the in-situ environment is also known to affect their in-situ liquefaction resistance (Towhata et al. 2016). The ageing effect is mostly attributed to weathering and/or cementation processes that occur in soils over time. No signs of weathering were observed in the tephras we studied, which have been preserved in the lakes by permanent reducing (anaerobic) conditions together with a lack of oxidising micro-organisms such as aerobic bacteria. Considering the low confining pressures as well as their lakebed in-situ conditions, we infer that the ageing effects would be minimal and would not be further discussed in a qualitative manner.

In summary, qualitatively speaking, it is reasonable to conclude that the liquefaction resistances i.e. CRRs of the Mamaku tephras, would be lower in-situ than the ones estimated from the undrained cyclic triaxial testing presented in this study.

### 6.5.4. *M* and $a_{max}$ combination curves for the three beds of Mamaku tephra from Lake Areare

The equivalent magnitude and peak ground acceleration values needed to trigger liquefaction were first obtained for the three beds of Mamaku tephra materials from Lake Areare that were subjected to undrained cyclic loading in the triaxial tests. The $CRR_{7.5}$ for the tested densities, as well as the extrapolated target density (Fig. 6.8a) were used to calculate the magnitude, *M* and peak ground acceleration, $a_{max}$, combinations for the Lake Areare Mamaku materials using Eq. 6.6 (Section 6.4.4). The values for input parameters for Eq. 6.6. the in-situ total and effective consolidation stresses the $\sigma_v$ and $\sigma'_v$ as well as the stress reduction coefficient $r_d$, for

the three beds of the tested Mamaku tephra are given in Table 6.4. $a_{max}$ was calculated across magnitude values within the range 5 to 8.5.

The $M$ and $a_{max}$ results for Ma-SM20, Ma-SM31 and Ma-ML70, are presented in Figs. 6.8b, 6.8c and 6.8d respectively. The dashed curves in the figures correspond to the tested densities, whereas the solid line curves show the results for the average relative density, $Dr_{av,in\text{-}situ}$ = 1.01. The standard deviation corresponds to the range of in-situ relative densities for the Mamaku tephra layers (in sediment cores) across the lakes (Table 6.1.). The grey areas in the figures below the full lines show the area of $M$ and $a_{max}$ combinations that are insufficient to cause liquefaction in situ for the Ma-SM20, Ma-SM31, and Ma-ML70 tephras at Lake Areare, whereas all the values above the full lines show the area of $M$ and $a_{max}$ combinations that are required to cause liquefaction.

In general, for the coarsest Mamaku tephra Ma-SM20, with the highest liquefaction resistance, the required $a_{max}$ across the magnitudes has the highest values, whereas the finest Ma-ML70, with the lowest liquefaction resistance requires noticeably lower peak ground accelerations to liquefy.

### 6.5.5. $M$ and $a_{max}$ combination curves for Mamaku tephra layers across 13 studied lakes

The $a_{max} - M$ combination curves for the Mamaku tephra layers in the other 13 lakes are plotted in Fig. 6.10. Fig. 6.10a shows the $a_{max} - M$ combination curves for all Mamaku tephra layers in the lakes where SSDSs were not observed (thin, light blue lines) as well as the average $a_{max} - M$ combination curve (dark blue line). Fig. 6.10b shows the $a_{max} - M$ combination curves for all the Mamaku layers in the lakes where SSDSs were observed (thin, light red lines) as well as the average $a_{max} - M$ combination curve (dark red line). The average curves for the Mamaku tephra layers in lakes with SSDSs (dark red) and the Mamaku tephra layers in lakes with no SSDS (dark blue) are plotted together and shown in Fig. 6.10c. The input parameters for $a_{max}$ (Eq. 6.6) – in-situ total and effective consolidation stresses the $\sigma_v$ and $\sigma'_v$ as well as the stress reduction coefficient $r_d$, for all the Mamaku tephra layers across the 13 lakes are given in Table 6.5. As for the tested Mamaku tephras from Lake Areare, $a_{max}$ was calculated across magnitude values within the range 5 to 8.5 for all the other Mamaku tephra layers too.

The peak ground acceleration values, $a_{max}$, needed to liquefy the tephras for lakes both with and without SSDSs along the full spectrum of magnitudes, from M = 5 to M = 8.5, fall

within a relatively small range of relatively low values, from ~ 0.02g to 0.08g. By comparing the average $a_{max} - M$ combination curves for the lakes with and without SSDSs (Fig. 6.10c), it can be noticed that the values of peak ground accelerations needed for liquefaction to be induced are very close and within the range of 0.023g for a magnitude of 8.5 and 0.061 for a magnitude of 5.

Considering that the threshold peak ground acceleration needed to trigger liquefaction, based on a statistical analysis of case studies, including a range of magnitudes between 5.9 and 8+, is considered to be 0.09 g (De Magistris et al. 2013), the results for the Mamaku tephra layers presented in this study are lower than the commonly considered peak ground acceleration threshold. It is important to note that paleoliquefaction case studies in shallow tephra layers (average depth for Mamaku tephra is ~ 2 m below lake bed) in lake environments are not typical and are not included in the statistical calculations behind the estimation of the threshold peak ground acceleration needed to trigger liquefaction. The liquefaction resistance of the tephras, expressed through *CRR*, as presented in Section 6.5.1., was within the common liquefaction resistance range for other sandy and silty materials found in literature. Yet, as discussed in Section 6.5.3, the in-situ liquefaction resistance is expected to be somewhat lower. Therefore, the estimated low peak ground accelerations are considered to be a result of relatively low liquefaction resistance of the Mamaku tephras as well as their shallow depth, i.e. low effective overburden stresses (Table 6.5) across the lakes.

A spatial presentation of the $a_{max} - M$ results, in relation to the SSDS occurrence, is shown through a single earthquake scenario in Fig. 6.11. That is, Fig. 6.11 shows the $a_{max}$ values needed for the Mamaku tephra layers in the 13 lakes to liquefy for an $M = 5$, ranging from 0.039 g for Lake Rotokaeo/Forest Lake (yellow) to 0.081 g for Lake Kainui (dark red/brown). The lakes marked with black circles are those where SSDSs were present in the corresponding Mamaku tephra layer. Similarly, the lakes marked with white circles are those where SSDSs were not found in the Mamaku tephra layer. The $a_{max}$ (g) values for magnitudes $M = 5$ as well as $M = 7.5$ are given in Table 6.5.

Considering that the focus of the presented study is the framework that analyses paleoliquefaction features in Mamaku tephra across the lowlands based on undrained cyclic triaxial test results of three beds of Mamaku tephra, and does not include regional attenuation evaluations of the credible $a_{max} - M$ combinations for the area, the following paragraphs discuss the obtained $a_{max}$ (g) between the lakes in relation to the SSDS occurrences alone. The $a_{max}$ (g)

values are briefly discussed in the context of the current seismic hazard in the Hamilton lowlands, in the addendum of this chapter. Other factors, such as possible earthquake sources, basin effect, directivity etc. are acknowledged but not included in the discussion.

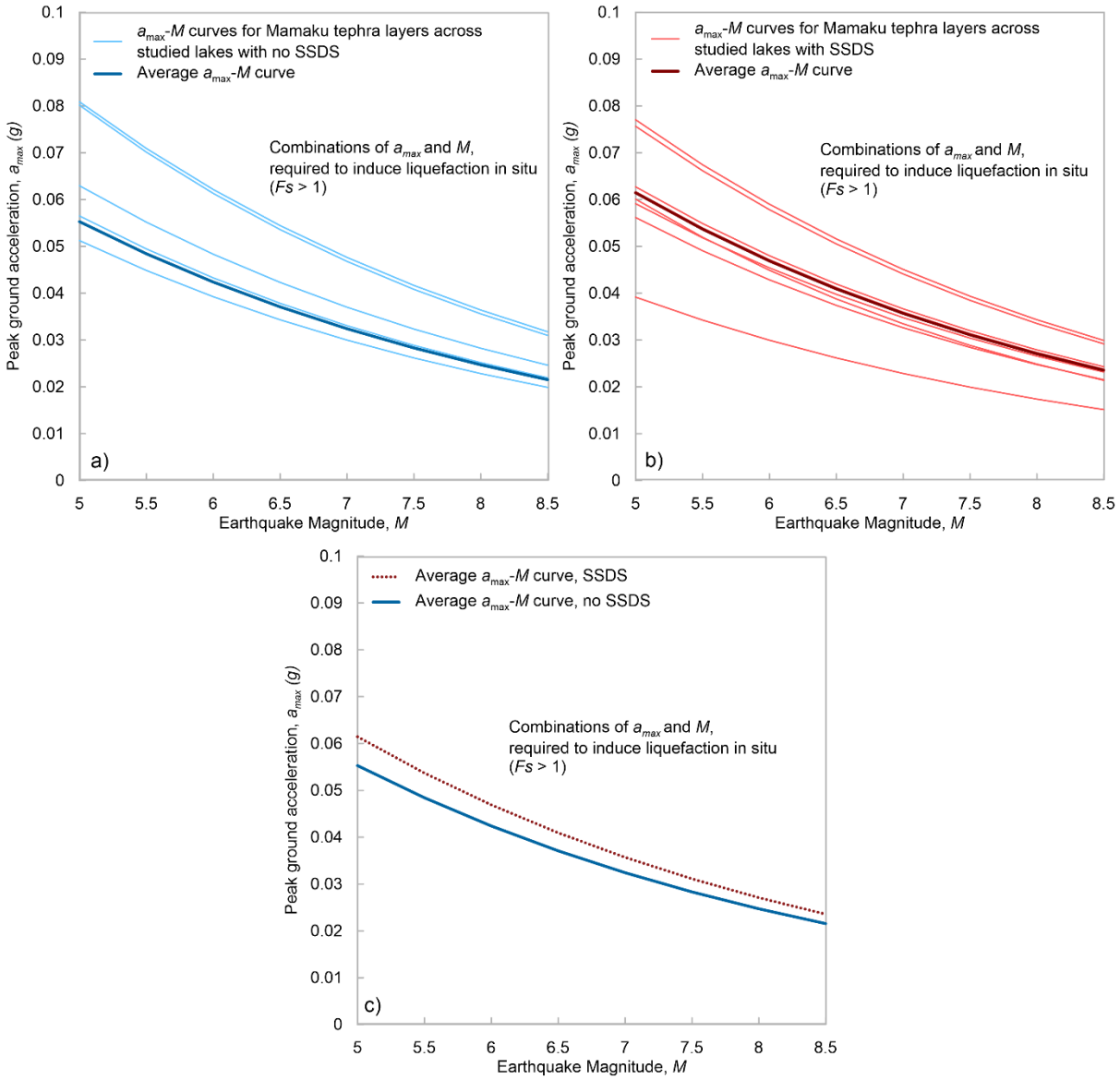


Fig. 6.10. $a_{max}$–$M$ combination curves for the Mamaku tephra layer across the 13 lakes that show (a) no SSDSs, (b) with SSDSs, and (c) with the corresponding average curves shown in separate graphs

By observing the triggering $a_{max}$ (g) values and the SSDS occurrence in the lakes in Fig. 6, there does not seem to be a clear and concise trend by means of shaking intensity and liquefaction occurrence. In other words, SSDSs have been identified in both lakes with lower triggering peak ground accelerations, such as Lake Rotokaeo/Forest Lake, FL ($a_{max}$ = 0.049g) as well as lakes that require higher liquefaction inducing peak ground accelerations, such as Lake Kainui, KN ($a_{max}$ = 0.081g). Similarly, SSDS seem to be missing in lakes within the full

range of liquefaction inducing peak ground accelerations as well, e.g. SSDS have not been identified neither in Lake Rotokauri, RI ($a_{max}$ = 0.051g) nor in Lake Pikopiko, PP ($a_{max}$ = 0.080g).

Considering the peak ground accelerations vary within the order of 0.01g, which is noticeably low, possible explanations such as, proximity of the lakes to the earthquake source faults, basin effects and directivity, seem to be less likely. Additionally, if we consider that the trigger peak ground accelerations that correspond to larger magnitudes, i.e. 6 and above, are even lower than the documented threshold peak ground acceleration needed to trigger liquefaction, ~0.0.9g (De Magistris et al. 2013), it would have been expected that all Mamaku tephra layers around the study area had SSDSs.

A likely explanation could be related to the small number of cores per lake that were sampled. That is, considering the small diameter of the cores (~60 to 85 mm) and the surface area of the lakes (up to 55 ha (Lowe and Green 2024)), and the fact that for most of the lakes, only two to three cores were sampled (with the exception of Hamilton Lake), it is possible that the presence of SSDSs was not identified in some of the lakes, and all the Mamaku tephras across the studied area have liquefied in the past. This explanation would imply that the tephras in the lakes are extremely vulnerable to even small levels of earthquake shaking and identifying large pre-historic earthquakes (magnitudes 6 and above) based on the geotechnical paleoliquefaction approach alone would be difficult. A study that analyses the frequency of SSDSs occurrence, length of dykes etc. (Kluger et al. unpublished data), is needed to complement the geotechnical approach in order to draw more precise conclusions about the implications of the discovered SSDSs for the local seismic hazard.

This research suggests the potential benefit to paleoliquefaction investigations of similar shallow deposits, very sensitive to liquefaction at low ground shaking in order to estimate past small magnitude earthquakes, e.g. $M \leq 5$, which are commonly not studied. Considering paleoseismic evidence of smaller earthquake events ($M \leq 5$) are not likely to be preserved in the sedimentary records, studying deposits that are very sensitive to liquefaction at low ground shaking, could potentially help identify those small events (Pillar Villamor, personal communication November 2023). Earthquakes with magnitudes of 5 and smaller, may not be as destructive as larger ones, but knowledge about the frequency of their occurrence, assists in determining the overall seismic hazard of an area of interest, as even smaller earthquakes can cause community concerns through damage, economic impact and stress.

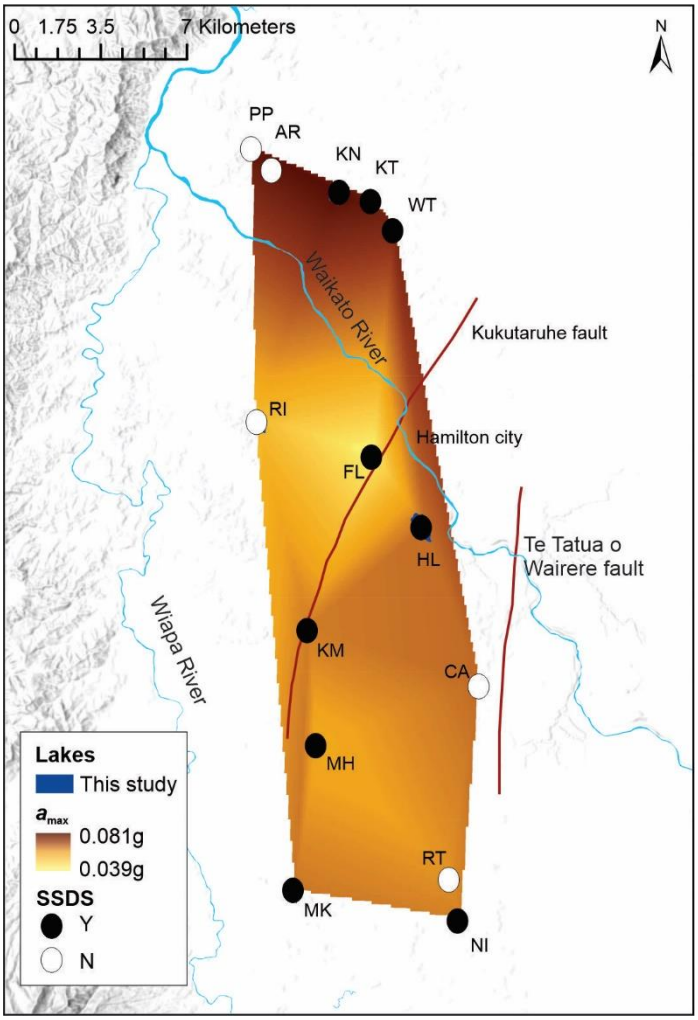


Fig. 6.11. $a_{max}$ values needed for the Mamaku tephra layer (in 13 lakes) to liquefy. Black circles mark the lakes with SSDS, and white circles mark lakes with no SSDS

## 6.6. Conclusions

In this study, three distinct beds (with different grain size distributions and pumice content) making up a natural ~8000-cal-year-old lacustrine tephra (volcanic ash) fall deposit, Mamaku tephra, were sampled from Lake Areare in the Hamilton lowlands, northern North Island. The beds were reconstituted and subjected to cyclic undrained triaxial tests performed at two different relative densities (medium to dense) and two different effective consolidation stresses (20 and 100 kPa), in order to obtain the liquefaction resistance curves for the materials in each bed. The liquefaction resistance obtained from the laboratory triaxial tests was used to estimate peak ground acceleration and magnitude ($a_{max} - M$) combination curves for the entire Mamaku tephra layer preserved in sediment cores from 13 lakes in the lowlands. Our conclusions can be summarised as follows:

- The liquefaction resistance curves of the tested material were in accordance with the established trends by means of relative density, i.e., higher density, resulting in higher resistance. Compared to that of both hard-grained soils and pumice sands, the liquefaction resistance of the three beds of the Mamaku tephra materals from Lake Areare was closer to the established trends typical for hard-grained soils and pumiceous non-crushable silts than to those for crushable pumiceous sands.
- The Mamaku tephra layers in cores taken from 13 lakes were found to be sensitive and vulnerable to liquefaction at very low peak ground accelerations, i.e. a range of 0.02–0.08 g through the range of magnitudes, $M$ = 5 – 8.5. The high vulnerability to liquefaction across all the Mamaku layers in the Hamilton lowlands was considered to be the result of the very low in-situ overburden stresses as well as the relatively low liquefaction resistance.
- Considering the low estimated values of $a_{max}$ across the study area, as well as the small difference between the $a_{max}$ thresholds in the layers that show SSDSs vs layers with no SSDSs across the lakes i.e., in the order of 0.01 g. we infer that it is most likely that SSDSs were missed as a result of small number of sampled cores in some of the lakes, and all the Mamaku tephras across the studied have liquefied in the past.
- The high vulnerability to very small levels of earthquake shaking makes speculating and/or identifying large pre-historic earthquakes (magnitudes 6 and above) based on the geotechnical paleoliquefaction approach rather difficult. Complementary geologically based paleoliquefaction analyses are needed for more conclusive results.
- The potential advantage of paleoliquefaction studies that investigate similar shallow, very sensitive to liquefaction at low ground shaking level layers to estimate past small magnitude earthquakes, e.g. $M \leq 5$ was discovered.

## Authorship contribution statement

**Jordanka Chaneva:** Investigation, Conceptualization, Methodology, Data curation, Writing – original draft. **Max O. Kluger:** Conceptualization, Methodology, Supervision, Writing - review and editing, Funding acquisition. **Tehnuka Ilanko:** Methodology, Writing - review and editing, **Vicki G. Moon:** Methodology, Supervision, Writing - review and editing, Funding acquisition. **David J. Lowe:** Supervision, Funding acquisition, Writing - review and editing. **Rolando P. Orense:** Supervision, Writing - review and editing, Funding acquisition.

## Acknowledgements

We acknowledge funding support from agencies of the New Zealand Government as follows: the MBIE Endeavour Fund (Smart Ideas) contract UOWX1903; the Marsden Fund contract UOW1902; the New Zealand Centre for Earthquake Resilience (QuakeCoRE); the Earthquake Commission Toka Tū Ake EQC (contracts 15/U713 and BIG 012 2020); and Waikato Regional Council (support for project on paleoseismicity and liquefaction). We also acknowledge a University of Waikato 2016 SIF grant. Richard Melchert, Tom Robertson, Ben Roche, Helen Turner, and Vittoria Gibbons are thanked for help in the field and/or lab. Mrs Hekeiterangi Broadhurst (Kuia Kaumatua) and Wiremu Puke (Ngāti Wairere, Ngāti Porou), of Ngāti Wairere (Hukanui Marae), Hazel Coromandel-Wander (Apakura, Wairoto Papakainga) and other members of Ngā Iwi Tōpū O Waipā, the Department of Conservation, and staff from Hamilton City Council and Waikato and Waipā district councils, are thanked for facilitating access to the lakes cored and sampled in the study.

## Addendum

This addendum discusses two points raised at the oral examination of this thesis related to the (1) methodology and (2) results presented in this chapter.

Firstly, the use of a $F_{SL} = 1$ in the calculation of the triggering $a_{max}$ – M combination values will be critically discussed. The deterministic liquefaction triggering approach in engineering practice, uses a $F_{SL} = 1$, which statistically corresponds to a probability of liquefaction, $PL = 15\%$ (Boulanger and Idriss, 2014). As this study analysed already (paleo) *liquefied* layers of tephra, taking a higher probability of liquefaction, thus lower factor of safety than 1, seems to be a reasonable approach. Published geotechnical approaches for studying paleo liquefaction features have not explored this in sufficient detail to date, therefore only a qualitative discussion and the potential implications to the results will be provided here. Exploring different (and higher than 15%) probabilities of liquefaction (thus lower $F_{SL}$) could provide more insight regarding the explanation as to why some tephras liquefied and others didn't. For example, all of the northern lakes (five in total) in this study (Fig. 11), show similar levels of liquefaction resistance, yet only 3 of them show SSDS (KN, KT and WT). In other words, 66% of the Mamaku tephras in the northern lakes with a similar CRR (~0.25) liquefied. So, the answer might be close to considering a probability of liquefaction of 66% (which corresponds to a $F_{SL} \sim 0.8$). Moreover, considering lower than one factor of safety, will result in higher

triggering $a_{max}$ – M combinations, which would be a more conservative approach. The scope of this thesis did not include a detailed analysis of how to select an appropriate $F_{SL}$ for the back analysis of peak ground acceleration values, but raises the potential for future research in the area as well as the impact it would have on the final results.

The second point of discussion in this addendum will be focused on including some information about the recorded earthquake history in the Hamilton lowlands in the last 120 years, and how that compares to the results from this study, considering the known active faults in the area. Currently there is only one strong motion sensor in Hamilton City (Fig. A1); this sensor was installed in 2014. Two sensors with slightly longer records are installed in the neighbouring Hauraki Basin within approximately 50 km of Hamilton (Fig. A1). Based on the recorded data during the period of 1900 - 2024 collected by GeoNet Geological hazard information for New Zealand, there are only 3 earthquakes with magnitude larger than 5 located within 50 km of Hamilton City (Table A1). All three earthquakes are relatively shallow with depths ranging from 7 to 25 km, and originate from faults outside of the Hamilton lowlands. Information about the ground motion recorded in Hamilton is only available for one of those earthquakes (01-04-2023).

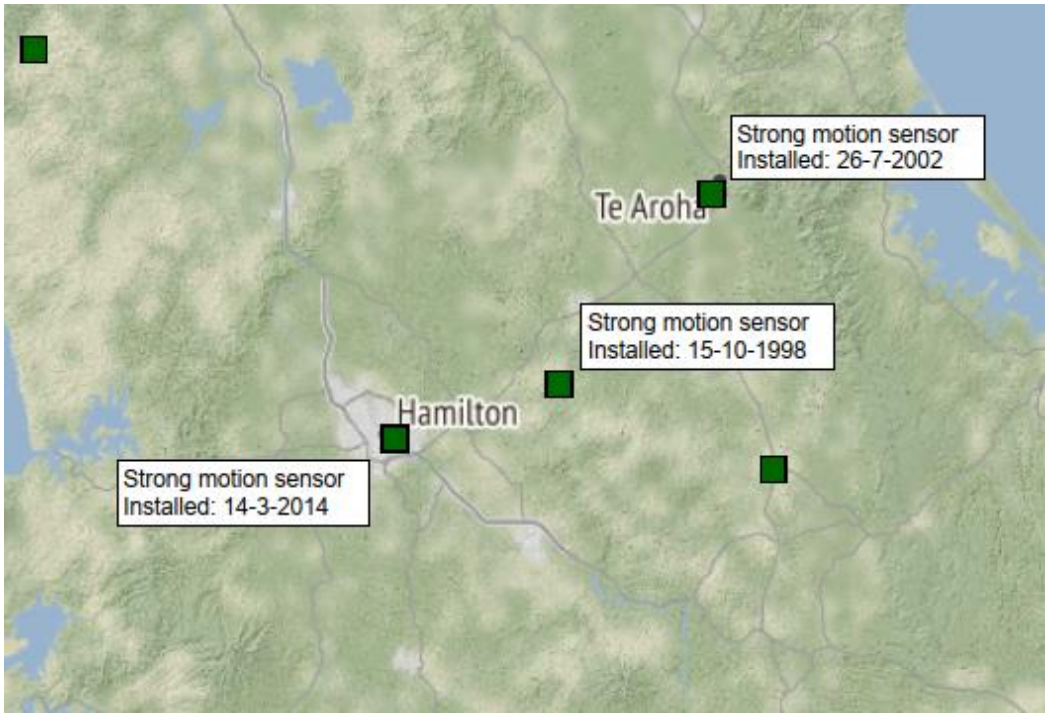


Fig. A1. Currently installed and running strong motion sensors in Hamilton and close to Hamilton city

Table A1. List of recorded earthquakes, with a $M$ >5 in the last ~100 years in the Hamilton Lowlands

| Date of earthquake | Epicenter distance from Hamilton city | Earthquake magnitude | PGA range in Hamilton lowlands |
|---|---|---|---|
| 26-05-1912 | ~50 km | 5.7 | Uknown |
| 11-07-1927 | ~50 km | 5.5 | Uknown |
| 01-04-2023 | ~50 km | 5.1 | 0.01 to 0.02 g |

This chapter analyzed the Mamaku tephra deposited in the lake sediments around 8000 cal. yr BP. The estimated average needed peak ground accelerations to trigger liquefaction in the Mamaku tephra across the studied lakes for the range of magnitudes 5 to 6 (considering a $F_{SL}$ = 1) is between 0.045g to 0.06g (Fig. 6.10). During the 5.1 earthquake in 2023, with an epicentre in the Hauraki Basins, the recorded peak ground acceleration in the Hamilton strong motion centre (Fig. A2) was 0.011. The range of peak ground accelerations in the lowlands was between 0.01 to 0.02g, which is lower than the estimated (minimum i.e. $F_{SL}$ = 1) liquefaction triggering peak ground accelerations for the Mamaku tephra.

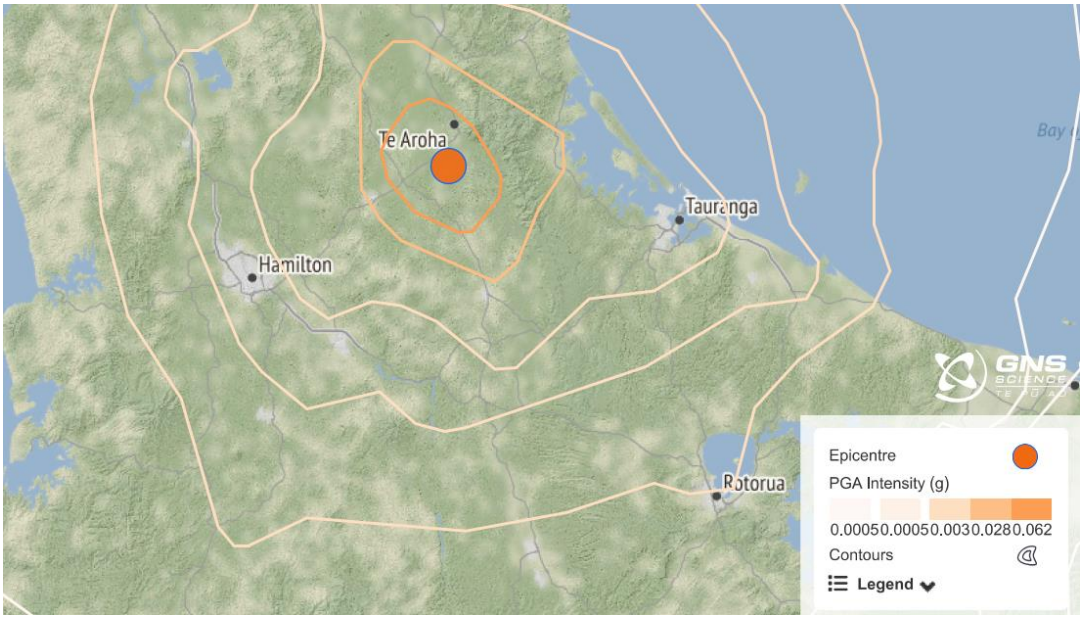


Fig. A2. Peak ground acceleration contour map from the M = 5.1 earthquake, 2023

Considering all of the above, in addition to the chapter content and results it can be inferred that: (1) An earthquake with an epicentre in the Hamilton lowlands, caused by a local fault (e.g. recently discovered faults in Hamilton (Moon and de Lange, 2017) has not been recorded in the last 120 years. (2) The ground motion data for the one of three earthquakes with epicentres

within 50km of Hamilton city, combined with the results from the minimum triggering peak ground accelerations for magnitudes $M$ = 5 to 6, suggest that earthquakes caused by more distant faults are not likely to have caused the liquefaction in the tephras. Therefore (3) there is a risk of hidden faults (or the newly discovered faults) within the lowlands that have the capacity to produce earthquakes that would cause the tephras to liquefy. The scope of this thesis does not include going into great detail in discussing or analysing site to source distances as well as sophisticated fault rupture modelling. Yet, the final results and the lack of recorded data are in the favour of confirming the primary hypothesis that inspired this research “The liquefaction in the tephras is caused by hidden faults”.

# Chapter 7: Conclusions and recommendations

## 7.1. Research summary

This PhD research was focused on geotechnical analyses of pre-historically liquefied lacustrine tephra layers in the Hamilton lowlands, North Island, New Zealand, in order to estimate the pre-historic earthquake parameters ($a_{max}$ and $M$) that might have caused the layers to liquefy. The research outcomes of this thesis complement a broader paleoliquefaction study within the frameworks of the "Tephra Seismites" project which also includes investigations from both geological and seismological perspectives (as described by Kluger et al. 2023). Moreover, the findings within the scope of the research objectives of the thesis add important engineering and scientific contribution as they also address key research questions in the context of liquefaction of pumiceous sand-silt mixtures, which had not been investigated before. The following section summarizes the most important findings in response to the research objectives (outlined earlier in sub-chapter 1.5).

The starting point for the research was to **characterize the geotechnical properties of all the tephras of interest, i.e. with identified soft sediment deformation structures in the studied lakes with the purpose of defining their liquefaction susceptibility**. Not all individual tephra layers of interest could be analysed in the context of undrained cyclic behaviour and liquefaction resistance through undrained triaxial testing, as mentioned in sub-chapter 2.1. Therefore, analysing the liquefaction susceptibility of the tephras was crucial as it (1) would support the hypothesis that they had indeed been liquefied in the past and (2) would assist the development of a framework that extends the liquefaction resistance results from the undrained cyclic tested tephras into the other relevant tephras in the lakes. This objective was addressed in Chapter 3 of this thesis. Four tephras, Tuhua (7.6 cal ka), Mamaku (8.0 cal ka), Waiohau (14.0 cal ka), and Rotorua (15.6 cal ka) were investigated by means of their grain-size properties, pumice contents, specific gravity, and mineralogical properties. Additionally, for the topmost two tephras, Tuhua and Mamaku that were sampled for large volume testing (as well as subsequent triaxial testing), the minimum and maximum dry densities were quantified as well. The liquefaction susceptibility was defined by analysing whether the tephra

properties fall in the range of the liquefiable soils by means of grain size, as well as analysing their plasticity following the current most conclusive method based on the Atterberg limit tests. For the tephras where Atterberg limits could be performed, the clay mineralogy of the clay-sized fractions (<2 μm) was studied in order to define their potential plasticity. The hypothesis was that if clay-sized particles lack clay minerals, the tephras were non-plastic and thus liquefaction susceptible. It was found that most of tephras that show SSDSs were liquefiable, as well as pumiceous across the size range of silts to sands by means of their grain sizes. The first finding supported the hypothesis that the SSDSs were earthquake induced liquefaction structures, and the second finding supported the second objective as it emphasized the need to fill in the research gaps related to liquefaction of pumiceous silts. An interesting result (a "byproduct" of the chapter) were the specific gravity vs pumice content, and characteristic void ratio vs pumice content trends. The trends implied that with a large enough data base, potential empirical correlations could be established to enable engineers to define pumice content by analysing other geotechnical properties, such as specific gravity and/or characteristic void ratios, through these correlations.

**The undrained monotonic and cyclic behaviour of a pumiceous silt** was studied as part of the second research objective with the purpose to **fill knowledge gaps, related to potential particle crushing affecting undrained cyclic behaviour as well as liquefaction resistance** of this type of soil material. Considering, as per previously published literature, pumiceous sands seem to exhibit different undrained cyclic behaviour and can even have higher liquefaction resistance compared to hard-grained soils (as a result of the crushable nature of the pumiceous sands), empirical correlations developed on hard-grained sands were considered to be not applicable for pumiceous sands. Therefore, the second research objective aimed to answer the questions of (1) whether pumiceous silts are also crushable and (2) if their cyclic undrained behaviour and liquefaction resistance are more similar to those of pumiceous sand or of hard-grained soils. This objective was addressed in Chapter 4. The results indicated that no particle crushing occurred in the samples during testing. In general, the Tuhua silt material behaved closer to the established trends typical for hard-grained soils than to those for pumiceous sands. It was inferred that the reason why the material did not undergo any significant particle crushing during sample reconstitution and/or testing, was because of a cushioning effect from the fines that prevented the coarse pumiceous particles from breaking. The broader science/engineering contribution from this objective was the added content by

means of the extensive undrained monotonic and cyclic loading investigation that was performed on a pumiceous silt for the first time.

The study on Tuhua silt, opened more questions that needed to be addressed before addressing the final aim. As mentioned before, the pumiceous tephras ranged from silts to silty sands to sandy silts to sands. If pumiceous sands were known to behave differently from hard-grained sands and to exhibit higher liquefaction resistance, pumiceous silt was now found to behave closer to hard-grained soils, the question posed was whether there was a **potential threshold of pumice content and/or fines content, at which sand-silt mixtures become crushable**. The third objective therefore involved the investigation of three beds making up Mamaku tephra, a silt and two silty sands with different fines contents as well as different pumice contents in order to study their crushability. Crushability as assessed by examining the changes in grain size and pumice content after testing as well as whether their cyclic undrained behaviour compared closer to hard-grained or pumiceous sand patterns (Chapter 5). The results showed no change in grain size or pumice content for the silty Mamaku Ma-ML70 as well as the silty Mamaku sand Ma-SM31 following cyclic undrained triaxial testing. Moreover, their cyclic behaviour, by means of pore pressure generation as well as double axial strain accumulation, was found to be similar to that of hard-grained sands and the non-crushable Tuhua silt, which indicated that no particle crushing had occurred in both Ma-ML70 and Ma-SM31. For the coarsest Mamaku sand bed, Ma-SM20 with 20% fines, both the grain-size distribution and the pumice content (before and after testing) changed, indicating that particle crushing was evident. The undrained cyclic behaviour results plotted the closest to the zone of crushable materials based on published data, compared to the other two Mamaku materials, yet still not evidently like the trends reported for pumiceous sand. It was inferred that Ma-SM20 underwent some particle crushing and a fines content threshold where particles begin to crush under cyclic triaxial testing between 31% and 20% was speculated.

Lastly, the **final part of the overarching aim**, which was to **estimate the pre-historic earthquake parameters ($a_{max}$ and $M$) that might have caused the deformation structures in the lacustrine tephra layers,** was covered in the fourth objective through proposing a **framework that extended the laboratory-obtained liquefaction resistance results on the collected tephras from one lake, into the other relevant tephras within the lakes in the Hamilton lowlands.** In this investigation (Chapter 6), the liquefaction resistance curves of the three distinct beds (with different grain size distributions and pumice content) of the Mamaku

tephra, were obtained. The liquefaction resistance obtained from the laboratory triaxial tests was used to estimate peak ground acceleration and magnitude ($a_{max} - M$) combination curves for the entire Mamaku tephra layer preserved in sediment cores from 13 lakes in the lowlands. Considering there were no Mamaku tephras coarser than Ma-SM20, which had shown signs of particle crushing during undrained cyclic testing, the empirical methods based on hard-grained soils were considered appropriate and thus used in the study. The Mamaku tephra layers in the lakes were found to be vulnerable to liquefaction at very low peak ground accelerations, i.e. with a range of 0.02 to 0.08 g through the range of earthquake magnitudes, $M$ = 5 to 8.5 considered. The high vulnerability to liquefaction across all the Mamaku layers in the Hamilton lowlands was considered to be the result of very low in-situ overburden stresses as well as the relatively low liquefaction resistance. The high vulnerability to very small levels of earthquake shaking made speculating and/or identifying large pre-historic earthquakes (magnitudes 6 and above) based on the geotechnical paleoliquefaction approach rather difficult. Complementary geologically based paleoliquefaction analyses obtained by other work within the "Tephra Seismites" project were found to be crucial for more conclusive results. A bonus research outcome was the discovered potential advantage of paleoliquefaction studies that investigate similar shallow deposits, very sensitive to liquefaction at low ground shaking to estimate past small magnitude earthquakes, e.g. $M \leq 5$, which are commonly not studied. Considering paleoseismic evidence of smaller earthquake events ($M \leq 5$) are not likely to be preserved in the sedimentary record, studying deposits that are very sensitive to liquefaction at low ground shaking could potentially help identify those small events. Earthquakes with magnitudes of 5 and smaller may not be as destructive as larger ones, but knowledge about the frequency of their occurrence, assists in understanding the overall seismic hazard of an area of interest, the activity of as even smaller earthquakes can cause community concerns through damage, economic impact and stress. In other words, as discussed in the addendum of chapter 6, although recent records have captured some magnitudes around 5, which are not necessarily a seismic risk for the urban areas around, the paleoliquefaction data suggests that there might have been more earthquakes of such magnitudes (or bigger) from different sources that if identified and discovered could impact the seismic hazard, and from an engineering perspective the earthquake design parameters.

Ultimately, this PhD thesis provides research contributions: (1) that complemented the geological and seismological research segments of a multidisciplinary paleoliquefaction project, (i.e., the "Tephra Seismites" project based at the University of Waikato), by estimating past earthquake parameters that could have triggered liquefaction in the lacustrine tephras, in

particular, the Mamaku tephra; (2) in the geotechnical package of approaches in paleoliquefaction studies, which have mostly used in-situ investigations as opposed to laboratory based ones in the past; and (3) that filled key research gaps related to undrained behaviour and liquefaction resistance of pumiceous silts and silty sands, which will assist both scientists as well as engineers in the future, as well as inspire future research that may address the additional research questions that were developed in the course of the work.

## 7.2. Recommendations for future research and engineering applications

In the following few paragraphs, I summarize the thoughts and take-away messages that I derived during my PhD study in regard to: (1) the geotechnical procedures for obtaining geotechnical properties of soils and in a form of (2) ideas that were inspired from my results as recommendations for future research that I believe both engineers and researchers working with pumiceous sand-silt mixtures in the future could benefit from.

In general, in my study I found that the pumiceous particles, which are potentially crushable due to their highly vesicular nature, are mostly present in the sand grain-size range (0.075 – 2 mm). In other words, within the grain-size range of fines (< 0.075 mm), the particles seemed to be mostly (~99%) broken-down pumice, i.e., glass shards. Considering that the particle crushing was inversely dependent on the fines content, i.e., the finer the sand-silt mixture, the less prone it was to particle crushing during triaxial testing, it can be inferred that the vulnerability to particle crushing of pumiceous soils comes from the sand particles. This suggests that choosing the most convenient testing procedures for deriving both the grain-size distribution as well as pumice content, of pumiceous soil mixtures is crucial. For example, grain-size distributions estimated with the standard sieving method, which are based on the mass of individual fractions of the soil mixture, might over-estimate the fines portion, considering the lighter yet larger sandy pumiceous particles. This might be even more pronounced in natural pumiceous sand-silt mixtures, where heavier, hard-grained, (e.g., quartz and/or feldspar particles as well as mafic mineral grains) are present as well. Particle-volume-based grain-size estimation procedures should provide a more accurate representation of the grain-size distribution of pumiceous sand-silt mixtures, compared to particle-mass-based procedures.

Similarly, for the pumice content evaluation, I found the pumiceous vs. hard-grained particles nomenclature is not fully inclusive and that a distinction between pumiceous (vesicular) and non-pumiceous (non-vesicular) might be more fitting. Previous studies on natural pumiceous soils, have analysed mixtures of pumiceous and (mostly) quarzitic sand particles. Considering difference in the structure of pumiceous (bubble wall texture surrounding vesicles) and quarzitic (solid mineral) particles, means the ease with which pumice particles can be broken down is much greater. Therefore, the terminology pumiceous vs hard grained initially seems to be appropriate. However, in natural sand-silt mixtures, containing fines particles that would inevitably contain glass shards (already broken-down pumice) which are unlikely to crush further once the vesicularity has been destroyed, characterizing the particles as pumiceous and non-pumiceous would be more suitable. In this context, considering that as pumiceous particles can have the same particle density as glass-shard particles (result of potentially lacking internal voids in the pumiceous particles – see Chapter 3), a more convenient methods for pumice content evaluation in pumiceous soil mixtures comprising fines, might be the ones based on the potential of particle breakage as opposed to particle density.

Considering all the above, and all the potentially relevant geotechnical aspects that could not have been covered in the scope of this thesis, the following investigations would potentially answer some of the questions related to pumiceous sand-silt mixtures:

- A comparative study between crushing potential-based and density-based pumice content procedures, on a large data base of pumiceous sand-silt mixtures (silty sands, sandy silts, and silts), complemented with a specific gravity vs pumice content correlation, and SEM based pumice content evaluation, in order to find the optimum pumice content method for these types of soils.
- A laboratory undrained testing campaign on varying natural (both pumiceous and quartz/feldspar rich) sand-silt mixtures, with different fines/pumice content, in order to observe whether there will be the crushing of particles if the fines are hard-grained, or mixed glass-shards with hard-grained particles (as opposed to glass-shards alone).
- A numerical simulation study, based on e.g., discrete element methods (DEM), where the effect of the cyclic loading upon the particles of sand-silt mixtures can be studied closely in order to observe the “cushioning” effect of the fines particles, as found in this study, on a particle element level.
- Complementing laboratory investigations with in-situ based ones, such as SPT, CPT

and *V*s-based methods, in order to investigate whether there the empirical correlations are applicable for pumiceous sand-silt mixtures. It would be interesting to investigate whether, for a pumiceous sand-silt mixture that did not show signs of particle crushing during undrained laboratory testing, the results from the in-situ investigations fall within the expected range of values for a corresponding hard-grained soil material. This would also assist future researchers/engineers in finding the threshold of fines/pumice content at which empirical correlations established on hard-grained soils, stop being applicable to pumiceous mixtures. In other words, the threshold should more or less be a match between laboratory based and in-situ based studies. In the in-situ based studies, the fines/pumice content threshold could potentially be the one where the in-situ values for e.g. cone tip resistance, number of blows etc. no longer falls within the range of values expected for that type of soil, and/or the empirically obtained e.g. CRR are not within the expected range of values obtained from laboratory testing.

- Lastly, a comparative study of undisturbed vs reconstituted undrained cyclic testing of pumiceous sand-silt mixtures would investigate the potential effects of different reconstitutions method with these types of soil mixtures.

# References


Aghaei Araei, Ata, and Ikuo Towhata. 2014. "Impact and Cyclic Shaking on Loose Sand Properties in Laminar Box Using Gap Sensors." *Soil Dynamics and Earthquake Engineering* 66:401–414. doi: 10.1016/j.soildyn.2014.08.004.

Andrews, Desmond C. a, and Geoffrey R. Martin. 2000. "Criteria for Liquefaction of Silty Soils." Pp. 1–8 in *12th World Conf. on Earthquake Engineering, Upper Hutt, New Zealand*.

Andrus, Ronald D., and Kenneth H. Stokoe. 2000. "Liquefaction Resistance of Soils from Shear-Wave Velocity." *Journal of Geotechnical and Geoenvironmental Engineering* 126(11):1015–25.

Asadi, M. B., M. S. Asadi, R. P. Orense, and M. J. Pender. 2017. "Dynamic Behaviour of Undrained Natural Pumiceous Soils." in *Proceedings of the 20th NZGS Geotechnical Synposium*.

Asadi, M. B., M. S. Asadi, R. P. Orense, and M. J. Pender. 2018. "Shear Wave Velocity-Based Assessment of Liquefaction Resistance of Natural Pumiceous Sands." *Geotechnique Letters* 8(4):262–67. doi: 10.1680/jgele.18.00102.

Asadi, M. S., R. P. Orense, M. B. Asadi, and M. J. Pender. 2019. "Maximum Dry Density Test to Quantify Pumice in Natural Soils." *Soils and Foundations* 59(2):532–43. doi: 10.1016/j.sandf.2019.01.002.

Asadi, M. S., M. J. Pender, and R. P. Orense. 2015. "Undrained Cyclic Strength of Undisturbed Pumiceous Deposits." P. 8 in *Proceedings of the 12th Australia New Zealand Conference on Geomechanics*.

Asadi, Mohammad Sadeq, Mohammad Bagher Asadi, Rolando P. Orense, and Michael J. Pender. 2018. "Undrained Cyclic Behaviour of Reconstituted Natural Pumiceous Sands." *Journal of Geotechnical and Geoenvironmental Engineering* 144(8):434–41. doi: 10.1061/(ASCE)GT.1943-5606.0001912.

ASTM-D-2487. 2018. "Classification of Soils for Engineering Purposes (USCS)." *American Society for Testing and Materials*.

ASTM-D4318-17e1. 2017. "Standard Test Methods for Liquid Limit, Plastic Limit and Plasticity Index of Soils." *American Society for Testing and Materials*.

ASTM-D5550-14. 2014. "Standard Test Methods for Specific Gravity of Soil Solids by Gas Pycnometer." *American Society for Testing and Material*.

ASTM D 5311 - 92. 2004. "Standard Test Method for Load-Controlled Cyclic Triaxial Strength of Soil." *American Society for Testing and Materials*. doi: 10.1520/D5311-11.2.

Been, K., and M. G. Jefferies. 1985. "A State Parameter for Sands." *Geotechnique* 35(2):99–112. doi: 10.1680/geot.1985.35.2.99.

Bielders, C. L., L. W. De Backer, and B. Delvaux. 1990. "Particle Density of Volcanic Soils as Measured with a Gas Pycnometer." *Soil Science Society of America Journal* 54(3):822–26. doi: 10.2136/sssaj1990.03615995005400030034x.

Bobei, D. C., S. R. Lo, D. Wanatowski, C. T. Gnanendran, and M. M. Rahman. 2009. "Modified State Parameter for Characterizing Static Liquefaction of Sand with Fines." *Canadian Geotechnical Journal* 46(3):281–95. doi: 10.1139/T08-122.

Bojadjieva, Julijana. 2015. “Dynamic Behaviour of Saturated Cohesionless Soils Based on Element and 1-g Experiments.”

Bojadjieva, J., Sheshov, V., Edip, K., Kitanovski, T., Chaneva, J., & Ivanovski, D. (2019, September). Comparison of cyclic simple shear and triaxial tests on natural sand. Keynote lecture at the *XVII European Conference on Soil Mechanics and Geotechnical Engineering*.

Bommer, Julian J., and Carlos E. Rodríguez. 2002. “Earthquake-Induced Landslides in Central America.” *Engineering Geology* 63(3–4):189–220. doi: 10.1016/S0013-7952(01)00081-3.

Boulanger, R. W., and J. T. Dejong. 2018. “Inverse Filtering Procedure to Correct Cone Penetration Data for Thin-Layer and Transition Effects.” Pp. 25–44 in *Cone Penetration Testing 2018 - Proceedings of the 4th International Symposium on Cone Penetration Testing, CPT 2018*.

Boulanger, R. W., and I. M. Idriss. 2014. “CPT and SPT Based Liquefaction Triggering Procedures, Report UCD/CGM-10/2.” *Center for Geotechnical Modeling* (April):1–138.

Boulanger, Ross W., and I. M. Idriss. 2006. “Liquefaction Susceptibility Criteria for Silts and Clays.” *Journal of Geotechnical and Geoenvironmental Engineering* 132(11):1413–26. doi: 10.1061/(ASCE)1090-0241(2006)132:11(1413).

Boulanger, Ross W., and I. M. Idriss. 2015. “Magnitude Scaling Factors in Liquefaction Triggering Procedures.” *Soil Dynamics and Earthquake Engineering* 79:296–303.

Bray, Jonathan D., and Rodolfo B. Sancio. 2006. “Assessment of the Liquefaction Susceptibility of Fine-Grained Soils.” *Journal of Geotechnical and Geoenvironmental Engineering*. doi: 10.1061/(asce)1090-0241(2006)132:9(1165).

Bray, Jonathan D., Rodolfo B. Sancio, M. F. Riemer, and T. Durgunoglu. 2004. “Liquefaction Susceptibility of Fine-Grained Soils.” in *Proc., 11th Int. Conf. on Soil Dynamics and Earthquake Engineering and 3rd Int. Conf. on Earthquake Geotechnical Engineering. Vol. 1. Stallion Press, Singapore*.

Canterbury Earthquakes Royal Commission. 2012. *Summary and Recommendations Volume 1: “Seismicity, Soils and the Seismic Design of Buildings.”*

Cappellaro, Claudio. 2019. “The Influence of Fines Content, Fabric and Layered Structure on the Undrained Cyclic Behaviour of Christchurch Sandy Soils.” University of Canterbury.

Cappellaro, Claudio, Misko Cubrinovski, Jonathan D. Bray, Gabriele Chiaro, Michael F. Riemer, and Mark E. Stringer. 2021. “Liquefaction Resistance of Christchurch Sandy Soils from Direct Simple Shear Tests.” *Soil Dynamics and Earthquake Engineering* 141:106489-(1-14). doi: 10.1016/j.soildyn.2020.106489.

Castro, G. 1969. “Liquefaction of Sands.” *Harvard Univ, Harvard Soil Mech Ser 81*.

Castro, Gonzalo. 1975. “Liquefaction and Cyclic Mobility of Saturated Sands.” *ASCE J Geotech Eng Div* 101(6):551–69. doi: 10.1061/ajgeb6.0000173.

Cetin, K. Onder, Raymond B. Seed, Armen Der Kiureghian, Kohji Tokimatsu, Leslie F. Harder, Robert E. Kayen, and Robert E. S. Moss. 2004. “Standard Penetration Test-Based Probabilistic and Deterministic Assessment of Seismic Soil Liquefaction Potential.” *Journal of Geotechnical and Geoenvironmental Engineering* 130(12):1314–40. doi: 10.1061/(ASCE)1090-0241(2004)130:12(1314).

Chaneva, Jordanka, Max O. Kluger, Vicki G. Moon, David J. Lowe, and Rolando P. Orense. 2022. “Geotechnical Properties of Liquefied Pumiceous Layers in Lakes.” Pp. 313–18 in

*Proceedings of the 7th International Young Geotechnical Engineers Conference – Scott (Ed.) © 2022 Australian Geomechanics Society, Sydney Australia, ISBN 978-0-9946261-5-8*.

Chaneva, Jordanka, Max O. Kluger, Vicki G. Moon, David J. Lowe, and Rolando P. Orense. 2023. "Monotonic and Cyclic Undrained Behaviour and Liquefaction Resistance of Pumiceous, Non-Plastic Sandy Silt." *Soil Dynamics and Earthquake Engineering* 168(December 2022):107825. doi: 10.1016/j.soildyn.2023.107825.

Chaneva, Jordanka, Max O. Kluger, Vicki G. Moon, David J. Lowe, and Rolando P. Orense. 2024. "Influence of Pumice and Fines Contents on the Extent of Particle Crushing in Pumiceous Sand-Silt Mixtures during Undrained Cyclic Triaxial Loading." in *Proc. 8th International COnference on Earthquake Geotechnical Engineering, Osaka, Japan*.

de Cristofaro, M., L. Olivares, R. P. Orense, M. S. Asadi, and N. Netti. 2022. "Liquefaction of Volcanic Soils: Undrained Behaviour under Monotonic and Cyclic Loading." *Journal of Geotechnical and Geoenvironmental Engineering* 148(1):04021176-(1-11). doi: 10.1061/(asce)gt.1943-5606.0002715.

Cubrinovski, M., B. A. Bradley, L. M. Wotherspoon, R. A. Green, J. D. Bray, C. Wood, M. J. Pender, J. Allen, A. Bradshaw, G. Rix, M. Taylor, K. Robinson, D. Henderson, S. Giorgini, K. Ma, A. Winkley, J. Zupan, T. O'Rourke, G. DePascale, and D. Wells. 2011. "Geotechnical Aspects of the 22 February 2011 Christchurch Earthquake." *Bulletin of the New Zealand Society for Earthquake Engineering* 44(4):205–26. doi: 10.5459/bnzsee.44.4.205-226.

Cubrinovski, Misko, and Kenji Ishihara. 2002. "Maximum and Minimum Void Ratio Characteristics of Sands." *Soils and Foundations* 142(6):65–78. doi: 10.3208/sandf.42.6_65.

Cubrinovski, Misko, T. Kokusho, and K. Ishihara. 2006. "Interpretation from Large-Scale Shake Table Tests on Piles Undergoing Lateral Spreading in Liquefied Soils." *Soil Dynamics and Earthquake Engineering* 26(2–4):275–286. doi: 10.1016/j.soildyn.2005.02.018.

Dash, H. K., and T. G. Sitharam. 2009. "Undrained Cyclic Pore Pressure Response of Sand-Silt Mixtures: Effect of Nonplastic Fines and Other Parameters." *Geotechnical and Geological Engineering* 27:501–17. doi: 10.1007/s10706-009-9252-5.

Van Dissen, R., R. Seebeck, Lichtfield N, N. Barnes, and P. Nicols. 2021. "Development of the New Zealand Community Fault Model – Version 1.0." Pp. 1–9 in *Proceedings of the 2021 New Zealand Society for Earthquake Engineering Annual Technical Conference, Christchurch*.

Dobry, R., R. S. Ladd, F. Y. Yokel, R. M. Chung, and D. Powell. 1982. "Prediction of Pore Water Pressure Buildup and Liquefaction of Sands during Earthquakes by the Cyclic Strain Method." *National Bureau of Standards, Building Science Series* (L).

Downs, GL. 2005. "Earthquakes." *Edbrooke SW. Geology of the Waikato Area. Institute of Geological and Nuclear Sciences 1:250,000 Geological Map 4. Lower Hutt, GNS Science* 56–58.

Edbrooke, SW. 2005. *Geology of the Waikato Area. Institute of Geological and Nuclear Sciences Geological Map 4*.

Eshel, G., Levy, G. J., Mingelgrin, U., & Singer, M. J. (2004). Critical evaluation of the use of laser diffraction for particle-size distribution analysis. *Soil Science Society of America Journal*, *68*(3), 736-743.

Evangelista, L., and F. Santucci. 2011. "Upgrading the Simplified Assessment of the Liquefaction Susceptibility for the City of Naples, Italy." P. 13 in *5th International Conference on Earthquake Engineering, Santiago, 10*.

Fannin, R. J., A. Eliadorani, and J. M. T. Wilkinson. 2005. “Shear Strength of Cohesionless Soils at Low Stress.” *Geotechnique* 55(6):467–78. doi: 10.1680/geot.2005.55.6.467.

Finn, W. D. Liam, Dennison J. Pickering, and Peter L. Bransby. 1971. “Sand Liquefaction in Triaxial and Simple Shear Tests.” *Journal of the Soil Mechanics and Foundations Division* 97(4):639–59. doi: 10.1061/jsfeaq.0001579.

Flisch, A., and A. Becker. 2003. “Industrial X-Ray Computed Tomography Studies of Lake Sediment Drill Cores.” *Geological Society Special Publication* 215:205–12. doi: 10.1144/GSL.SP.2003.215.01.19.

Fortin, David, Pierre Francus, Andrea Catalina Gebhardt, Annette Hahn, Pierre Kliem, Agathe Lisé-Pronovost, Rajarshi Roychowdhury, Jacques Labrie, and Guillaume St-Onge. 2013. “Destructive and Non-Destructive Density Determination: Method Comparison and Evaluation from the Laguna Potrok Aike Sedimentary Record.” *Quaternary Science Reviews* 71:147–53. doi: 10.1016/j.quascirev.2012.08.024.

Frolov, Y. S., and D. H. Maling. 1969. “The Accuracy of Area Measurement by Point Counting Techniques.” *Cartographic Journal* 6(1):21–35. doi: 10.1179/caj.1969.6.1.21.

Gardiner E., Stringer M., and Rees S., 2024, " Liquefaction resistance of soils with differing pumice contents", Proceedings of the 8th International Conference on Earthquake Geotechnical Engineering, Osaka, Japan 2024.

Ghazoui, Z., S. Bertrand, K. Vanneste, Y. Yokoyama, J. Nomade, A. P. Gajurel, and P. A. van der Beek. 2019. “Potentially Large Post-1505 AD Earthquakes in Western Nepal Revealed by a Lake Sediment Record.” *Nature Communications* 10(1):2258. doi: 10.1038/s41467-019-10093-4.

Gill, Olivia M., and Rolando P. Orense. 2019. “Field Characterisation and Mapping of Pumiceous Deposits in Central North Island, NZ.” *Japanese Geotechnical Society Special Publication* 6(2):79–87. doi: 10.3208/jgssp.v06.giz12.

Gladkov, A. S., E. U. Lobova, E. V. Deev, A. M. Korzhenkov, J. V. Mazeika, S. V. Abdieva, E. A. Rogozhin, M. V. Rodkin, A. B. Fortuna, T. A. Charimov, and A. S. Yudakhin. 2016. “Earthquake-Induced Soft-Sediment Deformation Structures in Late Pleistocene Lacustrine Deposits of Issyk-Kul Lake (Kyrgyzstan).” *Sedimentary Geology* 344:112–22. doi: 10.1016/j.sedgeo.2016.06.019.

Green, J. D. 1979. “Palaeolimnological Studies on Lake Maratoto, North Island, New Zealand.” *Paleolimnology of Lake Biwa & the Japanese Pleistocene* 7:416–38.

Green, J. D., and D. J. Lowe. 1985. “Stratigraphy and Development of c. 17 000 Year Old Lake Maratoto, North Island, New Zealand, with Some Inferences about Postglacial Climatic Change.” *New Zealand Journal of Geology and Geophysics* 28(4):675–99. doi: 10.1080/00288306.1985.10422541.

Green, J. D., and D. J. Lowe. 1994. “Origins and Development [of Lake Rotoroa].” *In: Clayton, J.S. et Al. “Lake Rotoroa: Change in an Urban Lake” NIWA Ecosistems Publication No. 9* 13–23.

Green, J. D., and D. J. Lowe. 2024. “[Waikato] Lakes in the Past – Paleolimnology and Paleolakes.” *The Hidden Gems of the Waikato – the History, Ecology and Management of the Waikato Lakes. Waikato Regional Council, Hamilton*.

Green, Russell A., Stephen F. Obermeier, and Scott M. Olson. 2005. “Engineering Geologic and Geotechnical Analysis of Paleoseismic Shaking Using Liquefaction Effects: Field Examples.” *Engineering Geology* 76(3–4):263–93. doi: 10.1016/j.enggeo.2004.07.026.

Hardin, Bobby O. 1985. “Crushing of Soil Particles.” *Journal of Geotechnical Engineering*

111(10):1177–92. doi: 10.1061/(ASCE)0733-9410(1985)111:10(1177).

Hariprasad, Chennarapu, Mekala Rajashekhar, and Balunaini Umashankar. 2016. "Preparation of Uniform Sand Specimens Using Stationary Pluviation and Vibratory Methods." *Geotechnical and Geological Engineering* 34:1909–22. doi: 10.1007/s10706-016-0064-0.

Hazirbaba, Kenan, and Ellen M. Rathje. 2009. "Pore Pressure Generation of Silty Sands Due to Induced Cyclic Shear Strains." *Journal of Geotechnical and Geoenvironmental Engineering* 135(12):1892–1905. doi: 10.1061/(asce)gt.1943-5606.0000147.

Hewitt, A. E., M. R. Balks, and D. J. Lowe. 2021. "The Soils of Aotearoa New Zealand." *Springer International Publishing* 332.

Holtz, V. G. 1969. "Soil as an Engineering Material." *Water Resources Technical Publication* 17:45.

Hounsfield, G. N. 1973. "Computerized Transverse Axial Scanning (Tomography): I. Description of System." *British Journal of Radiology* 46:1016–22. doi: 10.1259/0007-1285-46-552-1016.

Huang, An Bin, Wen Jong Chang, Huai Houh Hsu, and Yu Jie Huang. 2015. "A Mist Pluviation Method for Reconstituting Silty Sand Specimens." *Engineering Geology* 188:1–9. doi: 10.1016/j.enggeo.2015.01.015.

Huang, Y., H. L. Cheng, T. Osada, A. Hosoya, and F. Zhang. 2015. "Mechanical Behaviour of Clean Sand at Low Confining Pressure: Verification with Element and Model Tests." *Journal of Geotechnical and Geoenvironmental Engineering* 141(8):06015005. doi: 10.1061/(asce)gt.1943-5606.0001330.

Hume, Terry M., Alan M. Sherwood, and Campbell S. Nelson. 1975. "Alluvial Sedimentology of the Upper Pleistocene Hinuera Formation, Hamilton Basin, New Zealand." *Journal of the Royal Society of New Zealand* 5:421–62. doi: 10.1080/03036758.1975.10419362.

Hyodo, M., A. F. L. Hyde, and N. Aramaki. 1998. "Liquefaction of Crushable Soils." *Geotechnique* 48(4):527–43. doi: 10.1680/geot.1998.48.4.527.

Hyodo, M., Y. Nakata, A. F. L. Hyde, and N. Aramaki. 1998. "Undrained Cyclic Shear Behaviour and Particle Crushing of Sand under High Confining Stress." in *The geotechnics of hard soils - soft rocks. Proceedings of the second international symopsium on hard soils-soft rocks, Naples, October*.

Hyodo, Taichi, Yang Wu, and Masayuki Hyodo. 2022. "Influence of Fines on the Monotonic and Cyclic Shear Behaviour of Volcanic Soil 'Shirasu.'" *Engineering Geology* 301:106591-(1-18). doi: 10.1016/j.enggeo.2022.106591.

International, ASTM. 2011. "ASTM D2487-11 Standard Practice for Classification of Soils for Engineering Purposes (Unified Soil Classification System)." *ASTM Standard Practices (ASTM International)*.

Ishihara, K. 1993. "Liquefaction and Flow Failure during Earthquakes." *Geotechnique* 43(3):351–451. doi: 10.1680/geot.1993.43.3.351.

Ishihara, K., H. Kai-Lung, I. Nakazumi, and K. Sato. 1986. "Analysis of Landslides during the 1984 Naganoken-Seibu Earthquake." *Geologia Applicata e Idrogeologia* 21(2):175–215.

Ishihara, K., and Y. Koga. 1981. "Case Studies of Liquefaction in the 1964 Niigata Earthquake." *Soils and Foundations* 21(3):35–52. doi: 10.3208/sandf1972.21.3_35.

Ishihara, Kenji. 1996. "Cyclic Behaviour of Partially Saturated Collapsible Soils Subjected to Water

Permeation." *ASCE, Geotechnical Special Publication* 44:34–50.

Ishihara, Kenji. 1997. *Soil Behaviour in Earthquake Geotechnics*.

Ishihara, Kenji, Fumio Tatsuoka, and Susumu Yasuda. 1975. "Undrained Deformation and Liquefaction of Sand under Cyclic Stresses." *Soils and Foundations* 15(1):29–44. doi: 10.3208/sandf1972.15.29.

Ishihara, Kenji, and Ikuo Towhata. 1983. "Sand Response to Cyclic Rotation of Principal Stress Directions as Induced by Wave Loads." *Soils and Foundations* 23(4):11–26. doi: 10.3208/sandf1972.23.4_11.

Ishihara, Kenji, and Fumio Yamazaki. 1980. "Cyclic Simple Shear Tests on Saturated Sand in Multi-Directional Loading." *Soils and Foundations* 20(1):45–59. doi: 10.3208/sandf1972.20.45.

Ishihara, Kenji, and Susumi Yasuda. 1972. "Sand Liquefaction Due to Irregular Excitation." *Soils and Foundations* 12(4):65–77. doi: 10.3208/sandf1972.12.4_65.

Ishikawa, Tatsuya, Masayuki Yoshimi, Koichi Isobe, and Shoji Yokohama. 2021. "Reconnaissance Report on Geotechnical Damage Caused by 2018 Hokkaido Eastern Iburi Earthquake with JMA Seismic Intensity 7." *Soils and Foundations* 61(4):434–41. doi: 10.1016/j.sandf.2021.06.006.

Japanese Geotechnical Society Standard, JGS0161-2009. 2009. "Test Method for Minimum and Maximum Densities of Sand."

Kikkawa, Naotaka, Rolando P. Orense, and Michael J. Pender. 2013. "Observations on Microstructure of Pumice Particles Using Computed Tomography." *Canadian Geotechnical Journal* 50(11):1109–17. doi: 10.1139/cgj-2012-0365.

Kleyburg, M. A., V. G. Moon, D. J. Lowe, and C. S. Nelson. 2015. "Paleoliquefaction in Late Pleistocene Alluvial Sediments in the Hauraki and Hamilton Basins, and Implications for Paleoseismicity." Pp. 524–31 in *Proceedings, 12th Australia New Zealand Conference on Geomechanics (ANZ 2015)*.

Kluger, Max O., Stefan Kreiter, Florian T. Stähler, Majid Goodarzi, Tim Stanski, and Tobias Mörz. 2021. "Cone Penetration Tests in Dry and Saturated Ticino Sand." *Bulletin of Engineering Geology and the Environment* 80:4079–88. doi: 10.1007/s10064-021-02156-y.

Kluger, Max O., David J. Lowe, Vicki G. Moon, Jordanka Chaneva, Richard Johnston, Pilar Villamor, Tehnuka Ilanko, Richard A. Melchert, Rolando P. Orense, Remedy C. Loame, and Nic Ross. 2023. "Seismically-Induced down-Sagging Structures in Tephra Layers (Tephra-Seismites) Preserved in Lakes since 17.5 Cal Ka, Hamilton Lowlands, New Zealand." *Sedimentary Geology* (445 (106327)):1–22. doi: https://doi.org/10.1016/j.sedgeo.2022.106327.

Kluger, Max O., Vicki G. Moon, Stefan Kreiter, David J. Lowe, G. J. Churchman, Daniel A. Hepp, David Seibel, M. Ehsan Jorat, and Tobias Mörz. 2017. "A New Attraction-Detachment Model for Explaining Flow Sliding in Clay-Rich Tephras." *Geology* 45(2):131–34. doi: 10.1130/G38560.1.

Kobayashi, T. 2010. "Aira Tephra Formation and Ata Ignimbrite." Pp. 102–4 in *NTAV International Field Conference on Tephrochronology, Volcanism, and Human Activity, Kirishima City, Kagoshima, Japan*.

Kokusho, Takaji. 2020. "Earthquake-Induced Flow Liquefaction in Fines-Containing Sands under Initial Shear Stress by Lab Tests and Its Implication in Case Histories." *Soil Dynamics and Earthquake Engineering* 130:105948-(1-18). doi: 10.1016/j.soildyn.2019.105984.

Kramer, Steven L. 1996. *Geotechnical Earthquake Engineering*. Prentice-Hall International Series in Civil Engineering and Engineering Mechanics.

Kuerbis, R., and Y. P. Vaid. 1988. "Sand Sample Preparation - the Slurry Deposition Method." *Soils and Foundations* 4:107–18. doi: 10.3208/sandf1972.28.4_107.

Ladd, R. S. 1978. "Preparing Test Specimens Using Undercompaction." *Geotechnical Testing Journal* 1(1):16–23.

Lancelot, Laurent, Isam Shahrour, and Marwan Al Mahmoud. 2006. "Failure and Dilatancy Properties of Sand at Relatively Low Stresses." *Journal of Engineering Mechanics*. doi: 10.1061/(asce)0733-9399(2006)132:12(1396).

Langridge, R. M., W. F. Ries, N. J. Litchfield, P. Villamor, R. J. Van Dissen, M. S. Barrell, D. J. A., Rattenbury, D. W. Heron, and D. B. Haubrock, S., and Townsend. 2016. "The New Zealand Active Faults Database: New Zealand Journal of Geology and Geophysics,." *New Zealand Journal of Geology and Geophysics* 59(1):86–96.

Licata, V., A. D'Onofrio, and F. Silvestri. 2018. "Microstructural Factors Affecting the Static and the Cyclic Resistance of a Pyroclastic Silty Sand." *Geotechnique* 434–41. doi: 10.1680/jgeot.16.P.319.

Lowe, D. J. 1986. "Controls on the Rates of Weathering and Clay Mineral Genesis in Airfall Tephras: A Review and New Zealand Case Study." *Rates of Chemical Weathering of Rocks and Minerals; Academic Press, Orlando* 265–329.

Lowe, D. J. 1988. "Stratigraphy, Age, Composition, and Correlation of Late Quaternary Tephras Interbedded with Organic Sediments in Waikato Lakes, North Island, New Zealand." *New Zealand Journal of Geology and Geophysics* 31(2):125–65. doi: 10.1080/00288306.1988.10417765.

Lowe, D. J., and C. S. Nelson. 1983. "Guide to the Nature and Methods of Analysis of the Clay Fraction of Tephras from the South Auckland Region, New Zealand." *University of Waikato, Department of Earth Sciences, Occasional Report*.

Lowe, David J. 2011. "Tephrochronology and Its Application: A Review." *Quaternary Geochronology* 6(2):107–53. doi: 10.1016/j.quageo.2010.08.003.

Lowe, David J., and Russell A. Green. 2024. "Origins and Ages of Waikato Lake." in *Hidden gems of the Waikato – the history, ecology and management of Waikato lakes*.

Lowe, David J., Abbott P. M., Suzkui T, and Jensen B. J. L. 2022. "Global Tephra Studies: Role and Importance of the International Tephra Research Group 'Commission on Tephrochronology' in Its First 60 Years." *History of Geo- and Space Sciences* 13:93–132.

Lowe, David J., Phil A. R. Shane, Brent V. Alloway, and Rewi M. Newnham. 2008. "Fingerprints and Age Models for Widespread New Zealand Tephra Marker Beds Erupted since 30,000 Years Ago: A Framework for NZ-INTIMATE." *Quaternary Science Reviews* 27(1–2):95–126. doi: 10.1016/j.quascirev.2007.01.013.

De Magistris, F. S., G. Lanzano, G. Forte, and G. Fabbrocino. 2013. "A Database for PGA Threshold in Liquefaction Occurrence." *Soil Dynamics and Earthquake Engineering* 54:17–19.

Melchert, Richard A. 2023. "Sedimentology and Characterisation of Soft-Sediment Deformation Structures within Lacustrine Successions in 20,400-Yr-Old Lake Rotoroa, Hamilton, Northern New Zealand, MSc Thesis." University of Waikato.

Melchert, Richard A., Max O. Kluger, David J. Lowe, and Vicki G. Moon. 2023. "Using CT Visualisation to Characterise Liquefied Sedimentary Structures: New Insights into Earthquake Activity in the Hamilton Lowlands." in *Conference: New Zealand Geotechnical Society (NZGS) Student Poster Competition 2023*.

Mesri, G., and T. M. Hayat. 1993. "The Coefficient of Earth Pressure at Rest." *Canadian Geotechnical Journal* 30(4):647–66. doi: 10.1139/t93-056.

Mijic, Zorana, Jonathan D. Bray, Michael F. Riemer, Misko Cubrinovski, and Sean D. Rees. 2021. "Test Method for Minimum and Maximum Densities of Small Quantities of Soil." *Soils and Foundations* 61(2):533–40. doi: 10.1016/j.sandf.2020.12.003.

Miura, Sehchi, Kazuyoshi Yagi, and Tsuyoshi Asonuma. 2003. "Deformation-Strength Evaluation of Crushable Volcanic Soils by Laboratory and in-Situ Testing." *Soils and Foundations* 43(4):47–57. doi: 10.3208/sandf.43.4_47.

Monecke, Katrin, Flavio S. Anselmetti, Arnfried Becker, Michael Schnellmann, Michael Sturm, and Domenico Giardini. 2007. "Earthquake-Induced Deformation Structures in Lake Deposits: A Late Pleistocene to Holocene Paleoseismic Record for Central Switzerland." *Eclogae Geologicae Helvetiae* 99(3):343–62. doi: 10.1007/s00015-006-1193-x.

Moon, V., and W. D. Lange. 2017. "Potential Shallow Seismic Sources in the Hamilton Basin: Final Report for EQC Project No 16/717."

Nicol, A., H. Seebeck, and L. Wallace. 2017. "Quaternary Tectonics of New Zealand." *Shulmeister J, Editor, Landscape and Quaternary Environmental Change in New Zealand. Atlantis Advances in Quaternary Science* 3:1–34. doi: 10.2991/978-94-6239-237-3_1.

Obermeier, S. F. 1998. "Liquefaction Evidence for Strong Earthquakes of Holocene and Latest Pleistocene Ages in the States of Indiana and Illinois, USA." *Engineering Geology* 50(3–4):227–254. doi: 10.1016/S0013-7952(98)00032-5.

Olson, Scott M., Stephen F. Obermeier, and Timothy D. Stark. 2001. "Interpretation of Penetration Resistance for Back-Analysis at Sites of Previous Liquefaction." *Seismological Research Letters* 72(1):46–59. doi: 10.1785/gssrl.72.1.46.

Orense, R. P., M. B. Asadi, M. E. Stringer, and M. J. Pender. 2020. "Evaluating Liquefaction Potential of Pumiceous Deposits Trough Field Testing: Case Study of the Edgecumbe Earthquake." 53(2):101–10.

Orense, R. P., M. J. Pender, and a S. O'Sullivan. 2012. "Liquefaction Characteristics of Pumice Sands." *EQC Project 10/589*.

Orense, R., W. Vargas-Monge, and J. Cepeda. 2002. "Geotechnical Aspects of the January 13, 2001 El Salvador Earthquake." *Soils and Foundations* 42(4):57–68. doi: 10.3208/sandf.42.4_57.

Pender, M. J., T. W. Robertson, D. Gilion, N. Jennings, and G. Pemberton. 1987. "Edgecumbe Earthquake: Reconaissance Report." *Bulletin of the New Zealand Society for Earthquake Engineering,* 20(3):201–49.

Pender, M. J., L. D. Wesley, T. J. Larkin, and S. Pranjoto. 2006. "Geotechnical Properties of a Pumice Sand." *Soils and Foundations* 46(1):69–81. doi: 10.3208/sandf.46.69.

Persaud, M., P. Villamor, K. R. Berryman, W. Ries, J. Cousins, N. Litchfield, and B. V. Alloway. 2016. "The Kerepehi Fault, Hauraki Rift, North Island, New Zealand: Active Fault Characterisation and Hazard." *New Zealand Journal of Geology and Geophysics* 59:117–35. doi: 10.1080/00288306.2015.1127826.

Porcino, Daniela Dominica, Theodoros Triantafyllidis, Torsten Wichtmann, and Giuseppe Tomasello. 2022. "Using Different State Parameters for Characterizing Undrained Static and Cyclic Behaviour of Sand with Non-Plastic Fines." *Soil Dynamics and Earthquake Engineering* 159(May):107318-(1-17). doi: 10.1016/j.soildyn.2022.107318.

Rees, Sean David. 2010. "Effects of Fines on the Undrained Behaviour of Christchurch Sandy Soils." University of Canterbury.

Robertson, P. K., C. E. Wride, B. R. List, U. Atukorala, K. W. Biggar, P. M. Byrne, R. G. Campanella, D. C. Cathro, D. H. Chan, K. Czajewski, W. D. L. Finn, W. H. Gu, Y. Hammamji, B. A. Hofmann, J. A. Howie, J. Hughes, A. S. Imrie, J. M. Konrad, A. Kupper, T. Law, E. R. F. Lord, P. A. Monahan, N. R. Morgenstern, R. Phillips, R. Piche, H. D. Plewes, D. Scott, D. C. Sego, J. Sobkowicz, R. A. Stewart, B. D. Watts, D. J. Woeller, T. L. Youd, and Z. Zavodni. 2000. "The CANLEX Project: Summary and Conclusions." *Canadian Geotechnical Journal* 37(3):563–91. doi: 10.1139/t00-046.

Rodríguez-López, Juan Pedro, Nieves Meléndez, Ana Rosa Soria, Carlos Luis Liesa, and A. J. Van Loon. 2007. "Lateral Variability of Ancient Seismites Related to Differences in Sedimentary Facies (the Synrift Escucha Formation, Mid-Cretaceous, Eastern Spain)." *Sedimentary Geology* 201(3–4):461–484. doi: 10.1016/j.sedgeo.2007.07.009.

Rodríguez-Pascua, M. A., V. H. Garduño-Monroy, I. Israde-Alcántara, and R. Pérez-López. 2010. "Estimation of the Paleoepicentral Area from the Spatial Gradient of Deformation in Lacustrine Seismites (Tierras Blancas Basin, Mexico)." *Quaternary International* 219(1–2):66–78. doi: 10.1016/j.quaint.2009.11.006.

Rollins, K. M., Jorgensen, S. J., & Ross, T. E. (1998). Optimum moisture content for dynamic compaction of collapsible soils. *Journal of geotechnical and geoenvironmental engineering*, *124*(8), 699-708.

Rolo, R., J. J. Bommer, B. F. Houghton, J. W. Vallance, P. Berdousis, C. Mavrommati, and W. Murphy. 2004. "Geologic and Engineering Characterization of Tierra Blanca Pyroclastic Ash Deposits." *Special Paper 375 of the Geological Society of America* 55–67. doi: 10.1130/0-8137-2375-2.55.

Rowley, John R., and A. Orville Dahl. 1956. "Modifications in Design and Use of the Livingstone Piston Sampler." *Ecology* 37:849–51. doi: 10.2307/1933080.

Santucci de Magistris, Filippo, and Lorenza Evangelista. 2007. "Simplified Assessment of the Liquefaction Susceptibility for the City of Naples, Italy." in *4th International Conference on Earthquake Geotechnical Engineering, p.n.1491*.

Saucier, R. T. 1991. "Geoarchaeological Evidence of Strong Prehistoric Earthquakes in the New Madrid (Missouri) Seismic Zone." *Geology* 19(4):296–298. doi: 10.1130/0091-7613(1991)019<0296:GEOSPE>2.3.CO;2.

Seed, H. B., and I. M. Idriss. 1971. "Simplified Procedure for Evaluating Soil Liquefaction Potential." *ASCE J Soil Mech Found Div* 97:1249–73.

Seed, H. Bolton. 1979a. "Closure to Soil Liquefaction and Cyclic Mobility Evaluation for Level Ground during Earthquakes." *Journal of Geotechnical Engineering Division* 105(2):201–255.

Seed, H. Bolton. 1979b. "Soil Liquefaction and Cyclic Mobility Evaluation for Level Ground during Earthquakes." *ASCE J Geotech. Eng. Div.* 2:201–55.

Seed, H. Bolton, and Kenneth L. Lee. 1966. "Liquefaction of Saturated Sands during Cyclic Loading." *Journal of the Soil Mechanics and Foundations Division* 92(6):105–34. doi:

10.1061/jsfeaq.0000913.

Seed, H. Bolton, and William H. Peacock. 1971. “Test Procedures for Measuring Soil Liquefaction Characteristics.” *Journal of the Soil Mechanics and Foundations Division* 97(8):1099–1119. doi: 10.1061/jsfeaq.0001649.

Seed, Raymond B., K. O. Cetin, R. E. S. Moss, A. M. Kammerer, J. Wu, J. M. Pestana, M. F. Riemer, R. B. Sancio, J. D. Bray, R. E. Kayen, and A. Faris. 2003. “Recent Advances in Soil Liquefaction Engineering : A Unified and Consistent Framework.” *Report No.EERC 2003-06, Earthquake Engineering Research Center* (March 2017):1–72. doi: EERC 2003-06.

Shane, Phil. 2017. “The Southern End of the Pacific Ring of Fire: Quaternary Volcanism in New Zealand.” *Landscape and Quaternary Environmental Change in New Zealand. Atlantis Advances in Quaternary Science* 3:35–66. doi: 10.2991/978-94-6239-237-3_2.

Shilts, W. W., and J. J. Clague. 1992. “Documentation of Earthquake-Induced Disturbance of Lake Sediments Using Subbottom Acoustic Profiling.” *Canadian Journal of Earth Sciences* 29(5):1018–42. doi: 10.1139/e92-084.

Sladen, J. A., and Handford, G. 1987. "A Potential Systematic Error in Laboratory Testing of Very Loose Sands" *Canadian Geotechnical Journal,* 24, 462-466.

Standards, Working Group in the Committee for Propagating Japanese Technical, and The Committee for Propagating Japanese Technical Standards Abroad. 2020. *Technical Standards and Commentaries for Port and Harbour Facilities in Japan “Ground Liquefaction.”* MLIT (Ministry of Land, Infrastructure, Transport and Tourism, Japan).

Stirling, M., G. McVerry, M. Gerstenberger, N. Litchfield, R. Van Dissen, K. Berryman, P. Barnes, L. Wallace, P. Villamor, and Langridge R. 2012. “National Seismic Hazard Model for New Zealand: 2010 Update.” *Bulletin of the Seismological Society of America* 102(4):1514–42.

Stringer, M. E. 2019. “Separation of Pumice from Soil Mixtures.” *Soils and Foundations* 59(4):1073–84. doi: 10.1016/j.sandf.2019.05.004.

Stringer, Mark. 2022. “Response of Pumice-Rich Soils to Cyclic Loading.” Pp. 1–15 in *Conference on Performance-based Design in Earthquake. Geotechnical Engineering.* Cham: Springer International Publishing, 2022.

Suzuki, Motoyuki, and Tetsuro Yamamoto. 2004. “Liquefaction Characteristic of Undisturbed Volcanic in Cyclic Triaxial Test.” P. p.n.465 in *13th World Conference on Earthquake Engineering Vancouver*.

Talaganov, Kosta V. 1996. “Stress-Strain Transformations and Liquefaction of Sands.” *Soil Dynamics and Earthquake Engineering* 15(7):411–418. doi: 10.1016/0267-7261(96)00024-3.

Talwani, Pradeep, and William T. Schaeffer. 2001. “Recurrence Rates of Large Earthquakes in the South Carolina Coastal Plain Based on Paleoliquefaction Data.” *Journal of Geophysical Research: Solid Earth* 106:6621–42. doi: 10.1029/2000jb900398.

Taylor, M. L., M. Cubrinovski, B. A. Bradley, and K. Horikoshi. 2013. “The Undrained Cyclic Strength of Undisturbed and Reconstituted Christchurch Sands.” *Proc. 19th NZGS Geotechnical Symposium*.

Terzaghi, Karlo, and Ralph B. Peck. 1967. *Soil Mechanics in Engineering Practice*. Second edi. Wiley International, New York, 1967.

Thevanayagam, S., T. Shenthan, S. Mohan, and J. Liang. 2002. "Undrained Fragility of Clean Sands, Silty Sands, and Sandy Silts." *Journal of Geotechnical and Geoenvironmental Engineering* 128(10):849–59. doi: 10.1061/(asce)1090-0241(2002)128:10(849).

Towhata, Ikuo, Shigeru Goto, Yuichi Taguchi, Toshihiko Hayashida, Yuki Shintaku, and Yuki Hamada. 2016. "On Ageing of Liquefaction Resistance of Sand." Pp. 800–805 in *Japanese Geotechnical Society Special Publication 2.21*.

Tuttle, Martitia P. 2001. "The Use of Liquefaction Features in Paleoseismology: Lessonslearned in the New Madrid Seismic Zone, Central United States." *Journal of Seismology* 5(3):361–80. doi: 10.1023/A:1011423525258.

Tuttle, Martitia P., Ross Hartleb, Lorraine Wolf, and Paul W. Mayne. 2019. "Paleoliquefaction Studies and the Evaluation of Seismic Hazard." *Geosciences (Switzerland)* 9(7):311.

Tuttle, Martitia P., Eugene S. Schweig, John D. Sims, Robert H. Lafferty, Lorraine W. Wolf, and Marion L. Haynes. 2002. "The Earthquake Potential of the New Madrid Seismic Zone." *Bulletin of the Seismological Society of America* 92(6):2080–2089. doi: 10.1785/0120010227.

Tuttle, Martitia P., Pilar Villamor, Peter Almond, Sarah Bastin, Monica Giona Bucci, Robert Langridge, Kate Clark, and Caroline M. Hardwick. 2017. "Liquefaction Induced during the 2010-2011 Canterbury, New Zealand, Earthquake Sequence and Lessons Learned for the Study of Paleoliquefaction Features." *Seismological Research Letters* 88(5):1403–14. doi: 10.1785/0220170073.

Üner, Serkan. 2014. "Seismogenic Structures in Quaternary Lacustrine Deposits of Lake Van (Eastern Turkey)." *Geologos* 20(2):79–87. doi: 10.2478/logos-2014-0011.

USGS - Open file report 01-041. 2001. *Clay Mineral Identification Flow Diagram*.

Uzuoka, R., N. Sento, M. Kazama, and T. Unno. 2005. "Landslides during the Earthquakes on May 26 and July 26, 2003 in Miyagi, Japan." *Soils and Foundations* 45(4):149–63. doi: 10.3208/sandf.45.4_149.

V., Deutsches Institut für Normen e. 2018. "DIN EN ISO 17982-8, 2018." *Geotechnical Investigation and Testing - Laboratory Testing of Soil - Part 8: Unconsolidated Undrained Triaxial Test (ISO 17892-8:2018); German Version EN ISO 17892-8:2018*.

Vaid, Y. P., and S. Sivathayalan. 1996. "Static and Cyclic Liquefaction Potential of Fraser Delta Sand in Simple Shear and Triaxial Tests." *Canadian Geotechnical Journal* 33(2):281–89. doi: 10.1139/t96-007.

Vardanyan, A. A., A. M. Korzhenkov, A. A. Sorokin, and R. Yu Stakhovskaya. 2018. "Paleogeographic Conditions and Age of a Strong Earthquake According to Data from Studying of the Holocene Deposits from Lake Sevan, Armenia." *Izvestiya - Atmospheric and Ocean Physics* 54(8):859–66. doi: 10.1134/S0001433818080145.

Verdugo, Ramon, and Kenji Ishihara. 1996. "The Steady State of Sandy Soils." *Soils and Foundations* 36(2):81–91. doi: 10.3208/sandf.36.2_81.

Verma, Priyesh, Ainur Seidalinova, and Dharma Wijewickreme. 2019. "Equivalent Number of Uniform Cycles versus Earthquake Magnitude Relationships for Fine-Grained Soils." *Canadian Geotechnical Journal* 56(11):1596–1608. doi: 10.1139/cgj-2018-0331.

Villamor, P., P. Almond, M. P. Tuttle, M. Giona-Bucci, R. M. Langridge, K. Clark, W. Ries, S. H. Bastin, A. Eger, M. Vandergoes, M. C. Quigley, P. Barker, F. Martin, and J. Howarth. 2016.

"Liquefaction Features Produced by the 2010-2011 Canterbury Earthquake Sequence in Southwest Christchurch, New Zealand, and Preliminary Assessment of Paleoliquefaction Features." *Bulletin of the Seismological Society of America* 106(4). doi: 10.1785/0120150223.

Villamor, Pilar, K. Clark, G. Coffey, J. W. Hughes, H. G. Hogg, J. Moratalla, and K. Thingbaijam. 2024. "The Te Puninga Fault, Hauraki Plains: A New Seismic Source in the Low Seismicity Northern Region of New Zealand." *New Zealand Journal of Geology and Geophysics*. doi: https://doi.org/10.1080/00288306.2023.2296875.

Wang, Jaw Nan, and Edward Kavazanjian. 1989. "Pore Pressure Development during Non-Uniform Cyclic Loading." *Soils and Foundations* 29(2):1–14. doi: 10.3208/sandf1972.29.2_1.

Wesley, L. D., V. M. Meyer, S. Pranyoto, M. J. Pender, T. J. Larkin, and G. C. Duske. 1999. "Engineering Properties of a Pumice Sand." Pp. 901–7 in *Consolidating knowledge. Proceedings of the 8th Australia New Zealand conference on geomechanics, Hobart, February*.

Wesley, Laurence D. 2001. "Determination of Specific Gravity and Void Ratio of Pumice Materials." *Geotechnical Testing Journal* 24(4):418–22. doi: 10.1520/gtj11139j.

White, J. D. L., and B. F. Houghton. 2006. "Primary Volcaniclastic Rocks." *Geology* 34(8):677–80. doi: 10.1130/G22346.1.

Whitton, J. S., and G. J. Churchman. 1987. "Standard Methods for Mineral Analysis of Soil Survey Samples for Characterisation and Classification in NZ Soil Bureau." *New Zealand Soil Bureau Scientific Report* 79:1–27.

Wichtmann, Torsten. 2016. "Soil Behaviour under Cyclic Loading - Experimental Observations, Constitutive Description and Applications." *Publications of the Institute of Soil Mechanics and Rock Mechanics, Karlsruhe Institute of Technology (KIT)*.

Yamamoto, Yoichi, Masayuki Hyodo, and Rolando P. Orense. 2009. "Liquefaction Resistance of Sandy Soils under Partially Drained Condition." *Journal of Geotechnical and Geoenvironmental Engineering* 135(8):1032–43. doi: 10.1061/(asce)gt.1943-5606.0000051.

Yoshimine, Mitsutoshi, Hiroto Nishizaki, Kei Amano, and Yasuyo Hosono. 2006. "Flow Deformation of Liquefied Sand under Constant Shear Load and Its Application to Analysis of Flow Slide of Infinite Slope." *Soil Dynamics and Earthquake Engineering* 26(2–4):253–64. doi: 10.1016/j.soildyn.2005.02.016.

Youd, T. L., and S. N. Hoose. 1977. "Liquefaction Susceptibility and Geologic Setting." *The 6th World Conference on Earthquake Engineering, Vol. 6. Roorkee, India: Indian Society of Earthquake Technology* 2189–94.

Youd, T. Leslie. 1984. "Reccurence of Liquefaction at the Same Site." Pp. 231–38 in *8th World Conference on Earthquake Engineering, Prentice-Hall Inc.*

Youd, T. Leslie, and Izzat M. Idriss. 1997. "Proceedings of the NCEER Workshop on Evaluation of Liquefaction Resistance of Soils. Held in Salt Lake City, Utah on January 5-6, 1996." *Technical Report NCEER-97-0022*. doi: 10.1017/CBO9781107415324.004.

Youd, T. Leslie, and David M. Perkins. 1978. "Mapping Liquefaction-Induced Ground Failure Potential." *ASCE J Geotech Eng Div* 104(4):433–46.

Zlatovic, Sonja. 1994. "Residual Strenght of Silty Soils." University of Tokio.

# Appendix A: Supplementary figures, tables and equation

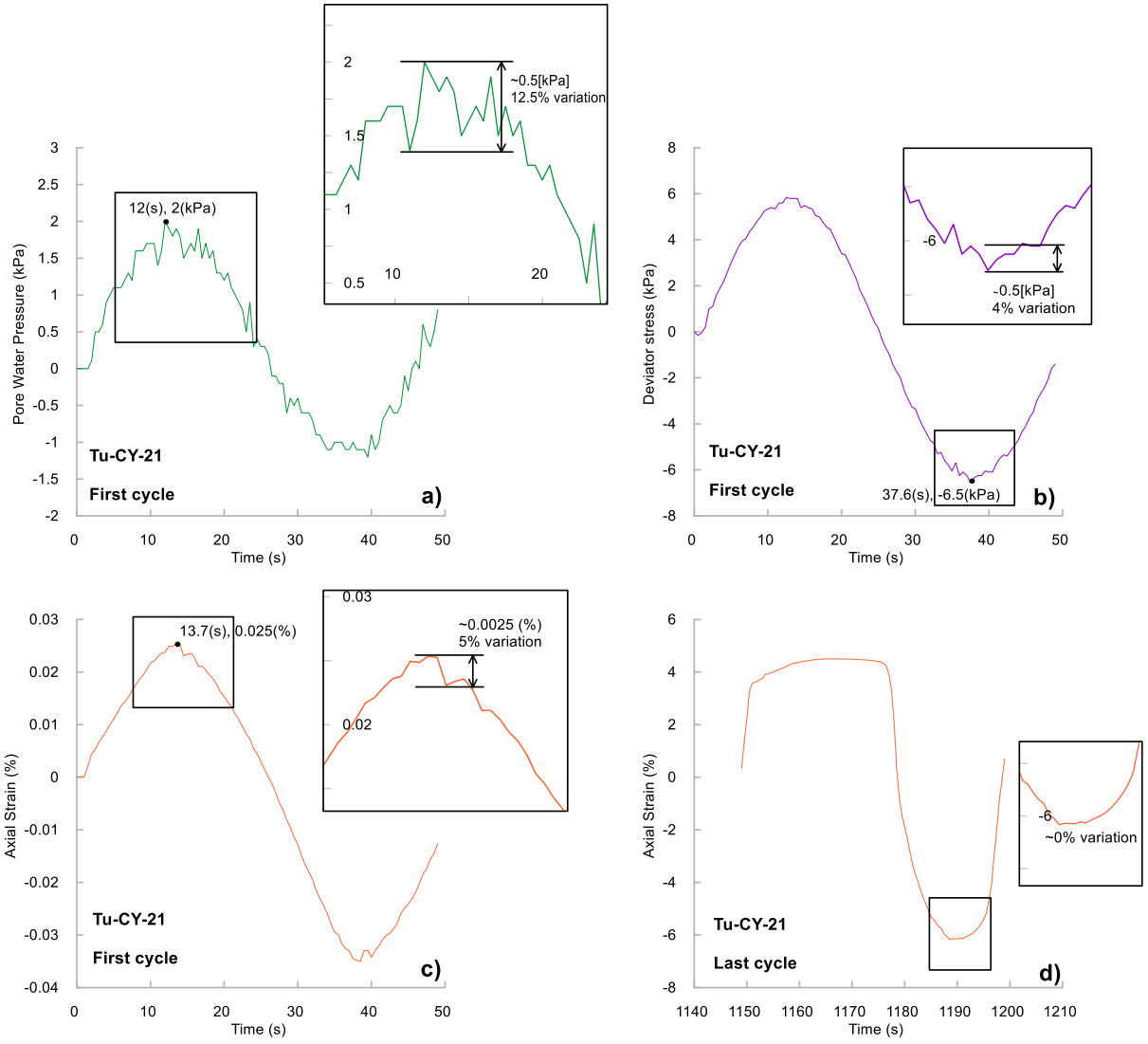


Fig. S1. Pore water pressure (a), deviator stress (b) and axial strain (c) and (d) vs time plots for a single cycle (first or last) of test Tu-CY-21, showing the transducer oscillations in order to confirm the data quality of the tests

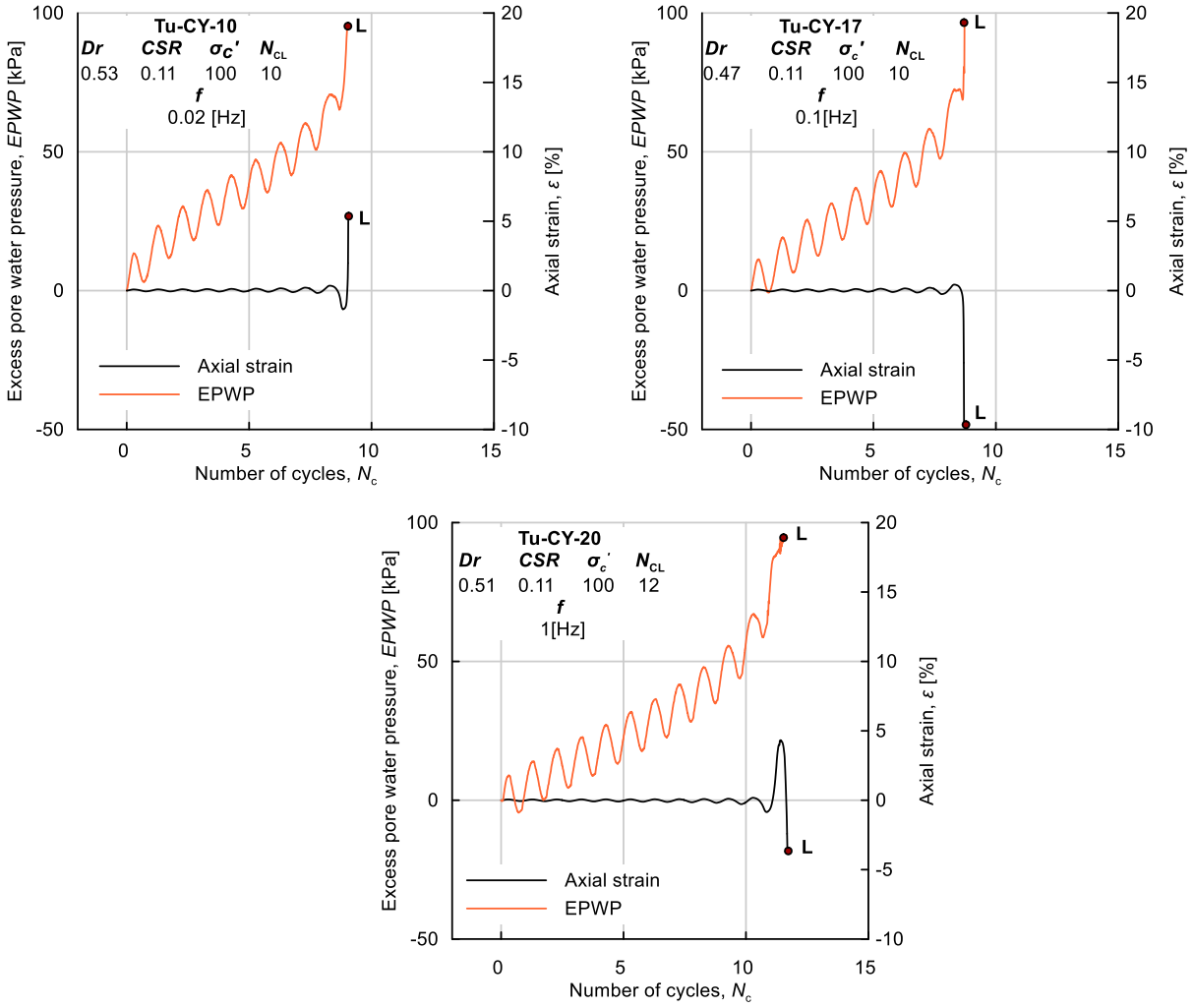


Fig. S2. Developments of axial strain and excess pore water pressure for tests Tu-CY-10, Tu-CY-17 and Tu-CY-20 that were tested under the similar conditions by means of relative density, ($\boldsymbol{Dr} \approx 0.5$), effective consolidation stress ($\boldsymbol{\sigma_c}' = 100$kPa) and same cyclic stress ratio ($CSR = 0.11$) with a different loading frequency ($\boldsymbol{f} = 0.02$, 0.1 and 1 Hz respectively)

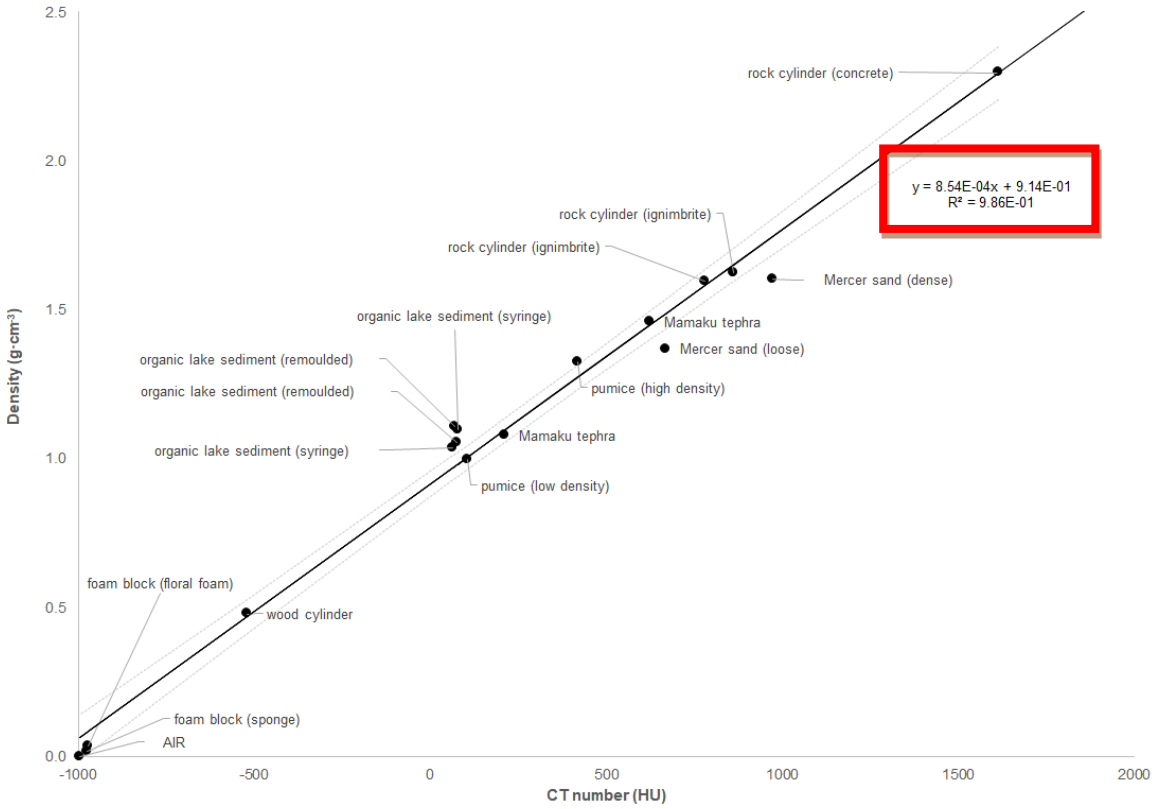


Fig. S3. Mean CT numbers and measured densities for manually segmented materials Regression equation shown in the top right corner (Ilanko et al. unpublished data)

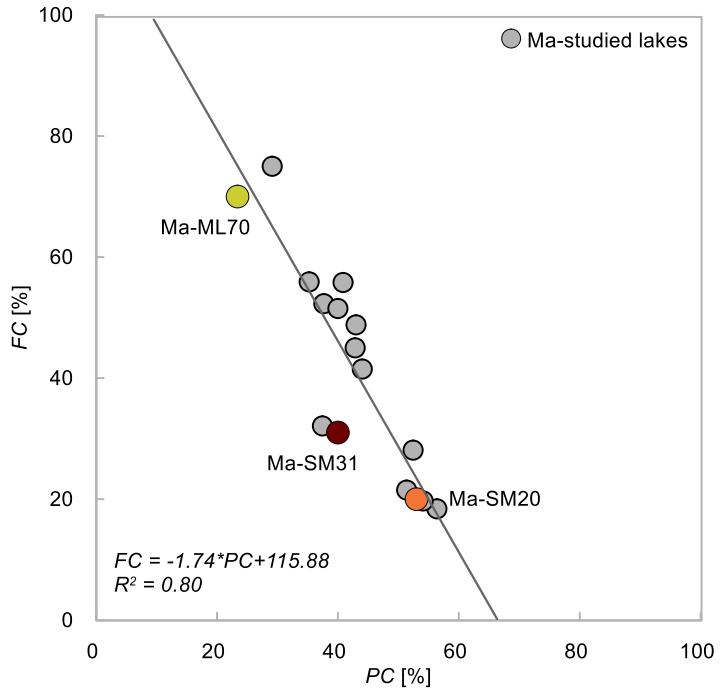


Fig. S4. Correlation between *FC* and *PC* for the three tested beds of Mamaku, as well as the Mamaku tephra layers from the other studied lakes.

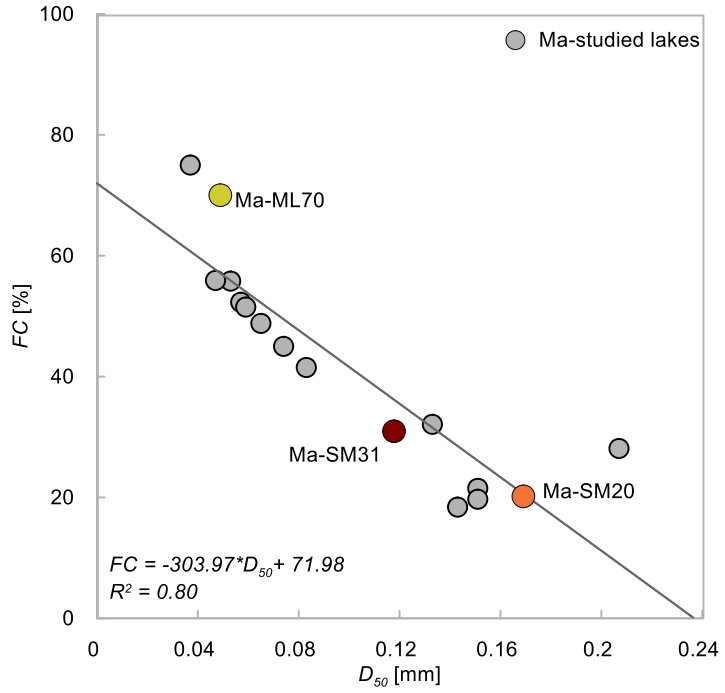


Fig. S5. Correlation between *FC* and $D_{50}$ for the three tested beds of Mamaku, as well as the Mamaku tephra layers from the other studied lakes.

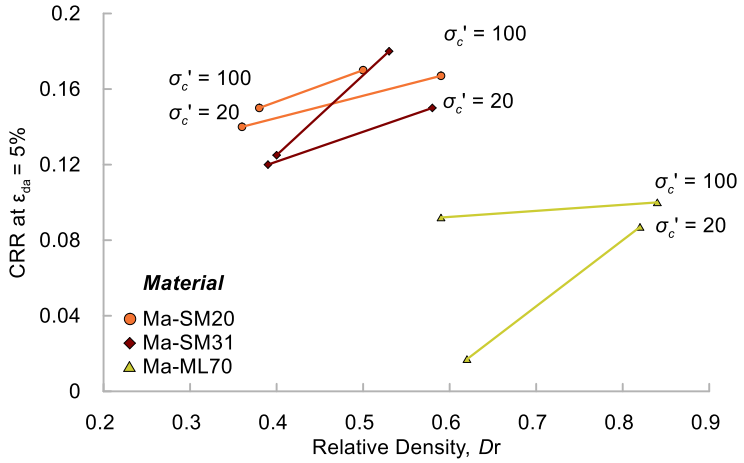


Fig. S6. *CRR* (at $\varepsilon_{da}$ = 5%) vs *D*r for the three tested beds of Mamaku tephra for both used consolidation stresses, 20 kPa and 100 kPa, showing the correlation between the *CRR* and consolidation stress

Table S1. Void ratio and relative density, initial as well as consolidated values, from both method (1) based on sample dimensions before testing and sample volume loss during consolidation and method (2) based on the Verdugo and Ishihara (1996) procedure

| Test series | Type of test | Label | $e_i$ | $Dr_{,i}$ | $e_{c1}$ | $e_{c2}$ | $Dr_{,c1}$ | $Dr_{,c2}$ | $e_c$ | $Dr_{,c}$ |
|---|---|---|---|---|---|---|---|---|---|---|
| 1 | Monotonic | Tu-CU-1 | 1.80 | 0.34 | 1.61 | 0.51 | n/a | n/a | 1.61 | 0.51 |
| | Monotonic | Tu-CU-3 | 1.51 | 0.60 | 1.41 | 0.69 | 1.42 | 0.68 | 1.42 | 0.69 |
| | Monotonic | Tu-CU-2 | 1.80 | 0.34 | 1.61 | 0.51 | n/a | n/a | 1.61 | 0.51 |
| | Monotonic | Tu-CU-4 | 1.53 | 0.58 | 1.45 | 0.65 | 1.46 | 0.64 | 1.46 | 0.65 |
| | Monotonic | Tu-CU-5 | 1.39 | 0.71 | 1.31 | 0.78 | 1.34 | 0.75 | 1.33 | 0.77 |
| | Monotonic | Tu-CUE-1 | 1.77 | 0.37 | 1.62 | 0.50 | n/a | n/a | 1.62 | 0.51 |
| | Monotonic | Tu-CUE-2 | 1.76 | 0.38 | 1.62 | 0.51 | 1.62 | 0.50 | 1.62 | 0.50 |
| 2 | Cyclic | Tu-CY-12 | 1.85 | 0.29 | 1.69 | 0.44 | n/a | n/a | 1.69 | 0.44 |
| | Cyclic | Tu-CY-11 | 1.79 | 0.35 | 1.62 | 0.50 | n/a | n/a | 1.62 | 0.5 |
| | Cyclic | Tu-CY-10 | 1.76 | 0.38 | 1.59 | 0.53 | n/a | n/a | 1.59 | 0.53 |
| | Cyclic | Tu-CY-7 | 1.82 | 0.33 | 1.65 | 0.47 | n/a | n/a | 1.65 | 0.47 |
| 3 | Cyclic | Tu-CY-4 | / | / | n/a | n/a | 1.45 | 0.65 | 1.45 | 0.65 |
| | Cyclic | Tu-CY-5 | 1.48 | 0.63 | 1.38 | 0.72 | 1.49 | 0.62 | 1.43 | 0.67 |
| | Cyclic | Tu-CY-2 | 1.45 | 0.65 | 1.38 | 0.72 | n/a | n/a | 1.38 | 0.72 |
| | Cyclic | Tu-CY-6 | 1.49 | 0.62 | 1.39 | 0.71 | 1.40 | 0.70 | 1.40 | 0.7 |
| 4 | Cyclic | Tu-CY-18 | 1.85 | 0.29 | 1.76 | 0.37 | 1.53 | 0.58 | 1.65 | 0.48 |
| | Cyclic | Tu-CY-16 | 1.83 | 0.32 | 1.74 | 0.40 | n/a | n/a | 1.74 | 0.4 |
| | Cyclic | Tu-CY-15 | 1.81 | 0.33 | 1.61 | 0.51 | n/a | n/a | 1.61 | 0.51 |
| | Cyclic | Tu-CY-14 | 1.81 | 0.34 | 1.69 | 0.43 | n/a | n/a | 1.69 | 0.43 |
| 5 | Cyclic | Tu-CY-19 | 1.49 | 0.61 | 1.42 | 0.68 | n/a | n/a | 1.42 | 0.68 |
| | Cyclic | Tu-CY-13 | 1.52 | 0.59 | 1.44 | 0.66 | 1.44 | 0.67 | 1.44 | 0.66 |
| | Cyclic | Tu-CY-8 | 1.34 | 0.76 | 1.45 | 0.65 | 1.42 | 0.68 | 1.43 | 0.67 |
| 6 | Cyclic | Tu-CY-21 | 1.33 | 0.76 | 1.27 | 0.82 | 1.31 | 0.78 | 1.29 | 0.8 |
| | Cyclic | Tu-CY-22 | 1.35 | 0.75 | 1.28 | 0.81 | n/a | n/a | 1.28 | 0.81 |
| | Cyclic | Tu-CY-23 | 1.34 | 0.75 | 1.30 | 0.79 | 1.29 | 0.74 | 1.30 | 0.79 |
| F | Cyclic | Tu-CY-17 | 1.83 | 0.31 | 1.67 | 0.45 | n/a | n/a | 1.67 | 0.45 |
| | Cyclic | Tu-CY-20 | 1.77 | 0.37 | 1.61 | 0.51 | n/a | n/a | 1.61 | 0.51 |

n/a = not available

Table S2. Roundness coefficient (Rc), aspect ratio (Ar), and angular coefficient (Ac) for all 80 particles (20 per fraction) used in the particle shape analysis of Tuhua Silt.

| Fraction [mm] | Fraction prop. [%] | Particle | a min | b min | Length | Area | Ar | Rc | Ac | Ave. Ar | Ave Rc | Ave Ac |
|---|---|---|---|---|---|---|---|---|---|---|---|---|
| >0.25 | 14.07 | 1 | 5.8 | 9.3 | 33.3 | 53.6 | 1.6 | 1.6 | 1.4 | 1.74 | 1.40 | 1.26 |
| | | 2 | 10.9 | 14.4 | 46.1 | 134.7 | 1.3 | 1.3 | 0.9 | | | |
| | | 3 | 5.9 | 13.4 | 35.3 | 67.8 | 2.3 | 1.5 | 1.6 | | | |
| | | 4 | 8.7 | 12.2 | 34.4 | 73.4 | 1.4 | 1.3 | 1 | | | |
| | | 5 | 6 | 12.8 | 31.5 | 49.5 | 2.1 | 1.6 | 1.7 | | | |
| | | 6 | 7.6 | 12.2 | 35 | 70.3 | 1.6 | 1.4 | 1.2 | | | |
| | | 7 | 9 | 14.9 | 44 | 118.5 | 1.7 | 1.3 | 1.1 | | | |
| | | 8 | 6 | 9.9 | 30.6 | 48 | 1.6 | 1.5 | 1.4 | | | |
| | | 9 | 6.7 | 15.8 | 39.5 | 78.1 | 2.3 | 1.6 | 1.8 | | | |
| | | 10 | 7.6 | 8.6 | 26.1 | 46.9 | 1.1 | 1.2 | 0.7 | | | |
| | | 11 | 7 | 10 | 33.2 | 60.6 | 1.4 | 1.4 | 1.2 | | | |
| | | 12 | 7.1 | 12.1 | 35.1 | 73.2 | 1.7 | 1.3 | 1.2 | | | |
| | | 13 | 6 | 9.9 | 27.8 | 48.4 | 1.7 | 1.3 | 1.1 | | | |
| | | 14 | 4.4 | 14 | 36.9 | 64 | 3.2 | 1.7 | 2.3 | | | |
| | | 15 | 8 | 9.7 | 30.4 | 62.7 | 1.2 | 1.2 | 0.8 | | | |
| | | 16 | 6.3 | 10.7 | 32.4 | 60.8 | 1.7 | 1.4 | 1.2 | | | |
| | | 17 | 7 | 12.5 | 33.6 | 63.9 | 1.8 | 1.4 | 1.3 | | | |
| | | 18 | 9.2 | 10.5 | 34.6 | 74.3 | 1.1 | 1.3 | 0.9 | | | |
| | | 19 | 5.6 | 11 | 27.1 | 42.1 | 2 | 1.4 | 1.4 | | | |
| | | 20 | 6.9 | 12.6 | 29.9 | 53.9 | 1.8 | 1.3 | 1.2 | | | |
| 0.125-0.25 | 20.92 | 1 | 7.9 | 12.9 | 35.1 | 78.2 | 1.6 | 1.3 | 1.1 | 1.87 | 1.45 | 1.38 |
| | | 2 | 4.1 | 11.4 | 29.2 | 43.2 | 2.8 | 1.6 | 2 | | | |
| | | 3 | 6.8 | 16.4 | 43.2 | 85.2 | 2.4 | 1.7 | 1.9 | | | |
| | | 4 | 9.4 | 13.4 | 41.4 | 104.4 | 1.4 | 1.3 | 1 | | | |
| | | 5 | 8.5 | 11.9 | 34.4 | 76.7 | 1.4 | 1.2 | 0.9 | | | |
| | | 6 | 7.7 | 18.5 | 47.6 | 106.5 | 2.4 | 1.7 | 1.9 | | | |
| | | 7 | 6.3 | 18.8 | 48.9 | 104.1 | 3 | 1.8 | 2.3 | | | |
| | | 8 | 8.9 | 12.8 | 36.3 | 81.9 | 1.4 | 1.3 | 1 | | | |
| | | 9 | 7.5 | 10.8 | 38.4 | 76.1 | 1.4 | 1.5 | 1.3 | | | |
| | | 10 | 9.3 | 16.4 | 42.4 | 85.4 | 1.8 | 1.7 | 1.6 | | | |
| | | 11 | 7.3 | 16.9 | 41.3 | 81.4 | 2.3 | 1.7 | 1.8 | | | |
| | | 12 | 5.9 | 14.1 | 35.9 | 69.6 | 2.4 | 1.5 | 1.7 | | | |
| | | 13 | 10.1 | 16.6 | 43.7 | 113.4 | 1.6 | 1.3 | 1.2 | | | |
| | | 14 | 8.9 | 13.8 | 38 | 93.6 | 1.5 | 1.2 | 1 | | | |
| | | 15 | 8.3 | 11.9 | 33.9 | 71.6 | 1.4 | 1.3 | 1 | | | |
| | | 16 | 5 | 10.6 | 26.3 | 39.4 | 2.1 | 1.4 | 1.5 | | | |
| | | 17 | 11.1 | 20.2 | 51.7 | 151.3 | 1.8 | 1.4 | 1.3 | | | |
| | | 18 | 10.6 | 13.3 | 39.5 | 103.1 | 1.3 | 1.2 | 0.8 | | | |
| | | 19 | 8.8 | 11.4 | 35 | 78.8 | 1.3 | 1.2 | 0.9 | | | |
| | | 20 | 6.4 | 11.8 | 34.5 | 58.4 | 1.8 | 1.6 | 1.5 | | | |
| 0.063-0.125 | 19.01 | 1 | 7.3 | 13.1 | 37.9 | 78.2 | 1.8 | 1.5 | 1.4 | 1.62 | 1.42 | 1.23 |
| | | 2 | 7.1 | 9.2 | 32.3 | 57.3 | 1.3 | 1.4 | 1.1 | | | |

| | | | | | | | | | | | |
|---|---|---|---|---|---|---|---|---|---|---|---|
| | | 3 | 12.1 | 14.5 | 47.4 | 115.6 | 1.2 | 1.5 | 1.1 | | |
| | | 4 | 6.9 | 9.8 | 30.5 | 54.5 | 1.4 | 1.4 | 1.1 | | |
| | | 5 | 10.5 | 13.7 | 45.1 | 123.7 | 1.3 | 1.3 | 1 | | |
| | | 6 | 9.6 | 15.4 | 42.6 | 100.4 | 1.6 | 1.4 | 1.2 | | |
| | | 7 | 7.3 | 15.2 | 44 | 85.7 | 2.1 | 1.8 | 1.8 | | |
| | | 8 | 5 | 11.1 | 26.9 | 41.3 | 2.2 | 1.4 | 1.5 | | |
| | | 9 | 5.4 | 10.1 | 27.5 | 43.6 | 1.9 | 1.4 | 1.3 | | |
| | | 10 | 6.1 | 8.8 | 30.1 | 50.9 | 1.6 | 1.4 | 1.2 | | |
| | | 11 | 8.7 | 13.6 | 41.5 | 87.4 | 1.9 | 1.6 | 1.5 | | |
| | | 12 | 7.3 | 13.9 | 37.5 | 74.9 | 1.9 | 1.5 | 1.4 | | |
| | | 13 | 8.2 | 9.7 | 29.9 | 57.3 | 1.2 | 1.2 | 0.8 | | |
| | | 14 | 9.1 | 13.1 | 36.6 | 88.7 | 1.4 | 1.2 | 0.9 | | |
| | | 15 | 6.1 | 11.6 | 32.2 | 57.1 | 1.9 | 1.4 | 1.4 | | |
| | | 16 | 9.6 | 10.9 | 32.9 | 66.1 | 1.1 | 1.3 | 0.9 | | |
| | | 17 | 8.2 | 14.1 | 39.1 | 83.8 | 1.7 | 1.5 | 1.3 | | |
| | | 18 | 7.7 | 12.7 | 37.2 | 79.9 | 1.6 | 1.4 | 1.2 | | |
| | | 19 | 5.7 | 11.5 | 35.8 | 68.2 | 2 | 1.5 | 1.5 | | |
| | | 20 | 10 | 13.8 | 45.5 | 116.9 | 1.4 | 1.4 | 1.1 | | |
| | | 21 | 6.6 | 10.3 | 33.1 | 65.3 | 1.6 | 1.3 | 1.1 | | |
| <0.063 | 46 | 1 | 5.5 | 11.5 | 30.6 | 43.8 | 2.1 | 1.7 | 1.8 | 1.92 | 1.51 | 1.48 |
| | | 2 | 6.5 | 11.8 | 37.3 | 72.9 | 1.8 | 1.5 | 1.4 | | |
| | | 3 | 4.8 | 11.1 | 34.5 | 59.7 | 2.3 | 1.6 | 1.7 | | |
| | | 4 | 6.7 | 14.8 | 37.3 | 73.7 | 2.2 | 1.5 | 1.6 | | |
| | | 5 | 6 | 9.7 | 28.1 | 49.3 | 1.6 | 1.3 | 1.1 | | |
| | | 6 | 5 | 14.7 | 36.2 | 67.3 | 2.9 | 1.5 | 2 | | |
| | | 7 | 4.7 | 11 | 30 | 40 | 2.3 | 1.8 | 2 | | |
| | | 8 | 7.2 | 12.1 | 37.6 | 78.8 | 1.7 | 1.4 | 1.3 | | |
| | | 9 | 5.7 | 11.9 | 30.8 | 47.1 | 2.1 | 1.6 | 1.6 | | |
| | | 10 | 6.4 | 7.1 | 25.8 | 35.7 | 1.1 | 1.5 | 1 | | |
| | | 11 | 5.2 | 10.3 | 25.8 | 35.2 | 2 | 1.5 | 1.5 | | |
| | | 12 | 4.3 | 8.3 | 22.4 | 28.8 | 2 | 1.4 | 1.4 | | |
| | | 13 | 4.6 | 6.3 | 19.4 | 24.6 | 1.4 | 1.2 | 0.9 | | |
| | | 14 | 5 | 10.1 | 29.9 | 43.1 | 2 | 1.7 | 1.7 | | |
| | | 15 | 6.2 | 9.5 | 27.8 | 46.4 | 1.5 | 1.3 | 1.1 | | |
| | | 16 | 4 | 11.2 | 26.5 | 36.1 | 2.8 | 1.5 | 1.9 | | |
| | | 17 | 6.6 | 10.7 | 30.9 | 55.1 | 1.6 | 1.4 | 1.2 | | |
| | | 18 | 5.5 | 8.3 | 26.9 | 38.9 | 1.5 | 1.5 | 1.2 | | |
| | | 19 | 9.1 | 14.3 | 47.1 | 96 | 1.6 | 1.8 | 1.6 | | |
| | | | | | | | | Final values | | 1.83 | 1.47 | 1.38 |

## Equation 6.1.

The following equation thread proves the deriving of Equation (6.1):

$$\boldsymbol{e_{in-situ}} = \frac{\boldsymbol{\rho_{p,average}} - \rho_{sat}}{\rho_{sat} - \boldsymbol{\rho_{water}}} \tag{6.1}$$

A generic version of Equation (6.1) is:

$$e = \frac{\boldsymbol{\rho_p} - \rho_{sat}}{\rho_{sat} - \boldsymbol{\rho_{water}}} \tag{6.1.1}$$

where $\rho_{water}$ is the density of water, taken as 1000 kg/m3, $\rho_{sat}$ is the saturated density of the sample and $\rho_p$ is the particle density of the sample sample. Expressing the densities through the corresponding masses and volumes and assuming full saturation $V_w = V_v$ (volume of water in the voids is equal to the volume of the voids in the sample), equation (6.1) becomes:

$$e = \frac{\frac{\boldsymbol{m_p}}{V_p} - \frac{m_{p+w}}{V_{p+w}}}{\frac{m_{p+w}}{V_{p+w}} - \frac{\boldsymbol{m_w}}{V_w}} \tag{6.1.2}$$

Where, $m_p$ is the mass of the soil particles, $m_{p+w}$ is the mass of the soil particles plus the mass of the water (in the voids), $m_w$ is the mass of the water (in the voids), $V_p$ is the volume of the particles, and $V_w$ is the volume of the water.

By mathematically tidying the equation 6.1.2, we can derive:

$$e = \frac{\frac{\boldsymbol{m_p}(V_{p+w}) - \boldsymbol{m}_{p+w}(V_p)}{V_p(V_{p+w})}}{\frac{V_w(\boldsymbol{m}_{p+w}) - \boldsymbol{m_w}(V_{p+w})}{V_w(V_{p+w})}} = \frac{\frac{\boldsymbol{m_p}V_p + \boldsymbol{m_p}V_w - \boldsymbol{m}_pV_p - \boldsymbol{m}_wV_p}{V_p}}{\frac{V_w\boldsymbol{m}_p + V_w\boldsymbol{m}_w - \boldsymbol{m_w}V_p - \boldsymbol{m_w}V_p}{V_w}} = \frac{\frac{\boldsymbol{m_p}V_w - \boldsymbol{m_w}V_p}{V_p}}{\frac{V_w\boldsymbol{m}_p - \boldsymbol{m_w}V_p}{V_w}} = \frac{V_w}{V_p} = \frac{V_v}{V_p} \tag{6.1.3}$$

Finally, Equation 6.1.1, becomes:

$$\boldsymbol{e} = \frac{\boldsymbol{\rho_p} - \rho_{sat}}{\rho_{sat} - \boldsymbol{\rho_{water}}} = \frac{\boldsymbol{V_v}}{\boldsymbol{V_s}} \tag{6.1.4}$$

Equation 6.1.4 is the commonly known equation of void ratio expressed through the volume of voids and the volume of particles (soilds) of the sample.

# Appendix B.1: Undrained cyclic triaxial tests – Tuhua silt

## Test series 2:

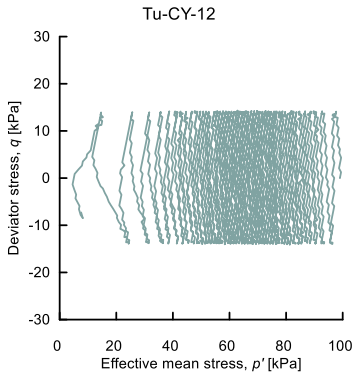


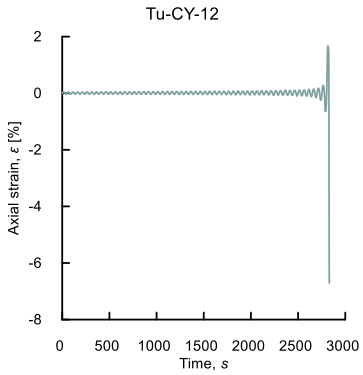


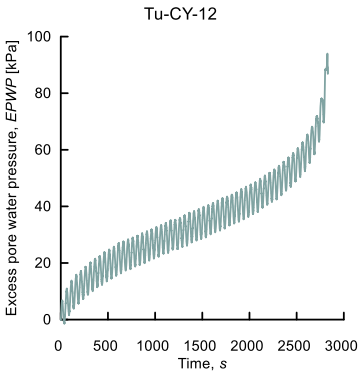


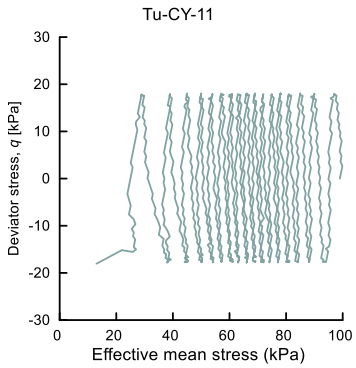


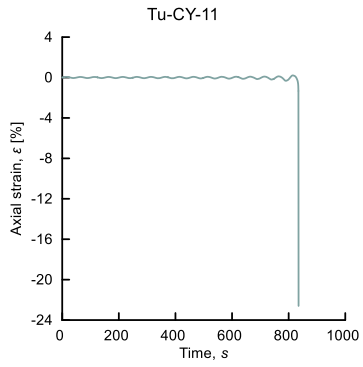


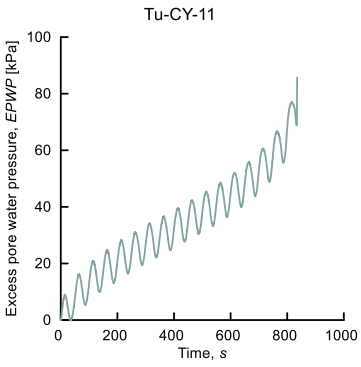


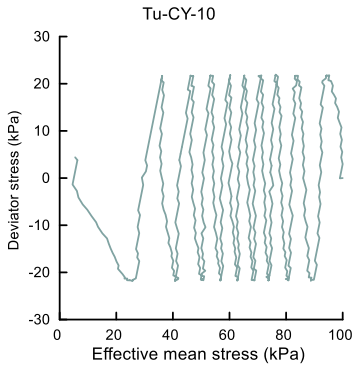


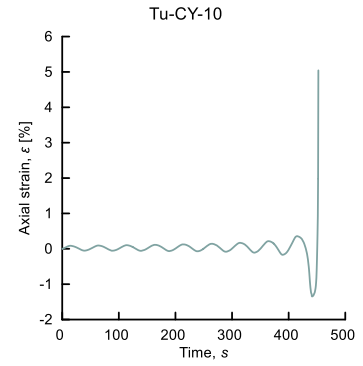


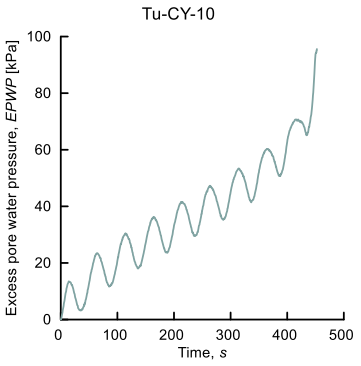


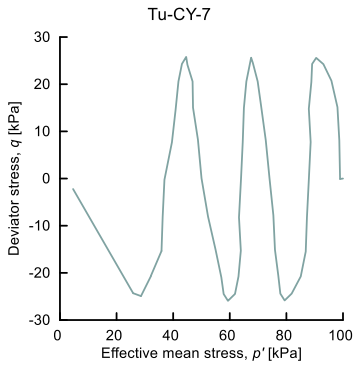


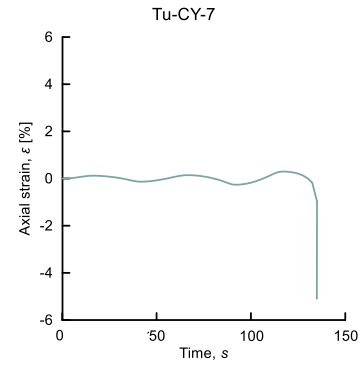


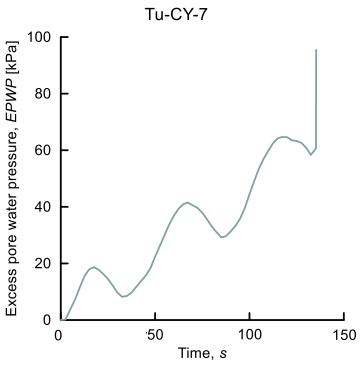

## Test series 3:

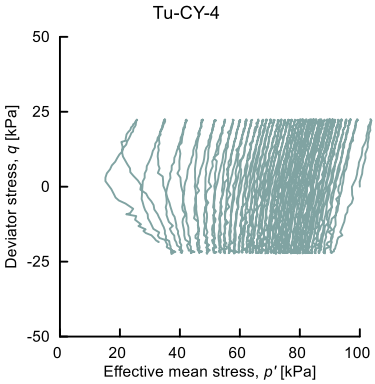


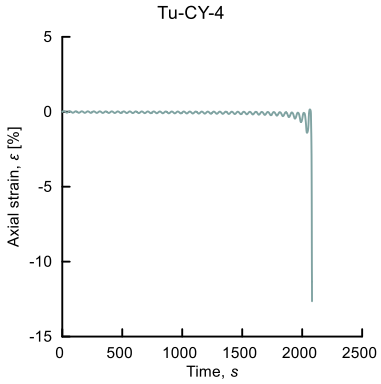


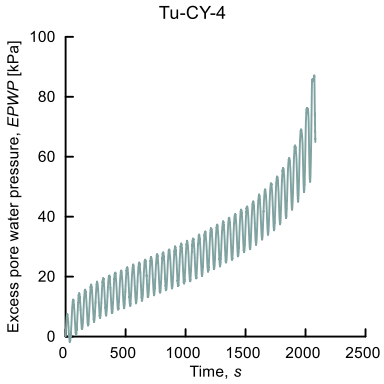


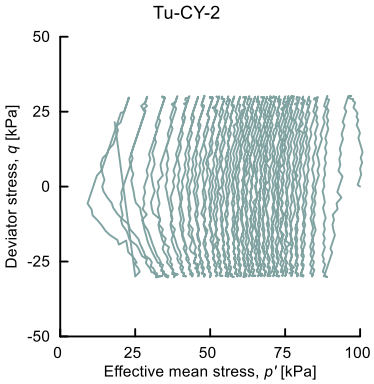


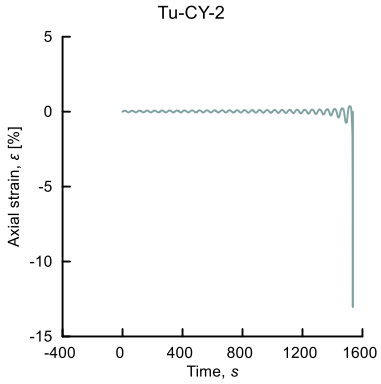


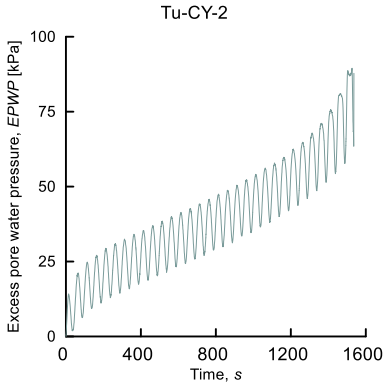


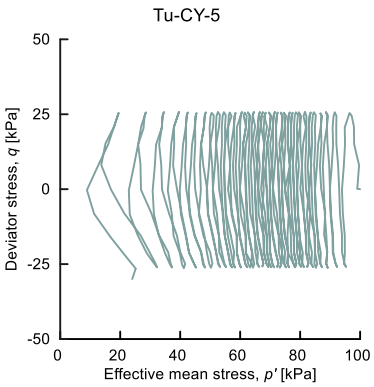


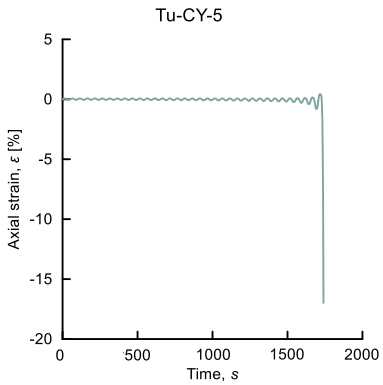


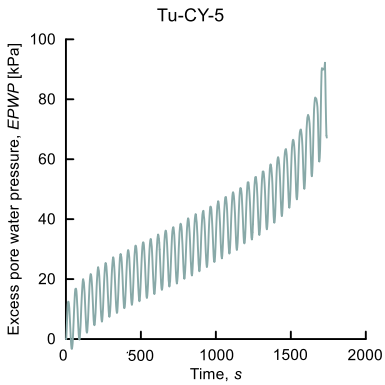


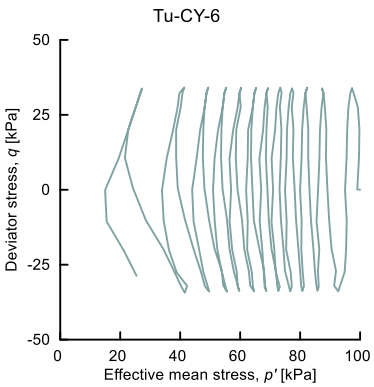


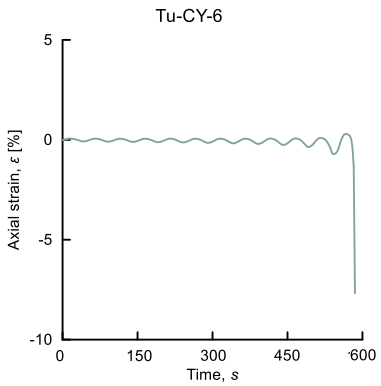


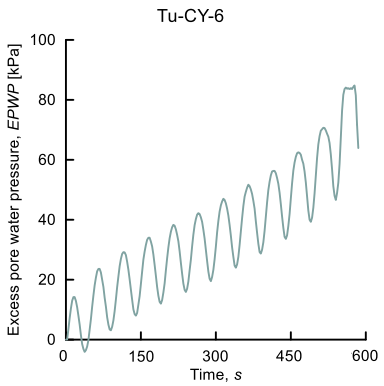

## Test series 4:

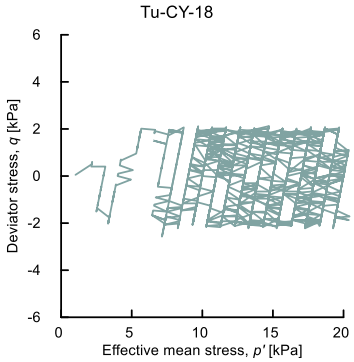


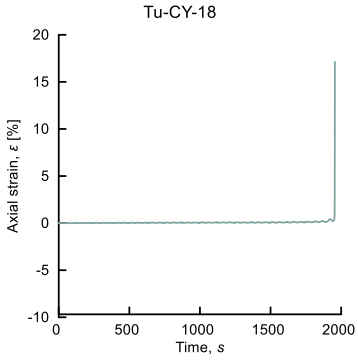


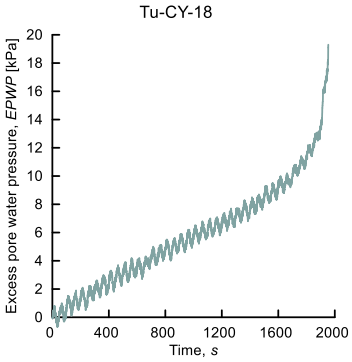


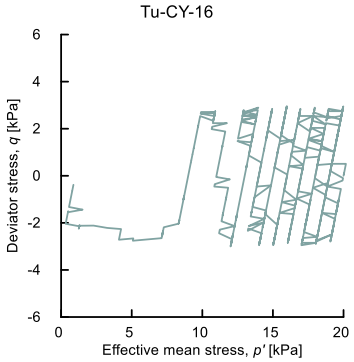


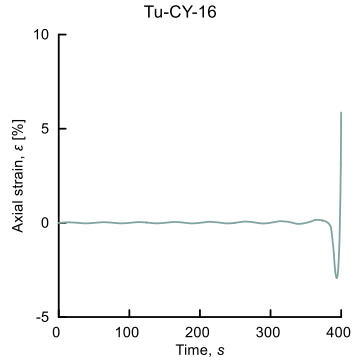


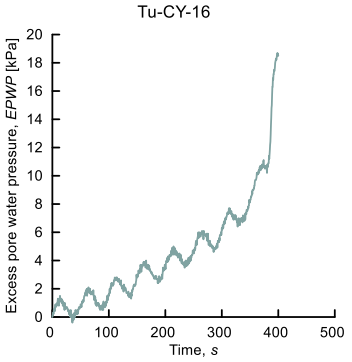


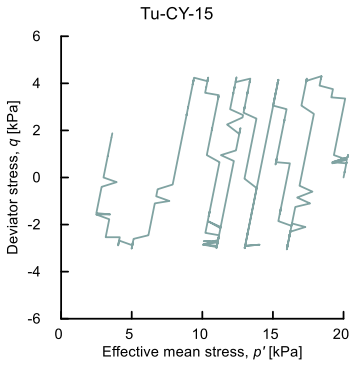


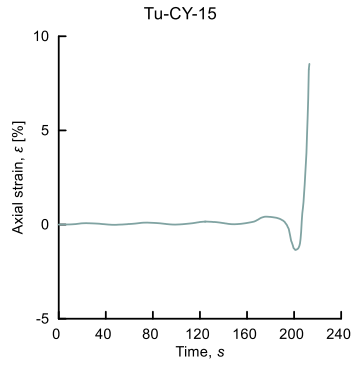


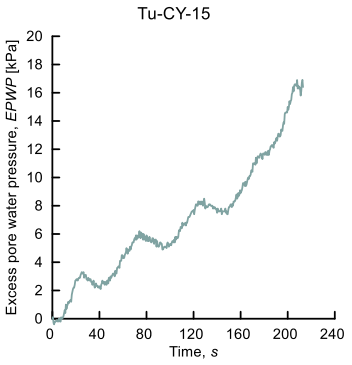


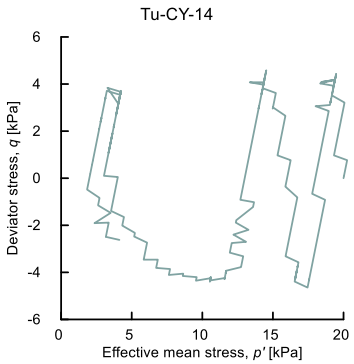


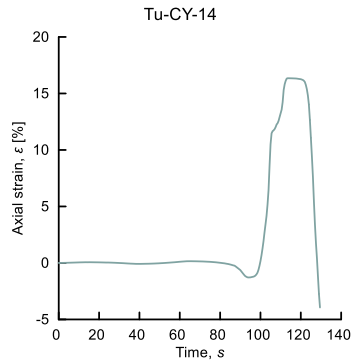


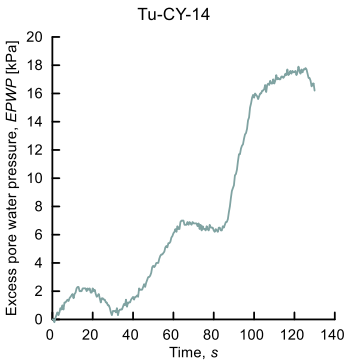

## Test series 5:

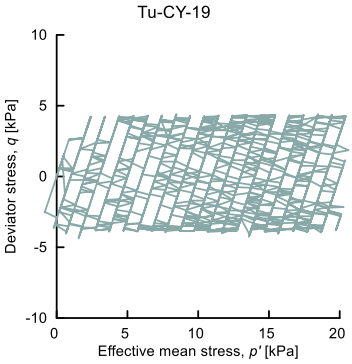


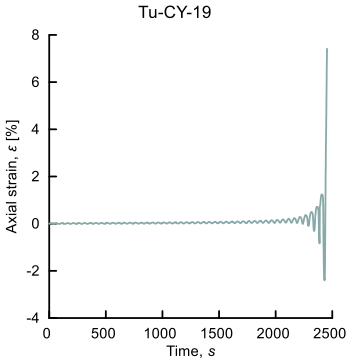


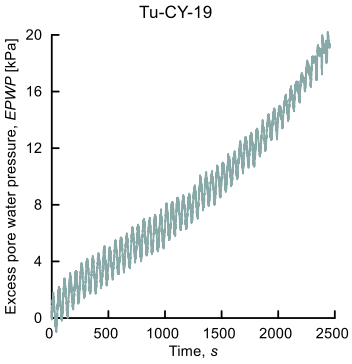


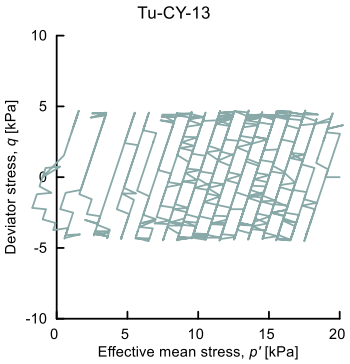


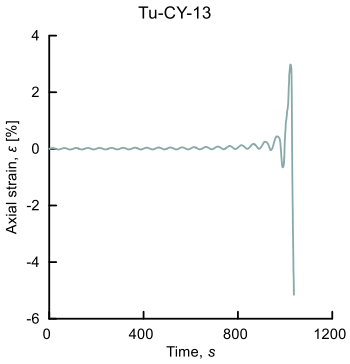


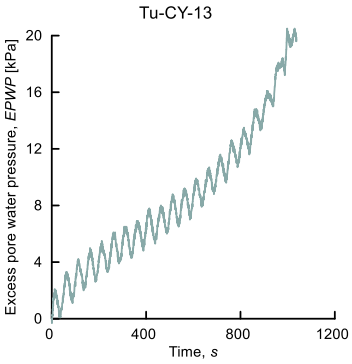


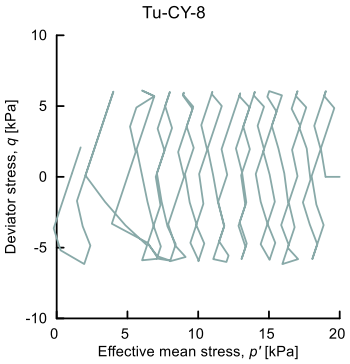


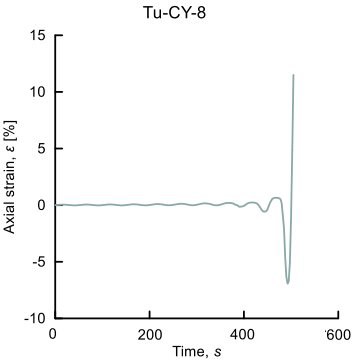


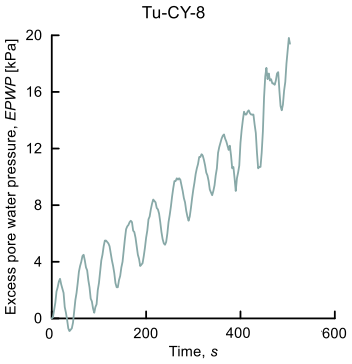

## Test series 6:

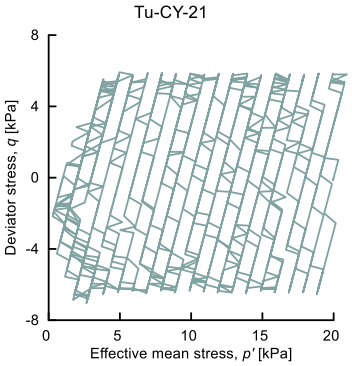


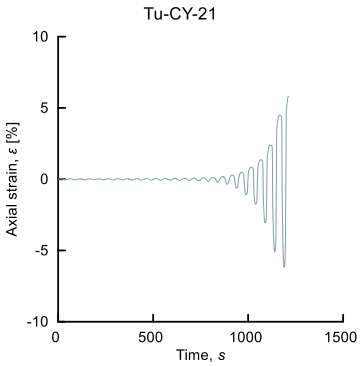


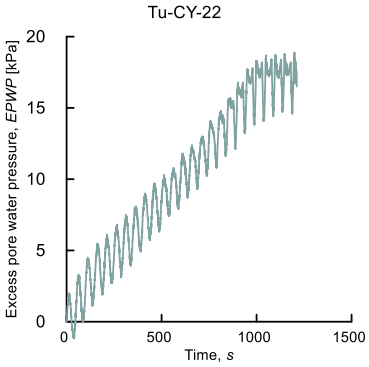


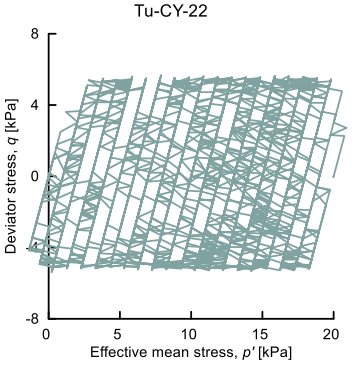


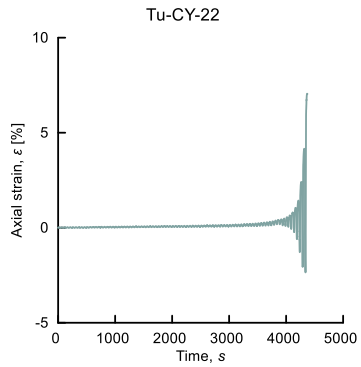


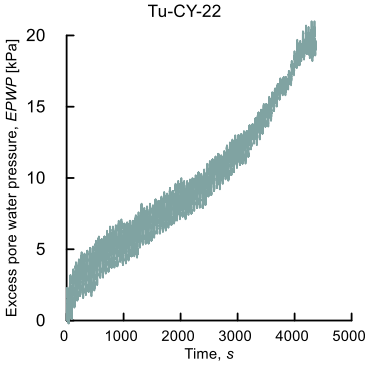


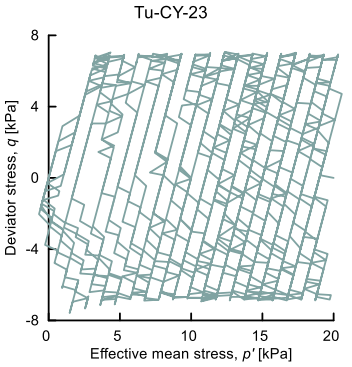


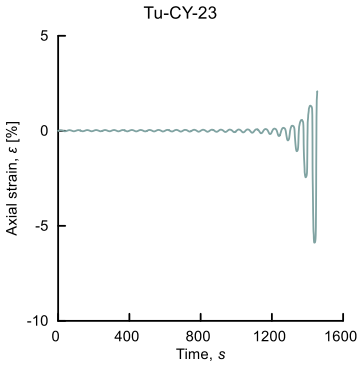


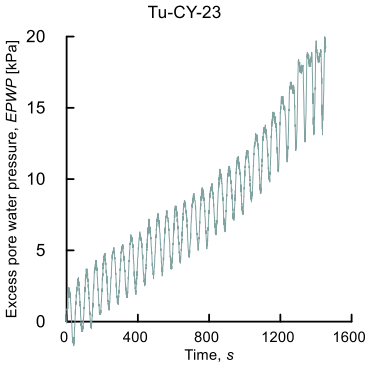

# Appendix B.2: Undrained cyclic triaxial tests – Mamaku tephras

**Test series 1:**

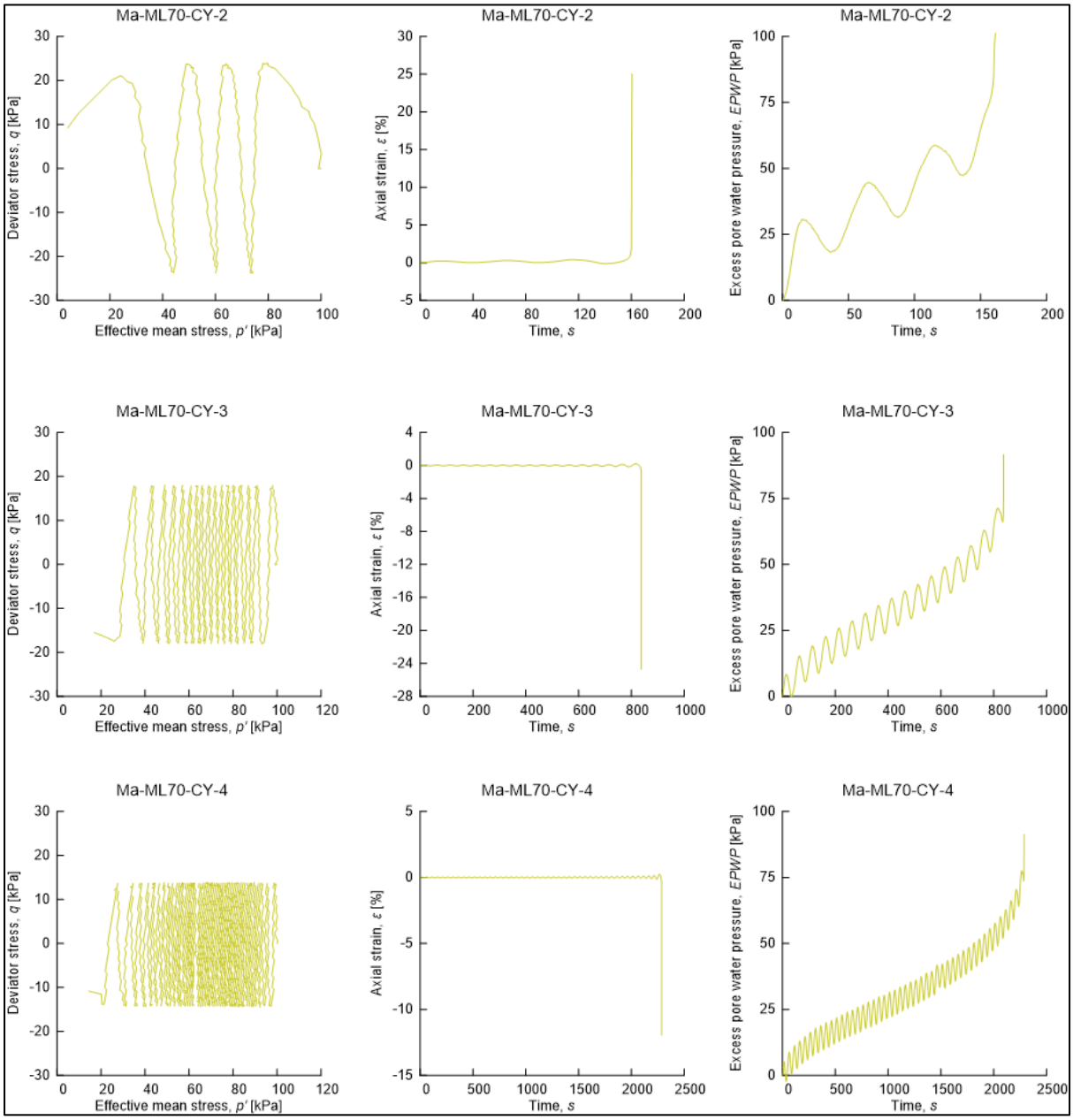

**Test series 2:**

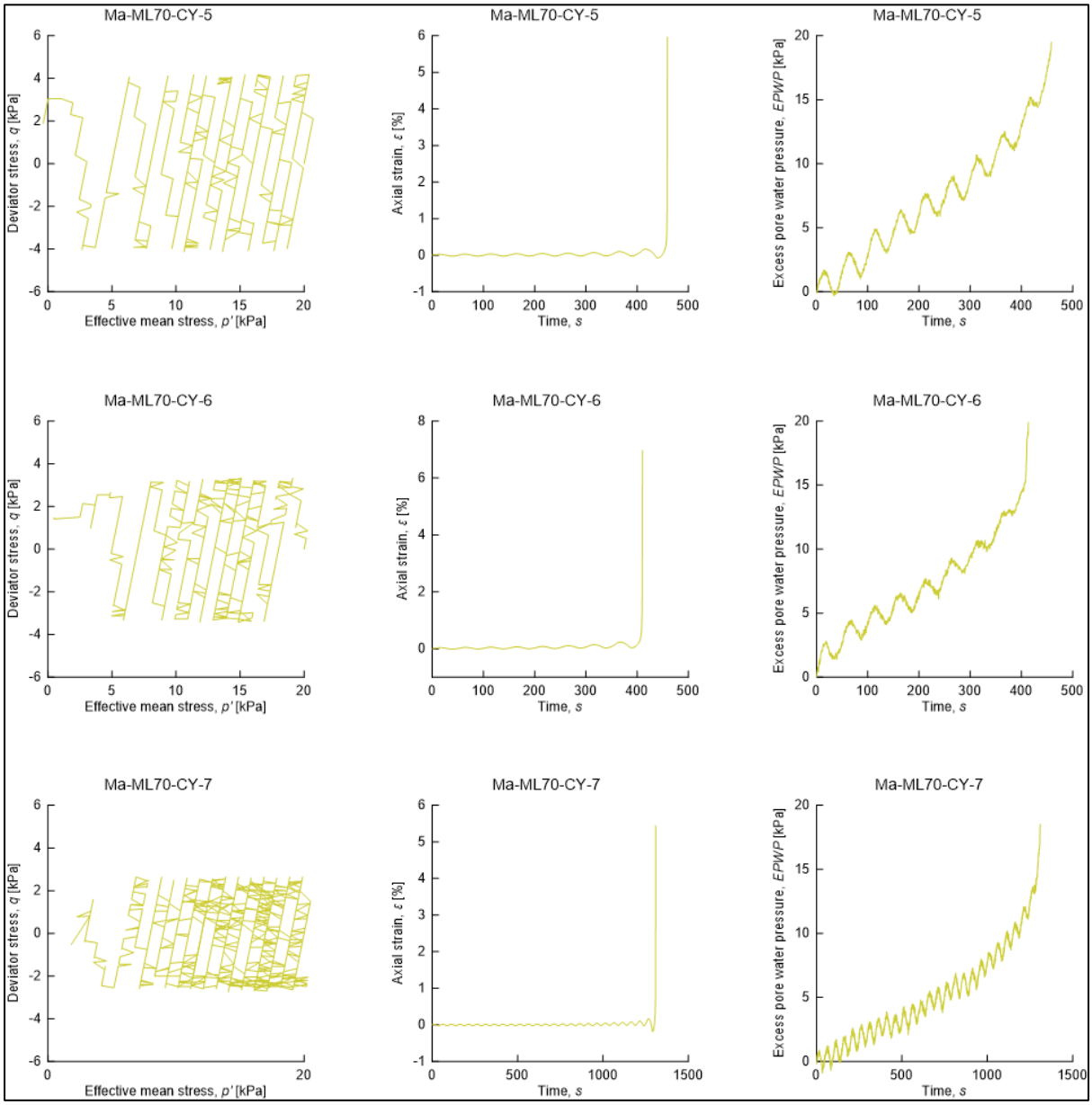

**Test series 3:**

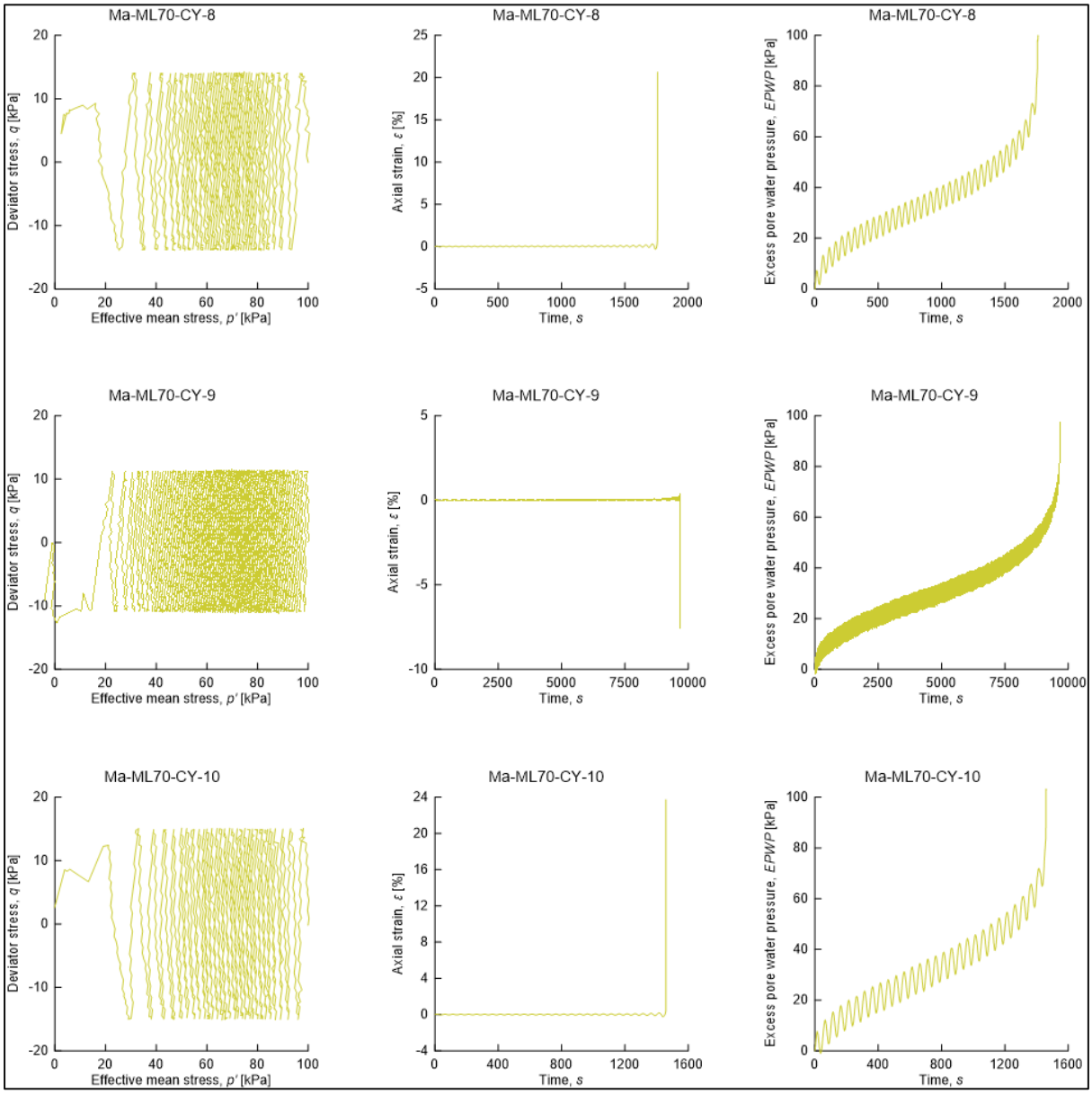

**Test series 5:**

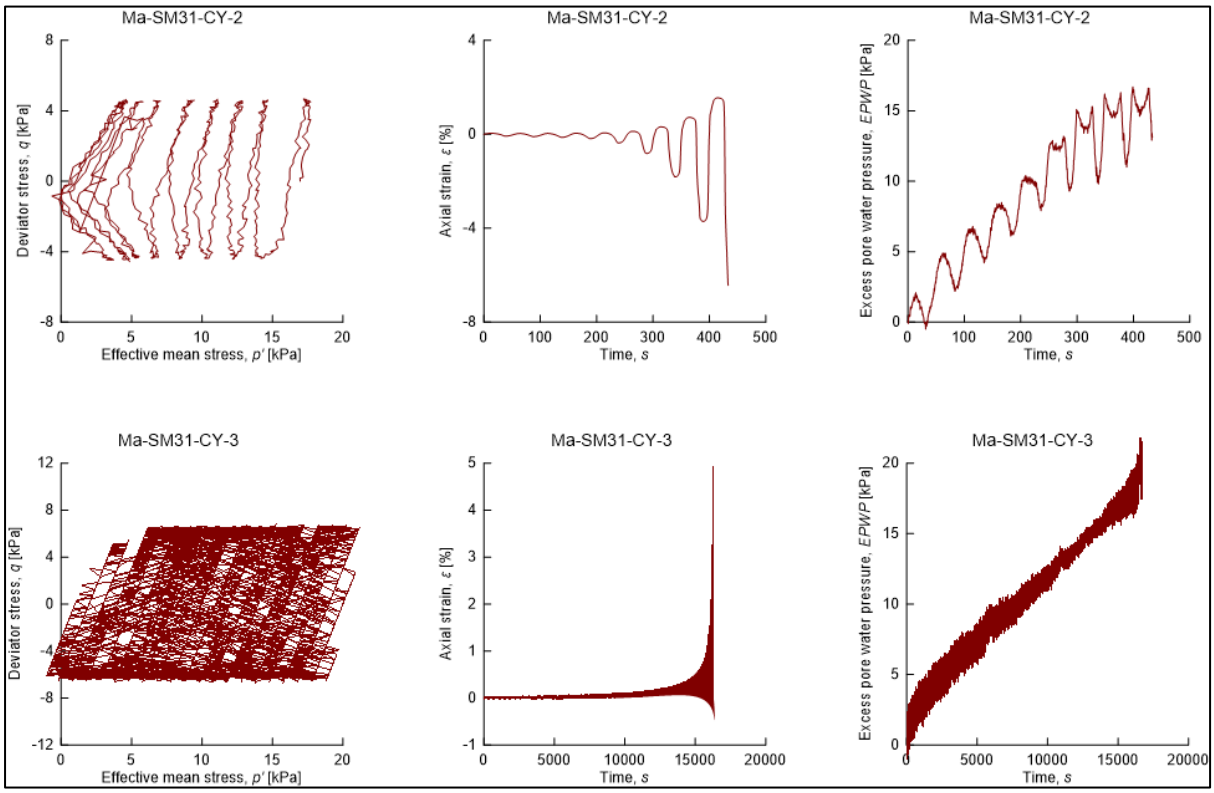

## Test series 6:

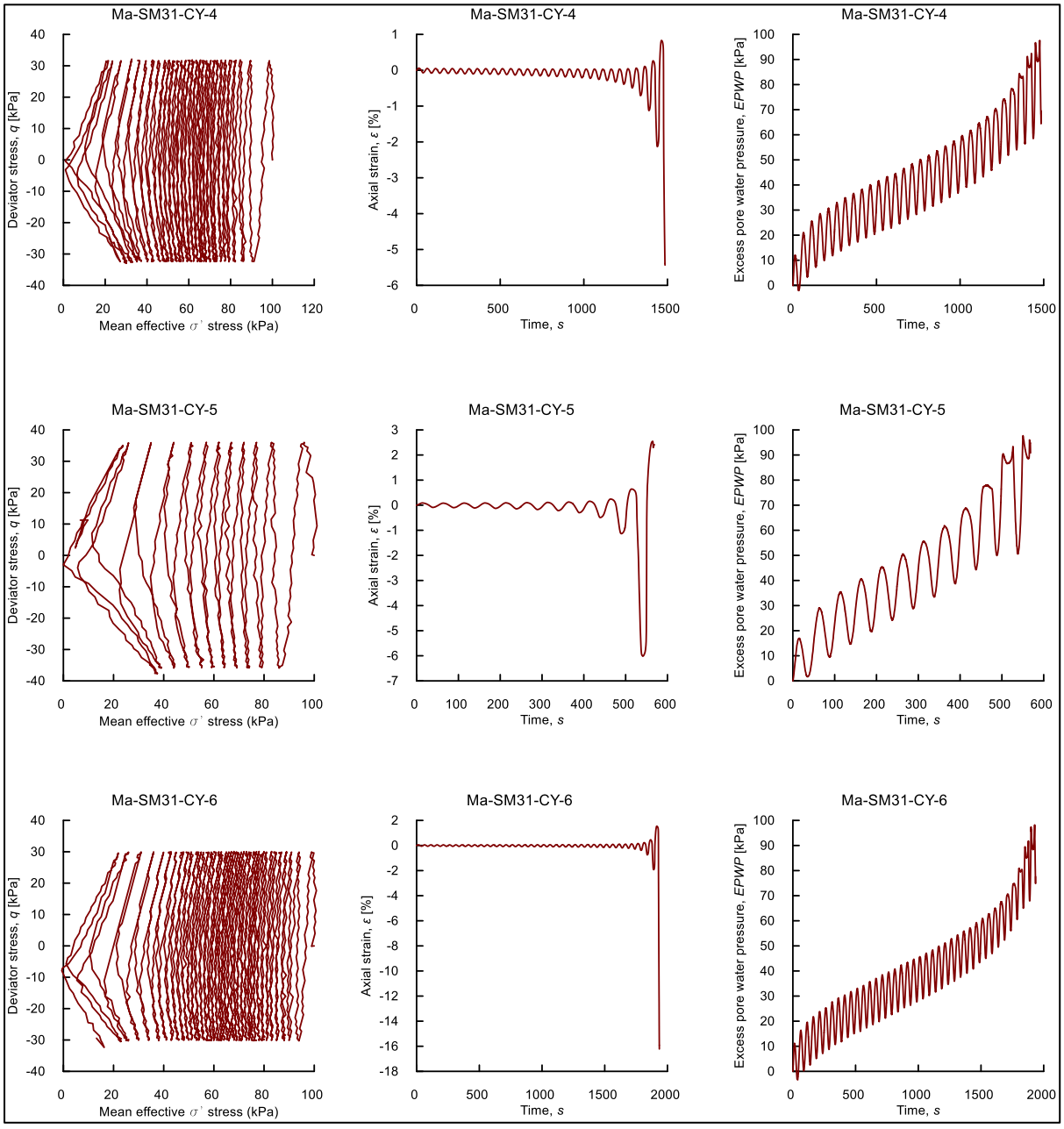

**Test series 7:**

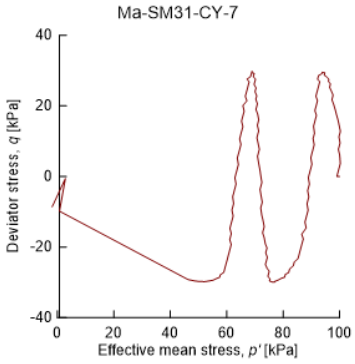


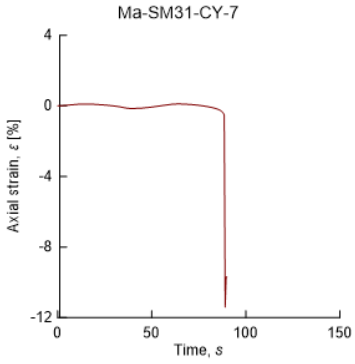


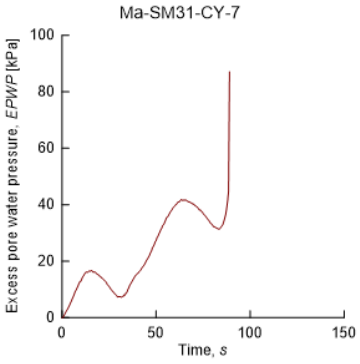


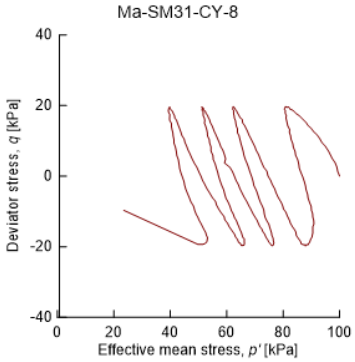


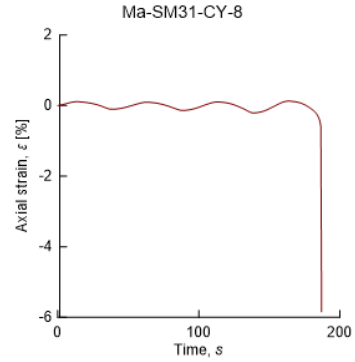


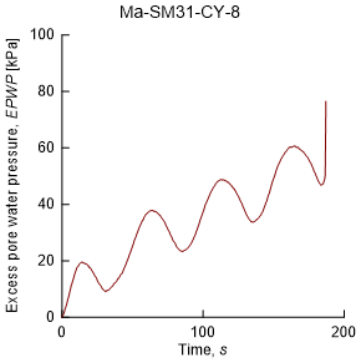


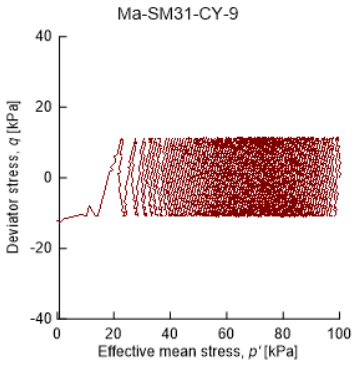


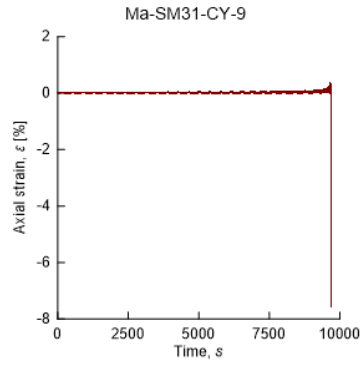


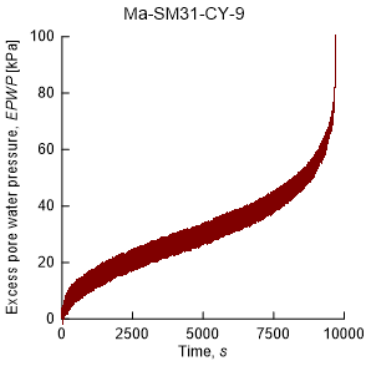

**Test series 8:**

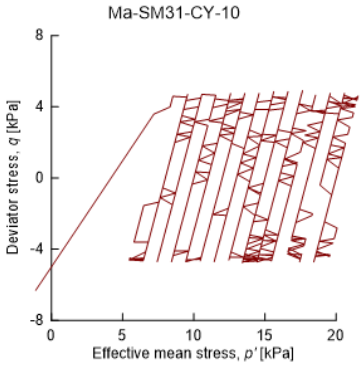


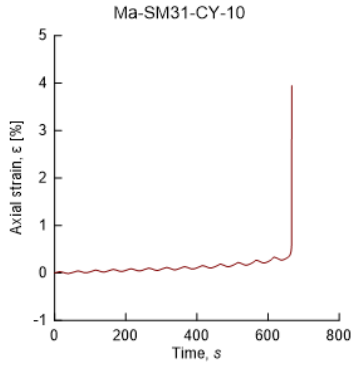


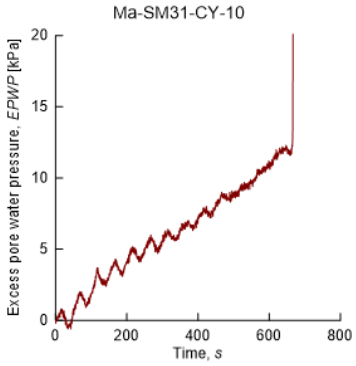


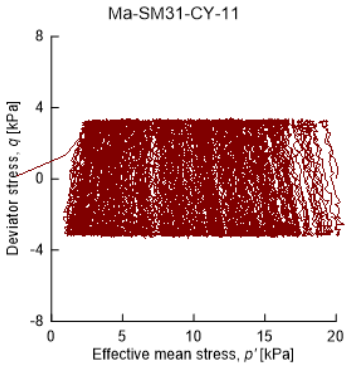


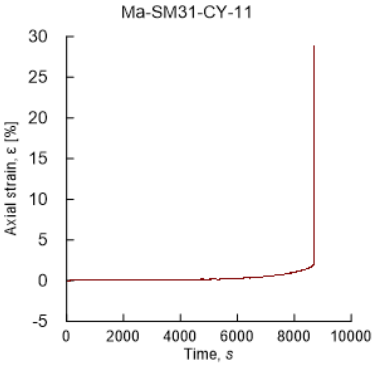


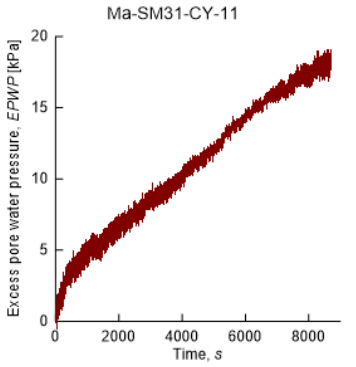


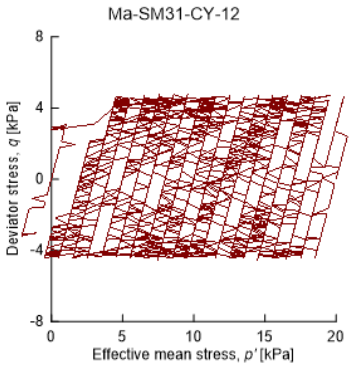


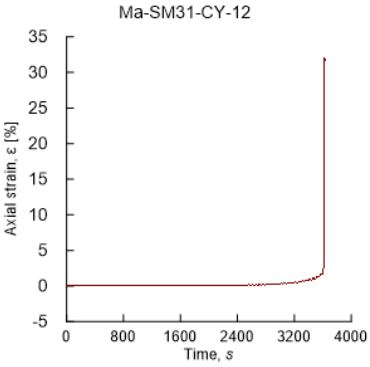


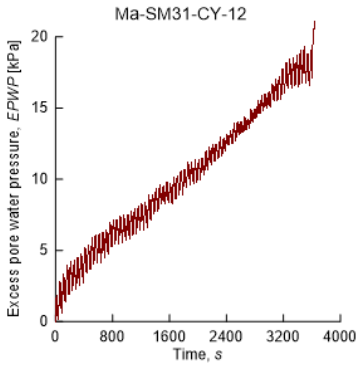

**Test series 9:**

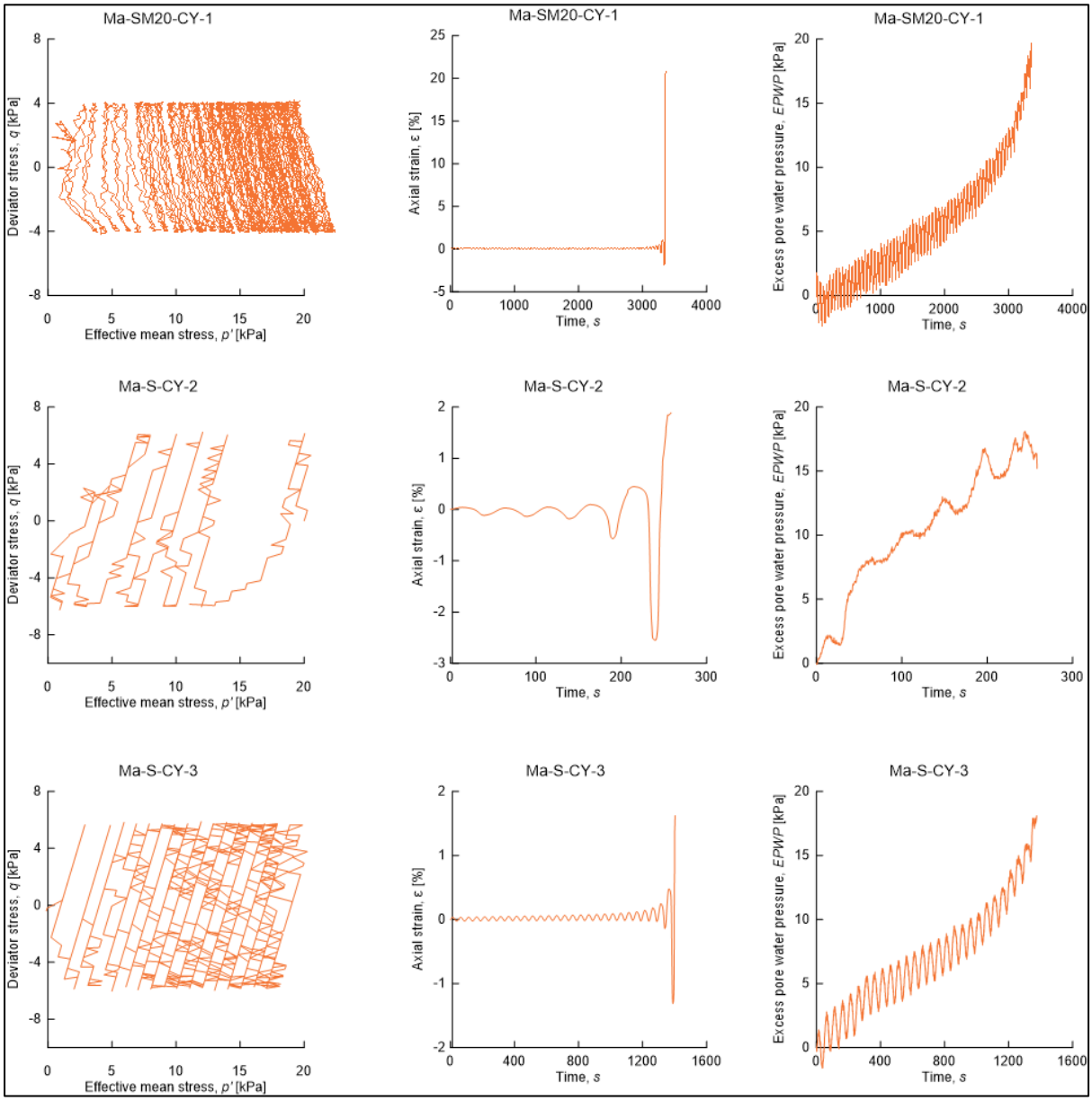

## Test series 10:

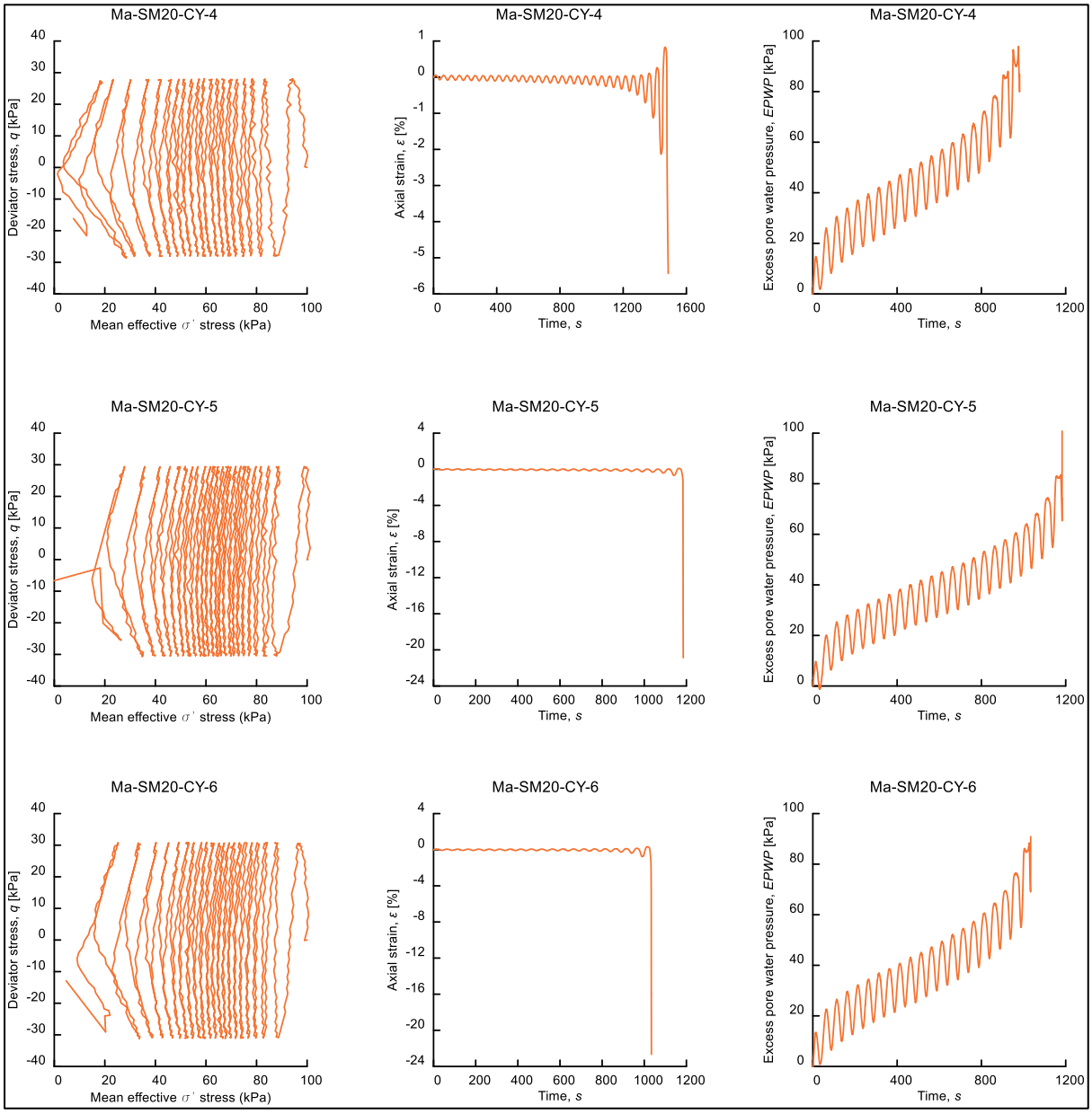

**Test series 11:**

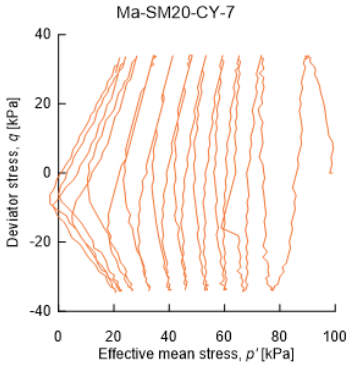


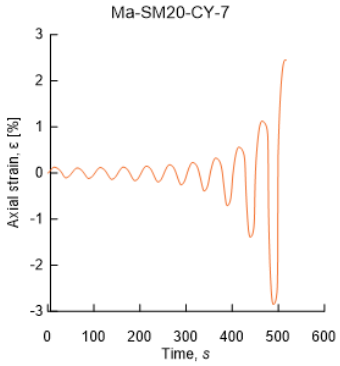


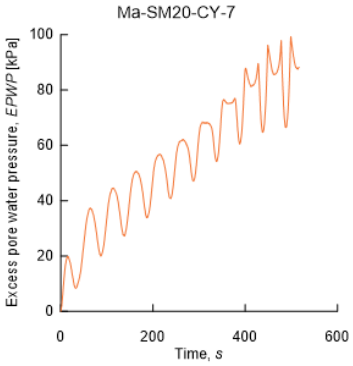


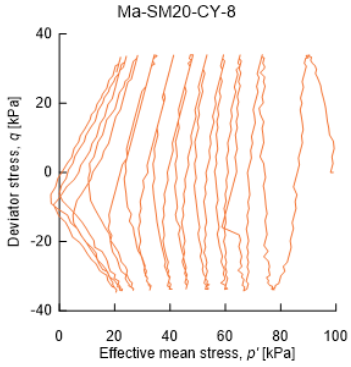


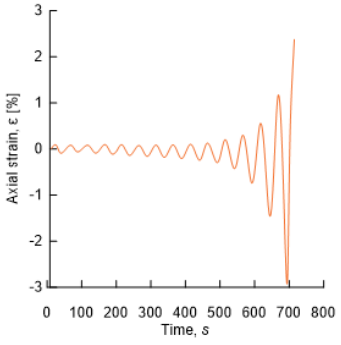


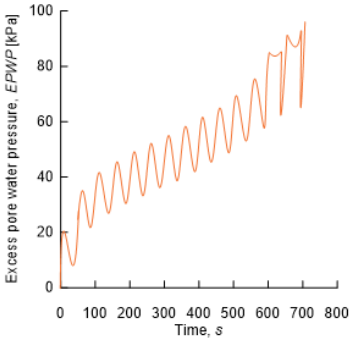


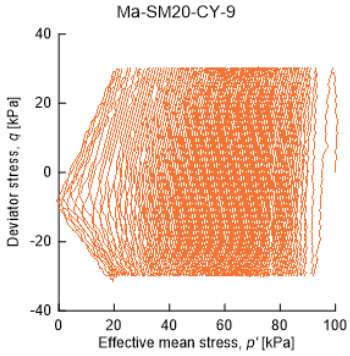


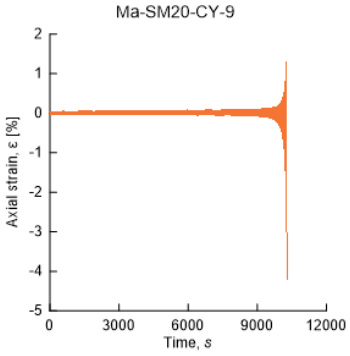


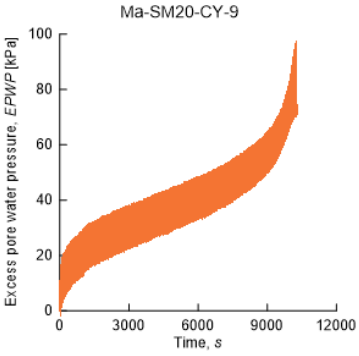

**Test series 12:**

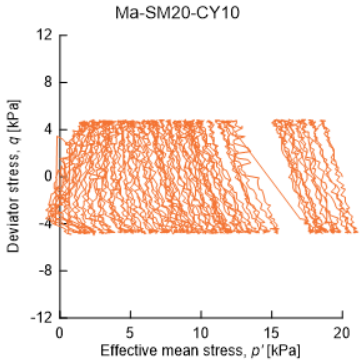


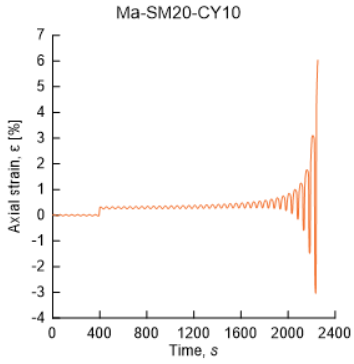


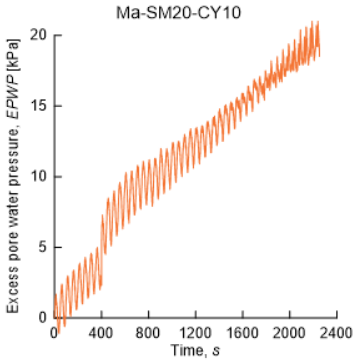


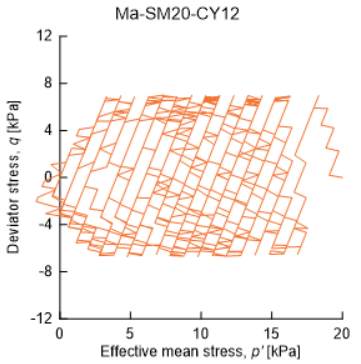


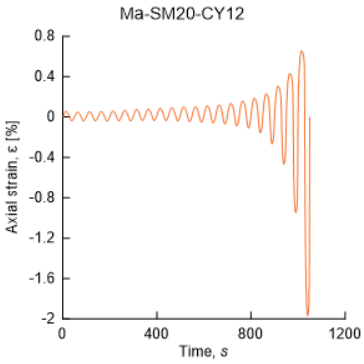


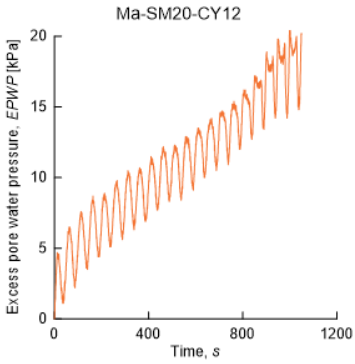

# Appendix C: Poster abstracts

## C. 1. Cyclic undrained behaviour and liquefaction resistance of a lacustrine pumiceous sandy silt, North Island, New Zealand

**Jordanka Chaneva**[1], Max O. Kluger[1], Vicki G. Moon[1], David J. Lowe[1] & Rolando P. Orense[2]

[1]*School of Science/Te Aka Mātuatua, University of Waikato, New Zealand, jc409@students.waikato.ac.nz*
[2]*Department of Civil and Environmental Engineering, University of Auckland, New Zealand*

Poster presented at the 2022 Te Hiranga Rū QuakeCoRE Annual Meeting, 29-31st August 2022, Napier New Zealand

### Abstract

Experimental data related to the mechanical behaviour of crushable pumiceous soils are quite limited compared with those for hard-grained soils. The main focus of previous studies has 2022 Te Hiranga Rū QuakeCoRE Annual Meeting – Poster Abstract Book Page 9 of 42 been on pumiceous sands, whereas pumiceous silts have not been investigated to date. A series of monotonic and cyclic triaxial tests were therefore performed to investigate the cyclic undrained behaviour and liquefaction resistance of a pumiceous sandy silt from northern New Zealand. The material tested, comprising tephra fallout from a volcanic eruption c. 7,600 years ago and preserved in Holocene lake sediments in the Hamilton Basin, is non-plastic sandy silt with pumice content of 45-48%. The samples were reconstituted in the laboratory using the under-compaction method and tested at two different consolidation stresses (20 kPa and 100 kPa) and three different relative densities (medium, medium-dense, and dense). The silt material tested exhibited three significant differences when compared with pumice sand. Firstly, it was more contractive even at medium to high relative densities, leading to a lower resistance to static (flow) liquefaction. Secondly, while it exhibited similar trends in excess pore pressure and axial strain accumulation (when relative density was used as a basis for comparison), the relative density had an only slight influence on the cyclic undrained behaviour. Thirdly, the material exhibited a significantly lower cyclic liquefaction resistance. In general, the cyclic undrained behaviour of the pumiceous sandy silt was similar to that of hardgrained silt. The difference in the response between pumiceous sandy silt and pumiceous sand may be explained by the lower degree of particle crushing the former experienced during cyclic shearing.

KEYWORDS: pumice; volcanic soil; silt; liquefaction; undrained triaxial tests; state parameter; lake sediment.

# C. 2. Towards an evaluation of earthquake hazard in the Hamilton lowlands using geotechnical analysis of liquefied volcanic-ash layers in lakes

**Jordanka Chaneva**[1], Max O. Kluger[1], Vicki G. Moon[1], David J. Lowe[1] & Rolando P. Orense[2]

[1]*School of Science/Te Aka Mātuatua, University of Waikato, New Zealand, jc409@students.waikato.ac.nz*
[2]*Department of Civil and Environmental Engineering, University of Auckland, New Zealand*

Abstract for the Disastrous Doctorates 2023 Symposium, 22-24th February, Wellington, New Zealand.

## Abstract

The Hamilton lowlands, North Island, New Zealand, are currently classed as having low to medium seismic hazard. There is urgent need to reassess this level of seismic hazard in light of the area's uncertain/barely known seismic history, the discovery of hidden faults in Hamilton and beyond, and the identification of paleoseismic-derived liquefaction features in tephra layers preserved in ~20,000 yr-old lakes in the lowlands. I use laboratory geotechnical analysis of the liquefied tephra layers to back calculate past earthquakes that might have caused the liquefaction. The tephra layers are pumiceous silts, sandy silts, silty sands, and sands. The analyses include (1) assessing the liquefaction susceptibility of the liquefied tephras; (2) determining their liquefaction potential by performing undrained cyclic triaxial tests under the range of densities and consolidation stresses relevant in situ; and (3) using the liquefaction resistance results from the liquefaction potential analysis to back calculate peak ground accelerations and moment magnitudes that caused the past liquefaction. The results will then be used within a wider research programme to (1) provide a means of improved detection and understanding of seismic geohazards; (2) inform the National Seismic Hazard Model, which underpins the New Zealand Building Code; (3) develop an ability to generate site-specific hazard assessments; and (4) lead to improvement in the earthquake resistance standards for buildings, critical facilities and infrastructure in and around Hamilton.

# C. 3. Particle crushing in pumiceous sands and silts during cyclic triaxial loading.

**Jordanka Chaneva[1],** Max O. Kluger[1], Vicki G. Moon[1], David J. Lowe[1] & Rolando P. Orense[2]

[1]*School of Science/Te Aka Mātuatua, University of Waikato, New Zealand, jc409@students.waikato.ac.nz*
[2]*Department of Civil and Environmental Engineering, University of Auckland, New Zealand*

Poster presented at the 2023 Te Hiranga Rū QuakeCoRE Annual Meeting, August 2023

## Abstract

Pumiceous particles have a distinct vesicular nature as well as a complex surface texture that makes them potentially vulnerable to crushing under cyclic loading. Pumiceous sand mixtures have received more scientific attention than pumiceous silts in this regard. Researchers have found the undrained cyclic behaviour of pumiceous sands to be significantly different than of that of hard-grained sands, because of the particle crushing process that occurs during cyclic testing and/or sample reconstitution. The liquefaction resistance of pumiceous sands is also considered to be higher, as a result of the pore-water pressure distribution that occurs during particle crushing. Methods based on field tests, such as CPT and SPT, are also considered unsuitable for these types of sands. The undrained behaviour of pumiceous silt was only studied once. The material (with 51% fines content and 48% pumice content) did not crush during sample reconstitution and undrained cyclic testing, which was attributed to the silty particles acting as cushions between the coarse sandy pumice particles. The thresholds of fines content and pumice content, at which pumiceous soil mixtures start to behave more closely as hard-grained soils, are yet to be unravelled and remain relevant for engineers and scientists. This paper analyses the particle crushing after sample reconstitution and undrained cyclic triaxial testing of five pumiceous natural soil mixtures from Northern New Zealand, having fines and pumice contents ranging between 18% and 80% and 30% and 60%, respectively. The results analyse the extent of particle crushing of the different soil mixtures and discuss potential influence of the fines content and/or the pumice content on the particle crushing.

KEYWORDS: pumiceous sand-silt mixtures, particle crushing, pumice content, fines content, cyclic triaxial testing

# Appendix D: Co-authored manuscript: Seismically-induced down-sagging structures in tephra layers (tephra-seismites) preserved in lakes since 17.5 cal ka, Hamilton lowlands, New Zealand

**Max O. Kluger**[1], David J. Lowe[1], Vicki G. Moon[1], Jordanka Chaneva[1], Richard Johnston[2], Pilar Villamor[3], Tehnuka Ilanko[1], Richard A. Melchert[1], Rolando P. Orense[4], Remedy C. Loame1, Nic Ross[5]

[1]*School of Science/Te Aka Mātuatua, University of Waikato, Hamilton, New Zealand.*
[2]*Faculty of Science and Engineering, Swansea University, Swansea, United Kingdom.*
[3]*GNS Science, Lower Hutt, New Zealand.*
[4]*Department of Civil and Environmental Engineering, University of Auckland, Auckland, New Zealand.*
[5]*Hamilton Radiology, Hamilton, New Zealand.*

Published in Sedimentary Geology 445, 2023; 106327;
DOI: doi.org/10.1016/j.sedgeo.2022.106327; 

## Abstract

We analysed numerous soft-sediment deformation structures (SSDS) identified in seven unconsolidated, up to 8-cm thick, siliceous tephra layers that had been deposited in ~35 riverine-phytogenic lakes within the Hamilton lowlands, northern North Island, New Zealand, since 17.5 calendar (cal) ka BP. Based on sediment/tephra descriptions and X-ray computed tomography scanning of cores taken from ten lakes, we classified these SSDS into elongated load structures (i.e., down-sagging structures) of different dimensions, ranging from millimetre-to decimetre-scale, and centimetre-long dykes. Down-sagging structures were commonly manifested as intrusions of internal tephra beds of very fine to medium sand into underlying organic lake sediments. The tephra layers commonly exhibited an upper silt bed, which was not directly affected by deformation. Dry bulk density and grain size distribution analyses of both the organic lake sediment and the internal tephra beds provided evidence for the deformation mechanism of down-sagging structures and their driving force: the organic lake sediment and the upper silt bed are less liquefiable, whereas the very fine to medium sand internal tephra beds are liquefiable. The tephra layers and encapsulating organic lake sediments formed three-layer (a-b-a) density systems, where 'a' denotes the sediment unit of lower density. We infer that downward-directed deformation was favoured by the a-b-a density system with the upper, less-liquefiable, silt bed within the tephra layer preventing upward intrusion during the liquefaction process. The spatial distribution and ages of SSDS within the lakes provided some evidence that liquefaction of the older tephra layers, i.e., Rerewhakaaitu, Rotorua, and Waiohau tephras, deposited 17.5, 15.6, and 14 cal ka BP, respectively, was triggered by a seismic source to the northeast of the Hamilton lowlands (i.e., Kerepehi and/or Te Puninga faults). In contrast, the liquefaction of the younger tephra layers, i.e., Opepe, Mamaku, and Tuhua tephras, deposited 10.0, 8.0, and 7.6 cal ka BP, respectively, may have been triggered by movement on local faults within the Hamilton lowlands, namely the Hamilton Basin faults, or by distant faulting at the Hikurangi subduction margin east of North Island.

KEYWORDS: Soft-sediment deformation structures (SSDS); tephra; liquefaction; paleoearthquakes; Kerepehi Fault; Te Puninga Fault

# 1. Introduction

Soft-sediment deformation structures (SSDS) occur in unconsolidated sediments during or shortly after their deposition, and before significant diagenesis (Owen et al., 2011). Common SSDS include water-escape and injection structures, load structures, convolute laminations, deformed cross-bedding, slumps, and collapse structures (Obermeier, 1996; Rodríguez-Pascua et al., 2000; Kang et al., 2010; Owen and Moretti, 2011; Mazumder et al., 2016). Water-escape and injection structures are commonly formed when sediment is transported upwards by the expulsion of water during the process of fluidisation and liquefaction, resulting in dykes, sills, disk-and-pillar structures, and sand volcanoes (Owen et al., 2011). Liquefaction describes the loss of grain contacts and a temporary transfer of grain weight to the pore fluid under undrained conditions, and is seen as the most common mechanism for the formation of dykes (Nichols, 1995).

Downward-directed SSDS occur either from mainly passive collapse of overlying materials into fissures and cracks, caused by extensional tectonics or glaciogenic processes (i.e., neptunian dykes) (Obermeier, 1996; Bektas et al., 2001; Montenat et al., 2007; Moretti and Sabato, 2007; Fortuin and Dabrio, 2008; Kang et al., 2010; El Taki and Pratt, 2012; Basilone et al., 2016; Lunina and Gladkov, 2016; Mazumder et al., 2016; Ozcelik, 2016; Gavrilov, 2017), or from liquefaction in reverse density gradient systems forming load structures (Anketell et al., 1970; Owen, 2003; Gladkov et al., 2016; Belzyt et al., 2021). Reverse density gradient systems are denoted as b-a density systems, where ‘a’ refers to the sediment unit of relatively lower density (Anketell et al., 1970). Load structures are common in two-layer b-a density systems, but have only been sparsely reported in three-layer a-b-a density systems, where a dense sediment is interlayered between members of relatively lower density (Moretti and Ronchi, 2011; Törő and Pratt, 2016).

To improve the understanding of sediment deformation processes in a-b-a density systems, a comprehensive multidisciplinary analysis was conducted on records of late Quaternary sediment cores taken from lakes, formed about 20 calendar (cal) ka, that lie in the Hamilton lowlands (northern New Zealand) amidst newly-discovered Hamilton Basin faults (Fig. 1) (Moon and de Lange, 2017). The cores comprise highly organic, unconsolidated lake sediments of low density with interlayered, silicic tephra-fall deposits (layers up to 8-cm thick) of relatively higher density, each of which forms an individual a-b-a density system with the enclosing lake sediment. Tephra deposits are the explosively-erupted, unconsolidated,

pyroclastic products of a volcanic eruption of any grain size or composition (Lowe, 2011). Paleoliquefaction in tephra deposits has been rarely investigated previously. Only a handful of papers on the topic is known to us (Sieh and Bursik, 1986; Mazumder et al., 2016; Yang et al., 2019; Molenaar et al., 2021). Following the commonly accepted concept of liquefaction discussed above, sediment deformations in a-b-a density systems should be directed upwards, following the direction of least resistance. However, in our lake records, the tephra layers were almost exclusively deformed downwards, forming SSDS in the form of several decimetre-long, elongated load structures (Fig. 2) (Lowe, 1988b).

The SSDS were imaged using X-ray computed tomography (CT), described in cross-section, and then analysed via bulk density measurement, grain size distribution analyses, and determination of Atterberg limits. Then, their mechanisms of deformation, the driving force of deformation, and possible triggering mechanisms, were interpreted following the protocols provided by Owen and Moretti (2011). The spatial and temporal occurrence of SSDS was mapped across the studied lakes within the Hamilton lowlands and an attempt was made to link the occurrence of the SSDS to seismic activity on regional faults including two faults in the adjacent Hauraki Plains, the Kerepehi and (newly-identified) Te Puninga faults (Persaud et al., 2016; Van Dissen et al., 2021), as well as on the local faults within the Hamilton lowlands (the Hamilton Basin faults) (Van Dissen et al., 2021).

## 2. Geological setting

The Hamilton lowlands lie within the tectonically formed Hamilton Basin in the northern North Island of New Zealand (Fig. 1a-b), adjacent to tephra-generating volcanic centres in the Taupō Volcanic Zone, offshore Tuhua Volcanic Centre, and distant Taranaki Maunga volcano (Fig. 1c). The basin's most recent infilling deposits – Quaternary ignimbrites, volcanogenic alluvium, and tephra deposits – underlie low hills surrounded and partly buried by younger, secondary volcaniclastic alluvium, the Hinuera Formation, deposited ~20 cal ka by the ancestral Waikato River (Hume et al., 1975; Selby and Lowe, 1992; Manville and Wilson, 2004; Peti et al., 2021).

Around 35 riverine and riverine-phytogenic lakes occur adjacent to the antecedent hills. Deposition of the Hinuera Formation across the mouths of small valleys formed alluvial dams, generating shallow basins in which groundwater and drainage formed these blocked-valley riverine lakes (Green and Lowe, 1985; Lowe and Green, 1992).

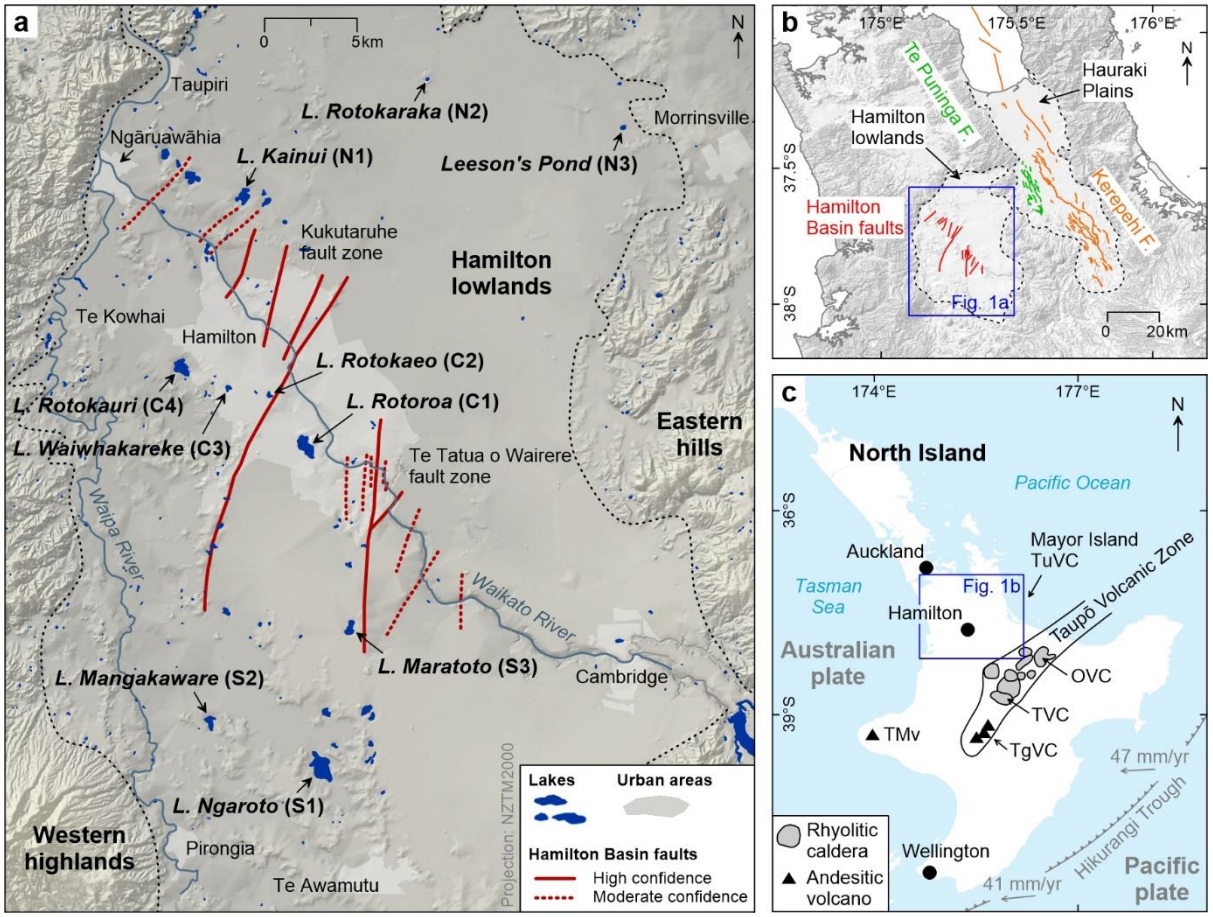


**Fig. 1.** Study area. (a) Locations of ten lakes cored in our study and recently identified faults (Moon and de Lange, 2017; Van Dissen et al., 2021) in the Hamilton lowlands (in the Hamilton Basin). Base map is a low-resolution DEM from Land Information New Zealand. *L.* = Lake. Abbreviated lake names are provided in parentheses. (b) Wider view of the locations of faults in the Hamilton Basin (Fig. 1a) and the Te Puninga and Kerepehi faults in adjacent Hauraki Plains (Persaud et al., 2016). (c) Map of the North Island, New Zealand, with general tectonic setting and the main volcanic centres active since 20 cal ka (Leonard et al., 2010). The tephra deposits preserved in the lakes originated from Okataina (OVC), Taupō (TVC), Tongariro (TgVC), and Tuhua (TuVC) volcanic centres, and Taranaki Maunga volcano (TMv).

In many cases, massive peat growth on top of the alluvium formed a second-storey dam, resulting in larger, peat-dominated riverine-phytogenic lakes (Green and Lowe, 1985, 1994). These closed-basin lakes have provided a repository since ~20 cal ka for ~40 distal tephra deposits, as well as numerous sparse cryptotephras, preserved in ~3–6 m of organic lake sediment (Lowe, 1988b; Loame et al., 2018). Derived from rhyolitic and andesitic eruptions in Taupō Volcanic Zone, Tuhua Volcanic Centre, and Taranaki Maunga volcano, these tephras range from sub-millimetre to ~8 cm in thickness, the thickest layers being rhyolitic (Lowe, 1988b, 2019).

SSDS have already been recorded in some of the tephra layers (Lowe, 1988b) as elongated, sometimes fissure-like load structures with pointy ends, each load structure being up to a few centimetres wide and up to 20 cm long (Fig. 2). The load structures were commonly associated with prominent collapse structures at the top of the tephra layer (Fig. 2b), indicating volume loss of the tephra layer during downward-directed intrusion into underlying organic lake sediments. Lowe (1988b) suggested (with some uncertainty expressed) that bioturbation was the only plausible mechanism that could have caused the downward-directed SSDS in the tephra layers because, at that time, the Hamilton lowlands were believed to lack active faults (Edbrooke, 2005; Langridge et al., 2016) and therefore designated as having low to moderate seismic risk (Stirling et al., 2012). However, new evidence of faults (Fig. 1) and seismic activity, including within the Hinuera Formation (Hume et al., 1975; Kleyburg et al., 2015; Persaud et al., 2016; Moon and de Lange, 2017; Van Dissen et al., 2021), now provide a seismogenic explanation for the downward-directed SSDS.

# 3. Materials and Methods

### *3.1. Coring*

Ten lakes from three different parts in the Hamilton lowlands were cored: three in the south (Ngāroto, Mangakaware, Maratoto), four in the centre (Rotoroa, Rotokaeo, Waiwhakareke, Rotokauri), and three in the north (Kainui, Rotokaraka, Leeson's Pond) (Fig. 1a). The distance between the southernmost lake (Ngāroto) and the northernmost one (Rotokaraka) is ~40 km. For each lake, one or more cores ~1.5–2 m in length were collected from partly overlapping sediment depths using a modified Livingstone piston corer with a 50-mm internal diameter PVC coring tube (Rowley and Dahl, 1956) for historical cores taken in the 1980s, and 65- or 80-mm internal diameter for cores taken more recently in 2016, 2020, and 2022.

The cores in most cases were collected from the deepest basin(s) of the lakes where typically the thickest sediments occur, and where the tephra beds are essentially horizontal (Lowe, 1985) and unaffected by other aseismic trigger mechanisms specific to other depositional environments (Owen and Moretti, 2011). In Lake Maratoto, the cores were extracted from ten sites throughout the lake (Green and Lowe, 1985), whereas at Lake Rotoroa, seven sites throughout the lake were selected for coring including in shallow areas. Where more than one core was required to fully capture the entire sediment thickness in the lake, overlapping cores were taken and then easily correlated using the distinctive physical properties of the glass-rich tephra layers present in the lake sediments, the layers being typically

different in colour and thickness (e.g., see illustrations in Green and Lowe, 1985; Lowe, 1988b, 2019), to generate a composite core ~3–5 m in length for each lake.

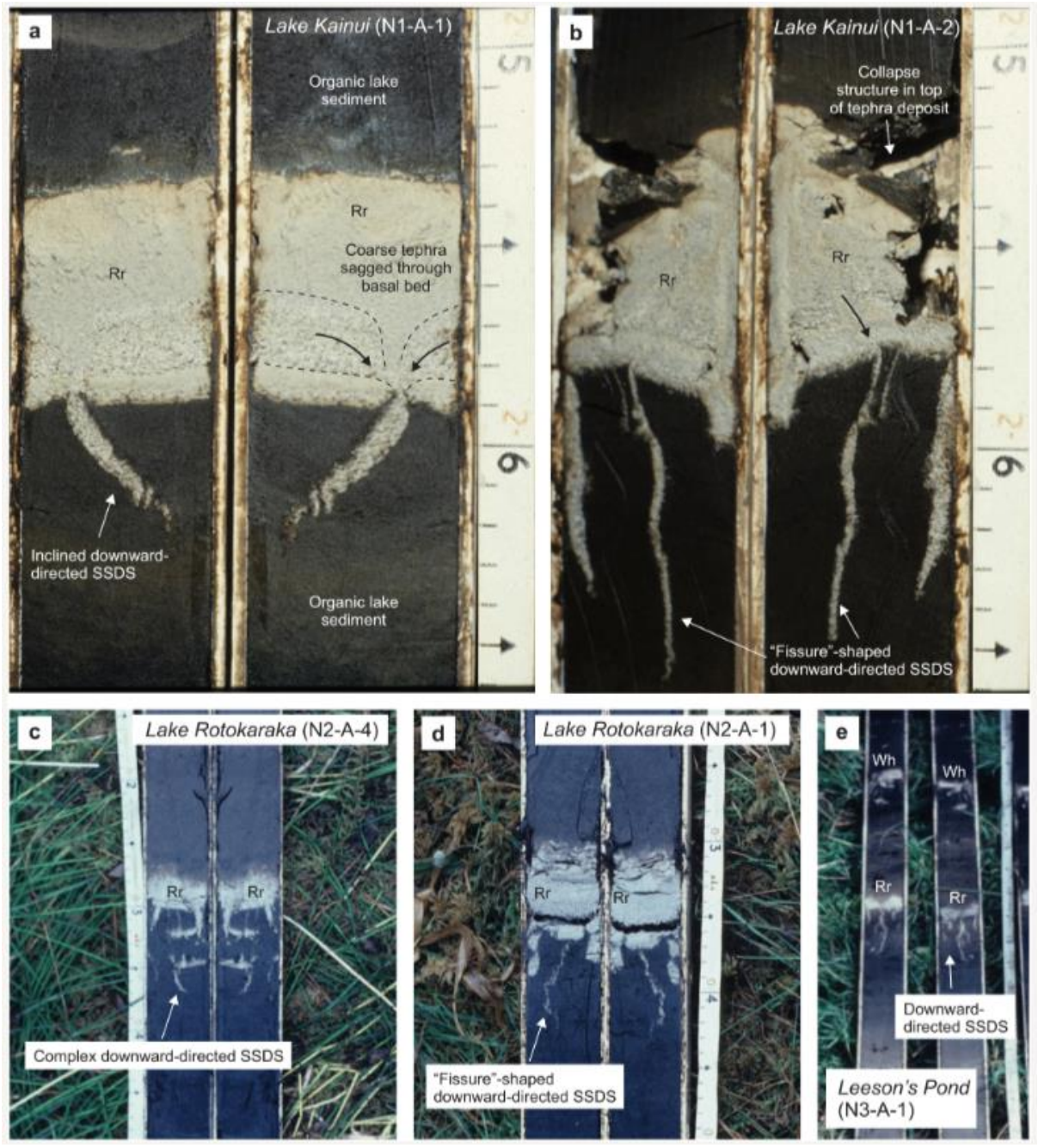


**Fig. 2.** Examples of downward-directed SSDSs in Rotorua (Rr) tephra layers in historic cores from various lakes (i.e., Kainui, Rotokaraka, Leeson's Pond). For locations of lakes see Fig. 1a. (a) Down-sagging structure with internal flow structures indicating pore pressure release (Lowe, 1988b). (b) Up to 20-cm long, fissure-like down-sagging structure (Lowe, 1988b). (c-e) Down-sagging structures. Wh = Waiohau tephra. The scale bars are in cm.

An example showing the construction of a composite core using tephrochronology is provided in supplementary Fig. S1. In most lakes, duplicate cores were also collected from different sites within the lake basin. Because of the duplication and the overlapping cores, the majority of tephra layers could be investigated more than once in each lake (up to 20 times in Lake Maratoto; Green and Lowe, 1985), increasing the confidence in characterising SSDS. The sediment strata and stratigraphy of all but two lakes (Waiwhakareke, Rotokaeo) have been described previously (Green and Lowe, 1985; Lowe, 1985, 1988b, 2019). Additional information about the sediment cores is provided in supplementary Table S1.

### *3.2. CT imaging*

X-ray computed tomography (CT) imaging was performed using a medical CT scanner on all whole-round cores prior to opening (except for historical cores from lakes Mangakaware, Maratoto, Rotokaraka, and Leeson's Pond, which were not available for CT imaging). CT volumes were processed using imageJ, Drishti ver. 2.7 (Limaye, 2012), VGStudio Max (ver. 2.1.5, Volume Graphics, Germany), and Syglass (ver. 1.6, IstoVisio, Inc. Morgantown, WV) (Pidhorskyi et al., 2018). Drishti and imageJ were used to create tiff slices from DICOM files. Slice data were loaded into Syglass, a volumetric virtual reality software. The physical cuts through the core samples were correlated to the precise virtual slice within the 3D CT data using a co-registration tool within Syglass utilising four fiducial markers across the 3D X-ray volume and the 2D core cut image – a methodology previously demonstrated in 3D scanning electron microscope data to confocal microscopy images of brain tissue (Thomas et al., 2021).

Once the physical core cut was identified in the 3D X-ray CT volumes, the data were loaded into VGStudio Max and, to aid subsequent segmentation, the outer plastic tubing of the core was excluded using the ellipse selection tool to isolate the material inside the tube in the sagittal plane. The organic lake sediments above and below the tephra layers were removed digitally in both VGStudio and Syglass by applying a global histogram threshold based on X-ray attenuation, which was significantly different between the two constituents, and allowed images and videos to be exported revealing only the tephra deposit. The global histogram threshold was chosen to best correlate the tephra SSDS (at a longitudinal slice through the centre of the X-ray CT volume) to the physical cut of the lake core.

### *3.3. Characterisation of tephra layers*

Individual tephra layers in each core were classified into three types: (i) 'SSDS' (i.e., some kind of SSDS was identified), (ii) 'intact' (i.e., no post-depositional deformation of tephra layer was identified), or (iii) 'discontinuous' (i.e., the tephra layer exhibited some kind of disruption that could not be definitely associated with any SSDS), on the basis of detailed sediment description and CT imaging. Supplementary Fig. S2 shows typical examples of tephra layers classified as discontinuous because they were disrupted, varied in thickness within the extent of the core, were partly covered by sawdust from the core liner, or were located at the base of the core and, thus, could not be characterised satisfactorily. Discontinuous tephra layers were not considered further because of uncertainty about whether the disturbance was caused by liquefaction or by other processes.

The other tephra layers (classified as 'SSDS' or 'intact'), and the organic lake sediments, were further characterised by means of dry bulk density measurements, grain size distribution analyses, organic content, and Atterberg limits. Locations and depths of samples analysed by the four methods are provided in supplementary Table S2. Bulk density was determined by cutting tephra layers and organic lake sediments into rectangular prisms of varying dimensions depending on the available volume. A cutter knife was used in order to cut prisms without causing too much disturbance to the soil structures of the samples. Volumes of bulk density samples varied from 1 to 40 $cm^3$. Dry bulk densities were determined multiple times to aid the reliable (reproducible) calculation of mean values with sufficient confidence: organic lake sediment (eight samples), Tuhua tephra (eleven samples), Mamaku tephra (six samples), Waiohau tephra (six samples), and Rotorua tephra (16 samples). Grain size distribution analyses were performed using a Malvern Mastersizer 3000. Grain size distribution curves were processed using GRADISTAT 9.1 (Blott and Pye, 2001) and basic statistical parameters were determined using the geometric method of moments (Krumbein and Pettijohn, 1938). Grain size nomenclature is based on standard sedimentological class boundaries (Folk, 1980) with clay defined as particles <2 μm in diameter. Where applicable, equivalent classes based on volcanological grain size classes (White and Houghton, 2006) are provided. Atterberg limits and organic content were determined on representative organic lake sediments (ASTM D 4318-17e1, 2017; ASTM D7348-21, 2021).

The dimensions of SSDS were analysed and compared to the total tephra thickness and the thickness of internal beds of tephra layers. For every instance where a tephra layer exhibited

one or more SSDS in a core, the area of all SSDS associated with this particular tephra layer was measured using a geographic information system (GIS). The total area of SSDS was then averaged by the number of SSDS observed in the tephra layer. The area of SSDS was considered here to represent a first level approximation of the volume of SSDS. The dimensions of SSDS were further quantified by measuring the maximal vertical length of the SSDS.

# 4. Sedimentary facies

The sedimentary succession as present in sediment cores taken from the riverine and riverine-phytogenic lakes in the Hamilton lowlands comprised three main geological units, namely pre-lake volcanogenic alluvial deposits (Hinuera Formation), organic lake sediments, and tephra-fall deposits interlayered within the organic lake sediments (Fig. 3).

## *4.1. Pre-lake deposits (Hinuera Formation)*

The oldest unit preserved in the core records comprised unconsolidated, brownish-greyish clays and clayey silts. This unit exhibited a massive soil texture with minor horizontal stratification and was only observed in six out of ten lakes within the Hamilton lowlands. In any event it was not involved in any soft-sediment deformation (Fig. 3c).

The unconsolidated clays and clayey silts of this unit were interpreted as pre-lake alluvial deposits of the Late Pleistocene Hinuera Formation (Schofield, 1965; Hume et al., 1975; Kear and Schofield, 1978). The Hinuera Formation refers to a thick (up to 90 m) heterogeneous unit of secondary volcaniclastic (Di Capua et al., 2022) gravelly sands, sandy gravels, sands, silts, and peat beds that form an alluvial plain within the Hamilton lowlands. Gravel-sized material was found to be dominated by fragments of rhyolitic breccia, rhyolite, pumice and ignimbrite, whereas sand and silt fractions were dominated by volcanic quartz, oligoclase/andesine plagioclase, pumice, and glass shards (Hume et al., 1975). The unconsolidated clays and clayey silts were likely deposited from suspension in abandoned braided channels and flood basins (Hume et al., 1975).

## *4.2. Organic lake sediment*

The main sedimentary unit preserved in the core records comprised unconsolidated, massive, olive-grey, dark brown to black, organic clayey silt. It hosted the tephra layers that exhibited SSDS. The organic content of this sediment ranged between 16 and 20 wt. % and

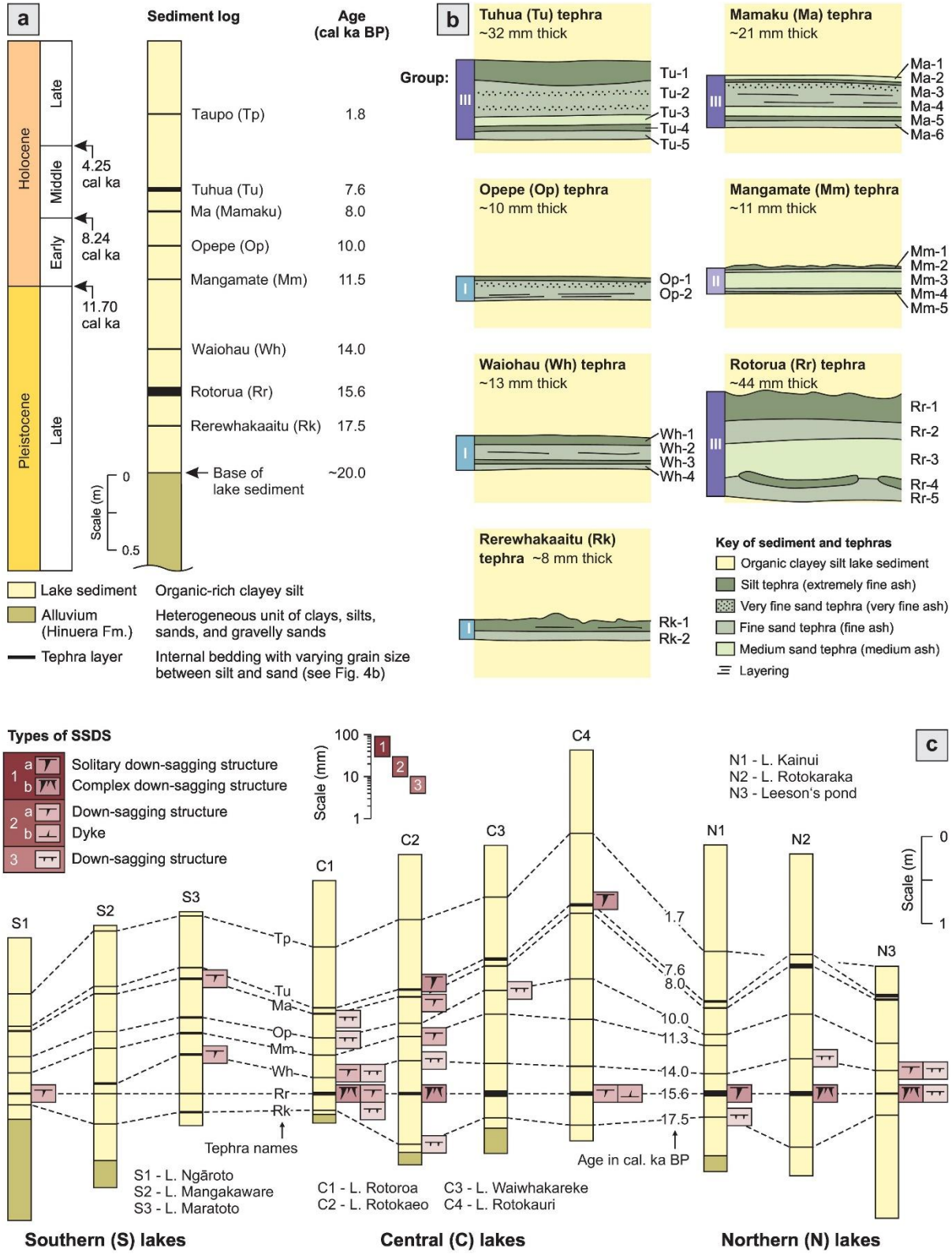


**Fig. 3.** (a) Stratigraphy of eight prominent tephra layers deposited in lakes throughout the Hamilton lowlands. The Pleistocene-Holocene boundary and the subdivisions of the Holocene follow Walker et al. (2009) and Walker et al. (2019), respectively. (b) Sedimentary facies of the seven most relevant tephra layers showing nomenclature, grain size classes, and thicknesses of internal beds used throughout the present study. Tephra layers were grouped (groups I–III) based on their thickness and internal bedding characteristics. (c) Correlation of

post-20-cal-ka major tephra layers between northern, central, and southern lakes within the Hamilton lowlands, indicating the different types of SSDS observed in specific tephra layers. Tephra names (Froggatt and Lowe, 1990; Moebis et al., 2011) and volcanic sources (in parentheses: see Fig. 1c) are as follows: Tp = Taupō (TVC); Tu = Tuhua (TuVC); Ma = Mamaku (OVC); Op = Opepe (TVC); Mm = Mangamate (TgVC); Wh = Waiohau (OVC); Rr = Rotorua (OVC); Rk = Rerewhakaaitu (OVC). Ages of tephras are from Moebis et al. (2011), Lowe et al. (2013), and Lowe et al. (2018).

bulk densities were commonly exceptionally low, with wet densities of $\rho \approx 1{,}100\ kg/m^3$ and dry densities of $\rho_d \approx 300\ kg/m^3$. The organic lake sediment was classified as highly compressible organic silt (OH) of low plasticity based on the Unified Soil Classification System (ASTM D2487-06, 2010), with an average plastic limit of $w_P = 119\%$ and liquid limit of $w_L = 301\%$. The organic clayey silts were deposited in late Quaternary, typically dystrophic, lake environments and were found to be rich in humic material, being mainly classified as dy-gyttja and gyttja, or peat in shallow-water cores (Green and Lowe, 1985).

### *4.3. Tephra deposits*

Eight prominent tephra layers were identified in the cores and correlated between lakes (Fig. 3c) using their stratigraphic positioning, physical properties, mafic and felsic mineralogical assemblages, and glass-shard major element compositions (Lowe, 1988b). Seven of these tephras (Taupō, Tuhua, Mamaku, Opepe, Waiohau, Rotorua, and Rerewhakaaitu) were rhyolitic, with colours ranging from white to light grey, and one (Mangamate tephra) was andesitic, and dark grey to dark olive in colour. They range in age from ~17.5 cal ka to ~1.7 cal ka BP (ages from Lowe et al., 2013). Each of the tephras is consistent in its mineralogical assemblages (dominated by volcanic glass, both vesicular and non-vesicular, with subordinate felsic and mafic minerals) across lakes in the lowlands (Lowe, 1988b). This lack of spatial variability in mineralogical assemblages is expected, given that these are distal tephras >100 km from their source vents (e.g., Juvigné and Porter, 1985; Lowe, 1988a; Alloway et al., 2013).

The observed tephra deposits commonly comprise horizontally bedded layers with distinctive boundaries with under- and overlying organic lake sediments (Fig. 3b). Taupō tephra, being the youngest tephra deposited at ~1.7 cal ka, was commonly only 1–3 mm thick and was therefore not considered further. The other seven tephra layers exhibited average thicknesses between 8 mm (i.e., Rerewhakaaitu tephra) and 44 mm (i.e., Rotorua tephra). Each of the tephra layers contained internal beds characterised by different grain sizes, varying between silt (i.e., extremely fine ash) and medium sand (i.e., medium ash). Except for

Mangamate tephra, the tephra layers commonly had an upper silt bed, typically up to several millimetres thick. The upper silt bed was underlain by coarser beds, the number and grain size varying between tephras.

Tephra layers were grouped (groups I–III) according to their total thickness and internal bedding characteristics (Fig. 3b). Group I tephras included Opepe (Op), Waiohau (Wh), and Rerewhakaaitu (Rk). They were thin (between 8 and 13 mm thick) and commonly exhibited only two dominant beds, which we designated by numbers: an upper silt bed (e.g., Op-1, Wh-1, and Rk-1) underlain by a fine sand bed (e.g., Op-2, Wh-2, and Rk-2). In Waiohau tephra, two additional beds were observed in some lakes underlying the fine sand bed (Wh-3 and Wh-4). Group II tephras included Mangamate (Mm) (commonly 11 mm thick), which comprised up to five beds with the central medium sand bed (Mm-3) being the thickest one. Group III tephras included the remaining three tephras, Tuhua (Tu), Mamaku (Ma), and Rotorua (Rr), which were significantly thicker (21–44 mm) than the other tephra layers. The group III tephras commonly comprised five main internal beds as follows (from top to base): an upper silt bed (Tu-1, Ma-2, Rr-1), a very fine to fine sand bed (Tu-2, Ma-3, Rr-2), a medium sand bed (Tu-3, Ma-4, Rr-3), a thin silt bed (Tu-4, Ma-5, Rr-4), and a very fine to fine sand bed at the base (Tu-5, Ma-6, Rr-5).

The variability in thicknesses of tephra layers and their internal beds was studied for the cores taken from the ten lakes considered in our study (Fig. 4). For the majority of tephra layers (i.e., Mamaku, Opepe, Waiohau, and Rerewhakaaitu), the thicknesses of the tephra layers and their internal beds were similar throughout the Hamilton lowlands. Mangamate tephra, exhibiting similar thicknesses throughout the Hamilton lowlands, was typically dominated by the central medium sand bed (Mm-3), but the full sequence of internal beds was only present at one lake (Lake Rotokaeo, C2). The remaining tephras (Tuhua and Rotorua) exhibited larger variability in tephra thickness.

The overall thickness of Tuhua tephra varied between 20 mm (in Lake Rotoroa, C1) and 42 mm (in Leeson's Pond, N3). A slight directional trend could be observed in the overall thickness of Tuhua tephra (Fig. 5). The thickness of Tuhua tephra seemed to increase from south to north. This observation is in accordance with Lowe (1988b) and Hopkins et al. (2021). The internal bedding characteristics of Tuhua tephra differed with overall tephra thickness. We observed that thicker layers commonly exhibited the full set of internal beds (Tu-1 to Tu-5),

whereas the thinner layers lacked some of the internal beds. For example, in Lake Rotokaraka (N2) only internal beds Tu-2 to Tu-4 could be observed.

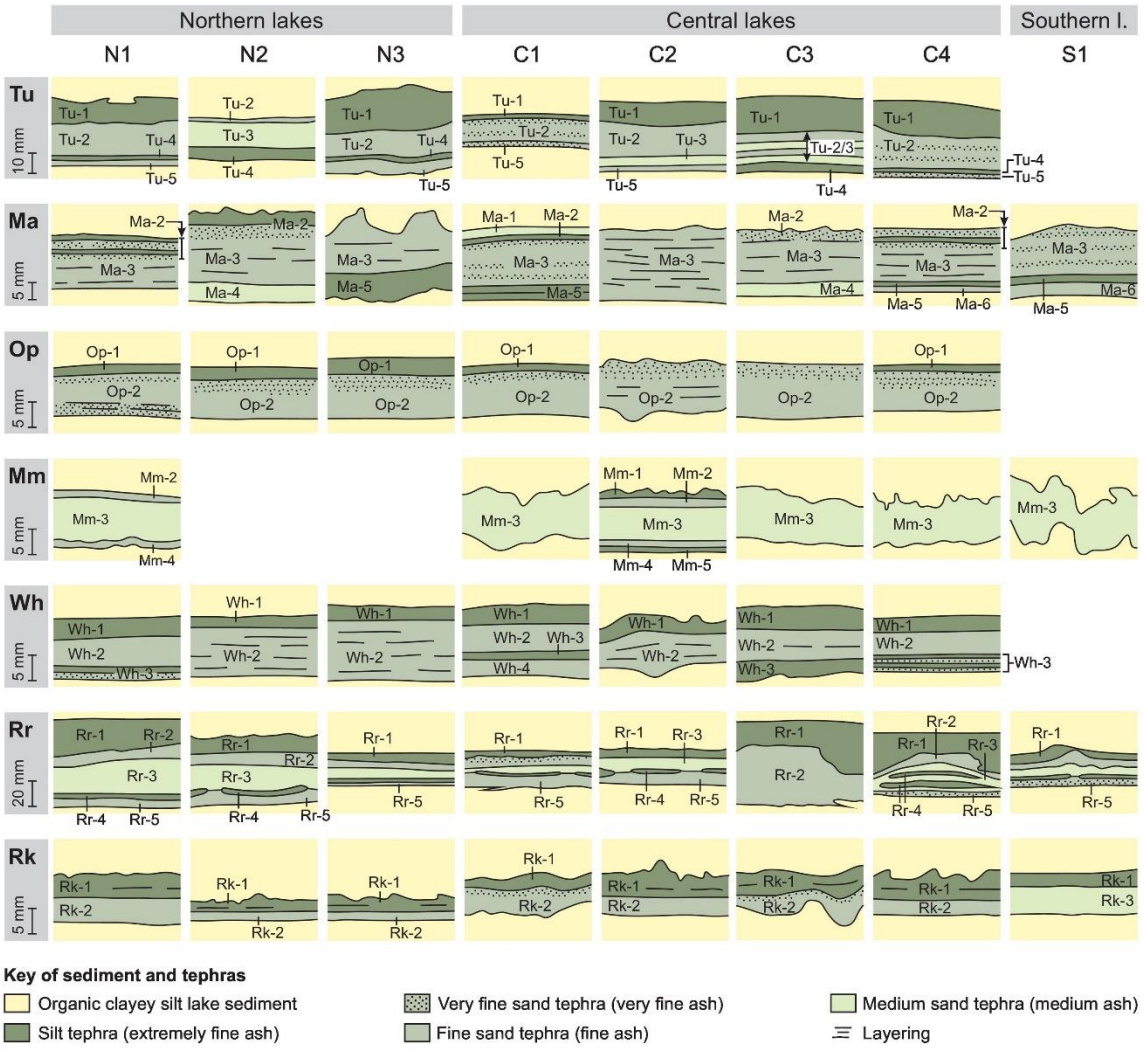


**Fig. 4.** Variability of tephra thickness and internal bedding characteristics between lakes. Note that internal bedding characteristics were not available for every tephra layer and lake due to lack of a specific tephra in that lake or due to incomplete sediment description. Full lake and tephra names are provided in Figs. 1a and 3a.

The overall thickness of Rotorua tephra varied between 25 mm (in Lake Rotoroa, C1) and 77 mm (in Lake Kainui, N1). A slight directional trend could also be observed for Rotorua tephra, increasing in thickness towards the north-west. This observation is contradictory to the published literature (Nairn, 1980; Lowe, 1988b). For Rotorua tephra, the thickness of internal beds was linked to the overall thickness of the tephra layer (with the exception of Lake Waiwhakareke, C3). For example, the thickness of the upper silt bed increased with overall thickness, but the proportions between internal beds remained more or less constant.

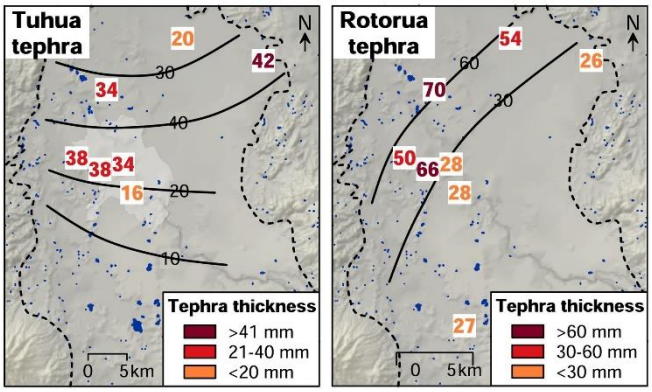


**Fig. 5.** Variability in thickness of Tuhua (Tu) and Rotorua (Rr) tephras within the Hamilton lowlands. The orientation of thickness contours (black solid lines) follow Lowe (1988b).

## 5. Description of SSDS

All seven major tephra layers exhibited SSDS in the form of mainly elongated load structures (i.e., down-sagging structures), dykes, and collapse structures, their occurrence and dimensions being variable throughout the Hamilton lowlands (Fig. 3c). SSDS were differentiated into three main types based on their dimensions, ranging between 30–100 mm (type 1), 10–30 mm (type 2), and <10 mm (type 3).

### *5.1. Type 1a solitary down-sagging structures*

The term 'type 1a solitary down-sagging structure' was used to describe elongated, ~30–100-mm long, solitary load structures that intruded (from the tephra layer) into underlying organic lake sediments. This type of SSDS was observed in six tephra layers and was restricted to deformations in the relatively thick Tuhua and Rotorua tephras deposited in central and north-western lakes (i.e., Rotokaeo, C2; Rotokauri, C4; Kainui, N1) (Figs. 1a, 3c).

Fig. 6 shows two typical examples of type 1a solitary down-sagging structures by means of core photos, our interpretation of internal beds and deformation features, and CT images from the outside of the whole-round core and as a longitudinal slice through the centre of the core. In the CT images, the organic lake sediment was removed using a high-pass filter. The organic lake sediment and SSDS sometimes exhibited similar CT densities. Therefore, it was not always possible to remove the entire organic lake sediment from CT datasets. As a result, the SSDS shown in CT images are slightly larger than those shown in the core photos. The two typical examples of type 1a solitary down-sagging structures (Fig. 6) are also available as rotational 360-degree videos in supplementary videos S1–S4.

The deformation involved all internal tephra beds (except for the upper silt beds Rr-1 and Tu-1) and underlying organic lake sediment. Type 1a solitary down-sagging structures shown in Fig. 6 were commonly up to 10-mm wide and up to 80-mm long, deformation features, which decreased in width towards the base. They exhibited sharp, distinct boundaries with surrounding organic lake sediment. Down-sagging structures appeared to be sheet-like in CT images and resembled load casts (*sensu* Owen, 2003). Disruptions of the thin silt beds (Rr-4, Tu-4) and underlying very fine to fine sand beds (Rr-5, Tu-5) indicate that the infill material of the down-sagging structure originated from the upper very fine to fine sand beds (Rr-2, Tu-2) or medium sand bed (Rr-3), or both.

The down-sagging structure Rr-6, which formed in the Rotorua tephra layer (Fig. 6a), exhibited a sheet-like geometry with vertical orientation and pointed end, whereas in the Tuhua tephra layer (Fig. 6b), three sheet-like down-sagging structures (Tu-6, Tu-7, Tu-8) were present, one of them (Tu-8) inclined at ~45 degrees, and all extending down towards Mamaku tephra, the latter occurring ~80 mm below the Tuhua tephra layer. In addition to the three down-sagging structures, a small normal fault with an offset of ~4 mm was observed in the lower beds of Tuhua tephra (Tu-4, Tu-5).

A collapse structure (C-1) was observed in the Tuhua tephra shown in Fig. 6b. Here, organic lake sediment overlying the tephra layer collapsed into the upper silt bed (Tu-1), corresponding to the down-sagging structure Tu-6 below.

### *5.2. Type 1b complex down-sagging structures*

The term ‘type 1b complex down-sagging structure’ was used to describe heterogeneous, ~30–100-mm long, often interconnected load structures that intruded from tephra layers into underlying organic lake sediments. This type of SSDS was observed in ten tephra layers and was restricted to deformations in Rotorua tephras deposited in central and north-eastern lakes (i.e., Rotoroa, C1; Rotokaeo, C2; Rotokaraka, N2; Leeson’s Pond, N3) (Figs. 1a, 3c).

Fig. 7 shows three typical examples of type 1b complex down-sagging structures. One of those examples is also available as rotational 360-degree videos in supplementary videos S5–S6. Similar to the type 1a SSDS, the type 1b complex down-sagging structures involved deformations in all internal beds of Rotorua tephra (except for the upper silt bed Rr-1) and the underlying organic lake sediment. Furthermore, down-sagging structures exhibited sharp, distinct boundaries with surrounding organic lake sediment. The infill material of the down-

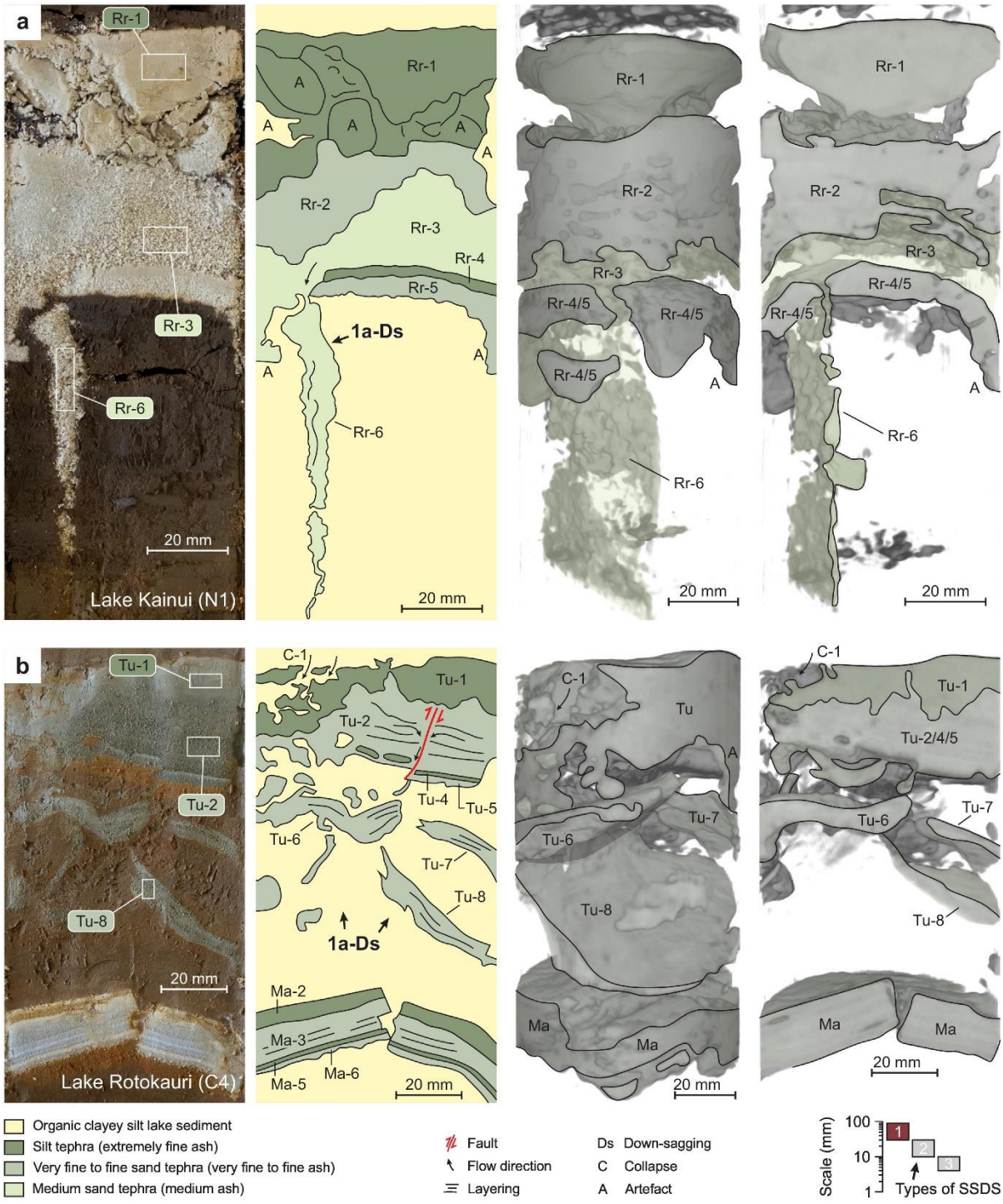


**Fig. 6.** SSDS in the shape of 30–100-mm long, type 1a solitary down-sagging structures observed in (a) Rotorua (Rr) and (b) Tuhua (Tu) tephras. Panels show (from left to right) core photos, interpretations of internal bedding and deformation structures, and CT images of the tephra layer and its deformation structures (with the organic lake sediment removed using a high-pass filter) from the outside of the whole-round core and as a longitudinal slice through the centre of the core. (a) Down-sagging structure (Rr-6) intrudes from medium sand bed (Rr-3) through basal beds (Rr-4, Rr-5) into underlying organic lake sediment. Note that the fractured appearance of the upper silt bed (Rr-1) is considered to be a coring artefact (i.e., A)

and does not represent deformation during the SSDS formation. (b) Three down-sagging structures (Tu-6, Tu-7, Tu-7) intrude from very fine to fine sand bed (Tu-2) through basal beds (Tu-4, Tu-5) into underlying organic lake sediment. Labels and boxes in left panel indicate locations chosen for grain size sampling.

sagging structures originated from the upper very fine to fine sand beds (Rr-2) or medium sand bed (Rr-3), or both.

Individual type 1b complex down-sagging structures shown in Fig. 7 were commonly 2–3 mm wide and up to 90 mm long (with most down-sagging structures being ~30–40 mm long) with pointed ends. Down-sagging structures were found to resemble load casts and pseudonodules (*sensu* Owen, 2003) in the split core. However, when considering the volumes of tephra and SSDS in CT scans, in which the less-dense organic lake sediment had been removed, down-sagging structures appeared to be continuous and no pseudonodules could be observed. Individual deformations, together forming the type 1b complex down-sagging structures, were observed to be curved (e.g., Rr-7), wavy (e.g., Rr-10), or straight (e.g., Rr-8, Rr-15, Rr-17), and often oriented vertically or at an angle between 90° (vertical) and 0° (horizontal). In one example (Rr-13), flame-like structures were observed within the down-sagging structure, being directed upwards, horizontally, as well as downwards. Sometimes (e.g., Rr-16), the down-sagging structure consisted of a main deformation feature from which and a number of smaller sub-deformations originate.

Distinct collapse structures (C-2 to C-5) were observed at the boundary between organic lake sediment and the tephra layers. Collapse structures corresponded to deformations within internal tephra beds below. For example, the collapse structure C-2 corresponded to the type 1b complex down-sagging structure Rr-9 (Fig. 7a). As a consequence of multiple collapse structures, the upper interface between the tephra layer and organic lake sediment appeared flame-like rather than straight (e.g., Fig. 7a). In one case (C-4, Rr-13), the organic lake sediment collapsed down into very fine to fine sand and medium sand beds (Rr-2, Rr-3), resulting in a normal fault with an offset of ~40 mm within the upper silt bed (Rr-1).

### *5.3. Type 2a down-sagging structures*

The term ‘type 2a down-sagging structure’ was used to describe ~10–30-mm long load structures that intruded from a tephra layer downwards into underlying organic lake sediments. Thirteen of this type of SSDS were observed across various lakes (Ngāroto, S1; Maratoto, S3;

Rotoroa, C1; Rotokaeo, C2; Rotokauri, C4; Leeson's Pond, N3; Fig. 1a). They occurred in Mamaku, Mangamate, Waiohau, and Rotorua tephras (Fig. 3c).

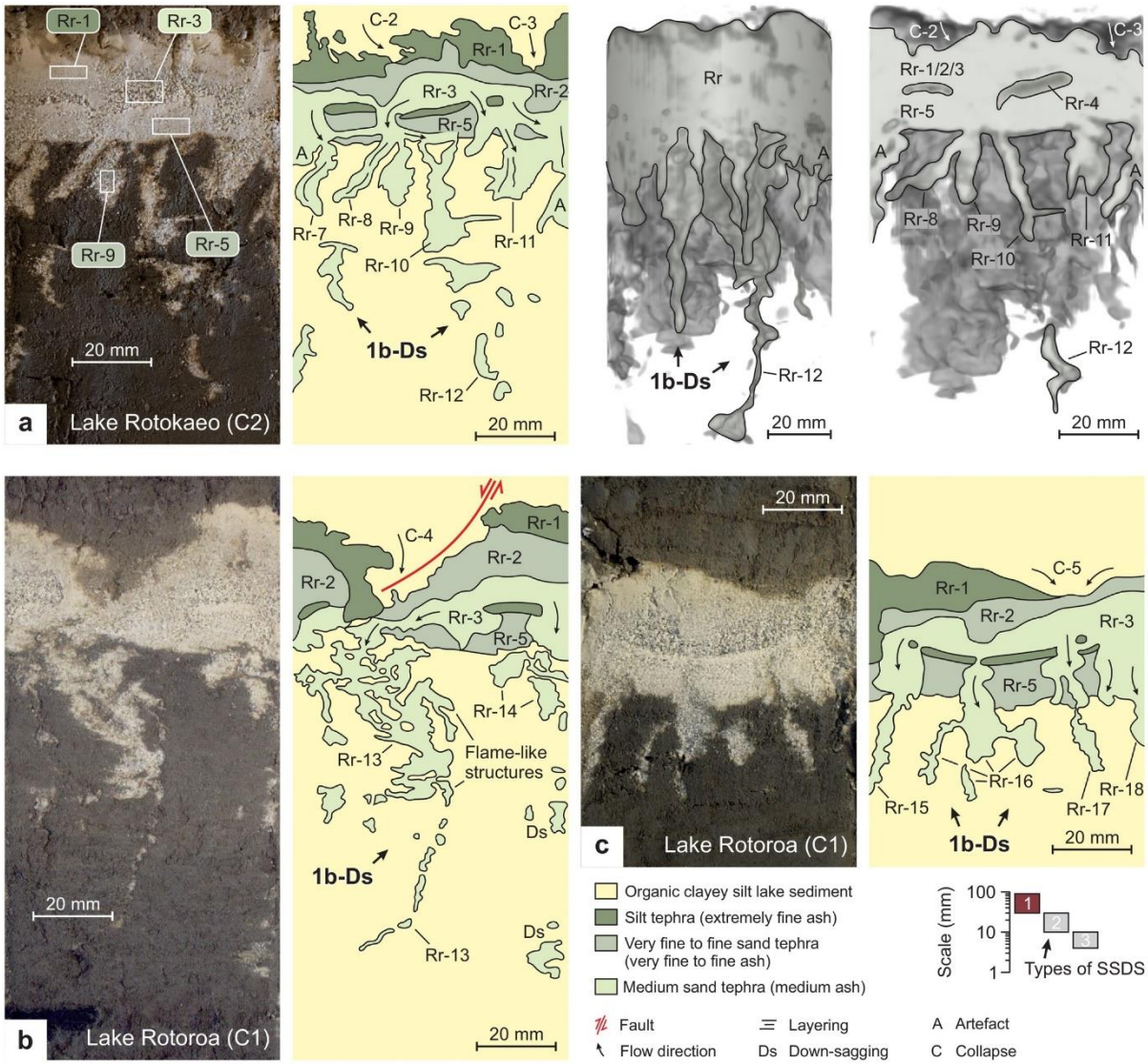


**Fig. 7.** SSDS in the shape of 30–100-mm long, type 1b complex down-sagging structures in Rotorua (Rr) tephra. Panels show (from left to right) core photos, interpretations of internal bedding and deformation structures, and (in 7(a) only) CT images of the tephra layer and its deformation structures (with the organic lake sediment removed using a high-pass filter) from the outside of the whole-round core and as a longitudinal slice through the centre of the core. Down-sagging structures (Rr-7 to Rr-18) intruding from medium coarse sand bed (Rr-3) through basal beds (Rr-4, Rr-5) into underlying organic lake sediment. Numerous collapse structures (C-2 to C-5) corresponded with deformations within tephra beds and indicate loss in tephra volume due to the process of down-sagging of tephra material. The labels and boxes in the upper left panel indicate locations chosen for grain size samples.

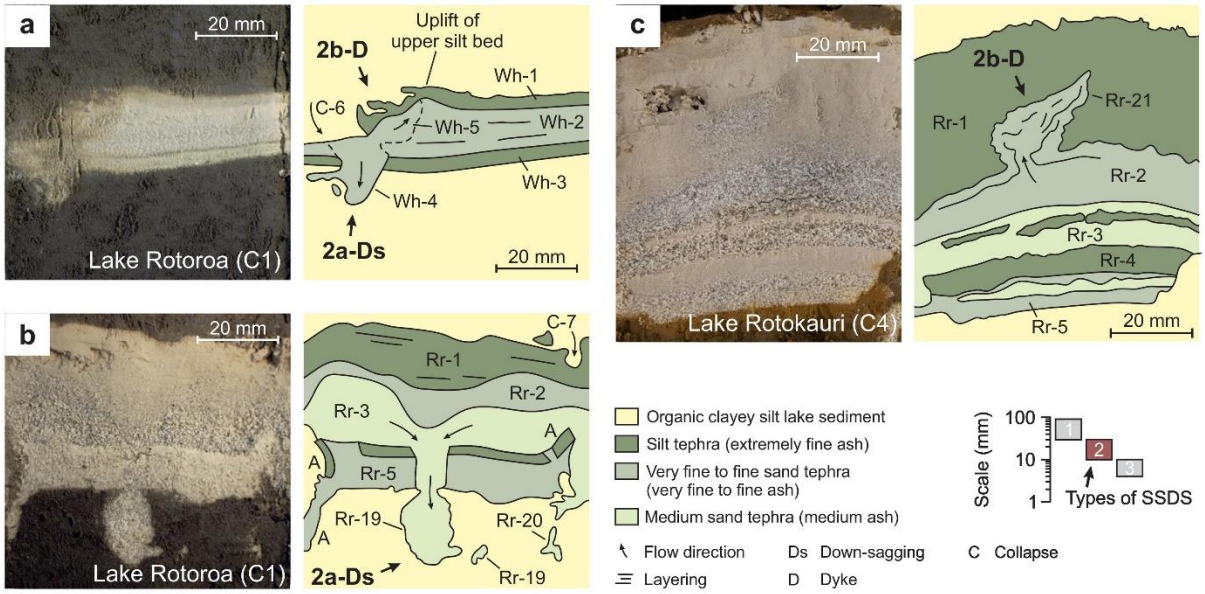


**Fig. 8.** SSDS in the shape of 10–30-mm long, type 2a down-sagging structures (a-b), and type 2b dykes (a, c) observed in (a) Waiohau (Wh) and (b-c) Rotorua (Rr) tephras. Panels show (from left to right) core photos and interpretations of internal bedding and deformation features. (a) Type 2a down-sagging structure (Wh-4), with associated collapse structure (C-6), intruding from very fine to fine sand bed (Wh-2) through the basal silt bed (Wh-3) into underlying organic lake sediment. A type 2b dyke (Wh-5) was observed in the same tephra layer, intruding upwards within very fine to fine sand bed (Wh-2). (b) Tephra intruded from medium sand bed (Rr-3) through basal beds (Rr-4, Rr-5) forming two type 2a down-sagging structures (R-19, R-20). (c) Type 2b dyke (Rr-21) intruding from very fine to fine sand bed (Rr-2) into silt bed above (Rr-1).

Fig. 8a-b shows typical examples of type 2a down-sagging structures. The down-sagging structure (Wh-4) involved deformations within the very fine to fine sand bed (Wh-2), underlying silt bed (Wh-3), and organic lake sediment below the tephra layer (Fig. 8a). The down-sagging structure was ~15 mm wide and ~15 mm long and decreased in width towards the bottom. The boundary between the down-sagging structure and the organic lake sediment was slightly more diffuse compared with that for the type 1 down-sagging structures. A distinct collapse structure (C-6) was also associated with this type 2a down-sagging structure. Further type 2a down-sagging structures were observed in Rotorua tephra (Fig. 8b). Here, tephra material from the medium sand bed (Rr-3) intruded downwards through basal tephra beds (Rr-4, Rr-5) forming two down-sagging structures (Rr-19, Rr-20). Rr-19 was ~15 mm wide and ~20 mm long and exhibited a rounded end, whereas Rr-20 was narrow and appeared discontinuous in the split core photo. Both down-sagging structures comprised load casts and pseudonodules, the latter likely being a result of the location of the plane of observation relative to the SSDS.

### *5.4. Type 2b dyke*

The term ‘type 2b dyke’ was used to describe ~10–30-mm long upward-directed intrusions from a tephra layer into the upper silt bed within the tephra layer. Two of this type of SSDS were observed at two lakes (Rotoroa, C1; Rotokauri, C4; Fig. 1a). They occurred in Waiohau and Rotorua tephras (Fig. 3c).

A type 2b dyke (Wh-5) was observed within the Waiohau tephra, which also provided the source of the type 2a down-sagging structure Wh-4 (Fig. 8a). The dyke, which originated from the very fine to fine sand bed (Wh-2), was ~10 mm wide, ~15 mm long, and inclined at ~45°. It seemed that the upper silt bed (Wh-1) was lifted upwards as a consequence of the deformation process of dyke Wh-5. A second type 2b dyke (Rr-21) was observed in Rotorua tephra (Fig. 8c). Here, tephra from the very fine to fine sand bed (Rr-2) intruded upwards into the upper silt bed (Rr-1), where it stopped propagating in the middle of the silt bed. The dyke was 18 mm wide, 25 mm long, slightly curved, and tapered upwards.

### *5.5. Type 3 down-sagging structures*

The term ‘type 3 down-sagging structure’ was used to describe small, less than 10-mm long, load structures that intruded from the tephra layer downwards into underlying organic lake sediments. Type 3 down-sagging structures were observed in nine tephra layers and occurred in Mamaku, Opepe, Waiohau, Rotorua, and Rerewhakaaitu tephras deposited in central and northern lakes (i.e., Rotoroa, C1; Rotokaeo, C2; Waiwhakareke, C3; Kainui, N1; Rotokaraka, N2; Leeson’s Pond, N3) (Figs. 1a, 3c).

Type 3 down-sagging structures were found to be irregularly shaped, downward-directed intrusions into underlying organic lake sediment, forming load casts (e.g., Ma-7, Wh-10) or pseudonodules (e.g., Ma-8, Wh-11). Pseudonodules appeared as small lumps (commonly up to ~5 mm long) entirely separated from the tephra layer. Down-sagging structures were commonly associated with the collapse of overlying organic lake sediment into the tephra layer (e.g., C-8, Ma-7; C-15, Wh-11).

## 6. Interpretation of SSDS

The different types of SSDS found in tephra deposits in the lakes within the Hamilton lowlands were interpreted by firstly establishing a deformation mechanism and driving force system and

then providing evidence for the most likely triggering mechanism using both the context-based and criteria-based approaches (Owen and Moretti, 2011; Owen et al., 2011).

### *6.1. Deformation mechanism*

The SSDS analysed in the present study (i.e., down-sagging structures and dykes) are commonly interpreted to be a consequence of liquefaction, although a number of other processes may also produce similar deformations in the sedimentary record (Moretti and van Loon, 2014). Liquefaction is a failure process that commonly occurs in water-saturated, loosely compacted granular materials. In those materials, shear stresses (e.g., from earthquake-induced shaking or rapid burial) may cause the grain fabric to collapse and become compact, leading to strength loss and temporary transfer of stress from the grain-to-grain contacts to the pore water. In environments where pore water pressure is prevented from dissipating, shear stresses may lead to a complete transfer of stress to the pore water, resulting in strength loss and viscous fluid-like behaviour of the granular material, with little or no yield strength (Owen and Moretti, 2011).

A number of compositional and geological characteristics define whether or not a sediment may be considered susceptible to liquefaction (Kramer, 1996). Compositional characteristics include the grain size distribution and the packing density (i.e., relative density) of the sediment (or tephra deposit). Liquefaction is commonly restricted to coarse silt to fine sand deposits (Moretti et al., 1999), although exceptions exist where liquefaction has been observed in gravelly soil (Cubrinovski et al., 2017; Zhou et al., 2020). Fine to medium silt is commonly considered less-liquefiable than coarse silt and sand (although cases exist, such as that of Ishihara, 1985), especially when clay minerals are present, preventing the collapse of the grain fabric during shearing (Boulanger and Idriss, 2006). In our study, SSDS were only observed in very fine to fine sand and medium sand tephra beds, whereas the upper silt beds and encapsulating organic lake sediments were not directly involved in the deformation process: the upper silt bed was passively involved in the collapse of organic lake sediment overlying the tephra layer and the organic lake sediment below the tephra layer deformed because of the intrusion of SSDS. Grain size distribution curves were obtained for the organic lake sediment, and for the upper silt beds (where applicable) and deformable beds (i.e., tephra source beds from which SSDS were initiated) of each of the seven major tephra layers (Fig. 10). For some thick tephra layers comprising SSDS (i.e., Tuhua, Rotorua), grain size distribution curves could also be obtained for the type 1a down-sagging structures. We

observed from these plots that the grain size distributions of the organic lake sediment and upper silt beds exhibited a large proportion of fines and were therefore systematically located outside the range for liquefiable soils defined by Tsuchida (1970), these ranges being widely used to distinguish liquefiable from less-liquefiable soils (Moretti et al., 1999; Rodríguez-Pascua et al., 2016; Villamor et al., 2016). The grain size distribution curves of deformable beds and down-sagging structures were mostly located within the liquefiable or potentially liquefiable ranges (Fig. 10).

The packing of the sediment (including tephra in our case) is another compositional characteristic governing liquefaction susceptibility (Owen and Moretti, 2011). Liquefaction develops most readily in loosely packed deposits, because when sheared, these become compacted and produce a more pronounced pore water pressure than more densely packed deposits. The packing (i.e., relative density) of individual internal tephra beds could not be directly assessed in the present study because of the relatively large amount of tephra material needed to perform the required laboratory tests from which relative density would be derived (i.e., dry bulk density, minimum and maximum dry density tests, DIN 18126, 1996). The finely bedded tephra-fall layers were deposited through water soon after being explosively erupted and carried by wind from source volcanoes (Fig. 1c). It is very likely that the internal bedding in the tephra layers largely reflects primary atmospheric dispersal and fallout processes (e.g., Alloway et al., 2013; Hopkins et al., 2015; Mastin et al., 2023) rather than substantial re-sorting or potential reworking during, or after, falling through the shallow lake-water columns: in the Hamilton lowlands, the lakes are closed-basin and ground-penetrating radar evaluation (Lowe, 1985) has shown (in Lake Maratoto) that individual, discrete tephra layers follow lake basin contours, a characteristic of tephra-fall beds (Houghton and Carey, 2015). Water sedimentation of quartz sand has been found to form deposits of medium densities (Wood et al., 2008). It is unknown how tephra-derived particles, overwhelmingly dominated by volcanic glass shards (Lowe, 1988b, a) and having a low particle density, large surface roughness, and usually high vesicularity, would deposit through water, but it may be expected that pumiceous tephra particles will form looser grain fabrics, within the loose to medium density range, than quartz sand.

Geological characteristics used for liquefaction susceptibility assessments include the sedimentary environment, groundwater conditions, age of deposition, and depth of burial (Youd, 1991). Fluvial, estuarine, and aeolian sediments are more often found to have liquefied because such materials occur in sedimentary environments that favour deposition of loose and

well-sorted fine to medium sands (Kramer, 1996). The sedimentary environment may also control the presence of permeability barriers within the sedimentary succession, such as mud layers, which increase the chance of liquefaction by creating zones of elevated pore water pressures (Obermeier, 1996; Owen and Moretti, 2011). The sedimentary environment in our study (i.e., lacustrine, together with tephra-fall deposition) favoured water-saturated successions of relatively loosely packed, relatively thin tephra deposits interlayered with fine-grained organic lake sediments. Furthermore, the sedimentation (atmospheric fallout) process of tephra layers generated the internal tephra bedding, typically with an upper silt bed at the top. It is plausible that the organic lake sediment above and below the tephra as well as the upper silt bed acted as permeability barriers and therefore increased the susceptibility to liquefaction in the very fine to fine and medium sand tephra beds. Deformation in Mangamate tephra was observed in only one lake (Lake Rotokaeo, C2). In this lake, Mangamate tephra exhibited an upper and lower silt bed. In all other lakes, Mangamate tephra was found to be intact and only consisted of the fine sand and medium sand beds (Mm-2 to Mm-4). Hence, it is concluded here that the lack of the upper silt bed in most lakes led to a lower liquefaction susceptibility for the Mangamate tephra layer.

Liquefaction susceptibility commonly decreases with time after deposition due to post-depositional processes, including cementation, consolidation, and compaction–the last two being the consequence of increase in overburden sediments with time. It has been shown that the liquefaction resistance of sandy soils increases by 40% within 400 years after deposition because of cementation and grain dislocation (Towhata et al., 2017) and that most liquefaction is observed in sediments buried less than 5 m (Obermeier, 1996). The tephra layers in our lacustrine study were deposited since ~17.6 ka cal BP and their interlayering within permanently saturated (anoxic) organic lake sediments has prevented significant alteration by hydrolysis or other chemical weathering processes (e.g., Churchman and Lowe, 2012). The high analytical totals of major elemental analyses of glass shards from the lacustrine tephras (Lowe, 1988b), which are extremely vulnerable to rapid hydration and dissolution (e.g., Kirkman and McHardy, 1980; Wolff-Boenisch et al., 2004; Churchman and Lowe, 2012), show that the glasses remain essentially pristine (shown also in other lacustrine-tephra studies, e.g., Newnham et al., 2004; Hopkins et al., 2015; Watson et al., 2016). In addition, the presence of easily weatherable silicate minerals, including olivine, in the ferromagnesian mineral assemblages (Lowe, 1988b) also indicates a lack of weathering. Only in special circumstances, such as very high acidity, are glasses and mafic minerals susceptible to dissolution in anoxic

environments (e.g., Hodder et al., 1991; Hodder et al., 1996). Hence, the tephra layers in our study have not undergone cementation, precluding a decrease in liquefaction susceptibility due to cementation.

Consolidation and compaction are similarly limited for the tephra layers in our study: they may be considered unconsolidated because the overburden stress is estimated to be very low (i.e., $\sigma_z < 20\ kPa$) due to the low bulk densities of organic lake sediments; and deformations described in our study occurred in tephra layers buried by less than 4.5 m of organic lake sediments. Thus, the liquefaction susceptibility of these tephras is likely to have persisted since their deposition.

Since liquefaction involves the temporary transition of the sediment body from solid-like to viscous fluid-like behaviour, the ensuing deformation will be ductile in character. Brittle features may only be observed in sediment that was adjacent to liquefied material when the deformation took place (Owen and Moretti, 2011). The SSDS observed in our study commonly featured ductile deformations characterised by internal flow structures (e.g., Figs. 6a, 7). Furthermore, SSDS commonly penetrated through basal (internal) tephra beds into underlying organic lake sediments, indicating high pore water pressure within the source tephra beds in which deformation was initiated. The boundaries between SSDS and organic lake sediments were found to be mostly brittle (although exceptions exist, e.g., the flame-like structure in type 1b down-sagging structure R-13), probably due to the low plasticity of the organic lake sediment. The upper silt beds exhibited collapse structures often associated with down-sagging structures below (e.g., Fig. 7). These collapse structures exhibited mainly ductile but also sometimes brittle deformations, indicating that the upper silt beds were at the transition between ductile and brittle soil behaviour.

The preceding discussion summarised the liquefaction-related compositional, geological, and morphological characteristics of organic lake sediments and tephra layers. It may be inferred here that the source tephra beds from which the deformation was initiated (i.e., very fine to fine sand and medium sand beds, equivalent to very fine to fine and medium ash beds in the volcanological grain size scale) exhibited considerably higher susceptibility to liquefaction than the upper silt beds (extremely fine ash beds) and organic lake sediments. We note that in order to obtain a holistic liquefaction susceptibility of the silt beds, Atterberg limits would have been required (Boulanger and Idriss, 2006). However, determining Atterberg limits on the internal tephra beds was not possible in our study due to the small volume of tephra

material available. Liquefaction is evidently a feasible deformation mechanism for the SSDS described in our study. In subsequent sections we assume that SSDS reported here were caused by liquefaction.

### *6.2. Driving forces of deformation*

#### *6.2.1 Influence of tephra thickness on occurrence and type of SSDS*

The analyses of sedimentary facies and SSDS revealed that the thickness of tephra layers and their internal beds varied somewhat throughout the lakes of the Hamilton lowlands (Fig. 4) and that deformation was commonly initiated within the very fine to fine sand and medium sand beds (e.g., Rr-2, Rr-3), but constrained by the upper silt bed (e.g., Rr-1), where deformation was limited to the collapse of organic lake sediments and upper silt beds into underlying tephra beds (Figs. 6-9). It may be assumed that variations in thickness (i.e., available volume during the deformation process) of tephra layers and their internal beds may have therefore controlled the occurrence and type of SSDS.

An initial assessment of the driving forces of deformation was performed by analysing the thicknesses of tephra layers and their internal beds and comparing them to the type and dimensions of SSDS. The total tephra thickness $h_{Tot}$ and the thicknesses of the upper silt bed $h_{Silt}$ and liquefiable ('deformable' in previous sections) beds $h_{Liq}$ were correlated to the dimensions of SSDS by means of the average area (visible in the split core) and the maximal vertical length of individual SSDS, respectively (Fig. 11). A fairly strong positive relationship was obtained for the correlation between the total tephra thickness and the average area of SSDS, with a Pearson's correlation coefficient of $R = 0.91$ (Fig. 11a). Hence, we conclude that the average area of SSDS linearly increases with the total tephra thickness. Furthermore, it was found that SSDS occurred in tephra layers of at least ~8 mm thickness and that the type of SSDS depended on the total tephra thickness and, thus, the available volume of liquefiable tephra material. Type 2 and 3 SSDS, having the smallest dimensions of SSDS analysed in our study, commonly occurred in tephra layers with total thicknesses less than ~20 mm (with some exceptions). Type 1b complex down-sagging structures exhibited larger dimensions and occurred in tephra layers of intermediate thickness (~30 mm). Type 1a solitary down-sagging structures exhibited the largest dimensions and occurred in tephra layers at least ~40 mm in thickness.

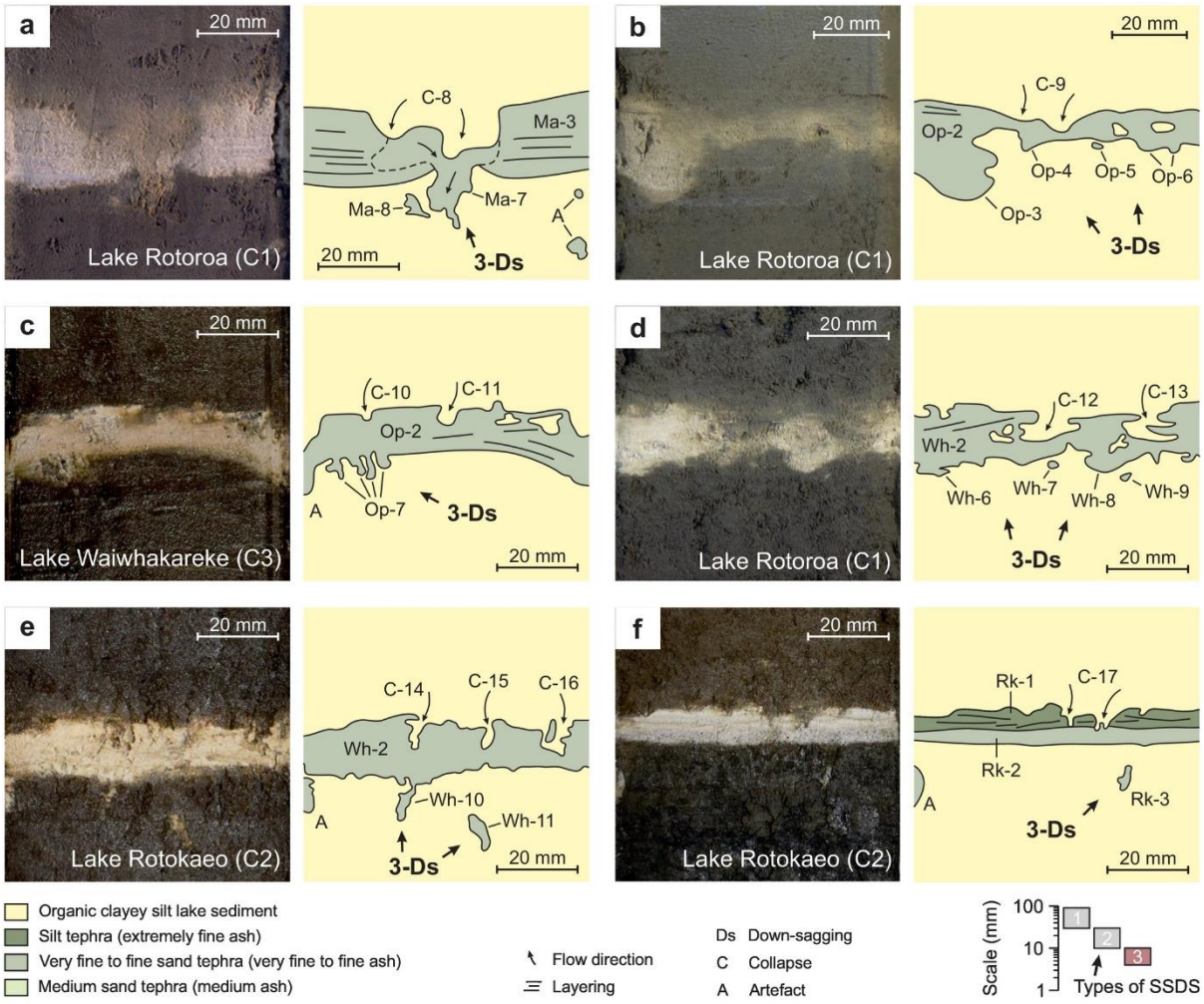


**Fig. 9.** SSDS in the shape of <10-mm long, type 3 down-sagging structures present in various tephras and lakes with collapse structures (C-8 to C-17) indicating loss of tephra volume due to the processes of deformation.

The thickness of the upper silt bed and the thickness of the liquefiable bed(s) correlated with the average area of SSDS too, with Pearson's correlation coefficients of $R = 0.91$ and $R = 0.70$, respectively (Fig. 11b-c). The fairly strong correlation between the thickness of the upper silt bed, which was not directly involved in the liquefaction process, and the average area of SSDS, is considered here to be a result of the intrinsic relationship between the total tephra thickness and the thickness of its internal beds.

It may be expected that with an increase in total tephra thickness, the thicknesses of internal beds would increase likewise, keeping the proportions more or less constant. This latter relationship can be directly observed, especially in Rotorua tephra (Fig. 4). The maximal vertical length of SSDS was only moderately correlated with the thickness of liquefiable bed(s) (Fig. 11d). Therefore, the maximal vertical length of SSDS is considered less suitable for assessing the dimensions and type of SSDS for a given tephra layer.

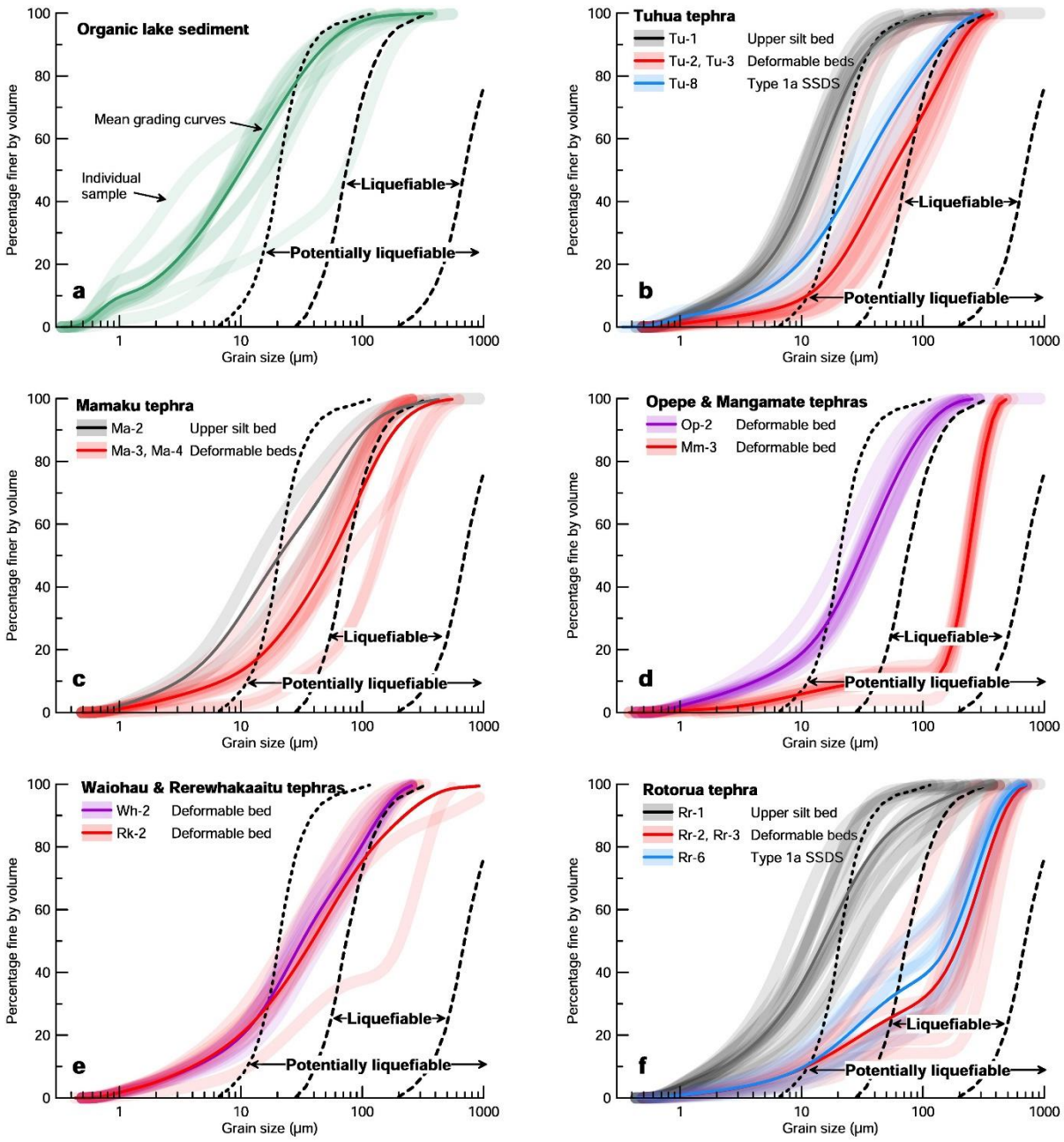


**Fig. 10.** Grain size distribution curves of (a) organic lake sediment and (b-f) tephra layers. If applicable, grain size distribution curves were distinguished for upper silt beds, deformable beds, and SSDS. Boundaries for liquefiable and potentially liquefiable soils are from Tsuchida (1970). In each plot, transparent and solid curves indicate individual and averaged grading curves, respectively.

The role of the liquefiable bed(s) on the occurrence and type of SSDS was further studied through relationships shown in Fig. 11e-f. In these graphs, the thickness of the liquefiable bed(s) was normalised by the total tephra thickness (Fig. 11e) and by the thickness of the upper silt bed (Fig. 11f). We observed from these graphs that type 1 and 2 (10–100-mm long) SSDS formed only in tephra layers in which the thickness of liquefiable bed(s) was less than 45% of the total tephra thickness (i.e., $h_{Def}/h_{Tot} < 0.45$) and up to two times thicker than

the upper silt bed (i.e., $h_{Def}/h_{Silt} < 2$). This finding implies that the presence of a thick upper silt bed (in relation to the liquefiable beds) is an important control for the liquefaction process forming these two types of SSDS in our study. Type 3 (<10-mm long) SSDS, on the other hand, formed over a wider range of proportions of internal tephra beds (i.e., $0.2 < h_{Def}/h_{Tot} < 1.0$ and $1 < h_{Def}/h_{Silt} < 9$), indicating that the liquefaction process forming this type of SSDS was driven to a lesser extent by the presence of an upper silt bed.

*6.2.2. Down-sagging structures*

The down-sagging structures reported in the present study exhibited internal flow structures and may resemble downward-directed dykes formed as consequence of fluidisation in the later stage of liquefaction (Owen et al., 2011). However, downward-directed dykes are physically impossible (even in reverse b-a density gradient systems) due to the normal hydraulic gradient in the pore water. The only exception for downward-directed dyke formation due to fluidisation is in subglacial environments, where the hydrogeological system may allow for injections being directed upwards, laterally, and downwards (Eyles and Clark, 1985). Downward-directed dykes are not feasible in our study because the northern North Island of New Zealand did not undergo significant glaciation (i.e., no glacierisation) before or since the formation of the lakes within the Hamilton lowlands (Newnham et al., 1989; Newnham et al., 1999; Barrell et al., 2013; Lorrey and Bostock, 2017).

Alternatively, the down-sagging structures could have formed as sand infills into fissures and cracks in environments controlled by extensional tectonics. This type of SSDS is commonly referred to as Neptunian dyke and is considered to form passively due to gravity and not necessarily because of a the process of fluidisation and liquefaction (Moretti and Sabato, 2007; Basilone et al., 2016). The Hamilton lowlands are not known to have been affected by any extensional tectonics in the past 20 kyrs (e.g., Edbrooke, 2005). Furthermore, it is considered unlikely here that fissures and cracks could form in the soft, unconsolidated, organic lake sediment. Therefore, it is not possible that the down-sagging structures reported in our study are Neptunian dykes.

We conclude that the down-sagging structures most closely represent some sort of load structures. The driving force of deformation of load structures is considered to be related to gravitational instabilities caused by the reverse density gradient system between the tephra layer and the relatively less-dense organic lake sediment below (Anketell et al., 1970).

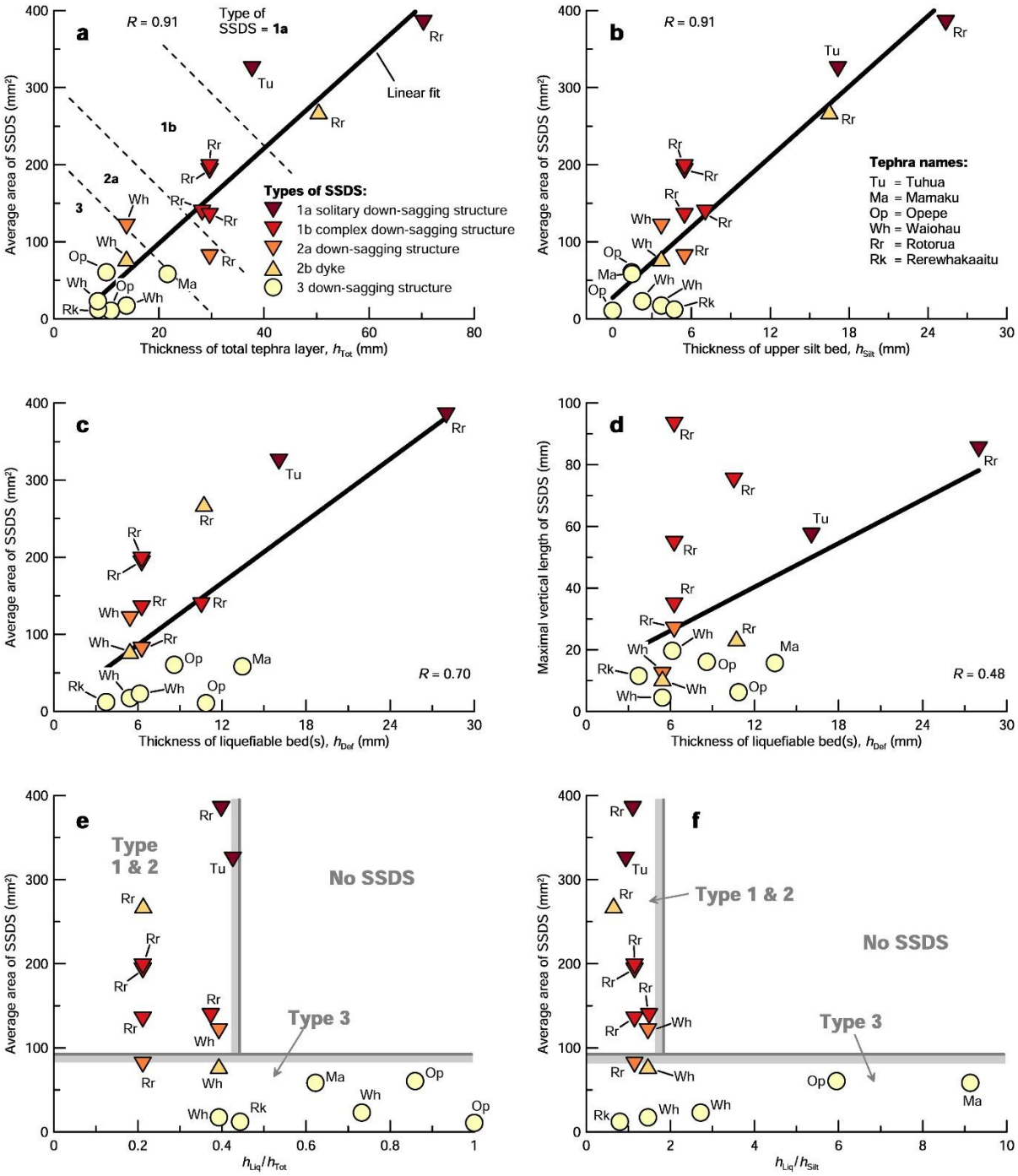


**Fig. 11.** Correlation between intact tephra and SSDS dimensions. (a-c) Correlations between average area of SSDS and tephra thickness, specifically: (a) thickness of total tephra layer; (b) thickness of upper silt bed; and thickness of liquefiable bed(s). (d) Correlation between thickness of liquefiable bed(s) and maximal vertical length of SSDS. (e-f) Influence of proportions of liquefiable bed(s) on occurrence and type of SSDS, with respect to (e) thickness of total tephra layer and (f) thickness of upper silt bed.

In our study, all types of down-sagging structures occurred in tephra deposits interlayered with organic lake sediment and commonly containing an upper silt bed. To better understand the driving mechanism in such a system, dry bulk densities and mean grain sizes

were obtained for the relevant internal beds of the Tuhua and Rotorua tephras, these being the two thickest tephra layers in our study. These parameters were plotted next to conceptual representations of those tephra layers once liquefied (Fig. 12a-b). The SSDS shown in these conceptual three-dimensional models represent simplifications of the type 1a solitary down-sagging structures presented for Tuhua and Rotorua tephras in Fig. 6.

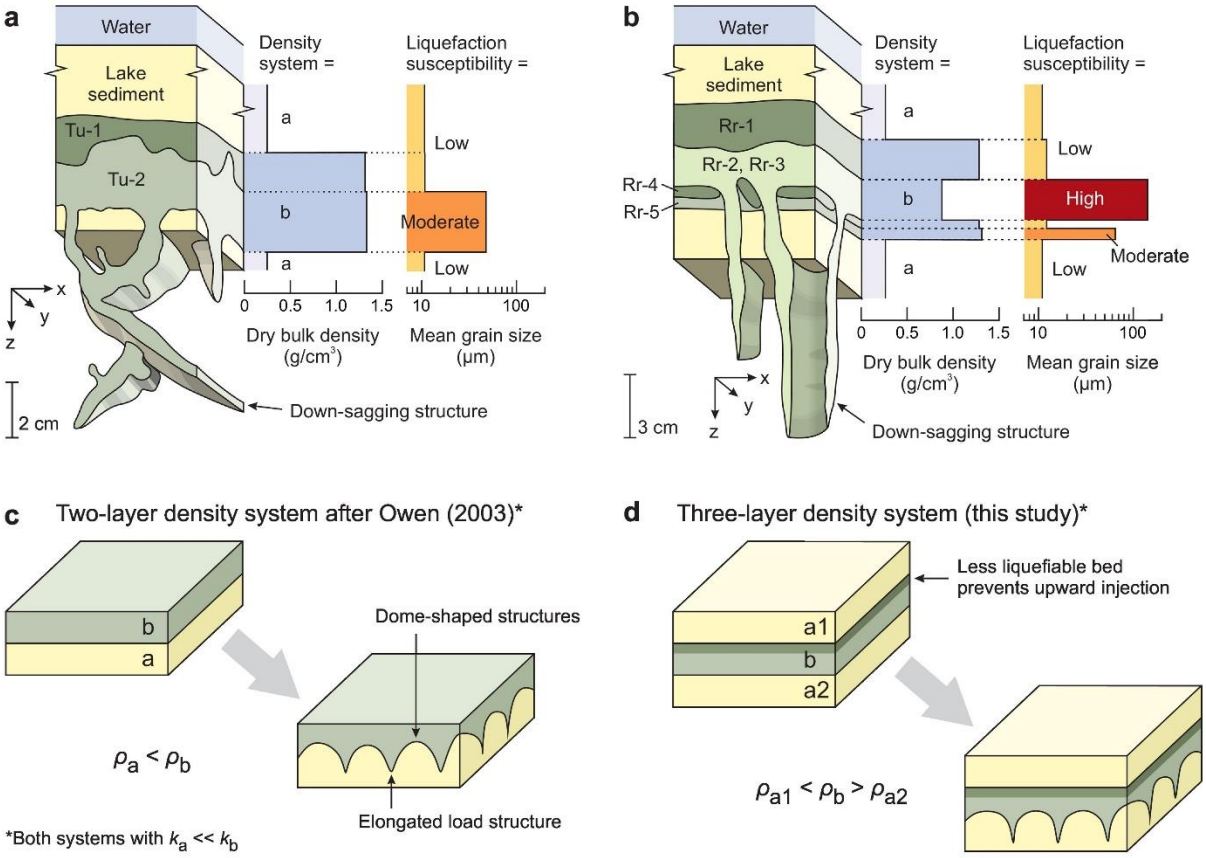


**Fig. 12.** Schematics illustrations of density systems in our study. (a-b) Variability in bulk dry density and mean grain size of organic lake sediments and internal beds of (a) Tuhua and (b) Rotorua tephras. Both tephras formed a-b-a density systems together with overlying and underlying organic lake sediment. The liquefiable internal tephra beds exhibited considerably higher mean grain sizes than organic lake sediments, and upper silt beds indicate higher degree of liquefaction susceptibilities. (c-d) Schematic diagrams showing the driving force of load structure formation for reverse density gradients that occur in (c) two-layer b-a density systems (after Owen, 2003) and (d) three-layer a-b-a density systems (this study). The two-layer density system is solely controlled by the reverse density contrast of the two layers, whereas in the three-layer density system, the less liquefiable upper silt bed prevented upward-directed dyke formation. The three-layer density system is considered a valid model for load structure formation (i.e., down-sagging structures) reported in our study. $\rho$ and $k$ denote the densities and relative kinematic viscosities of the reverse density system, respectively (Anketell et al., 1970).

Both Tuhua and Rotorua tephra layers exhibited dry bulk densities up to ~four times larger than those of the overlying and underlying organic lake sediment and, thus, created three-layer a-b-a density systems. Furthermore, the mean grain size $\bar{x}$ (here representing the position of the grain size distribution curve relative to the boundaries of liquefiable soils) was found to be considerably larger for the liquefiable beds ($60 \leq \bar{x} \leq 130\ \mu m$) than for the organic lake sediments and upper silt beds (the last two having $\bar{x} \approx 10\ \mu m$). Based on these grain size results, the liquefiable beds of Tuhua (Tu-2) and Rotorua (Rr-2, Rr-3) tephras are considered to have moderate (i.e., "potentially liquefiable", *sensu* Tsuchida, 1970) and high susceptibilities to liquefaction (i.e., "liquefiable", *sensu* Tsuchida, 1970), respectively, whereas the organic lake sediment and upper silt beds may be considered to have low susceptibility to liquefaction.

Collecting dry bulk density samples from the other tephra samples was not feasible because of their thinness. The grain size distribution curves of the upper silt beds (where applicable), and of the liquefiable beds of the remaining tephra layers (i.e., Mamaku, Opepe, Mangamate, Waiohau, Rerewhakaaitu), followed similar trends as shown for Tuhua and Rotorua tephras (Fig. 10). Therefore, we conclude that the remaining tephras probably deformed because of a similar driving mechanism as that described for the Tuhua and Rotorua tephras.

Building on the early work of Anketell et al. (1970), Owen (2003) published comprehensive concepts for load structure formation in reverse b-a density systems. Hence, the morphologies of load structures depend on the contrast in density $\rho$ and relative kinematic viscosity $k$ between the upper and lower layer (Fig. 12c). For reverse b-a density systems (i.e., $\rho_a < \rho_b$), for which the relative kinematic viscosity of the lower layer is much smaller than that of the upper layer (i.e., $k_a \ll k_b$), it may be expected that narrow, elongated, downward-directed load structures comprising the relatively denser material, would form together with wide, upward-directed dome-shaped structures comprising the relatively less-dense material (Owen, 2003). The down-sagging structures we have reported here resemble the narrow, elongated load structures of this model.

We adapted the concept for load structure formation published by Owen (2003) to three-layer (a-b-a) density systems (Fig. 12d), where units a1 and a2 represent the organic lake sediment above and below unit b of relatively higher density (i.e., a tephra layer containing the upper silt bed). The organic lake sediment is assumed to exhibit a considerably lower kinematic viscosity than the tephra layer. The upper, less-dense unit a1 likely exhibits a slightly lower

density and stress state than the underlying, less-dense unit a2, due to normal consolidation of the sediment column in the lake. Therefore, liquefaction in unit b would cause upward-directed intrusion into the overlying sediment unit a1. However, the presence of a less-liquefiable permeability barrier at the top of the central unit b is preventing upward-directed dyke formation. Instead, the tephra liquefies, resulting in loss of shear strength, and behaves in a viscous fluid-like manner, while sagging downwards into the underlying less-dense organic lake sediment. A similar driving force of deformation has been proposed for multi-layered reverse density systems (Moretti and Ronchi, 2011).

Wide, upward-directed, dome-shaped structures are commonly associated with this type of load structure (Owen, 2003). However, wide, upward-directed dome-shaped structures were not seen in our study. This is probably a result of the coring and sampling approach used in our study. The use of sediment/well cores to study large-scale SSDS, which can vary in dimensions and type within relatively small lateral distances (Morsilli et al., 2020), has limitations, as discussed comprehensively by Ezquerro et al. (2015).

Törő and Pratt (2016) studied a lacustrine sedimentary record from the Eocene Green River Formation (Wyoming, U.S.A.) and reported small upward- and downward-directed SSDS in three-layer a-b-a systems. It is considered likely here that the concept for load structure formation in three-layer (a-b-a) density systems of our study could be applicable to other lacustrine sedimentary records, such as the one studied by Törő and Pratt (2016).

*6.2.3. Dykes*

Dykes were observed only twice among the large number of down-sagging structures described in our study and were restricted to small intrusions from the liquefiable source beds into the upper less-liquefiable silt beds (Fig. 8). Such upward-directed injection follows the deformation mechanism for sand liquefaction in normal density gradients (Rodríguez-Pascua et al., 2000; Owen and Moretti, 2011; Belzyt et al., 2021).

*6.2.4. Collapse structures*

In the present study, we observed distinctive collapse structures, sometimes with associated faults, that coincided with the down-sagging structures (Figs. 6-9). Collapse structures were characterised by the mixing of overlying organic lake sediment with parts of the upper silt bed of the tephras, sometimes forming fold-like structures (e.g., Fig. 7a). Similar deformation structures have been interpreted as water-escape structures due to fluidisation

following liquefaction in sandy beds that were constrained by less-permeable beds (Moretti and Sabato, 2007). Here, the collapse structures and associated faults are instead considered to have resulted from the collapse of organic lake sediment and the upper silt bed into voids created by the down-sagging of tephra material into underlying organic lake sediments.

### *6.3. Triggering mechanism*

#### *6.3.1. Non-seismic triggers*

Liquefaction can be triggered by many different allochthonous processes (Owen and Moretti, 2011), such as pressure fluctuations due to water waves and turbulent water flow (e.g., Dzuynski and Smith, 1963; Okusa, 1985), tsunamis (e.g., Benson et al., 1997), tidal shear (e.g., Wells et al., 1980), rapid sediment loading (Anketell et al., 1970), groundwater seepage (e.g., Li et al., 1996), periglacial processes (Harris et al., 2002), and impacts of extra-terrestrial objects (Alvarez et al., 1998).

The lakes of our study occur in basins formed within sheltered embayments in the Hamilton lowlands with no connection to the ancestral Waikato River once formed because of the latter's subsequent entrenchment after ~17.5 cal ka BP (Lowe and Green, 1992; Newnham et al., 2003). Therefore, pressure fluctuations due to water waves and turbulent flow, tsunamis, and tidal shear are considered unlikely to be trigger mechanisms. Moreover, the tephras were deposited very rapidly, mantling the lake-bed morphology, a characteristic of tephra-fall deposition (Lowe, 1985; Lowe, 2011; Houghton and Carey, 2015). They were then buried by very slow deposition of organic lake sediments with typical sedimentation rates of ~0.1–0.5 mm/yr (Green and Lowe, 1985; Newnham et al., 1989), making it highly unlikely that overlying sediments caused significant excess pore pressure within tephra layers. Seepage has not been observed as a liquefaction trigger in lacustrine environments, and is known to produce predominantly tubular SSDS (Li et al., 1996). In the present study, down-sagging structures were observed to be sheet-like rather than tubular (e.g., Fig. 6), excluding seepage as a potential triggering mechanism. There are no indications that impacts of extra-terrestrial objects or periglacial processes, played a role in triggering liquefaction in our study, and the northern North Island environment is too temperate for periglacial processes (e.g., Newnham et al., 1989; Newnham et al., 1999; Leathwick et al., 2003; Lorrey and Bostock, 2017).

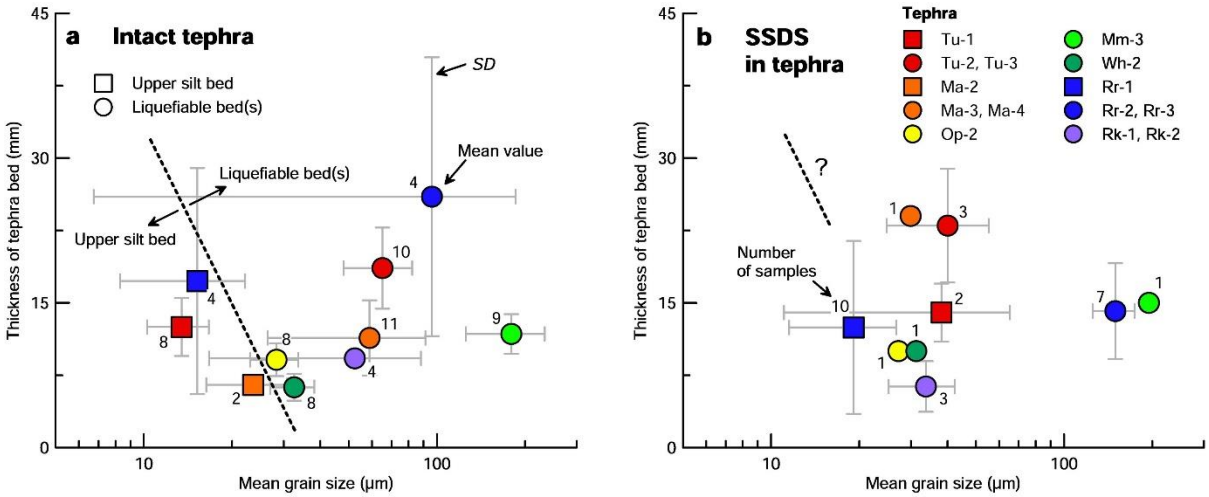


**Fig. 13.** Mean grain size and thickness of internal tephra beds of the seven major tephra layers compared between (a) intact tephra layers and (b) tephra layers that exhibited SSDS. The influence of tephra properties on the liquefaction susceptibility can be considered neglectable on the basis of available data. Note that a considerable number of tephras could not be included in the comparison because grain size data and internal bedding characteristics were not available for all cores. Dashed lines indicate a potential threshold between the tephra properties of the upper silt bed and the liquefiable beds.

*6.3.2. Seismic trigger*

A number of criteria are commonly used in order to assess the likelihood for seismic (autochthonous) triggers of SSDS (Owen and Moretti, 2011). In recent earthquakes, liquefaction has been observed in wide areas around the epicentre (Cubrinovski et al., 2011). Seismically induced SSDS should therefore be of large lateral and areal extent. In the present study, SSDS were observed in nine out of ten lakes extending over a wide area (with a maximum extent of ~40 km) within the Hamilton lowlands (Figs. 1, 3). We acknowledge here that core records analysed in our study were not suitable to comprehensively assess the lateral extent of liquefaction because sediment cores can only reflect sedimentary successions at a single location (Ezquerro et al., 2015), but, nevertheless, we obtained multiple cores from lakes across the study area and, thus, providing a degree of replication from multiple locations (Table S1).

The effect of seismically-induced liquefaction on susceptible sediment is pervasive, which means that SSDS should be laterally continuous, with some notable exceptions (Morsilli et al., 2020), unless there is some significant variation in sediment properties (Owen and Moretti, 2011). The present study found that internal bedding characteristics and grain size distribution of some tephra layers varied throughout the Hamilton lowlands (Figs. 4, 10). The

influence of this variability on liquefaction susceptibility of these tephras was studied by comparing mean grain size and thicknesses of liquefiable beds and upper silt bed between tephra layers that resisted the triggering and stayed intact (i.e., no SSDS observed) and those that liquefied (i.e., SSDS observed) (Fig. 13). The available data of mean grain size and thickness of internal beds compiled in Fig. 13 exhibited a considerable scatter. However, the tephra properties of intact tephra layers were commonly within the standard deviation of those obtained for liquefied tephra layers, indicating variations in tephra properties were not a significant influence on whether or not liquefaction was triggered. Fig. 13 also highlights the fact that the deformation of tephra layers did not cause a significant change in thickness of tephra layers and their upper silt beds. We note that a considerable number of tephras could not be included in the comparison because detailed grain size data and internal bedding characteristics were not available for all cores. Interestingly, Fig. 13a could also be used to differentiate the bedding characteristics of upper silt beds and liquefiable beds of intact tephra layers (dashed line in Fig. 13a).

The pervasive nature of SSDS could be observed in the 1b complex down-sagging structures because deformation in the associated tephra layers was not restricted to a single SSDS per core. Other types of SSDS, especially the type 2 down-sagging structures and dykes, are considered less pervasive as only single SSDS were observed in each core. This observation may have been influenced by the use of sediment cores, being only 50 to 80 mm wide, rather than natural outcrops (Ezquerro et al., 2015) (which do not exist). However, it may be concluded here that the presence of at least one type of pervasive SSDS, the type 1b complex down-sagging structure, is a sufficient indication for a seismic trigger of all SSDS because the different types of SSDS occurred in the same tephra layers within the same sedimentary successions.

Earthquakes are recurring events (Owen and Moretti, 2011). Therefore, seismically induced SSDS should be repeated throughout a vertical sedimentary succession. In our study, SSDS were reported for the seven major tephra layers deposited between 17.5 and 7.6 cal ka BP. Timing of triggering is difficult to obtain, however, because the organic lake sediment and tephra layers are considered to be essentially unconsolidated with minor or no ageing effects having taken place since deposition. One or more triggering events may have caused liquefaction in the lakes within the Hamilton lowlands.

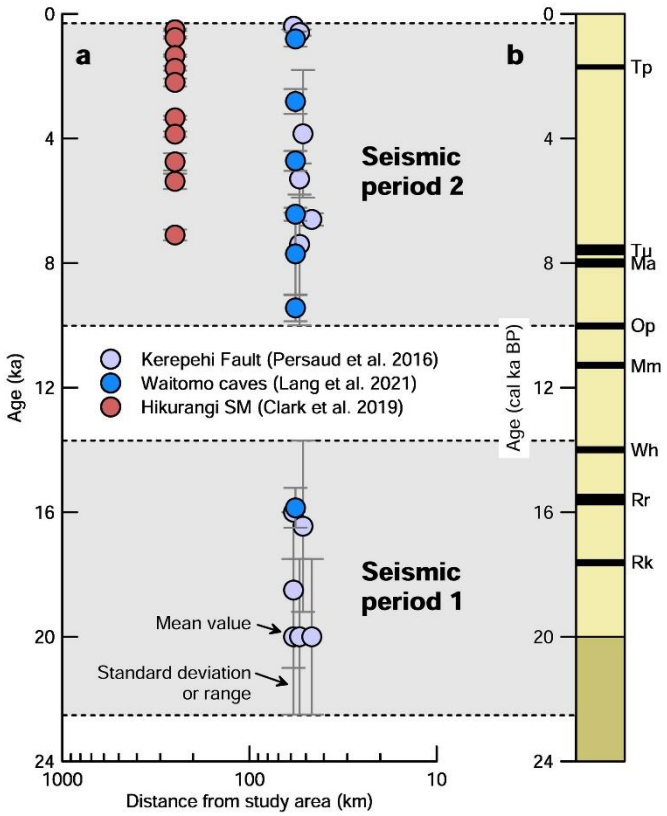


**Fig. 14.** Paleoseismic activity in the surroundings of the Hamilton lowlands detected by means of fault rupture within the zone of Kerepehi and Te Puninga faults (located ~50 km northeast of the study area) (Persaud et al., 2016; Van Dissen et al., 2021), damage observed in the Waitomo caves (located ~57 km south of the study area) (Lang et al., 2021; Williams, 2021), and subduction earthquakes in the Hikurangi Subduction Margin (SM) (located ~250 km southeast of the study area) (Clark et al., 2019). The paleoseismic activity clusters within two time periods, extending from 22.5 to 13.7 and 10.0 to 0.3 cal ka, respectively. The three oldest tephra layers (Rerewhakaitu, Rotorua, Waiohau) were deposited during the first seismic period, whereas the three youngest tephra layers (Opepe, Mamaku, Tuhua) were deposited during the second seismic period. Liquefaction in the three oldest tephra layers could have been triggered either by activity in the first or second seismic period, or both, whereas the three youngest tephra layers were likely triggered by activity in the second seismic period.

Subsequent events may have caused re-liquefaction, although this is often considered a rare phenomenon (Obermeier, 1996; Owen and Moretti, 2011). Therefore, the repeated occurrence of SSDS could not be used as a valid criterion to assess seismic triggering in the present study.

Morphological similarities between SSDS and structures formed by liquefaction in recent earthquakes might seem a valuable criterion for recognising a seismic origin (Owen and Moretti, 2011). The load structures and dykes reported in our study resembled liquefaction

structures that have been unambiguously linked with seismic triggering (Rodríguez-Pascua et al., 2000).

The proximity of faults that have been active during the formation of SSDS, and which have the potential to have caused moment magnitude $M > 5$ earthquakes (Rodríguez-Pascua et al., 2000), is considered as strong evidence for the seismically-induced triggering of liquefaction (Owen and Moretti, 2011). A number of faults may have been active since the deposition of the first tephra layer (Fig. 14). Large (moment magnitude $M > 7.2$) paleoearthquakes occurred between 7.3 and 0.5 cal ka BP at the offshore subduction margin, the Hikurangi Trough located ~250 km to the southeast of our study area (Fig. 1b) (Clark et al., 2019). At least three of the earthquakes that occurred at the Hikurangi Trough since the deposition of the tephra layers in the Hamilton lowlands originated from ruptures longer than 450 km along the margin (Clark et al., 2019). Assuming a fault width of 150 km and using the new fault scaling relationship from the National Hazards Model 2022 for New Zealand (Gerstenberger et al., 2022), we calculated moment magnitudes of $8.4 \leq M \leq 8.9$ for the three events. From global and New Zealand-specific liquefaction observations (Maurer et al., 2015), the maximal distance from a $M$-8.9 rupture at which liquefaction can occur is somewhere between 150 and 250 km. We note that in order for earthquake waves originating from faulting within the Hikurangi Trough to reach the Hamilton lowlands, they must travel through the Taupō Volcanic Zone, the deposits in which are known to attenuate seismic waves (McVerry et al., 2006). Thus, the actual maximal distance at which liquefaction can occur may be considerably smaller. Nevertheless, we conclude here that there is still a potential for faulting within the Hikurangi Trough to have caused liquefaction within the Hamilton lowlands, despite attenuation of seismic waves within the Taupō Volcanic Zone.

Two periods of seismic activity were inferred from paleoseismic mapping at the Kerepehi and Te Puninga faults located within the Hauraki plains up to ~46 to ~58 km to the northeast (Fig. 1b), and from fault activity observations and damage mapped in the Waitomo Caves, located ~57 km to the south (Persaud et al., 2016; Lang et al., 2021; Van Dissen et al., 2021; Williams, 2021; Villamor, 2022) (Fig. 14). The Kerepehi and Te Puninga faults were estimated to have caused large ($M = 7$) earthquakes (Persaud et al., 2016; Villamor, 2022). Ground motion simulations of an $M$-7 earthquake at the Kerepehi Fault yielded peak ground accelerations between 0.15 and 0.27 g at the lakes of the present study (Dempsey et al., 2021), well above the minimum peak ground acceleration of 0.07 g needed to cause liquefaction in

sandy soils of New Zealand (Maurer et al., 2015). However, the liquefaction threshold of Maurer et al. (2015) should be applied with care here because it does not encompass the liquefaction of pumiceous tephra-derived soils, which in some cases have been found to exhibit considerably higher liquefaction resistance than sandy (non-pumiceous) soils (Asadi et al., 2018).

The two periods of seismic activity identified for the Hauraki Plains align well with the time of deposition of six of the seven major tephra layers (Fig. 14). The first seismic period (~22.3 to ~13.7 cal ka BP) encompasses deposition of the three oldest tephra layers (i.e., Rerewhakaaitu, Rotorua, and Waiohau), whereas the second seismic period (~10.0 to ~0.3 cal ka BP) encompasses deposition of the three youngest tephra layers (i.e., Opepe, Mamaku, Tuhua). It may be concluded here that fault activity at the Kerepehi and/or Te Puninga faults is a plausible seismic trigger for liquefaction that caused SSDS in our study.

Some aspects of the frequency or complexity of SSDS in our study were found to decrease with distance from a fault that may have been active during the deformation process, which is considered to be the strongest evidence for the seismic triggering of SSDS (Pope et al., 1997; Owen and Moretti, 2011). A potential zonation of SSDS within the Hamilton lowlands was assessed spatially and temporarily through Fig. 15. For two time periods, reflecting the deposition of the three oldest tephras (i.e., Rerewhakaaitu, Rotorua, Waiohau) and the three youngest tephras (i.e., Opepe, Mamaku, Tuhua), respectively, the number of each type of SSDS was plotted, for each lake, in relation to the total number of cores in which a particular tephra layer could be observed (i.e., was present and not classified as discontinuous). For example, in Lake Rotoroa (C1), the total number of SSDS observed for Waiohau tephra was two (i.e., one type 2a down-sagging structure and one type 3 down-sagging structure). The total number of Waiohau tephra layers assessed at this lake (i.e., classified as intact or showing signs of SSDS) was eight. Dividing the number of SSDS by the number of total tephra layers assessed yielded a frequency estimate for SSDS occurrence for a particular lake (being 25% in this particular example). The total number of observations varied between lakes, affecting the confidence of the presented analysis. For example, at Lake Ngāroto the total number of tephra layers analysed was relatively low, providing some uncertainty when obtaining a frequency of SSDS occurrence. In contrast, at Lake Maratoto, where around 30 sediment cores were taken (Green and Lowe, 1985), the total number of tephra layers being analysed ranged from 13 to 20 between different tephras, providing higher certainty when calculating the frequency of SSDS occurrence.

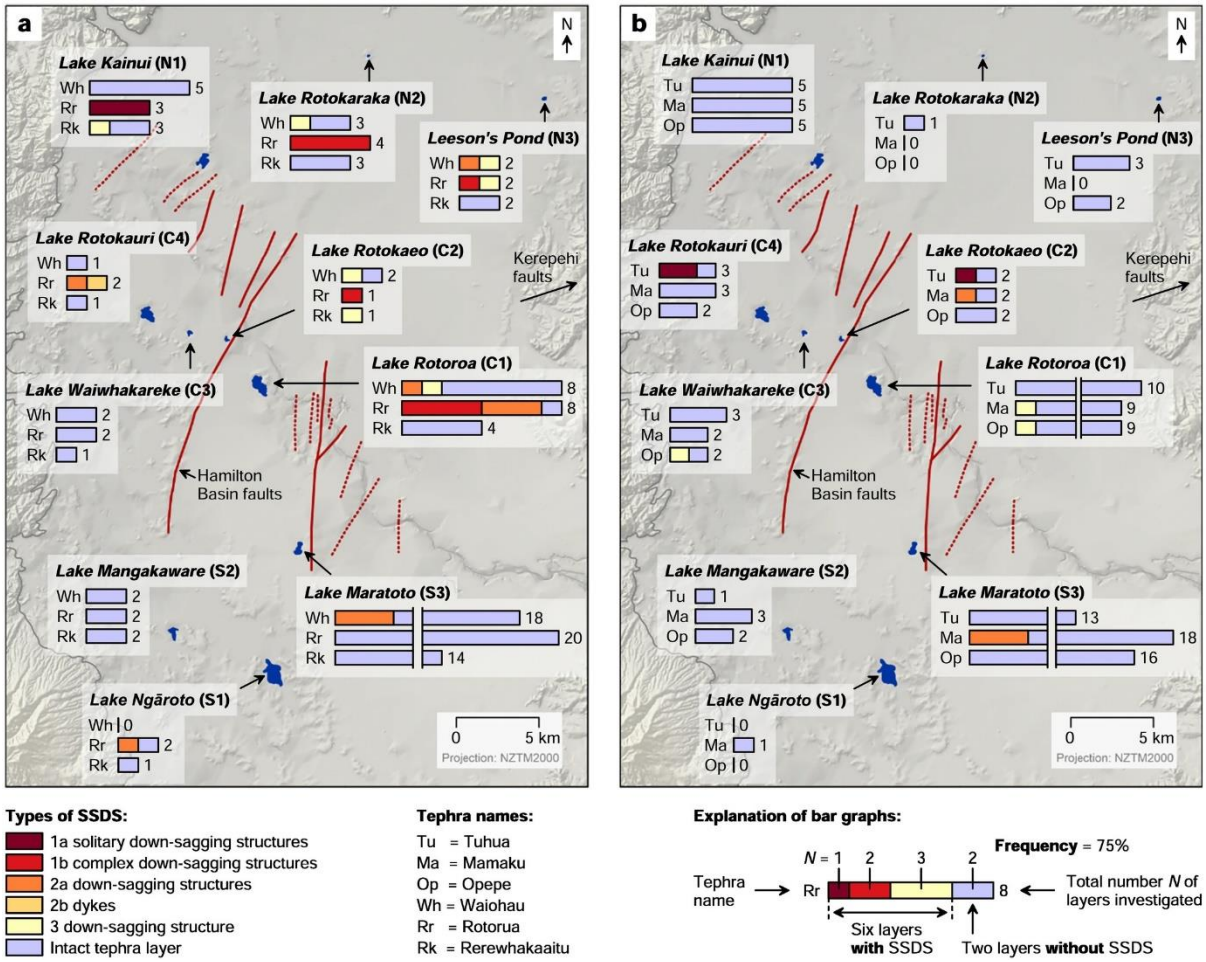


**Fig. 15.** Spatial and temporal analysis of SSDS observed in the ten lakes within the Hamilton lowlands. Type and frequency of SSDS occurrence for (a) the older tephra layers (i.e., (Rerewhakaitu, Rotorua, Waiohau), deposited between 17.5 and 14.0 cal ka BP, and (b) the younger tephra layers (i.e., Opepe, Mamaku, Tuhua), deposited between 10.0 and 7.6 cal ka BP.

When considering the three oldest tephra layers (Fig. 15a), the complexity (i.e., type 1–3 SSDS exhibit descending degree of complexity) and frequency of SSDS increased consistently towards the northeast, suggesting a link between seismic activity on the Kerepehi and/or Te Puninga faults and liquefaction in the Hamilton lowlands. We acknowledge that the trend in complexity of SSDS could be partly the result of variability in tephra thickness as discussed earlier (see Fig. 11). However, a clear connection between tephra thickness variability (Fig. 4) and complexity of SSDS (Fig. 15) could not be found. The trend in complexity towards the northeast could not be observed for the three youngest tephra layers (Fig. 15b). For these layers, the occurrence of SSDS was instead restricted to the central part of the study area, with the complexity and frequency of SSDS being lower than that for the

older tephra layers. The occurrence of SSDS within the younger tephra layers matches the location of the recently-mapped Hamilton Basin faults (Moon and de Lange, 2017; Van Dissen et al., 2021). The Hamilton Basin faults occur in the upper Hamilton Ash beds, dated at ~74 ka BP (Lowe, 2019). Hence, the Hamilton Basin faults are currently considered older than the tephra layers analysed in the present study, because the riverine and riverine-phytogenic lakes in which these occur were formed by deposition of the ~20-ka-BP-old Hinuera Formation (Kear and Schofield, 1978; Lowe and Green, 1992; McCraw, 2011). It is currently unknown if the Hamilton Basin faults were active after the deposition of the Hinuera Formation. However, from the spatial proximity of the SSDS in the younger tephra layers to the Hamilton Basin faults, we infer that they may have been triggered by a near-field seismic source within the Hamilton lowlands, therefore potentially from one or more of the Hamilton Basin faults. Alternatively, liquefaction in the younger tephra layers could have been triggered by far-field earthquakes from the offshore Hikurangi subduction margin.

# 7. Conclusions

The present study analysed a large number of soft-sediment deformation structures (SSDS) that occurred in seven unconsolidated, up to 8-cm thick, silicic tephra layers that were deposited in ~35 riverine and riverine-phytogenic lakes within the Hamilton lowlands, central North Island, New Zealand, since 17.5 cal ka BP. Based on sediment descriptions, X-ray computed tomography (CT) scanning, and analyses of dry bulk density, grain size distribution, and Atterberg limits of samples from cores taken from ten lakes, the following conclusions are made.

- SSDS were classified into elongated load structures (i.e., down-sagging structures) of different dimensions, ranging from millimetre- to decimetre-scale, and centimetre-long dykes.
- Deformations commonly involved the intrusion of very fine sand to medium sand internal tephra beds into underlying organic lake sediments. Tephra layers commonly exhibited an upper silt bed, which was not directly involved in the deformation process.
- The organic lake sediment and the upper silt bed are considered as less liquefiable, whereas the very fine sand to medium sand internal tephra beds are considered as liquefiable.

- The dimensions of SSDS linearly increased with the thickness of the source tephra layer.
- The tephra layers, and the organic lake sediments above and below them, form three-layer (a-b-a) density systems. It is inferred here that downward-directed deformation was favoured by this three-layer (a-b-a) density system, together with the presence of an upper, less-liquefiable silt bed preventing upward intrusion during the liquefaction process.
- The spatial and temporal occurrence of SSDS within the Hamilton lowlands provided some evidence that liquefaction of the older tephras, deposited between 17.5 and 14 cal ka BP, was triggered by a seismic source to the northeast (i.e., Kerepehi and/or Te Puninga faults in the adjacent Hauraki Plains).
- Liquefaction of the younger tephra layers, deposited between 10.0 and 7.6 cal ka BP, may have been triggered by local faults within the Hamilton lowlands, namely one or more of the Hamilton Basin faults, or by distant faulting at the Hikurangi subduction margin.

## Declaration of competing interest

The authors declare that they have no known competing financial interests or personal relationships that could have appeared to influence the work reported in this paper.

## Acknowledgments

We thank iwi of Ngāti Wairere (especially Mrs Hekeiterangi Broadhurst and Wiremu Puke) and Ngā Iwi Tōpū O Waipā, Zeke Fiske and Hamilton City Council, Tony Roxburgh and Waipā District Council, the Department of Conservation, and private land owners for their ongoing support in providing access to lakes for coring and in other ways. Marcus Vandergoes, Susie Wood, Andrew Rees, and Henry Gard, representing the Lakes380 project, are thanked for sediment coring in 2020 and 2022 (Vandergoes and Rees also undertook coring in 2016), Phillip Hassall from Hamilton Radiology for supporting core CT scanning, Alex Harpur for helping to describe sediment cores in 2016, Vittoria Gibbons for laboratory assistance, and Simon Lovatt and Carol Robinson for administrative support relating to

funding. The paper is an output of the Commission on Tephrochronology (COT) of the International Association of Volcanism and Chemistry of the Earth's Interior (IAVCEI). We thank Massimo Moretti and an anonymous referee for their constructive comments on our paper.

MOK, DJL, VGM, JC, TI, PV, RAM, and RPO were supported by an MBIE Endeavour Fund (Smart Ideas) project "Evaluating earthquake risk using liquefied volcanic-ash layers in lakes" (contract UOWX1903). MOK, DJL, VGM, JC, TI, and PV were supported by the Marsden Fund project "Earth-shaking insight from liquefied volcanic-ash (tephra) layers in lakes: using geotechnical experiments, CT-scanned lake sediment cores, and tephrochronology to map and date prehistoric earthquakes" (contract UOW1902). DJL and RCL were supported by an Earthquake Commission (EQC) project "Hidden hazards: revealing volcanic ashfall hazards in the Waikato region by detecting and analysing cryptotephras in sediments" (contract 15/U713). PV and DJL were supported by an Earthquake Commission (EQC) project "Paleoseismology of the newly discovered Te Puninga Fault, Hauraki Plains" (contract BIG 012 2020). DJL and RCL were supported by a Waikato University SIF Research Grant (2016) "Tephra seismites: a new tool to evaluate, date, and map paleoseismicity using tephra liquefaction in lake sediments". RCL was supported by a PhD fees-scholarship, funded by Waikato Regional Council. PV was supported by an MBIE Strategic Science Investment Fund (GNS-Hazards and Risk Management Programme). RPO was supported by the NZ Centre for Earthquake Resilience (QuakeCoRE). RJ was supported by an AIM Facility fund in part from the UK's Engineering and Physical Sciences Research Council (EP/M028267/1).

## References

Alloway, B.V., Lowe, D.J., Larsen, G., Shane, P.A.R., and Westgate, J.A., 2013. Tephrochronology. In: Elias, S., and Mock, C. (eds.), The Encyclopaedia of Quaternary Science, 2nd edition. Elsevier, Amsterdam, 277-304.

Alvarez, W., Staley, E., O'Connor, D., and Chan, M.A., 1998. Synsedimentary deformation in the Jurassic of southeastern Utah—A case of impact shaking? Geology 26, 579-582.

Anketell, J.M., Cegła, J., and Dżułyński, S., 1970. On the deformational structures in systems with reversed density gradients. Annales Societatis Geologorum Poloniae 40, 3-30.

Asadi, M.S., Asadi, M.B., Orense, R.P., and Pender, M.J., 2018. Undrained cyclic behaviour of reconstituted natural pumiceous sands. Journal of Geotechnical and

Geoenvironmental Engineering 144, 04018045, https://doi.org/10.1061/(ASCE)GT.1943-5606.0001912.

ASTM D2487-06, 2010. Standard Practice for Classification of Soils for Engineering Purposes (Unified Soil Classification System). ASTM International, https://doi.org/10.1520/D2487-06

ASTM D7348-21, 2021. Standard Test Methods for Loss on Ignition (LOI) of Solid Combustion Residues. ASTM International, https://doi.org/10.1520/D7348-21

ASTM D 4318-17e1, 2017. Standard test methods for liquid limit, plastic limit, and plasticity index of soils. ASTM International, https://doi.org/10.1520/D4318-17E01.

Barrell, D.J.A., Almond, P.C., Vandergoes, M.J., Lowe, D.J., Newnham, R.M., and NZ-INTIMATE members., 2013. A composite pollen-based stratotype for inter-regional evaluation of climatic events in New Zealand over the past 30,000 years (NZ-INTIMATE project). Quaternary Science Reviews 74, 4-20, http://dx.doi.org/10.1016/j.quascirev.2013.04.002.

Basilone, L., Sulli, A., and Morticelli, M.G., 2016. The relationships between soft-sediment deformation structures and synsedimentary extensional tectonics in Upper Triassic deep-water carbonate succession (Southern Tethyan rifted continental margin—Central Sicily). Sedimentary Geology 344, 310-322, http://dx.doi.org/10.1016/j.sedgeo.2016.01.010.

Bektas, O., Çapkinoglu, S., and Akdag, K., 2001. Successive extensional tectonic regimes during the Mesozoic as evidenced by neptunian dikes in the Pontide Magmatic Arc, Northeast Turkey. International Geology Review 43, 840-849, https://doi.org/10.1080/00206810109465051.

Belzyt, S., Pisarska-Jamroży, M., Bitinas, A., Woronko, B., Phillips, E.R., Piotrowski, J.A., and Jusienė, A., 2021. Repetitive Late Pleistocene soft-sediment deformation by seismicity-induced liquefaction in north-western Lithuania. Sedimentology 68, 3033-3056, https://doi.org/10.1111/sed.12883.

Benson, B.E., Grimm, K.A., and Clague, J.J., 1997. Tsunami deposits beneath tidal marshes on northwestern Vancouver Island, British Columbia. Quaternary Research 48, 192-204, https://doi.org/10.1006/qres.1997.1911.

Blott, S.J., and Pye, K., 2001. GRADISTAT: a grain size distribution and statistics package for the analysis of unconsolidated sediments. Earth Surface Processes and Landforms 26, 1237-1248, https://doi.org/10.1002/esp.261.

Boulanger, R.W., and Idriss, I.M., 2006. Liquefaction susceptibility criteria for silts and clays. Journal of Geotechnical and Geoenvironmental Engineering 132, 1413-1426, https://doi.org/10.1061/(ASCE)1090-0241(2006)132:11(1413).

Churchman, G.J., and Lowe, D.J., 2012. Alteration, formation, and occurrence of minerals in soils. In: Huang, P. M., Li, Y., and Sumner, M. E. (eds.), Handbook of Soil Sciences. Properties and Processes, 2nd edition CRC Press, USA, 20.21-20.72.

Clark, K., Howarth, J., Litchfield, N., Cochran, U., Turnbull, J., Dowling, L., Howell, A., Berryman, K., and Wolfe, F., 2019. Geological evidence for past large earthquakes and tsunamis along the Hikurangi subduction margin, New Zealand. Marine Geology 412, 139-172, https://doi.org/10.1016/j.margeo.2019.03.004.

Cubrinovski, M., Bradley, B., Wotherspoon, L., Green, R., Bray, J., Wood, C., Pender, M., Allen, J., Bradshaw, A., and Rix, G., 2011. Geotechnical aspects of the 22 February 2011 Christchurch earthquake. Bulletin of the New Zealand Society for Earthquake Engineering 44, 205-226, https://doi.org/10.5459/bnzsee.44.4.205-226.

Cubrinovski, M., Bray, J.D., De La Torre, C., Olsen, M.J., Bradley, B.A., Chiaro, G., Stocks, E., and Wotherspoon, L., 2017. Liquefaction effects and associated damages observed at the Wellington CentrePort from the 2016 Kaikoura earthquake. Bulletin of the New Zealand Society for Earthquake Engineering 50, 152-173, https://doi.org/10.5459/bnzsee.50.2.152-173.

Dempsey, D., Eccles, J.D., Huang, J., Jeong, S., Nicolin, E., Stolte, A., Wotherspoon, L., and Bradley, B.A., 2021. Ground motion simulation of hypothetical earthquakes in the upper North Island of New Zealand. New Zealand Journal of Geology and Geophysics 64, 570-588, https://doi.org/10.1080/00288306.2020.1842469.

Di Capua, A., De Rosa, R., Kereszturi, G., Le Pera, E., Rosi, M., and Watt, S.F.L., 2022. Volcanically derived deposits and sequences: a unified terminological scheme for application in modern and ancient environments. Geological Society, London, Special Publications 520, 1-25, https://doi.org/10.1144/SP520-2021-201.

DIN 18126, 1996. Soil, investigation and testing - Determination of density of non-cohesive soils for maximum and minimum compactness. Deutsches Institut für Normen e. V., https://dx.doi.org/10.31030/7209583.

Dzuynski, S., and Smith, A.J., 1963. Convolute lamination, its origin, preservation, and directional significance. Journal of Sedimentary Research 33, 616-627, https://doi.org/10.1306/74D70ED4-2B21-11D7-8648000102C1865D.

Edbrooke, S.W., 2005. Geology of the Waikato area. Institute of Geological and Nuclear Sciences 1:250,000 Geological Map 4. 1 sheet and 68p. IGNS, Lower Hut, 0478098774.

El Taki, H., and Pratt, B.R., 2012. Syndepositional tectonic activity in an epicontinental basin revealed by deformation of subaqueous carbonate laminites and evaporites: seismites in Red River strata (Upper Ordovician) of southern Saskatchewan, Canada. Bulletin of Canadian Petroleum Geology 60, 37-58, https://doi.org/10.2113/gscpgbull.60.1.37.

Eyles, N., and Clark, B.M., 1985. Gravity-induced soft-sediment deformation in glaciomarine sequences of the Upper Proterozoic Port Askaig Formation, Scotland. Sedimentology 32, 789-814, https://doi.org/10.1111/j.1365-3091.1985.tb00734.x.

Ezquerro, L., Moretti, M., Liesa, C.L., Luzón, A., and Simón, J.L., 2015. Seismites from a well core of palustrine deposits as a tool for reconstructing the palaeoseismic history of a fault. Tectonophysics 655, 191-205, http://dx.doi.org/10.1016/j.tecto.2015.05.025.

Folk, R.L., 1980. Petrology of Sedimentary Rocks. Hemphill Publishing Company, Austin, Texas. 190 p.

Fortuin, A.R., and Dabrio, C.J., 2008. Evidence for Late Messinian seismites, Nijar Basin, south-east Spain. Sedimentology 55, 1595-1622, https://doi.org/10.1111/j.1365-3091.2008.00959.x.

Froggatt, P.C., and Lowe, D.J., 1990. A review of late Quaternary silicic and some other tephra formations from New Zealand: their stratigraphy, nomenclature, distribution,

volume, and age. New Zealand Journal of Geology and Geophysics 33, 89-109, https://doi.org/10.1080/00288306.1990.10427576.

Gavrilov, Y.O., 2017. Reflection of seismic paleoevents in Mesozoic–Cenozoic terrigenous sequences of the northern Caucasus. Lithology and Mineral Resources 52, 1-19, https://doi.org/10.1134/S0024490217010035.

Gerstenberger, M.C., Bora, S., Bradley, B.A., DiCaprio, C., Van Dissen, R.J., Atkinson, G.M., Chamberlain, C., Christophersen, A., Clark, K.J., Coffey, G.L., and et al., 2022. New Zealand National Seismic Hazard Model 2022 revision: model, hazard and process overview. GNS Science.

Gladkov, A.S., Lobova, E.U., Deev, E.V., Korzhenkov, A.M., Mazeika, J.V., Abdieva, S.V., Rogozhin, E.A., Rodkin, M.V., Fortuna, A.B., and Charimov, T.A., 2016. Earthquake-induced soft-sediment deformation structures in Late Pleistocene lacustrine deposits of Issyk-Kul lake (Kyrgyzstan). Sedimentary Geology 344, 112-122, https://doi.org/10.1016/j.sedgeo.2016.06.019.

Green, J.D., and Lowe, D.J., 1985. Stratigraphy and development of c. 17 000 year old Lake Maratoto, North Island, New Zealand, with some inferences about postglacial climatic change. New Zealand Journal of Geology and Geophysics 28, 675-699, https://doi.org/10.1080/00288306.1985.10422541.

-, 1994. Origins and development. In: Clayton, J., and de Winton, M. (eds.), Lake Rotoroa: Change in an Urban Lake. National Institute of Water and Atmospheric Research Ecosystems Publication, Wellington, NZ, 13-23.

Harris, C., Murton, J., and Davies, M.C.R., 2002. Soft-sediment deformation during thawing of ice-rich frozen soils: results of scaled centrifuge modelling experiments. Sedimentology 47, 687-700, https://doi.org/10.1046/j.1365-3091.2000.00322.x.

Hodder, A.P.W., de Lange, P.J., and Lowe, D.J., 1991. Dissolution and depletion of ferromagnesian minerals from Holocene tephras in an acid bog, New Zealand, and implications for tephra correlation. Journal of Quaternary Science 6, 195-208, https://doi.org/10.1002/jqs.3390060303.

Hodder, A.P.W., Naish, T.R., and Lowe, D.J., 1996. Towards an understanding of thermodynamic and kinetic controls on the formation of clay minerals from volcanic glass under various environmental conditions. In: Pandalai, S. G. (ed.), Recent Research Developments in Chemical Geology. Research Signpost, Trivandrum, India, 1-11.

Hopkins, J.L., Lowe, D.J., and Horrocks, J.H., 2021. Tephrochronology in Aotearoa New Zealand. New Zealand Journal of Geology and Geophysics 64, 153-200, https://doi.org/10.1080/00288306.2021.1908368.

Hopkins, J.L., Millet, M.-A., Timm, C., Wilson, C.J.N., Leonard, G.S., Palin, M.J., and Neil, H., 2015. Tools and techniques for developing tephra stratigraphies in lake cores: a case study from the basaltic Auckland Volcanic Field, New Zealand. Quaternary Science Reviews 123, 58-75, https://doi.org/10.1016/j.quascirev.2015.06.014.

Houghton, B.F., and Carey, R.J., 2015. Pyroclastic fall deposits. In: Sigurdsson, H. (ed.), The Encyclopaedia of Volcanoes, Second Edition. Elsevier, San Diego, 599-616.

Hume, T.M., Sherwood, A.M., and Nelson, C.S., 1975. Alluvial sedimentology of the Upper Pleistocene Hinuera Formation, Hamilton Basin, New Zealand. Journal of the Royal

Society of New Zealand 5, 421-462, https://doi.org/10.1080/03036758.1975.10419362.

Ishihara, K., 1985. Stability of natural deposits during earthquakes. 11th International Conference on Soil Mechanics and Foundation Engineering. International Society for Soil Mechanics and Geotechnical Engineering, 321-376

Juvigné, E.T., and Porter, S.C., 1985. Mineralogical variations within two widespread Holocene tephra layers from Cascade Range volcanoes, U.S.A. Géographie Physique et Quaternaire 39, 7-12.

Kang, H.C., Paik, I.S., Lee, H.I., Lee, J.E., and Chun, J.H., 2010. Soft-sediment deformation structures in Cretaceous non-marine deposits of southeastern Gyeongsang Basin, Korea: Occurrences and origin. Island Arc 19, 628-646, https://doi.org/10.1111/j.1440-1738.2010.00738.x.

Kear, D., and Schofield, J.C., 1978. Geology of the Ngaruawahia subdivision. New Zealand Geological Survey Bulletin 88, 1-168.

Kirkman, J.H., and McHardy, W.J., 1980. A comparative study of the morphology, chemical composition and weathering of rhyolitic and andesitic glass. Clay minerals 15, 165-173, https://doi.org/10.1180/claymin.1980.015.2.07.

Kleyburg, M.A., Moon, V.G., Lowe, D.J., and Nelson, C.S., 2015. Paleoliquefaction in Late Pleistocene alluvial sediments in Hauraki and Hamilton basins, and implications for paleoseismicity. Proceedings of 12th Australia New Zealand Conference on Geomechanics (ANZ 2015). NZ Geotechnical Society, 524-531, https://hdl.handle.net/10289/9952.

Kramer, S.L., 1996. Geotechnical Eartqhuake Engineering, Prentice Hall, New Jersey. 653 p.

Krumbein, W.C., and Pettijohn, F.J., 1938. Manual of sedimentary petrography. Geologiska Föreningen i Stockholm Förhandlingar 61, 225-227, https://doi.org/10.1080/11035893909452786.

Lang, J., Baker, J., Williams, P., Rowland, J., Clark, K., Howarth, J., Hellstrom, J., Cross, T., and Goded, T., 2021. Macro-characterisation of cave damage for palaeoseismological investigations in regions of low strain: a case study from central–western North Island (Waitomo caves), New Zealand. Quaternary Science Reviews 272, 107202, https://doi.org/10.1016/j.quascirev.2021.107202.

Langridge, R.M., Ries, W.F., Litchfield, N.J., Villamor, P., Van Dissen, R.J., Barrell, D.J.A., Rattenbury, M.S., Heron, D.W., Haubrock, S., and Townsend, D.B., 2016. The New Zealand active faults database. New Zealand Journal of Geology and Geophysics 59, 86-96, https://doi.org/10.1080/00288306.2015.1112818.

Leathwick, J., Wilson, G., Rutledge, D., Wardle, P., Morgan, F., Johnston, K., McLeod, M., and Kirkpatrick, R., 2003. Land Environments of New Zealand. Bateman, Auckland. 184 p.

Leonard, G.J., Begg, J.G., and Wilson, C.J.N., 2010. Geology of the Rotorua area: scale 1:250,000. Institute of Geological and Nuclear Sciences 1:250,000 geological map 5. 1 sheet and 99p. IGNS, Lower Hutt.

Li, Y., Craven, J., Schweig, E.S., and Obermeier, S.F., 1996. Sand boils induced by the 1993 Mississippi River flood: Could they one day be misinterpreted as earthquake-induced liquefaction? Geology 24, 171-174.

Limaye, A., 2012. Drishti: a volume exploration and presentation tool. Developments in X-ray Tomography VIII. International Society for Optics and Photonics, 85060X

Loame, R.C., Lowe, D.J., Pittari, A., Davies, S.M., Magill, C.R., Vandergoes, M.J., Rees, A.B.H., and Ross, N., 2018. Using CT scanning for reconnaissance and detection of cryptotephras in ~22,000-yr-old lake sediments, central Waikato region, New Zealand. Book of Abstracts, Crossing New Frontiers: INTAV International Field Conference on Tephrochronology, 'Tephra Hunt in Transylvania', 41-42

Lorrey, A.M., and Bostock, H., 2017. The climate of New Zealand through the Quaternary. In: Shulmeister, J. (ed.), Landscape and Quaternary environmental Change in New Zealand. Atlantis Advances in Quaternary Science, Vol. 3. Atlantis Press, Paris, 67-139.

Lowe, D.J., 1985. Application of impulse radar to continuous profiling of tephra-bearing lake sediments and peats: an initial evaluation. New Zealand Journal of Geology and Geophysics 28, 667-674, https://doi.org/10.1080/00288306.1985.10422540.

-, 1988a. Late Quaternary volcanism in New Zealand: towards an integrated record using distal airfall tephras in lakes and bogs. Journal of Quaternary Science 3, 111-120, https://doi.org/10.1002/jqs.3390030202.

-, 1988b. Stratigraphy, age, composition, and correlation of late Quaternary tephras interbedded with organic sediments in Waikato lakes, North Island, New Zealand. New Zealand Journal of Geology and Geophysics 31, 125-165, https://doi.org/10.1080/00288306.1988.10417765.

Lowe, D.J., 2011. Tephrochronology and its application: a review. Quaternary Geochronology 6, 107-153, https://doi.org/10.1016/j.quageo.2010.08.003.

Lowe, D.J., 2019. Using soil stratigraphy and tephrochronology to understand the origin, age, and classification of a unique Late Quaternary tephra-derived Ultisol in Aotearoa New Zealand. Quaternary 2, 1-34, https://doi.org/10.3390/quat2010009.

Lowe, D.J., Blaauw, M., Hogg, A.G., and Newnham, R.M., 2013. Ages of 24 widespread tephras erupted since 30,000 years ago in New Zealand, with re-evaluation of the timing and palaeoclimatic implications of the Lateglacial cool episode recorded at Kaipo bog. Quaternary Science Reviews 74, 170-194, https://doi.org/10.1016/j.quascirev.2012.11.022.

Lowe, D.J., and Green, J.D., 1992. Lakes. In: Soons, J. M., and Selby, M. J. (eds.), Landforms of New Zealand: Second Edition. Longman Paul, Auckland, 107-143.

Lowe, D.J., Rees, A.B.H., Newnham, R.M., Hazell, Z.J., Gehrels, M.J., Charman, D.J., and Amesbury, M.J., 2018. Isochron-informed Bayesian age modelling for tephras and cryototephras: application to mid-Holocene Tuhua tephra, northern New Zealand. Book of Abstracts, Crossing New Frontiers: INTAV International Field Conference on Tephrochronology, 'Tephra Hunt in Transylvania', 95-96

Lunina, O.V., and Gladkov, A.S., 2016. Soft-sediment deformation structures induced by strong earthquakes in southern Siberia and their paleoseismic significance. Sedimentary Geology 344, 5-19, http://dx.doi.org/10.1016/j.sedgeo.2016.02.014.

Manville, V., and Wilson, C.J.N., 2004. The 26.5 ka Oruanui eruption, New Zealand: a review of the roles of volcanism and climate in the post-eruptive sedimentary

response. New Zealand Journal of Geology and Geophysics 47, 525-547, https://doi.org/10.1080/00288306.2004.9515074.

Mastin, L.G., Carey, S.N., Van Eaton, A.R., Eychenne, J., and Sparks, R.S.J., 2023. Understanding and modeling tephra transport: lessons learned from the 18 May 1980 eruption of Mount St. Helens. Bulletin of Volcanology 85, 1-21, https://doi.org/10.1007/s00445-022-01613-0.

Maurer, B.W., Green, R.A., Quigley, M.C., and Bastin, S., 2015. Development of magnitude-bound relations for paleoliquefaction analyses: New Zealand case study. Engineering Geology 197, 253-266, https://doi.org/10.1016/j.enggeo.2015.08.023.

Mazumder, R., van Loon, A.J.T., Malviya, V.P., Arima, M., and Ogawa, Y., 2016. Soft-sediment deformation structures in the Mio-Pliocene Misaki Formation within alternating deep-sea clays and volcanic ashes (Miura Peninsula, Japan). Sedimentary Geology 344, 323-335, http://dx.doi.org/10.1016/j.sedgeo.2016.02.010.

McCraw, J.D., 2011. The wandering River: Landforms and geological History of the Hamilton Basin. Geosciences Society of New Zealand, Wellington, Guidebook No. 16, 88p. 88 p.

McVerry, G.H., Zhao, J.X., Abrahamson, N.A., and Somerville, P.G., 2006. Response spectral attenuation relations for crustal and subduction zone earthquakes. Bulletin of the New Zealand Society for Earthquake Engineering 39, 1-58, https://doi.org/10.5459/bnzsee.39.1.1-58

Moebis, A., Cronin, S.J., Neall, V.E., and Smith, I.E., 2011. Unravelling a complex volcanic history from fine-grained, intricate Holocene ash sequences at the Tongariro Volcanic Centre, New Zealand. Quaternary International 246, 352-363, https://doi.org/10.1016/j.quaint.2011.05.035.

Molenaar, A., Van Daele, M., Vandorpe, T., Degenhart, G., De Batist, M., Urrutia, R., Pino, M., Strasser, M., and Moernaut, J., 2021. What controls the remobilization and deformation of surficial sediment by seismic shaking? Linking lacustrine slope stratigraphy to great earthquakes in South–Central Chile. Sedimentology 68, 2365-2396, https://doi.org/10.1111/sed.12856.

Montenat, C., Barrier, P., d'Estevou, P.O., and Hibsch, C., 2007. Seismites: An attempt at critical analysis and classification. Sedimentary Geology 196, 5-30, https://doi.org/10.1016/j.sedgeo.2006.08.004.

Moon, V., and de Lange, W., 2017. Final Report on EQC Potential shallow seismic sources in the Hamilton Basin Project 16/717. University of Waikato.

Moretti, M., Alfaro, P., Caselles, O., and Canas, J.A., 1999. Modelling seismites with a digital shaking table. Tectonophysics 304, 369-383, https://doi.org/10.1016/S0040-1951(98)00289-3.

Moretti, M., and Ronchi, A., 2011. Liquefaction features interpreted as seismites in the Pleistocene fluvio-lacustrine deposits of the Neuquén Basin (Northern Patagonia). Sedimentary Geology 235, 200-209, https://doi.org/10.1016/j.sedgeo.2010.09.014.

Moretti, M., and Sabato, L., 2007. Recognition of trigger mechanisms for soft-sediment deformation in the Pleistocene lacustrine deposits of the Sant'Arcangelo Basin (Southern Italy): seismic shock vs. overloading. Sedimentary Geology 196, 31-45, https://doi.org/10.1016/j.sedgeo.2006.05.012.

Moretti, M., and van Loon, A.J.T., 2014. Restrictions to the application of 'diagnostic' criteria for recognizing ancient seismites. Journal of Palaeogeography 3, 162-173, https://doi.org/10.3724/SP.J.1261.2014.00050.

Morsilli, M., Bucci, M.G., Gliozzi, E., Lisco, S., and Moretti, M., 2020. Sedimentary features influencing the occurrence and spatial variability of seismites (late Messinian, Gargano Promontory, southern Italy). Sedimentary Geology 401, 105628, https://doi.org/10.1016/j.sedgeo.2020.105628.

Nairn, I.A., 1980. Source, age, and eruptive mechanisms of Rotorua Ash. New Zealand Journal of Geology and Geophysics 23, 193-207, https://doi.org/10.1080/00288306.1980.10424206.

Newnham, R.M., Eden, D.N., Lowe, D.J., and Hendy, C.H., 2003. Rerewhakaaitu Tephra, a land-sea marker for the Last Termination in New Zealand, with implications for global climate change. Quaternary Science Reviews 22, 289-308, https://doi.org/10.1016/S0277-3791(02)00137-3.

Newnham, R.M., Lowe, D.J., and Green, J.D., 1989. Palynology, vegetation and climate of the Waikato lowlands, North Island, New Zealand, since c. 18,000 years ago. Journal of the Royal Society of New Zealand 19, 27-150, https://doi.org/10.1080/03036758.1989.10426443.

Newnham, R.M., Lowe, D.J., Green, J.D., Turner, G.M., Harper, M.A., McGlone, M.S., Stout, S.L., Horie, S., and Froggatt, P.C., 2004. A discontinuous ca. 80 ka record of Late Quaternary environmental change from Lake Omapere, Northland, New Zealand. Palaeogeography, Palaeoclimatology, Palaeoecology 207, 165-198, https://doi:10.1016/j.palaeo.2004.02.007.

Newnham, R.M., Lowe, D.J., and Williams, P.W., 1999. Quaternary environmental change in New Zealand: a review. Progress in Physical Geography 23, 567-610, http://ppg.sagepub.com/content/23/4/567.

Nichols, R.J., 1995. The liquification and remobilization of sandy sediments. Geological Society, London, Special Publications 94, 63-76, https://doi.org/10.1144/GSL.SP.1995.094.01.06.

Obermeier, S.F., 1996. Use of liquefaction-induced features for paleoseismic analysis—an overview of how seismic liquefaction features can be distinguished from other features and how their regional distribution and properties of source sediment can be used to infer the location and strength of Holocene paleo-earthquakes. Engineering Geology 44, 1-76, https://doi.org/10.1016/S0013-7952(96)00040-3.

Okusa, S., 1985. Wave-induced stresses in unsaturated submarine sediments. Geotechnique 35, 517-532, https://doi.org/10.1680/geot.1985.35.4.517.

Owen, G., 2003. Load structures: gravity-driven sediment mobilization in the shallow subsurface. Geological Society, London, Special Publications 216, 21-34, https://doi.org/10.1144/GSL.SP.2003.216.01.03.

Owen, G., and Moretti, M., 2011. Identifying triggers for liquefaction-induced soft-sediment deformation in sands. Sedimentary Geology 235, 141-147, https://doi.org/10.1016/j.sedgeo.2010.10.003.

Owen, G., Moretti, M., and Alfaro, P., 2011. Recognising triggers for soft-sediment deformation: current understanding and future directions. Sedimentary Geology 235, 133-140, https://doi.org/10.1016/j.sedgeo.2010.12.010.

Ozcelik, M., 2016. Evaluation of soft sediment deformation structures along the Fethiye–Burdur Fault Zone, SW Turkey. Journal of Earth System Science 125, 343-358, https://doi.org/10.1007/s12040-016-0671-4.

Persaud, M., Villamor, P., Berryman, K.R., Ries, W., Cousins, J., Litchfield, N., and Alloway, B.V., 2016. The Kerepehi Fault, Hauraki Rift, North Island, New Zealand: active fault characterisation and hazard. New Zealand Journal of Geology and Geophysics 59, 117-135, https://doi.org/10.1080/00288306.2015.1127826.

Peti, L., Hopkins, J.L., and Augustinus, P.C., 2021. Revised tephrochronology for key tephras in the 130-ka Ōrākei Basin maar core, Auckland Volcanic Field, New Zealand: implications for the timing of climatic changes. New Zealand Journal of Geology and Geophysics 64, 235-249, https://doi.org/10.1080/00288306.2020.1867200.

Pidhorskyi, S., Morehead, M., Jones, Q., Spirou, G., and Doretto, G., 2018. syGlass: interactive exploration of multidimensional images using virtual reality Head-mounted displays. arXiv preprint arXiv:1804.08197, https://doi.org/10.48550/arXiv.1804.08197.

Pope, M.C., Fred Read, J., Bambach, R., and Hofmann, H.J., 1997. Late Middle to Late Ordovician seismites of Kentucky, southwest Ohio and Virginia: sedimentary recorders of earthquakes in the Appalachian basin. Geological Society of America Bulletin 109, 489-503.

Rodríguez-Pascua, M.A., Calvo, J.P., De Vicente, G., and Gómez-Gras, D., 2000. Soft-sediment deformation structures interpreted as seismites in lacustrine sediments of the Prebetic Zone, SE Spain, and their potential use as indicators of earthquake magnitudes during the Late Miocene. Sedimentary Geology 135, 117-135, https://doi.org/10.1016/S0037-0738(00)00067-1.

Rodríguez-Pascua, M.A., Silva, P.G., Perucha, M.A., Giner-Robles, J.L., Heras, C., Bastida, A.B., Carrasco, P., Roquero, E., Lario, J., Bardají, T., Pérez-López, R., and Elez, J., 2016. Seismically induced liquefaction structures in La Magdalena archaeological site, the 4th century AD Roman Complutum (Madrid, Spain). Sedimentary Geology 344, 34-46, https://doi.org/10.1016/j.sedgeo.2016.01.025.

Rowley, J.R., and Dahl, A.O., 1956. Modifications in design and use of the Livingstone piston sampler. Ecology 37, 849-851, https://doi.org/10.2307/1933080

Schofield, J.C., 1965. The Hinuera Formation and associated Quaternary events (with an appendix on experimental alluviation). New Zealand Journal of Geology and Geophysics 8, 772-791.

Selby, M.J., and Lowe, D.J., 1992. The middle Waikato Basin and hills. In: Soons, J. M., and Selby, M. J. (eds.), Landforms of New Zealand: Second Edition. Longman Paul, Auckland, 233-255.

Sieh, K., and Bursik, M., 1986. Most recent eruption of the Mono Craters, eastern central California. Journal of Geophysical Research: Solid Earth 91, 12539-12571, https://doi.org/10.1029/JB091iB12p12539.

Stirling, M., McVerry, G., Gerstenberger, M., Litchfield, N., Van Dissen, R., Berryman, K., Barnes, P., Wallace, L., Villamor, P., and Langridge, R., 2012. National seismic hazard model for New Zealand: 2010 update. Bulletin of the Seismological Society of America 102, 1514-1542, https://doi.org/10.1785/0120110170.

Thomas, C.I., Ryan, M.A., Scholl, B., Guerrero-Given, D., Fitzpatrick, D., and Kamasawa, N., 2021. Targeting functionally characterized synaptic architecture using inherent fiducials and 3D correlative microscopy. Microscopy and Microanalysis 27, 156-169, https://doi.org/10.1017/S1431927620024757.

Törő, B., and Pratt, B.R., 2016. Sedimentary record of seismic events in the Eocene Green River Formation and its implications for regional tectonics on lake evolution (Bridger Basin, Wyoming). Sedimentary Geology 344, 175-204, https://doi.org/10.1016/j.sedgeo.2016.02.003.

Towhata, I., Taguchi, Y., Hayashida, T., Goto, S., Shintaku, Y., Hamada, Y., and Aoyama, S., 2017. Liquefaction perspective of soil ageing. Géotechnique 67, 467-478, http://dx.doi.org/10.1680/jgeot.15.P.046.

Tsuchida, H., 1970. Prediction and countermeasure against the liquefaction in sand deposits. Abstract of the seminar in the Port and Harbor Research Institute, 31-333

Van Dissen, R.J., Seebeck, H., Litchfield, N., Barnes, P., Nicol, A., Langridge, R.M., Barrell, D., Villamor, P., Ellis, S., Rattenbury, M., Bannister, S., Gerstenberger, M., and Ghisetti, F., 2021. Development of the New Zealand Community Fault Model – version 1.0. Proceedings of the 2021 New Zealand Society for Earthquake Engineering Annual Technical Conference, 1-9

Villamor, P., 2022. Paleoseismology of the newly discovered Te Puninga Fault, Hauraki Plains. EQC project number 20790 (Biennial Grants 2020) (GNS-EQC00036). Final Report BIG 012 2020, 31 December 2022. GNS Science.

Villamor, P., Almond, P., Tuttle, M.P., Giona-Bucci, M., Langridge, R.M., Clark, K., Ries, W., Bastin, S.H., Eger, A., and Vandergoes, M., 2016. Liquefaction features produced by the 2010–2011 Canterbury earthquake sequence in southwest Christchurch, New Zealand, and preliminary assessment of paleoliquefaction features. Bulletin of the Seismological Society of America 106, 1747-1771, https://doi.org/10.1785/0120150223.

Walker, M., Head, M.J., Lowe, J., Berkelhammer, M., BjÖrck, S., Cheng, H., Cwynar, L.C., Fisher, D., Gkinis, V., Long, A., Newnham, R., Rasmussen, S.O., and Weiss, H., 2019. Subdividing the Holocene Series/Epoch: formalization of stages/ages and subseries/subepochs, and designation of GSSPs and auxiliary stratotypes. Journal of Quaternary Science 34, 173-186, https://doi.org/10.1002/jqs.3097.

Walker, M., Johnsen, S., Rasmussen, S.O., Popp, T., Steffensen, J.P., Gibbard, P., Hoek, W., Lowe, J., Andrews, J., and Björck, S., 2009. Formal definition and dating of the GSSP (Global Stratotype Section and Point) for the base of the Holocene using the Greenland NGRIP ice core, and selected auxiliary records. Journal of Quaternary Science 24, 3-17, https://doi.org/10.1002/jqs.1227.

Watson, E.J., Swindles, G.T., Lawson, I.T., and Savov, I.P., 2016. Do peatlands or lakes provide the most comprehensive distal tephra records? Quaternary Science Reviews 139, 110-128, https://doi.org/10.1016/j.quascirev.2016.03.011.

Wells, J.T., Prior, D.B., and Coleman, J.M., 1980. Flowslides in muds on extremely low angle tidal flats, northeastern South America. Geology 8, 272-275.

White, J.D.L., and Houghton, B.F., 2006. Primary volcaniclastic rocks. Geology 34, 677-680, https://doi.org/10.1130/G22346.1.

Williams, P.W., 2021. Quaternary uplift and fault movement near Waitomo, North Island, New Zealand. New Zealand Journal of Geology and Geophysics, 1-11, https://doi.org/10.1080/00288306.2021.1996401.

Wolff-Boenisch, D., Gislason, S.R., Oelkers, E.H., and Putnis, C.V., 2004. The dissolution rates of natural glasses as a function of their composition at pH 4 and 10.6, and temperatures from 25 to 74 C. Geochimica et Cosmochimica Acta 68, 4843-4858, https://doi.org/10.1016/j.gca.2004.05.027.

Wood, F.M., Yamamuro, J.A., and Lade, P.V., 2008. Effect of depositional method on the undrained response of silty sand. Canadian Geotechnical Journal 45, 1525-1537, https://doi.org/10.1139/T08-079.

Yang, Q., Bursik, M., and Pouget, S., 2019. Stratigraphic and sedimentologic framework for tephras in the Wilson Creek Formation, Mono Basin, California, USA. Journal of Volcanology and Geothermal Research 374, 197-225, https://doi.org/10.1016/j.jvolgeores.2019.02.007.

Youd, T.L., 1991. Mapping of earthquake-induced liquefaction for seismic zonation. Proceedings of the Fourth International Conference on Seismic Zonation, 111-147

Zhou, Y.-G., Xia, P., Ling, D.-S., and Chen, Y.-M., 2020. Liquefaction case studies of gravelly soils during the 2008 Wenchuan earthquake. Engineering Geology 274, 105691, https://doi.org/10.1016/j.enggeo.2020.105691.

# Appendix E: Co-authorship forms

# Co-Authorship Form

**Postgraduate Studies Office**
Student and Academic Services Division
*Wahanga Ratonga Matauranga Akonga*
The University of Waikato
Private Bag 3105
Hamilton 3240, New Zealand
Phone +64 7 838 4439
Website: http://www.waikato.ac.nz/sasd/postgraduate/

This form is to accompany the submission of any PhD that contains research reported in published or unpublished co-authored work. **Please include one copy of this form for each co-authored work**. Completed forms should be included in your appendices for all the copies of your thesis submitted for examination and library deposit (including digital deposit).

Please indicate the chapter/section/pages of this thesis that are extracted from a co-authored work and give the title and publication details or details of submission of the co-authored work.

As it stands in the submitted thesis, chapter 3 has been published in Proceedings of the 7th International Young Geotechnical Engineers Conference – Scott (Ed.) ©2022 Australian Geomechanics Society, Sydney Australia, ISBN 978-0-9946261-5-8

| | |
|---|---|
| Nature of contribution by PhD candidate | Investigation, Conceptualization, Methodology, Data curation, Writing |
| Extent of contribution by PhD candidate (%) | 90% |

## CO-AUTHORS

| Name | Nature of Contribution |
|---|---|
| Max O. Kluger | Methodology, Supervision, Review and editing, Funding acquisition |
| Vicki G. Moon | Methodology, Supervision, Review and editing, Funding acquisition |
| David J. Lowe | Supervision, Review and editing, Funding acquisition |
| Rolando P. Orense | Supervision, Review and editing, Funding acquisition |
| | |
| | |

## Certification by Co-Authors

The undersigned hereby certify that:

the above statement correctly reflects the nature and extent of the PhD candidate's contribution to this work, and the nature of the contribution of each of the co-authors; and

| Name | Signature | Date |
|---|---|---|
| Max O. Kluger |  | 19 Jan 2024 |
| Vicki G. Moon |  | 22 Jan 2024 |
| David J. Lowe | 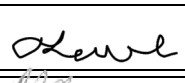 | 10 Jan 2024 |
| Rolando P. Orense |  | 22 Jan 2024 |
| | | |
| | | |

# Co-Authorship Form

**Postgraduate Studies Office**
Student and Academic Services Division
*Wahanga Ratonga Matauranga Akonga*
The University of Waikato
Private Bag 3105
Hamilton 3240, New Zealand
Phone +64 7 838 4439
Website: http://www.waikato.ac.nz/sasd/postgraduate/

This form is to accompany the submission of any PhD that contains research reported in published or unpublished co-authored work. **Please include one copy of this form for each co-authored work**. Completed forms should be included in your appendices for all the copies of your thesis submitted for examination and library deposit (including digital deposit).

Please indicate the chapter/section/pages of this thesis that are extracted from a co-authored work and give the title and publication details or details of submission of the co-authored work.

As it stands in the submitted thesis, chapter 4 has been published in Soil Dynamics and Earthquake Engineering 168, 2016; 107825 Doi: 10.1016/j.soildyn.2023.107825; © 2023 Elsevier Ltd.

| | |
|---|---|
| Nature of contribution by PhD candidate | Investigation, Conceptualization, Methodology, Data curation, Writing |
| Extent of contribution by PhD candidate (%) | 85% |

## CO-AUTHORS

| Name | Nature of Contribution |
|---|---|
| Max O. Kluger | Methodology, Supervision, Review and editing, Funding acquisition |
| Vicki G. Moon | Methodology, Supervision, Review and editing, Funding acquisition |
| David J. Lowe | Supervision, Review and editing, Funding acquisition |
| Rolando P. Orense | Supervision, Review and editing, Funding acquisition |
| | |
| | |

## Certification by Co-Authors

The undersigned hereby certify that:

the above statement correctly reflects the nature and extent of the PhD candidate's contribution to this work, and the nature of the contribution of each of the co-authors; and

| Name | Signature | Date |
|---|---|---|
| Max O. Kluger | 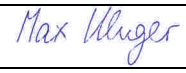 | 19 Jan 2024 |
| Vicki G. Moon |  | 22 Jan 2024 |
| David J. Lowe | 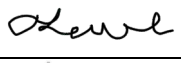 | 10 Jan 2024 |
| Rolando P. Orense |  | 22 Jan 2024 |
| | | |
| | | |

# Co-Authorship Form

**Postgraduate Studies Office**
Student and Academic Services Division
*Wahanga Ratonga Matauranga Akonga*
The University of Waikato
Private Bag 3105
Hamilton 3240, New Zealand
Phone +64 7 838 4439
Website: http://www.waikato.ac.nz/sasd/postgraduate/

This form is to accompany the submission of any PhD that contains research reported in published or unpublished co-authored work. **Please include one copy of this form for each co-authored work**. Completed forms should be included in your appendices for all the copies of your thesis submitted for examination and library deposit (including digital deposit).

Please indicate the chapter/section/pages of this thesis that are extracted from a co-authored work and give the title and publication details or details of submission of the co-authored work.

As it stands in the submitted thesis, chapter 5 has been accepted for the Proceedings of the 8th International Conference on Earthquake Geotechnical Engineering, to be held in May 2024, Osaka Japan

| | |
|---|---|
| Nature of contribution by PhD candidate | Investigation, Conceptualization, Methodology, Data curation, Writing |
| Extent of contribution by PhD candidate (%) | 90% |

## CO-AUTHORS

| Name | Nature of Contribution |
|---|---|
| Max O. Kluger | Supervision, Review and editing, Funding acquisition |
| Vicki G. Moon | Supervision, Review and editing, Funding acquisition |
| David J. Lowe | Supervision, Review and editing, Funding acquisition |
| Rolando P. Orense | Supervision, Review and editing, Funding acquisition |
| | |
| | |

## Certification by Co-Authors

The undersigned hereby certify that:

the above statement correctly reflects the nature and extent of the PhD candidate's contribution to this work, and the nature of the contribution of each of the co-authors; and

| Name | Signature | Date |
|---|---|---|
| Max O. Kluger | 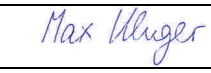 | 19 Jan 2024 |
| Vicki G. Moon |  | 22 Jan 2024 |
| David J. Lowe | 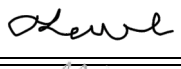 | 10 Jan 2024 |
| Rolando P. Orense |  | 22 Jan 2024 |
| | | |
| | | |

# Co-Authorship Form

**Postgraduate Studies Office**
Student and Academic Services Division
*Wahanga Ratonga Matauranga Akonga*
The University of Waikato
Private Bag 3105
Hamilton 3240, New Zealand
Phone +64 7 838 4439
Website: http://www.waikato.ac.nz/sasd/postgraduate/

This form is to accompany the submission of any PhD that contains research reported in published or unpublished co-authored work. **Please include one copy of this form for each co-authored work**. Completed forms should be included in your appendices for all the copies of your thesis submitted for examination and library deposit (including digital deposit).

Please indicate the chapter/section/pages of this thesis that are extracted from a co-authored work and give the title and publication details or details of submission of the co-authored work.

As it stands in the submitted thesis, chapter 6 will be submitted to Engineering Geology, soon after the submission of the thesis.

| | |
|---|---|
| Nature of contribution by PhD candidate | Investigation, Conceptualization, Methodology, Data curation, Writing |
| Extent of contribution by PhD candidate (%) | 90% |

## CO-AUTHORS

| Name | Nature of Contribution |
|---|---|
| Max O. Kluger | Methodology, Supervision, Review and editing, Funding acquisition |
| Tehuka Ilanko | Methodology, Supervision, Review and editing, Funding acquisition |
| Vicki G. Moon | Supervision, Review and editing, Funding acquisition |
| David J. Lowe | Supervision, Review and editing, Funding acquisition |
| Rolando P. Orense | Supervision, Review and editing, Funding acquisition |
| | |

## Certification by Co-Authors

The undersigned hereby certify that:

the above statement correctly reflects the nature and extent of the PhD candidate's contribution to this work, and the nature of the contribution of each of the co-authors; and

| Name | Signature | Date |
|---|---|---|
| Max O. Kluger |  | 19 Jan 2024 |
| Tehnuka Ilanko |  | 22 Jan 2024 |
| Vicki G. Moon | 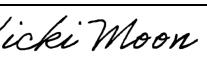 | 22 Jan 2024 |
| David J. Lowe | 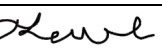 | 10 Jan 2024 |
| Rolando P. Orense |  | 22 Jan 2024 |
| | | |